

# **NDE Reliability Issues for the Examination of CASS Components**

## AVAILABILITY OF REFERENCE MATERIALS IN NRC PUBLICATIONS

### NRC Reference Material

As of November 1999, you may electronically access NUREG-series publications and other NRC records at NRC's Library at [www.nrc.gov/reading-rm.html](http://www.nrc.gov/reading-rm.html). Publicly released records include, to name a few, NUREG-series publications; *Federal Register* notices; applicant, licensee, and vendor documents and correspondence; NRC correspondence and internal memoranda; bulletins and information notices; inspection and investigative reports; licensee event reports; and Commission papers and their attachments.

NRC publications in the NUREG series, NRC regulations, and Title 10, "Energy," in the *Code of Federal Regulations* may also be purchased from one of these two sources.

#### 1. The Superintendent of Documents

U.S. Government Publishing Office  
Washington, DC 20402-0001  
Internet: [bookstore.gpo.gov](http://bookstore.gpo.gov)  
Telephone: (202) 512-1800  
Fax: (202) 512-2104

#### 2. The National Technical Information Service

5301 Shawnee Road  
Alexandria, VA 22312-0002  
[www.ntis.gov](http://www.ntis.gov)  
1-800-553-6847 or, locally, (703) 605-6000

A single copy of each NRC draft report for comment is available free, to the extent of supply, upon written request as follows:

Address: **U.S. Nuclear Regulatory Commission**  
Office of Administration  
Multimedia, Graphics, and Storage &  
Distribution Branch  
Washington, DC 20555-0001  
E-mail: [distribution.resource@nrc.gov](mailto:distribution.resource@nrc.gov)  
Facsimile: (301) 415-2289

Some publications in the NUREG series that are posted at NRC's Web site address [www.nrc.gov/reading-rm/doc-collections/nuregs](http://www.nrc.gov/reading-rm/doc-collections/nuregs) are updated periodically and may differ from the last printed version. Although references to material found on a Web site bear the date the material was accessed, the material available on the date cited may subsequently be removed from the site.

### Non-NRC Reference Material

Documents available from public and special technical libraries include all open literature items, such as books, journal articles, transactions, *Federal Register* notices, Federal and State legislation, and congressional reports. Such documents as theses, dissertations, foreign reports and translations, and non-NRC conference proceedings may be purchased from their sponsoring organization.

Copies of industry codes and standards used in a substantive manner in the NRC regulatory process are maintained at—

#### The NRC Technical Library

Two White Flint North  
11545 Rockville Pike  
Rockville, MD 20852-2738

These standards are available in the library for reference use by the public. Codes and standards are usually copyrighted and may be purchased from the originating organization or, if they are American National Standards, from—

#### American National Standards Institute

11 West 42nd Street  
New York, NY 10036-8002  
[www.ansi.org](http://www.ansi.org)  
(212) 642-4900

Legally binding regulatory requirements are stated only in laws; NRC regulations; licenses, including technical specifications; or orders, not in NUREG-series publications. The views expressed in contractor prepared publications in this series are not necessarily those of the NRC.

The NUREG series comprises (1) technical and administrative reports and books prepared by the staff (NUREG-XXXX) or agency contractors (NUREG/CP-XXXX), (2) proceedings of conferences (NUREG/CP-XXXX), (3) reports resulting from international agreements (NUREG/IA-XXXX), (4) brochures (NUREG/BR-XXXX), and (5) compilations of legal decisions and orders of the Commission and Atomic and Safety Licensing Boards and of Directors' decisions under Section 2.206 of NRC's regulations (NUREG-0750).

**DISCLAIMER:** This report was prepared as an account of work sponsored by an agency of the U.S. Government. Neither the U.S. Government nor any agency thereof, nor any employee, makes any warranty, expressed or implied, or assumes any legal liability or responsibility for any third party's use, or the results of such use, of any information, apparatus, product, or process disclosed in this publication, or represents that its use by such third party would not infringe privately owned rights.

# **NDE Reliability Issues for the Examination of CASS Components**

Manuscript Completed: July 2019

Date Published: September 2019

Prepared by:

R. E. Jacob

S. L. Crawford

T. L. Moran

M. R. Larche

M. S. Prowant

A. A. Diaz

C. A. Nove\*

Pacific Northwest National Laboratory

P.O. Box 999

Richland, Washington 99352

\*U.S. Nuclear Regulatory Commission

Carol Nove, NRC Project Manager





## ABSTRACT

The relatively low cost and corrosion resistance of cast austenitic stainless steel (CASS) materials resulted in their extensive use for piping systems in nuclear power plants (NPPs). However, CASS component welds are among the most challenging volumetric examinations required to be performed for detection of potential service degradation. Effective and reliable inspection methods for CASS materials are essential to achieving the objectives of defense-in-depth. A complicating issue is the presence of thermal aging embrittlement, a known degradation mechanism that occurs in CASS NPP materials. Further, while not as yet reported in CASS, many unforeseen instances of cracking in safety-related piping system welds have been experienced in other austenitic materials. Currently, a performance-based method to qualify NDE in CASS is not available.

Pacific Northwest National Laboratory (PNNL) has performed nondestructive examination (NDE) research under the sponsorship of the U.S. Nuclear Regulatory Commission (NRC) for over four decades. A primary objective of the research has been to assess the effectiveness and reliability of conventional and advanced NDE methods for the inspection of light-water reactor components. One of the tasks being performed within this framework is to evaluate state-of-the-art technical approaches for examining safety-related nuclear reactor components that pose significant challenges to traditional NDE methods. A specific area of research in this regard is the volumetric examination of coarse-grained weldments and base materials. This report summarizes, compiles, and assesses relevant investigations performed by PNNL and other domestic and international organizations for welds adjacent to CASS components to provide a comprehensive evaluation on this subject.

The primary objectives of the report are to assess the overall feasibility for advanced NDE methods to reliably and effectively examine field CASS piping components and to determine if techniques similar to those described in existing standards could be applied to develop performance demonstration requirements for CASS piping components. This report discusses improving the reliability of CASS examinations through the use of advanced low-frequency phased-array techniques, coupled with other “best practice” examination parameters, and makes recommendations for consideration by NRC Staff regarding the development of effective performance-based qualifications for CASS weldments. In addition to the PNNL research documented here, over 230 historical and more recent publications have been reviewed in the development of this document. The report is expected to be a useful resource for engineers and scientists involved in NDE of CASS for purposes of inservice inspection on existing plants during current and extended periods of operation. Finally, researchers and NDE practitioners conducting future investigations to advance the state-of-the-art should find the information contained in this report to be beneficial.



## FOREWORD

The requirement to inspect nuclear power plant systems, structures, and components (SSCs) is part of U.S. Nuclear Regulatory Commission's (NRC's) defense-in-depth philosophy. Inservice inspection (ISI) of welds in the primary coolant circuit of light water reactors is required to ensure that service-induced degradation does not compromise the structural integrity or the leak-tightness of safety-related components. Section XI of the American Society of Mechanical Engineers Boiler and Pressure Vessel Code (ASME Code), *Rules for Inservice Inspection of Nuclear Power Plant Components*, provides requirements for the examination, testing, and inspection of nuclear power plant SSCs, and is incorporated by reference in 10 CFR 50.55a. For those SSCs requiring qualified ultrasonic examination, ASME Code, Appendix VIII, *Performance Demonstration for Ultrasonic Examination Systems*, first published in the 1989 Addenda, provides the qualification requirements for performance-based testing of ultrasonic examination systems (i.e., procedures, equipment, and personnel) used to detect and size flaws during ISI. While Appendix VIII has successfully addressed the performance demonstration requirements for the majority of the ultrasonic examinations that require qualification, Appendix VIII, *Supplement 9 – Qualification Requirements for Cast Austenitic Piping Welds* remains “in the course of preparation.”

Cast austenitic stainless steel (CASS) piping was used in several United States pressurized water reactors. Since the initial construction of these plants, a need has existed to develop effective and reliable nondestructive examination (NDE) techniques for these CASS components and associated weldments. Because CASS presents significant inspection challenges, efforts to develop reliable and effective ultrasonic examination methods for CASS have been conducted by both the NRC and industry for decades; however, until the introduction of low frequency, phased-array ultrasonic testing (LF PA-UT), reliable examination has been elusive. While operating experience in the United States has not included failures of CASS components, research has shown that CASS is subject to thermal aging embrittlement. Thus, as plants age into their initial or subsequent license renewal periods of operation (to 60 years or 80 years, respectively), the likelihood of CASS degradation and failures increases.

Additionally, the wide-spread implementation of risk-informed ISI (RI-ISI) programs has resulted in the reduction of Class 1 and Class 2 welds subject to periodic ISI examinations. RI-ISI evaluations assume that NDE is highly reliable; that is, that the probability of detection is very high and degradation will be detected before a safety-related component is unacceptably compromised. With a lower number of welds being inspected, the inspections that are conducted must be effective and reliable. Thus, for CASS weldments, in order to maintain defense-in-depth, the ability to perform effective and reliable inspections has grown in significance as fewer welds are being inspected and the potential for thermal aging embrittlement is increasing with plant age.

Research has shown that examination of CASS piping weldments using conventional ultrasonic examination techniques has not provided sufficiently reliable detection and sizing performance for qualification via an ASME Code, Section XI, Appendix VIII qualification program. However, research in the last few years has shown that flaw detection in CASS weldments is possible with a high degree of confidence and low probability of false calls when techniques using low-frequency, phased-array probes are used, thus opening the possibility of successful development and implementation of Supplement 9 for qualification requirements for cast austenitic piping welds.

Since 1978, the NRC has sponsored research at Pacific Northwest National Laboratory (PNNL) on the challenging problem of examining CASS weldments. This NUREG/CR describes the challenges associated with CASS examinations, documents the history and evolution of CASS research at PNNL, and presents the results of their latest confirmatory research and laboratory evaluations using LF-PA-UT on thick-section CASS components. It also provides a technical basis to support future NRC rulemaking related to ASME Code, Section XI, Appendix VIII, Supplement 9 performance demonstration requirements. Further, the appendices provide the reader with a broader look at worldwide CASS research and related issues, and the reference chapter provides approximately 230 references related to CASS inspections including several PNNL reports documenting the progression of their NRC-sponsored research into CASS examinations.

Results of the research presented in this NUREG/CR show that there are specific examination attributes that must be accounted for and addressed in order to achieve an effective and reliable ultrasonic examination of CASS components. The examiner must apply an adequate sound field for the examination. In addition, spatial encoding and generation of volumetric ultrasonic images for analyses are needed. Having a good understanding of probe performance, sound field dimensions, propagation characteristics, and the material being examined are critical toward achieving an effective examination. Finally, effective training and practice on representative CASS mockups will further support successful examinations.

# TABLE OF CONTENTS

<b>ABSTRACT .....</b>	<b>iii</b>
<b>FOREWORD .....</b>	<b>v</b>
<b>LIST OF FIGURES .....</b>	<b>ix</b>
<b>LIST OF TABLES .....</b>	<b>xvii</b>
<b>EXECUTIVE SUMMARY .....</b>	<b>xix</b>
<b>ACKNOWLEDGMENTS .....</b>	<b>xxiii</b>
<b>ABBREVIATIONS AND ACRONYMS .....</b>	<b>xxv</b>
<b>1 INTRODUCTION.....</b>	<b>1-1</b>
1.1 Background.....	1-1
1.2 Objectives .....	1-2
1.3 Highlights of CASS Examination and Materials Research Activities .....	1-2
1.3.1 Examination of CASS Piping Systems .....	1-3
1.3.2 CASS Research Highlights .....	1-3
<b>2 CASS OVERVIEW AND MICROSTRUCTURAL VARIABILITY .....</b>	<b>2-1</b>
<b>3 INSPECTION REQUIREMENTS FOR CASS WELDMENTS AND REGULATORY BACKGROUND.....</b>	<b>3-1</b>
3.1 Inspection Requirements .....	3-1
3.2 Plant Life Extension Requirements for CASS.....	3-2
<b>4 EXPECTED SERVICE DEGRADATION IN CASS.....</b>	<b>4-1</b>
<b>5 INTRODUCTION TO ULTRASONIC EXAMINATION ISSUES IN CASS.....</b>	<b>5-1</b>
5.1 Implications of Anisotropy .....	5-1
5.2 UT Beam Propagation and Sound Field Distortion in CASS .....	5-2
5.3 In Situ Microstructure Assessments.....	5-8
<b>6 CASS RESEARCH LEADING TO LOW-FREQUENCY UT .....</b>	<b>6-1</b>
6.1 Early Work, Round-Robin Exercises, and Cooperative Results .....	6-1
6.2 Development of LF-SAFT .....	6-3
6.3 Transition to Low-Frequency Phased Array UT.....	6-7
<b>7 UT FLAW DETECTION OF A CASS TO CARBON STEEL DISSIMILAR METAL WELD.....</b>	<b>7-1</b>
7.1 Wrought Stainless Steel Spatial and Depth Resolution and Probe Spot Size Summary .....	7-1
7.1.1 Specimen Description.....	7-1
7.1.2 CASS Manoir Ring Spatial and Depth Resolution Summary .....	7-10
7.1.3 Conclusions .....	7-16

7.2	Dissimilar Metal Weld Specimen .....	7-16
7.2.1	Specimen 14C-146.....	7-16
7.3	Eddy Current Validation of Flaw True State.....	7-32
7.3.1	ET Data Acquisition .....	7-33
7.3.2	Eddy Current Testing Results.....	7-35
7.3.3	Eddy current testing conclusions.....	7-39
7.4	UT Hardware, Setup, and Data Acquisition .....	7-39
7.4.1	Data Acquisition.....	7-42
7.5	Data Analysis and Results.....	7-49
7.5.1	UT Line Scans.....	7-49
7.6	Summary and Discussion .....	7-80
<b>8</b>	<b>CONDUCTING EFFECTIVE AND RELIABLE EXAMINATIONS IN CASS PIPING WELDS.....</b>	<b>8-1</b>
8.1	Applying Adequate Sound Fields for CASS Examinations .....	8-1
8.1.1	Optimizing Frequency.....	8-1
8.1.2	Applying Effective Beam Propagation Angles .....	8-3
8.1.3	Introducing Sufficient Sound Field Intensities.....	8-23
8.2	Use of Encoded Data with Volumetric Analytical Imaging Techniques.....	8-24
8.2.1	The Use of Modeling to Facilitate Reliable Examinations .....	8-29
8.3	Training of Examiners for CASS Examinations .....	8-32
8.4	CASS “Best Effort” Examinations and the Need for Applicable Qualification Criteria .....	8-33
8.4.1	Introduction.....	8-33
8.4.2	Discussion .....	8-34
<b>9</b>	<b>CONCLUSIONS.....</b>	<b>9-1</b>
<b>10</b>	<b>REFERENCES.....</b>	<b>10-1</b>
<b>APPENDIX A</b>	<b>HISTORICAL CASS RESEARCH .....</b>	<b>A-1</b>
<b>APPENDIX B</b>	<b>WORKSHOPS – INSPECTION OF CASS PIPING.....</b>	<b>B-1</b>
<b>APPENDIX C</b>	<b>COOPERATIVE AND INTERNATIONAL CASS RESEARCH.....</b>	<b>C-1</b>
<b>APPENDIX D</b>	<b>MPATS DETECTION AND CHARACTERIZATION CRITERIA .....</b>	<b>D-1</b>
<b>APPENDIX E</b>	<b>CASS WELDMENT EXAMINATION COVERAGE ISSUES.....</b>	<b>E-1</b>
<b>APPENDIX F</b>	<b>LITERATURE REVIEW FOR CASS RESEARCH .....</b>	<b>F-1</b>

## LIST OF FIGURES

Figure 2-1	Cast Stainless Steel Material in Primary Coolant System for Westinghouse-Designed Pressurized Water Reactor Four-Loop Plant (based on Westinghouse diagrams; illustration courtesy of A. Chockie, CGI). .....	2-1
Figure 2-2	Example of Equiaxed Grain Structure (specimen courtesy of EPRI) .....	2-3
Figure 2-3	Variation of Grains in Mixed/Banded CCSS Piping from IHI Southwest Technologies, Inc. ....	2-4
Figure 2-4	Portion of CCSS Piping Specimen Showing Dendritic Grain Structure Consistent Throughout Circumference.....	2-4
Figure 2-5	Portion of Later Vintage CCSS Piping Segment Showing Slightly More Refined Equiaxed Grains Throughout .....	2-5
Figure 3-1	Licensee Calculated Volumetric Coverage and Largest Undetected Flaw for Weld 30-RC-21B-10 (adapted from PNNL 2013b).....	3-2
Figure 5-1	Experimental Set-up for Assessing Sound Fields in CASS Specimens. <i>Top left</i> – schematic for experiment, <i>top right</i> – photo of receiving pinducer on specimen as seen from side of immersion tank, <i>bottom left</i> – axial view showing fiducial emitter used to mark spatial coordinates, and <i>bottom right</i> – sample image of as-received sound field and fiducial emitter. ....	5-3
Figure 5-2	Sound Field Images on Wrought Stainless Steel Specimen at Same Metal Path and 45° Propagation Angle Using 500 kHz ( <i>left</i> ), 800 kHz ( <i>middle</i> ) and 1.0 MHz ( <i>right</i> ) for Benchmarking Purposes. ....	5-3
Figure 5-3	Sound Field in Fully Dendritic Specimen at a 45° Refracted Angle and 0° Beam Skew. In this example, sound fields at 500 kHz ( <i>top row</i> ), 800 kHz ( <i>middle row</i> ), and 1.0 MHz ( <i>bottom row</i> ) probe frequencies are illustrated in slices 0–3, <i>left to right</i> . The data file for one 500 kHz scan ( <i>upper right</i> ) was corrupted. ....	5-4
Figure 5-4	Sound Field in Fully Equiaxed Specimen at a 45° Refracted Angle and 0° Beam Skew. In this example, sound fields at 500 kHz ( <i>top row</i> ), 800 kHz ( <i>middle row</i> ), and 1.0 MHz ( <i>bottom row</i> ) probe frequencies are illustrated in slices 0–3, <i>left to right</i> . ....	5-5
Figure 5-5	Sound Field in Mixed/Banded Specimen at a 45° Refracted Angle and 0° Beam Skew. In this example, sound fields at 500 kHz ( <i>top row</i> ), 800 kHz ( <i>middle row</i> ), and 1.0 MHz ( <i>bottom row</i> ) probe frequencies are illustrated in slices 0–3, <i>left to right</i> . ....	5-6
Figure 5-6	Second Mixed/Banded Specimen at a 45° Refracted Angle and 0° Beam Skew with 0.5, 0.8, and 1.0 MHz Probe Frequencies, <i>Top to Bottom</i> , and Slices 0–3, <i>Left to Right</i> . ....	5-7
Figure 5-7	Illustration of the Rayleigh Critical Angle Technique .....	5-8
Figure 5-8	A Representative Axial-Radial Cross Section of a CASS Specimen, Showing Typical Grain Structures on Either Side of the Weld Outside and Inside Diameter Geometry, and Microstructure of a Specimen. ....	5-9
Figure 5-9	Scatter Plot of Longitudinal Wave against Shear Wave Time-of-Flight (TOF).....	5-10

Figure 5-10	Feritscope and XRF Measurement Grids. The figure shows the fine-grid scans on the outer-diameter surface and the side (axial-radial cross section) surfaces for the columnar and equiaxed grain sections. ....	5-11
Figure 6-1	Logistic Curve Fit to Probability of Detection Data with 95% Bounds (cast stainless steel, near-side inspections, all teams): (a) probability of detection versus depth; (b) probability of detection versus length. ....	6-2
Figure 6-2	Application Window and Controls for SAA Size Filter .....	6-5
Figure 6-3	Application Window and Controls for Fuse All Tool.....	6-6
Figure 6-4	Beam Forming Using PA (courtesy of R/D Tech, Inc.).....	6-7
Figure 6-5	Modified Tomoscan III with Typical Acquisition Data Station .....	6-8
Figure 6-6	Zetec DYNARAY Off-the-Shelf Phased Array Instrument with Low-Frequency Capabilities .....	6-8
Figure 6-7	Typical Analysis Images Used for Phased-Array Inspection .....	6-10
Figure 6-8	Example of Volumetrically Merged PA Data.....	6-11
Figure 6-9	Typical Analysis Images Used for Phased Array Inspection (Figure 2.6, NUREG/CR-6933).....	6-12
Figure 6-10	Typical Analysis Screen with Mid-Range Angle (53°) Selected, Showing Weld Root with TRL Array (Figure 2.7, NUREG/CR-6933).....	6-12
Figure 6-11	Typical Analysis Screen with High Angle (65°) Selected, Showing Flaws with TRL Array (Figure 2.8, NUREG/CR-6933).....	6-13
Figure 6-12	500 kHz Prototype Phased Array .....	6-14
Figure 6-13	Improved Design of 500 kHz Phased Array Probe.....	6-15
Figure 6-14	Current (latest) Generation of 500 kHz PA Probe .....	6-16
Figure 6-15	Side View of Sound Profile Generated in Zetec UltraVision Software to Assess Beam Intensity and Coherence of 500 kHz Phased Array for 45° ( <i>left</i> ) and 60° ( <i>right</i> ) Propagation Angles in Isotropic Stainless-Steel Media. ....	6-17
Figure 7-1	Wrought Stainless-Steel Resolution Specimen. The axial holes for spatial resolution (primary) and circumferential holes for lateral resolution used in this study are encircled by the red and blue ovals, respectively. The green arrow indicates the scan direction for both sets of holes. ....	7-2
Figure 7-2	500 kHz PA Probe .....	7-3
Figure 7-3	800 kHz PA Probe .....	7-3
Figure 7-4	1.5 MHz PA Probe.....	7-4
Figure 7-5	2.0 MHz PA Probe.....	7-4
Figure 7-6	Data Acquisition System and Laboratory Workstation. <i>Left</i> : DYNARAY PA data acquisition system (courtesy of Zetec). <i>Right</i> : Laboratory workstation for both data acquisition and data analysis, with the DYNARAY system on the lower shelf. ....	7-5
Figure 7-7	True Depth and Half Path Focusing. Illustration of true depth focusing, where the ultrasonic beam is focused at the ID surface for all refraction angles ( <i>left</i> ) and half path focusing, where the beam is focused at a constant distance from the probe ( <i>right</i> ). ....	7-5
Figure 7-8	Rayleigh Resolution for a Focused Circular Probe. Peaks are resolved if a 19% dip is realized. ....	7-6



Figure 7-9	A Series of Axially Oriented Spatial Resolution Holes at 1.5 MHz, True Depth Focus. All holes were resolved. ....	7-7
Figure 7-10	A Series of Circumferentially Oriented Spatial Resolution Holes at 1.5 MHz, True Depth Focus. Only Holes 1 and 2 were resolved in this example. ....	7-7
Figure 7-11	Manoir Ring Specimen. Sets of resolution holes were machined axially (red oval) and circumferentially (blue ovals). The circumferential holes at the center of the specimen are straight and those at the edge are angled. The scan origin is indicated by the green arrows. ....	7-11
Figure 7-12	A Series of Circumferentially Oriented Resolution Holes at 800 kHz, Half Path Focus, 0° Beam Skew. The hole true-state positions correspond to the label positions. Only Holes 1 and 2 were resolved. ....	7-12
Figure 7-13	DMW Mockup as Received by PNNL.....	7-17
Figure 7-14	Axial Schematic of the Mockup. This figure shows the general construction of the mockup, with the carbon steel end on the left and the CASS end on the right.....	7-17
Figure 7-15	Axial Detail of the Weld Joint.....	7-18
Figure 7-16	End Schematic of the Mockup. This view shows the flaw placement, the specimen circumferential origin (center of Flaw 1), and the cutout region. ....	7-19
Figure 7-17	Section of the Mockup Cut for Grain Size Measurements. The mockup came with a section in the cutout region that was removed (see red dashed line). The section was cut, polished, and etched axially and circumferentially.....	7-20
Figure 7-18	Cut and Polished Axial and Circumferential Sections. This figure shows the cut sections in the orientation as they were on the original specimen. The sections are sitting with the OD upward. ....	7-21
Figure 7-19	The Polished and Etched Axial Section. This figure shows the axial grain structure of the removed section. Note the heterogeneity in grain size and structure. The OD is at the top of the figure.....	7-22
Figure 7-20	The Polished and Etched Circumferential Section. This figure shows the circumferential grain structure of the removed section, revealing considerable heterogeneity in grain structure type, size, and distribution. The OD is at the top of the figure. ....	7-23
Figure 7-21	False Color Image of the Different Grain Regions Identified in the Axial Section.....	7-23
Figure 7-22	False Color Image of the Different Grain Regions Identified in the Circumferential Section .....	7-24
Figure 7-23	Details of the Five Implanted Flaws. The through-wall depths and positions relative to the weld centerline of the five implanted flaws are shown in axial views as reported by FlawTech. ....	7-26
Figure 7-24	Photograph of Flaw 1 (10% circ). The red oval encircles the flaw location. This flaw is not readily visible, and it is unclear whether imperfections on the inner-diameter surface are flaw-related. The CASS end is upward. ....	7-28
Figure 7-25	Photograph of Flaw 2 (20% axial). The red oval encircles the flaw location. Imperfections visible on the inner-diameter surface may be flaw-related, but the whole flaw is not visible. The CASS end is upward.....	7-29

Figure 7-26	Photograph of Flaw 3 (20% circ). This flaw is visible within the red oval, approximately spanning the region between 105–205 mm on the ruler. The CASS end is upward. ....	7-30
Figure 7-27	Photograph of Flaw 4 (16% circ). This flaw is in the butter region on the carbon steel side of the weld. It is visible below the ruler within the red oval and spans from approximately 110–190 mm on the ruler. The CASS end is upward. Some grind marks are visible above the ruler. ....	7-31
Figure 7-28	Photograph of Flaw 5 (40% axial). This axially-oriented flaw is visible within the red oval, spanning from approximately 140–155 mm on the ruler. The CASS end is upward. ....	7-32
Figure 7-29	UniWest US-3228 Pencil Probe .....	7-34
Figure 7-30	Zetec Spot Probe.....	7-34
Figure 7-31	Data Acquisition Using the US-3228 Probe.....	7-35
Figure 7-32	Data Acquisition Using the Zetec Spot Probe .....	7-35
Figure 7-33	UniWest US-3228 Plus-Point 400kHz Calibration Data. Pink pixels are at or above the maximum amplitude of the detection notch, seen at the far right. ....	7-36
Figure 7-34	Flaw 1 Results Acquired with the Zetec Spot Probe in Plus-point ( <i>left</i> ) and Cross-point Configurations ( <i>right</i> ).....	7-37
Figure 7-35	Flaw 2 Results Acquired with the Zetec Spot Probe in Plus-point ( <i>left</i> ) and Cross-point Configurations ( <i>right</i> ).....	7-37
Figure 7-36	Comparison of FlawTech-reported True-state and ET-measured Flaw Lengths and Positions. Results for both probes in plus-point configuration (0° rotation) and cross-point configuration (45° rotation) are shown. ....	7-38
Figure 7-37	500 kHz RTD Probes. 30° probe ( <i>left</i> ) and 45° probe ( <i>right</i> ), inverted. The bottom of the 45° probe shows the cork damping medium between the elements and provides an example of wedge contouring required for adequate coupling of probes of this size. ....	7-40
Figure 7-38	Corner Scan on the Vertically Oriented Specimen. This scan is being done with the 800 kHz PA probe. ....	7-43
Figure 7-39	Scanning the Horizontally Oriented Mockup. The red arrow is the positive axial direction, and the blue arrow is the positive circumferential direction. The weld centerline (WCL) is indicated by the white line. ....	7-44
Figure 7-40	Illustration of How Circumferential Scanning Affects Impingement Angle. Circumferential scanning results in a higher impingement angle due to the curvature of the pipe. At higher refraction angles, a beam that might otherwise interact with the ID surface might miss the surface altogether if pipe curvature is not accounted for in the focal laws. ....	7-47
Figure 7-41	True-depth Focusing during Circumferential Scanning of Axial Flaws. The curvature of the pipe forces the focal distance and angle of impingement to increase at higher angles. ....	7-48
Figure 7-42	Impingement Angle versus Refraction Angle .....	7-48
Figure 7-43	Line Scan with the 500 kHz PA Probe. Multi-line merge with all lines and all angles ( <i>top</i> ) and single-line merge with all angles from one line ( <i>middle</i> ) of Flaws 1 and 3 (red arrows). Multi-line merge of Flaw 4 (red arrow) ( <i>bottom</i> ). Flaws 2 and 5 were axially oriented and not visible in these scans.....	7-50

Figure 7-44	Line Scan with the 1.5 MHz PA Probe. Multi-line merge with all lines and all angles ( <i>left</i> ) and single-line merge with all angles from one line ( <i>right</i> ). This scan covers the region containing Flaws 1 and 3 (red arrows). Flaw 2 is axially oriented and was not visible in this scan. The tip of Flaw 3 is indicated by the blue arrows. The tip of Flaw 1 was visible but not well resolved. ....	7-51
Figure 7-45	Flaw 1 (10% through-wall) as Visualized with the Six Different Probes. This illustrates an example of how visualization of a single flaw varied with the different probes. Clockwise in each panel: sectoral view, C-scan, B-scan, and D-scan. ....	7-54
Figure 7-46	Example Comparison of TD and HP Focusing. Minimal differences are visible between the two focusing types. Clockwise in each panel: sectoral view, C-scan, B-scan, and D-scan. ....	7-61
Figure 7-47	Example Comparison of Different Beam Skews. Images show scans of Flaw 3 (20% through-wall) with the 500 kHz PA probe at 41°. Clockwise in each panel: sectoral view, C-scan, B-scan, and D-scan. ....	7-62
Figure 7-48	Example of a Flaw with Signal Dropout. Flaw 3 (25% through-wall) is shown measured with the 800 kHz probe. In spite of signal dropout at the -6 dB level, it is known that the signal emanates from a single defect. Clockwise in the figure: sectoral view, C-scan, B-scan, and D-scan. ....	7-63
Figure 7-49	Length RMSE and SNR. The length RMSE (blue) for the PA probes is much lower than that of the 500 kHz RTD probes while the SNR (green) for the PA probes is higher. The 500 kHz PA probe had the highest SNR overall with length RMSE comparable to that of the 800 kHz PA probe. Note: data acquired at 1500 and 2000 kHz were scanned from the carbon steel side of the mockup. The probe labels refer to the PA probes in kHz and RTD probes in refracted angle. ....	7-64
Figure 7-50	Comparison of the 30° RTD Probe and the 500 kHz PA Probe. Flaw 3 (20% through-wall) is shown as scanned with the 30° RTD probe ( <i>left</i> ) and the 500 kHz PA probe at 30° refraction angle ( <i>right</i> ). The SNR of the RTD probe is 6.8 dB while the SNR of the PA probe is 13.8 dB. Note that the signal intensities are not normalized. ....	7-67
Figure 7-51	Flaw 2 (20% through-wall, axial) as Scanned by the 500 kHz PA Probe. The skew 0° scan is on the left and the skew 180° scan is on the right. The refraction angle is 35°, and the impingement angle is 45°. Clockwise in the panels: sectoral view, C-scan, B-scan, and D-scan. ....	7-68
Figure 7-52	Flaw 2 (20% through-wall, axial) as Scanned by the 800 kHz PA Probe. The skew 0° scan is on the left and the skew 180° scan is on the right. The refraction angle is 26°, and the impingement angle is 32°. Clockwise in the panels: sectoral view, C-scan, B-scan, and D-scan. ....	7-68
Figure 7-53	Flaw 5 as Scanned by the 2.0 MHz PA Probe. The refraction angle is 26° and the impingement angle is 32°. Spurious signals and strong background signals complicate flaw detection. Clockwise in the panels: sectoral view, C-scan, B-scan, and D-scan. ....	7-69
Figure 7-54	No-Flaw Region as Scanned by the 2.0 MHz PA Probe. The refraction angle is 26° and the impingement angle is 32°. Spurious signals and strong background signals persist in and near the weld region. Clockwise in the panels: sectoral view, C-scan, B-scan, and D-scan. ....	7-70

Figure 7-55	Example of a Far-Side Detection. This figure shows Flaw 4 (16% through-wall) as detected by the 500 kHz PA probe at 48°. Clockwise in the image: sectoral view, C-scan, B-scan, and D-scan. ....	7-70
Figure 7-56	An Example of Improved Tip Visualization with Increasing Refraction Angle. Shown are scans of Flaw 3 (20% through-wall) with the 500 kHz PA probe. The tip, best visualized in the B-scan and D-scan, begins to appear at 39° and is stronger (compared to the corner response) at 45° (red arrows). Clockwise in the panels: sectoral view, C-scan, B-scan, and D-scan. ....	7-75
Figure 7-57	Example of a Tip Signal that is Stronger than a Corner Response. This figure shows Flaw 5 (40% through-wall, axial) as scanned with the 800 kHz PA probe. The tip, visible in the B-scans and D-scans, becomes brighter than the corner at 35°. An artifact, whose signal intensity remains relatively consistent, is indicated by the red arrow. Clockwise in the image: sectoral view, C-scan, B-scan, and D-scan. ....	7-76
Figure 7-58	Example of a Tip Signal in a Far-Side Detection. This figure shows Flaw 4 (16% through-wall) as detected by the 800 kHz PA probe at 42°. The flaw tip is indicated by the red arrow. Clockwise in the image: sectoral view, C-scan, B-scan, and D-scan. ....	7-77
Figure 7-59	Example of a Tip Signal in a 10% Through-Wall Flaw showing Flaw 1 as Detected by the 1.5 MHz PA Probe at 41°. The red arrow indicates the tip signal, which is better resolved in the B-scan than in the D-scan. Clockwise in the image: sectoral view, C-scan, B-scan, and D-scan. ....	7-77
Figure 7-60	Detection of an Axial Flaw at 1.5 MHz. Spurious signals in and around the weld region complicate detection and measurement of the flaw. Clockwise in the panels: sectoral view, C-scan, B-scan, and D-scan. ....	7-78
Figure 7-61	The No-Flaw Region as Scanned by the 1.5 MHz PA Probe. Clockwise in the panels: sectoral view, C-scan, B-scan, and D-scan. ....	7-78
Figure 7-62	Possible Implantation Artifact. Scan of Flaw 3 (20% Through-wall) at 800 kHz, 29° refracted angle, TD84. Circled in red are artifacts that approximately form an arc above the flaw corner response, possibly indicating the edges of the implanted flaw coupon. ....	7-79
Figure 7-63	Possible Fabrication Artifact. Scan of a no-flaw region at 800 kHz, 29° refracted angle, TD84. ....	7-80
Figure 8-1	POD Curves for 500 kHz versus 1.0 MHz and Greater Frequencies Applied During EPRI CASS Round Robin Exercise. Note the improved POD for the lower frequency application. ....	8-2
Figure 8-2	Specimen B-519E. This specimen from PNNL has a smaller-to-medium grain equiaxed microstructure. Figure adapted from PNNL-23393 (Crawford et al. 2014). ....	8-5
Figure 8-3	Manoir Ring. This pipe segment from the Manoir Foundry exhibits a small-grained equiaxed microstructure. ....	8-5
Figure 8-4	Specimen ONP-D-5. This specimen originated from the Westinghouse Owners Group and has a larger, coarse-grained equiaxed microstructure. Figure adapted from NUREG-CR/6933 (Anderson et al. 2007). ....	8-6
Figure 8-5	Specimen B-519C. This specimen from PNNL has a medium-grained, columnar microstructure with little or no banding. Figure adapted from PNNL-23393 (Crawford et al. 2014). ....	8-6

Figure 8-6	Westinghouse Specimen. This specimen from Westinghouse, Inc. shows a columnar microstructure with large grains and some banding. Figure adapted from NUREG/CR-6933 (Anderson et al. 2007). ....	8-7
Figure 8-7	IHI Southwest Specimen. Mixed/banded grain microstructure with considerable circumferential heterogeneity. Figure adapted from NUREG/CR-6933 (Anderson et al. 2007).....	8-7
Figure 8-8	Specimen 14C-146. Mixed/banded-grain microstructure, predominately equiaxed in the midwall regions and columnar near the OD and ID. ....	8-8
Figure 8-9	Incremental Beam Simulations of 500 kHz TRL Transducer, 20°–70° .....	8-9
Figure 8-10	Example of Acquired Data. This figure shows an example of a B-scan ( <i>left</i> ) with end-of-block and noise regions enclosed, and the selected end-of-block D-scan ( <i>right</i> ). ....	8-10
Figure 8-11	End-of-Block Signal for All Specimens. The end-of-block D-scan signal from each specimen at 500 kHz and 30° is shown. A) B-519E; B) Manoir (skew 0); C) Manoir (skew 180); D) ONP-D-5; E) B-519C; F) Westinghouse (skew 0); G) Westinghouse (skew 180); H) IHI (skew 0); I) IHI (skew 180); J) 14C-146 (section 1); K) 14C-146 (section 2); L) wrought stainless steel. ....	8-12
Figure 8-12	Example of Data Analysis. The end-of-block signal is shown as an echo-dynamic curve (black line). The mean noise (light blue line) was determined from the noise (dark blue line). Regions of dropout are identified as those with signal dropping below the 3:1 (pink) or 2:1 (green) SNR thresholds. Regions of dropout are shown with bold lines. Numbers on the right indicate the percentage dropout and maximum dropout length for each respective noise threshold. Data shown are from 14C-146 at 40°. ....	8-13
Figure 8-13	Example Data from the Westinghouse Specimen. UT corner scan data and the associated 3:1 SNR dropout graphs are shown for 25°–50° refraction angles at 500 kHz.....	8-14
Figure 8-14	Noise and Percent Dropout vs. Angle. The noise (% of FSH, left axis) and dropout (% of scan length, right axis) at 500 kHz are plotted vs. refraction angle for several example scans. The noise levels from the WSS specimen are included for comparison. ....	8-16
Figure 8-15	Specimen B-505 Showing Machined ID Notches Used for Reflectors in This Flaw Persistence Study. Only the notches located parallel and adjacent to the end of block on each side were measured. Note the side-drilled holes and other notch near the weld counterbore were not measured and did not affect scans on the target notches.....	8-27
Figure 8-16	Noise Level for a Single A-scan (blue) and Peak Noise of a Scan Area (purple) .....	8-28
Figure 8-17	C-scan of Notch and Corner Response Collected, Highlighting Analyzed Scan Lines. The two-line scans used for analysis are labeled with their maximum SNR levels: 3.26 and 2.12. ....	8-28



## LIST OF TABLES

Table 1-1	CASS Studies Employing Conventional UT Methods .....	1-5
Table 1-2	Significant Findings or Events that Influenced CASS Research .....	1-10
Table 7-1	Hole Separation Values for Probe Spatial Resolution Measurements .....	7-1
Table 7-2	Phased Array Probe Specifications .....	7-2
Table 7-3	Average Beam Spot Size in mm (in.) .....	7-8
Table 7-4	Ratio of Edge-to-Edge Separation to the -3 dB Spot Size (Wrought Stainless Steel).....	7-9
Table 7-5	Ratio of Edge-to-Edge Separation to the -6 dB Spot Size (Wrought Stainless Steel).....	7-9
Table 7-6	Spacing of Holes .....	7-11
Table 7-7	Percentage of Time that Holes are Resolved in Relation to Probe Frequency and Beam Skew .....	7-13
Table 7-8	Percentage of Time that Holes are Resolved in Relation to Flaw Orientation as well as Probe Frequency and Beam Skew .....	7-14
Table 7-9	Average Probe Spot Sizes, in mm (in.) .....	7-14
Table 7-10	Ratio of Edge-to-Edge Separation to the -3 dB Spot Size (CASS) .....	7-15
Table 7-11	Ratio of Edge-to-Edge Separation to the -6 dB Spot Size (CASS) .....	7-15
Table 7-12	Grain Size Measurements Made from the Axial and Circumferential Cut Sections. Boldface and italic type indicate average grain extents that exceed $0.2\lambda$ for at 800 kHz and 500 kHz, respectively. ....	7-25
Table 7-13	FlawTech-reported True-state Flaw Orientations, Lengths, and Depths. Depth % is the percentage of through-wall thickness. Measured depth results of UT scans from the carbon steel side are included in the last column. ....	7-27
Table 7-14	Phased Array Probe Specifications (includes 2 MHz probe).....	7-40
Table 7-15	RTD Probe Specifications .....	7-41
Table 7-16	Spot Sizes of the 500 kHz PA and RTD Probes.....	7-41
Table 7-17	Wedge Specifications. Axial wedges are used to detect circumferentially oriented flaws and vice versa. ....	7-42
Table 7-18	Scan Matrix. This table shows the completed scans for each probe and the mockup orientation. ....	7-45
Table 7-19	Flaw Characteristics as Measured from the Line Scans. The table shows the measured length, depth, and SNR of the three circumferential flaws with all four PA probes in comparison to the FlawTech-reported lengths and depths. The length RMSE value is given. There was insufficient data for a depth RMSE value. ....	7-52
Table 7-20	Comparison of TD and HP Focusing.....	7-58
Table 7-21	Comparison of Beam Skews at 500 and 800 kHz. The table shows the ratio of the corner to tip signal in dB, length, depth, and SNR of the five flaws. ....	7-59
Table 7-22	Length Sizing and SNR Measured by the 500 and 800 kHz PA Probes and the 500 kHz RTD Probes. Length RMSE and mean SNR are also shown. Recall that the axial flaws (Flaw 2 and Flaw 5) were not scanned with the RTD probes. ....	7-65

Table 7-23	Length Sizing and SNR Measured by the 1.5 and 2.0 MHz PA Probes. Length RMSE and mean SNR are also shown. Length measurements in boldface indicate that a -6 dB gap was present but ignored. ....	7-66
Table 7-24	Flaw Depth Sizing with the 500 kHz PA Probe. The measured depth, depth RMSE, and the corner-to-tip signal ratio (in dB) are shown. ....	7-71
Table 7-25	Flaw Depth Sizing with the 800 kHz PA Probe. The measured depth, depth RMSE, and the corner-to-tip signal ratio (in dB) are shown. ....	7-72
Table 7-26	Flaw Depth Sizing with the 500 kHz PA Probe. The measured depth, depth RMSE, and the corner-to-tip signal ratio (in dB) are shown. . A C:T ratio <0 indicates a brighter tip signal than corner signal.....	7-72
Table 7-27	Flaw Depth Sizing with the 800 kHz PA Probe. The measured depth, depth RMSE, and the corner-to-tip signal ratio (in dB) are shown. A C:T ratio <0 indicates a brighter tip signal than corner signal.....	7-73
Table 7-28	Flaw Depth Sizing with the 1.5 MHz PA Probe. The measured depth, depth RMSE, and the corner-to-tip signal ratio (in dB) are shown. A C:T ratio <0 indicates a brighter tip signal than corner signal.....	7-73
Table 7-29	Flaw Depth Sizing with the 2.0 MHz PA Probe. The measured depth, depth RMSE, and the corner-to-tip signal ratio (in dB) are shown. A C:T ratio <0 indicates a brighter tip signal than corner signal.....	7-74
Table 8-1	Description of Specimens.....	8-4
Table 8-2	Beam Models .....	8-9
Table 8-3	Index Range .....	8-10
Table 8-4	Signal Dropout at the 2:1 SNR Level, by Percentage of Scanned Section .....	8-18
Table 8-5	Signal Dropout at the 2:1 SNR Level, by Length of Maximum Dropout .....	8-19
Table 8-6	Signal Dropout at the 3:1 SNR Level, by Percentage of Scanned Section .....	8-20
Table 8-7	Signal Dropout at the 3:1 SNR Level, by Length of Maximum Dropout .....	8-21
Table 8-8	1.0 MHz Transducer Specifications.....	8-26
Table 8-9	Persistence Measurements along Scan Lines for Signals Above 2:1 SNR.....	8-29



## EXECUTIVE SUMMARY

This report summarizes past work and documents the latest research sponsored by the U.S. Nuclear Regulatory Commission (NRC) and conducted at the Pacific Northwest National Laboratory (PNNL) to evaluate the effectiveness and reliability of nondestructive examination (NDE) methods for the inspection of cast austenitic stainless steel (CASS) weldments. Under a series of multi-year NRC-sponsored programs at PNNL beginning in 1978, the Laboratory has performed NDE research focused on assessing various methods and techniques for improving detection, localization, and characterization of cracks in coarse-grained components.

The general scope of this work, while having evolved over many years, encompasses CASS with dissimilar metal weld (DMW) and similar metal weld materials located within the primary pressure boundary of light-water reactors.

The intent of this report is to provide:

- A comprehensive summary of CASS-related research important to understanding the current state-of-the-art. This report summarizes and compiles the studies and investigations on CASS materials and associated DMWs performed by PNNL and documented in various NUREGs and technical letter reports.
- The result of recent confirmatory research and laboratory evaluations not previously addressed in a report.
- A resource for engineers and scientists involved in the NDE of CASS for purposes of inservice inspection (ISI) on existing plants during current and extended periods of operation.
- A comprehensive and detailed resource for researchers and NDE practitioners conducting future investigations to advance the state-of-the-art.
- A technical basis to support future NRC rulemaking activities related to performance demonstration requirements in American Society of Mechanical Engineers Boiler and Pressure Vessel Code (ASME Code), Section XI, Appendix VIII, Supplement 9 – Qualification Requirements for Cast Austenitic Piping Welds.

In developing this report, over 230 research papers, conference presentations, published reports, and regulatory documents have been reviewed and considered during the development of the technical bases and key takeaways documented in this report, which underpin the conclusions provided herein. The results of work conducted in this area both domestically and in countries such as France, Japan, Sweden, South Korea, Finland, Belgium, and Canada have helped to further substantiate the reported PNNL findings. Historical efforts in CASS NDE research provide fundamental insights regarding the direction and evolution of technical focus areas and help the reader better understand the various issues that comprise the examination challenges inherent with CASS materials. In addition, this report addresses topic areas related to enhancing CASS examinations, including materials science and ultrasonic physics, probe design and specifications, data acquisition and analytical/imaging techniques, inspection parameters and examination protocols, signal-to-noise ratio (SNR) requirements, examiner training, modeling and simulation, ASME Code guidelines and provisions, regulatory considerations, and other areas that form the totality of this work. The feasibility of using advanced NDE methods for effectively and reliably examining CASS piping components has been demonstrated (Anderson et al. 2007; Diaz et al. 2012). These methods, along with existing standards, are assessed with respect to the development of performance demonstration requirements for CASS piping weldments. The most

recent CASS research conducted at PNNL is also reported here, and these results further support the message that effective CASS examinations can be implemented with available techniques, instrumentation, and protocols to support ISI in commercial U.S. nuclear power plants.

Chapters of this report as well as the Appendices highlight key CASS research activities from the mid-1970s through the mid- to late-1980s that influenced the direction of more recent CASS studies. During this period, the results of PNNL assessments and early international round-robin studies identified significant issues with detection and discrimination performance of conventional ultrasonic testing (UT) methods in these materials. Simultaneously, CASS research at Westinghouse and Argonne National Laboratory focused on characterizing material properties and degradation mechanisms led to the determination that these materials were susceptible to thermal aging embrittlement that could potentially manifest during the first 40-year life cycle of a reactor and anytime thereafter. From these early efforts, it was also recognized that conventional UT techniques available at that time were challenged with providing effective and reliable detection performance in CASS components. These events drove NDE researchers to investigate in situ measurement methods that might allow CASS microstructures to be characterized and categorized, enabling inspection parameters to be optimized prior to implementing an examination. While marginal progress was made with CASS materials comprising purely columnar or purely equiaxed microstructures, it became evident that a priori knowledge of the microstructure was insufficient in providing the necessary information to improve detection performance directly.

In the late 1980s and through the 1990s, PNNL efforts were redirected toward developing UT methods that were inherently less sensitive to the effects of the anisotropic, coarse-grained structures. This new focus led to the development and implementation of lower-frequency ultrasonic techniques coupled with advanced signal processing methods to help improve resolution in the ultrasonic images. PNNL led this research by evaluating synthetic aperture focusing techniques (SAFT) and employing multiple incident angles using non-conventional frequencies between 250 kHz and 450 kHz. Early successes using this approach resulted in the development of flaw detection and discrimination criteria where a comprehensive, dual-sided weld examination approach (with multiple angles and multiple frequencies) was applied in concert with SAFT processing. Similar achievements with low-frequency (LF) ultrasonic efforts by the French and Japanese confirmed these early PNNL results in conjunction with advanced signal processing and conditioning methods. In addition, research efforts in the 1990s and early 2000s also investigated the development and application of other signal processing algorithms for noise reduction and image enhancement. Researchers in Sweden and at PNNL applied split-spectrum and cut-spectrum processing methods to CASS ultrasonic data, while others (including PNNL) researched the use of wavelet processing and maximum entropy processing techniques for enhancing detection and discrimination capabilities. In the early 2000s, advances in technology gave way to significant reductions in time for both data acquisition and data analysis protocols using ultrasonic phased-array (PA) technology. These efforts eventually led to the larger body of more recent studies focused on implementing LF-PA ultrasonic methods for the examination of CASS components.

In context with the historical aspects of CASS research, this report provides information on CASS microstructures and their variability, CASS metals chemistry, locations of CASS components in various reactor designs, fabrication and casting issues, and the impact of various microstructures on the propagation of sound fields in these materials. Inspection requirements and related regulatory background information is provided, as are discussions on expected service degradation in CASS and UT examination issues that arise as a result of CASS grain structures.

This report also documents more recent NDE CASS research focused on both volumetric and surface examination studies of a large-bore CASS DMW mockup where UT and eddy current testing examinations were conducted. In addition, results from research activities focused on evaluating flaw signal response “persistence” and flaw signal response “dropout” as a function of CASS microstructures, examination frequency, and SNR are documented here. Preliminary results from a PNNL analysis of the most recent CASS round robin conducted by the Electric Power Research Institute (EPRI) NDE Center are briefly discussed as well. All of this more recent research is new, not previously reported in any PNNL report, and the results of this new research have significant ramifications to the overall findings and conclusions reported here.

The research summarized and documented herein shows that there are specific examination attributes that must be accounted for and addressed in order to achieve an effective and reliable ultrasonic examination of CASS components. It is imperative that the examiner apply an adequate sound field for the examination. In addition, spatial encoding and generation of volumetric ultrasonic images for analyses are needed. Having a good understanding of probe performance, sound field dimensions, propagation characteristics, and the material being examined is critical toward achieving an effective examination. Finally, effective training on CASS materials is deemed necessary. These required attributes are summarized here:

- Selecting appropriate UT frequencies, propagation angles, and beam-forming methods for establishing effective sound fields to detect, then characterize, flaws in varied coarse-grained CASS microstructures.
- The importance of using encoded data with off-line imaging and analyses for the discrimination between cracks, geometrical reflectors, and material noise inherent in CASS.
- The use of UT modeling to optimize examinations, providing preliminary validation of search unit design, theoretical sound field intensities, and potential for adequate volumetric coverage.
- Indoctrinating examiners through specialized training in CASS microstructures that may be encountered, resultant sound field effects, and methods to discriminate between flaws, geometry, and other coherent noise in CASS configurations.

From a review of the work conducted at PNNL over 40 years, and from the larger body of work conducted internationally, the results are compelling. Conclusions generated from this work indicate that for CASS piping thicknesses greater than approximately 41 mm (1.6 in.), the use of 500 kHz PA-UT is required to provide suitable penetration of ultrasonic energy for effective and reliable flaw detection. Once detected, higher frequencies (up to 1.0 MHz) may be applied for flaw characterization. However, the frequency for initial detection screening should not exceed 500 kHz for these thicker-walled components.

For CASS weldments with wall thicknesses equal to or less than 41 mm (1.6 in.), results from NDE research show that a slightly higher examination frequency (800 kHz) will provide the most effective overall detection. Research shows that this frequency exhibits much better SNRs than higher frequencies in laboratory trials. Similar to the thick-walled recommendation, it may be appropriate to apply higher frequencies (1.5–2.0 MHz), depending on the level of sound field degradation experienced for flaw characterization, but it is not recommended to exceed 800 kHz for initial detection in these thinner-walled components.

The most recent NDE research conducted at PNNL and reported in Chapters 7 and 8 shows that the use of LF-PA-UT is the only current commercially-available technology capable of optimizing appropriate sound field energies within the areas of interest; i.e., near the inner-diameter (ID)

surface of the CASS weldment. This work included an assessment of LF (500 kHz), conventionally designed probes to compare and contrast against results from PA probes. These conventionally designed probes were fabricated by Applus RTD and consisted of dual-element, transmit-receive longitudinal, single-angle probe designs. These two probes (one at 30° and one at 45° refracted longitudinal [RL]) were constructed to have optimized apertures and design specifications for beam crossover zones at the ID surface of thick-walled CASS components examined in Chapter 7 of this report. The work reported here indicates that the LF-PA-UT technique provides a more effective approach at applying adequate sound field intensities at the ID surface, with sufficient SNRs, when attempting to detect and discriminate flaw responses from other geometrical or metallurgical reflectors. In addition, it is a necessity that the PA focal laws be appropriately modeled and applied to ensure robust sound field intensities reach the intended volumes of interest in the component. Furthermore, the PA probe must be designed with a sufficiently large active array aperture to ensure effective insonification of the targeted examination volume.

Specific guidance related to examination angles is a critical element toward achieving an effective examination in CASS materials. The NDE research shows the significant impact on signal response amplitudes encountered due to the wide variability of CASS microstructures. Since a definitive set of beam propagation angles cannot be predicted for universally effective and reliable examinations in all CASS materials, multiple examination angles over a suitably wide range are required. Using many angles would help to provide the most effective angles to penetrate the “windows” in varied CASS microstructures.

The evidence in this report shows that spatially encoded UT data for CASS component examinations should be used whenever possible. The most recent research provided in this report (see Chapters 7 and 8) suggests that using non-encoded (real-time) scanning methods with transient signal analyses results in a poor likelihood that an examiner will be able to distinguish between coherent reflections caused by geometry or microstructural variations in CASS and responses caused by flaws. Further, due to the potential for lower-than-normal SNRs in CASS, there is a high probability that flaw signals could be overlooked due to their extremely short screen persistence times when scanning in a real-time mode. The current technical basis shows that that spatial encoding, coupled with off-line post-processing and imaging techniques, is the most effective examination method for CASS piping examinations.

Examiner training is critical for achieving, demonstrating, and maintaining the necessary skills for conducting effective and reliable ultrasonic examinations of CASS components. Inspections would be improved if examiners were provided access to realistic CASS mockups with simulated service-induced flaws (cracks) for hands-on practice. Formal classroom training and hands-on practice are important factors in effective examinations of CASS components. Training and qualification activities focused on improving CASS examinations should be developed to support performance demonstrations.

The relevance, extent, breadth, and depth of the body of work conducted in CASS NDE research over many decades, both at PNNL and worldwide, are conveyed in this report. Details and explanations supporting the conclusions and recommendations are provided throughout. Finally, an extensive reference chapter that supports the conclusions outlined in this report is presented at the end of this report.

## ACKNOWLEDGMENTS

The work described in this report was sponsored by the U.S. Nuclear Regulatory Commission (NRC), Office of Nuclear Regulatory Research (RES). The authors gratefully acknowledge the guidance and technical insights provided by Contracting Officer Representative (COR) Ms. Carol Nove (RES) and deputy COR Mr. Bruce Lin (RES) during the development of this report. Finally, at the NRC, the authors wish to thank the past NRC Program Monitors for their support, technical motivation, and insights over the 40-year period comprising the technical effort for NDE research at PNNL. These individuals are Dr. Joseph Muscara, Dr. Allen Hiser, Jr., Mr. Craig Hrabal, Ms. Deborah Jackson, and Mr. Wallace Norris. Special thanks to Mr. Norris who was a significant contributor to this document.

The authors wish to thank Steven Doctor (PNNL Emeritus) and Mike Anderson (PNNL Retired) as the previous program managers and principal investigators on CASS materials research at PNNL, Royce Mathews (PNNL Retired), Gerald Posakony (PNNL Emeritus – Deceased), Robert Ferris (PNNL Retired), Robert Bowey (PNNL Deceased), George Schuster (PNNL Retired), and a long list of technical support staff, many now retired, who spent much of their careers providing technical support on various aspects of NDE CASS research work over the past 40 years. Finally, we gratefully acknowledge Ms. Kay Hass for her invaluable assistance in the technical editing and formatting of this report, and her patience during this process. In addition, the authors recognize and thank Ms. Lori Bisping for her outstanding level of support and attention to detail as the lead administrator and project coordination backbone of this programmatic effort for over three decades. Finally, we also would like to thank Ms. Tara O'Neil, Nuclear Subsector Manager, for her guidance and support in shepherding this work to completion.

There are many other contributors and colleagues representing academia, vendors, national laboratories, and industrial research organizations both domestically and internationally that the authors wish to thank. Due to the extensive list of individuals, we regret not being able to acknowledge each person here.



## ABBREVIATIONS AND ACRONYMS

AEC	Atomic Energy Commission
ANL	Argonne National Laboratory
ASME	American Society of Mechanical Engineers
ASTM	American Society for Testing and Materials
BW	bandwidth
BWR	boiling water reactor
CASS	cast austenitic stainless steel
CCSS	centrifugally cast stainless steel
CCSSRRT	Centrifugally Cast Stainless Steel Round Robin Test
CEA	Commissariat à l'énergie atomique
CFR	Code of Federal Regulations
CGI	Chockie Group International
dB	decibels
DID	Defense-in-depth
DMW	dissimilar metal weldment
EDM	electro-discharge machining
EFPY	effective full-power years
Emc <sup>2</sup>	Engineering Mechanics Corporation of Columbus
EPRI	Electric Power Research Institute
ET	eddy current testing
FCP	false call probability
FMC	full matrix capture
GALL	Generic Aging Lessons Learned
GDC	General Design Criteria
IGSCC	intergranular stress corrosion cracking
INPO	Institute for Nuclear Power Operations
IRSN	Institut de Radioprotection et de Sûreté Nucléaire
ISI	inservice inspection
LF	low frequency
LWR	light-water reactor
LF-PA	low-frequency phased array
MHz	megahertz

MOU	Memorandum of Understanding
MPATS	Multi-Parameter Analysis Tool Set
NDE	nondestructive examination
NPP	nuclear power plant
NRC	U.S. Nuclear Regulatory Commission
P-M	peak to mean
PA	phased array
PFM	probabilistic fracture mechanics
PIRR	Piping Inspection Round Robin
PISC	Programme for the Inspection of Steel Components
P-M	peak-to-mean
PNNL	Pacific Northwest National Laboratory
POD	probability of detection
P-P	peak-to-peak
PRA	probabilistic risk assessment
PWR	pressurized water reactor
PWSCC	primary water stress corrosion cracking
RCP	reactor coolant pump
RF	radio frequency
RL	refracted longitudinal
RMSE	root mean square error
RPV	reactor pressure vessel
RT	reference temperature
RTD	receive-transmit-dual
SAA	signal amplitude anomalies
SAFT	synthetic aperture focusing technique
SCC	stress corrosion cracking
SCSS	statically cast stainless steel
SG	steam generator
SIA	Structural Integrity Associates, Inc.
SNR	signal-to-noise ratio
TFC	thermal fatigue crack
TFM	total focusing method
TG CASS	Task Group on Cast Stainless Steel



TLR	technical letter report
TRL	transmit-receive longitudinal
UT	ultrasonic testing
WEC	Westinghouse Electric Corporation
WOG	Westinghouse Owner's Group
XRF	x-ray fluorescence



# 1 INTRODUCTION

## 1.1 Background

Pacific Northwest National Laboratory (PNNL) has been performing nondestructive examination (NDE) research under the sponsorship and guidance of the U.S. Nuclear Regulatory Commission (NRC) for 40 years. One of the primary objectives of the research has been to assess the effectiveness and reliability of conventional and advanced NDE methods for the inspection of light-water reactor (LWR) components. A specific task has been to evaluate state-of-the-art technical approaches for inspecting nuclear reactor components that pose significant challenges to conventional ultrasonic testing (UT) inspection methods<sup>1</sup> used by the commercial nuclear power industry.

Among the components that present significant challenges to UT examinations are those fabricated of cast austenitic stainless steel (CASS). As such, the types of PNNL NDE studies reported and discussed here have generally been focused on performing confirmatory research on CASS materials that employs a three-tiered approach aimed at (1) evaluating detection capabilities, (2) discriminating flaw responses from coherent background responses, and (3) characterizing flaws. This NDE research often provides analyses and results in terms of probability of detection (POD), root-mean-square-error (RMSE), and false call probability (FCP). However, it should be noted that the PNNL studies have not addressed the implications of false calls in CASS in relation to operating/management costs, mitigating degradation, component repair, or replacement ramifications. In addition, the CASS NDE research discussed herein was conducted over many years and included a variety of mockups containing a wide spectrum of flaw distributions, sizes, and types, typically described in detail in their respective technical reports. The reader is reminded that PNNL's NDE research generally has been conducted in a laboratory environment where the data are not constrained by field conditions and are typically collected under non-blind examination protocols. Finally, it should be noted that during the course of PNNL's NDE research on CASS, the work scope did not include collecting multiple identical scans to establish statistical relevance for the purpose of quantifying repeatability, but rather enough data were collected to ensure high-quality results while minimizing the amount of data acquisition, where possible. If a data set was identified as suspect, e.g., where the quality of the data may have been impacted or compromised due to poor coupling, noise, or other factors, then the data were re-acquired. PNNL routinely applies procedures for probe calibration, real-time data acquisition monitoring, and post-acquisition analysis to ensure data quality, but a rigorous statistical evaluation of NDE examination repeatability with associated error bars was not conducted on CASS and, thus, is not provided here.

---

<sup>1</sup> As related to the examination of cast austenitic stainless steel, conventional UT refers to the use of single- or dual-element, pulse-echo or transmit-receive transducer configurations operating at frequencies at or above 1.0 megahertz (MHz). The conventional designation, as used in this report, is meant to associate ultrasonic sound fields propagated in an ordinary manner; that is, having a "dead zone" in the near field with more linear beam characteristics (such as reduction of sound field intensity and beam divergence) in the far field. Conventional UT methods typically employ only a single fixed angle for each transducer configuration, may or may not be spatially encoded, and can be scanned manually or by using automated fixtures.

## **1.2 Objectives**

The intent of this report is to provide:

- A comprehensive summary of CASS-related research important to understanding the current state-of-the-art. In this regard, this report summarizes and compiles the studies and investigations on CASS materials and associated dissimilar metal weldments (DMWs) performed by PNNL and documented in various NUREGs and technical letter reports.
- The result of recent confirmatory research and laboratory evaluations not previously addressed in a report.
- A resource for engineers and scientists involved in the NDE of CASS for purposes of inservice inspection (ISI) on existing plants during current and extended periods of operation.
- A comprehensive and detailed resource for researchers and NDE practitioners conducting future investigations to advance the state-of-the-art.
- A technical basis to support future NRC rulemaking activities related to performance demonstration requirements in American Society of Mechanical Engineers Boiler and Pressure Vessel Code (ASME Code), Section XI, Appendix VIII, Supplement 9.

The report addresses the significant and influential CASS-related activities that have been performed since the NRC was established by the Energy Reorganization Act of 1974. The feasibility for using advanced NDE methods for effectively and reliably examining CASS piping components has been demonstrated (Anderson et al. 2007; Diaz et al. 2012), and these methods are assessed with respect to the development of performance demonstration requirements for CASS piping weldments. In addition, UT techniques (such as Supplement 10 DMW examination protocols) similar to those described in existing standards are assessed to determine if they could satisfactorily be applied to develop performance demonstration requirements for CASS piping weldments.

## **1.3 Highlights of CASS Examination and Materials Research Activities**

A considerable amount of research relevant to this subject has been conducted by PNNL and other organizations. The challenge in developing the varied sections and their organization within this report was to balance the need to provide detailed data and results for researchers and NDE practitioners, who may use the information for subsequent work, with the needs of others that may read the report for different purposes, for example, to simply become familiar with the body of work that has transpired or gain a fundamental understanding of current technology for CASS examinations.

The remainder of this introduction is a high-level overview of issues related to CASS examinations and material degradation research. Among the items briefly discussed are how and why CASS was used in certain portions of nuclear power plant (NPP) piping, what makes CASS difficult to inspect, research programs that address CASS examination and degradation issues, and the current technology for NDE application to CASS as of the publication date of this report. This overview identifies significant research results and events that have had the most influence in directing the objectives and scope of subsequent activities. Highlighted items are more fully discussed in later portions in the report, along with other CASS-related activities and findings. Complete references are provided in Chapter 10 and a more detailed description of historical CASS research, and events that shaped this research, are attached in the Appendices.

### 1.3.1 Examination of CASS Piping Systems

The relative cost and corrosion resistance of CASS piping resulted in it being used extensively in the primary coolant systems of many pressurized water reactors (PWRs). Through Title 10 of the *Code of Federal Regulations* (10 CFR) Part 50, Appendix A, General Design Criteria (GDC), the NRC requires that the reactor coolant pressure boundary be designed, fabricated, erected, and tested so as to have an extremely low probability of abnormal leakage, rapidly propagating failure, or gross rupture. The provisions for the inspection of primary piping systems were developed, in part, to assure compliance with the GDC and are contained in Section XI of the ASME Code, entitled *Rules for Inservice Inspection of Nuclear Power Plant Components*. The ASME Code is incorporated by reference into the NRC's regulations, and therefore NPP licensees are required to implement and adhere to the ISI provisions of Section XI.

ASME Section XI requires that essentially 100% of designated portions of selected Class 1 and Class 2 piping welds be periodically inspected using a volumetric examination method. UT is the method most commonly employed by the nuclear industry to conduct these inspections. However, CASS materials have highly coarse-grained and inhomogeneous microstructures, contributing to their anisotropic nature (anisotropic means that certain material and physical properties are directionally dependent within the crystalline lattice). The large and dissimilar size of the anisotropic grains, relative to the interrogating acoustic pulse wavelength, strongly affects the propagation of ultrasound by causing severe attenuation (loss of energy or magnitude), redirection, changes in velocity, and scattering of ultrasonic energy. Research has shown that the microstructure of CASS piping can change drastically between the inner and outer diameters and around the circumference and axial length of individual piping segments. Large and small equiaxed, columnar, mixed grains, and banding (layers of significantly different grain structures) are common; and it is challenging to determine appropriate acoustic beam propagation angles that can exploit any potential "windows" or paths for sound to optimally travel through the grain structure.

### 1.3.2 CASS Research Highlights

The first U.S. study to assess CASS UT techniques was conducted by Westinghouse Electric Corporation (WEC) in 1976 (Pade and Enrietta 1981). The test parameters and optimistic results raised questions, so the NRC subsequently requested that PNNL conduct an industry survey to determine the state of practice for weldment inspections in the commercial nuclear industry. The survey revealed that selection of search units was highly variable and that most NDE personnel expressed low confidence in their ability to examine CASS piping (Becker et al. 1981; Morris and Becker 1982).

As a result of the conflicting information between the WEC study and PNNL industry survey, the NRC sponsored PNNL to conduct a Piping Inspection Round Robin (PIRR) study in 1981–1982. The PIRR assessed the capability of the U.S. nuclear industry to detect and size cracks in CASS weldments similar in configuration to those in the primary coolant piping system installed in NPPs. Six teams participated in the PIRR, with none of the teams achieving reliable detection using conventional UT methods. Additionally, in line with the previous industry survey, two teams stated that they had no confidence in their ability to inspect CASS pipe (Heasler and Doctor 1996).

The need to implement effective and reliable CASS examination methods intensified with the 1982 publication of a German study (Trautwein and Gysel 1982) revealing that CASS materials are susceptible to thermal aging embrittlement. In 1985, WEC performed studies to establish levels of thermal aging embrittlement and the effects of such embrittlement on the fracture of

CASS piping components (Bamford et al. 1985). The NRC sponsored subsequent research at Argonne National Laboratory (ANL) (Chopra 1991) confirming these findings and also concluding that, based on the particular CASS component material composition, thermal aging embrittlement could occur in the first 40-year term of an NPP.

In 1984, PNNL and WEC worked cooperatively on a program to resolve the apparent differences between the WEC and PIRR studies (Taylor 1984). The program revealed that the surprisingly good results from the early WEC study were the result of the use of mechanical fatigue cracks in the test specimens and the absence of realistic geometrical conditions that might mask a flaw or affect scanning areas. During the cooperative program, WEC specimens once again contained mechanical fatigue cracks. However, PNNL specimens used in the WEC-PNNL cooperative program contained thermal fatigue cracks (TFCs), which were found to be more acoustically representative of service-induced cracks that have been reported in the field. Mechanical fatigue cracks are more open and planar and have shown relatively high probabilities of detection. On the other hand, TFCs tend to be tight, have rough textures, and were essentially undetectable with the current field UT techniques of that era. This was clearly shown by only 2 of 29 TFCs having been detected using these conventional UT methods.

Because results from studies using conventional fixed-angle UT techniques for the examination of CASS weldments were unsatisfactory, organizations such as PNNL began conducting investigations into advanced techniques for the purpose of improving the effectiveness and reliability of these examinations, as summarized below. It should be noted, however, that evaluations of fixed-angle probes for the examination of CASS weldments have continued into 2017. Table 1-1 lists the CASS studies that employed conventional UT methods. There are some notable time gaps in the timeline. For example, no fixed-angle studies were found between 1996 and 2005. There were several reasons for this. As noted in a German study, phased array technology had been widely applied for UT during the construction and operation of NPPs since the mid-1990s (Pudovikov et al. 2012). Thus, there was little incentive to conduct studies using fixed-angle probes. In the United States, as noted in a 2013 PVP paper (Chockie and Griesbach 2013), *“For many years some believed that the inspection of CASS as specified in the ASME Code may not be warranted. This was based on the fact that even severely aged CASS is considered capable of tolerating major flaws.”* The EPRI (2005a) report is also notable in explaining the gaps in the research time line; as stated in the report, *“No conventional UT examination technology or process was identified that could be reliably applied for the examination of primary coolant piping system welds in CASS material.”* As discussed in Appendix B of this report regarding the Chockie Group International (CGI) CASS technical workshops, much of the CASS-related Electric Power Research Institute (EPRI) UT technique research since 2009 focused on validating the results of the PNNL research using phased-array (PA) techniques.

**Table 1-1 CASS Studies Employing Conventional UT Methods**

Year	Study/Authors	Result Summary
1982	Morris and Becker	PNNL conducted NRC-sponsored industry survey revealing lack of confidence in the inspection of CASS piping
1982	PIRR	Round-robin study results substantiated lack of confidence in detection reliability
1984	Westinghouse/PNNL	Two cracks detected in 29 inspections of CASS specimens of thermal fatigue cracks
1988	Wolf Creek EPRI Workshop	Westinghouse team used LF, fixed-angle search unit; technique detected mechanical fatigue cracks; limited success in detecting thermal fatigue cracks
1992	PISC III	Better detection rates achieved at the cost of oversizing, rejection of acceptable flaws, and high false call rates; large spread in flaw sizing; superiority of automated scanning systems for inspection CASS demonstrated. EPRI Report TR-1011600 (EPRI 2005a)
1996	Seabrook Trial	LF-Synthetic Aperture Focusing Technique better at detecting indications than standard conventional probe inspection protocol then currently used by industry
2005 <sup>2</sup>	EPRI	"No conventional UT examination technology or process was identified that could be reliably applied for the examination of primary coolant piping system welds in CASS material." EPRI Report TE-1011600 (EPRI 2005a)
	PNNL	Conventional transducer experienced signal loss/high background noise. NUREG/CR-6933 (Anderson et al. 2007)
2012	JNES, <sup>(a)</sup> JPEIC, <sup>(b)</sup> and the University of Toyama	Conventional, encoded UT techniques did not detect flaws approximately 20 mm (0.8 in.) through-wall and smaller. Conventional UT techniques were considered inadequate for depth sizing; difficulties in length sizing flaws. It was determined that the structural integrity of CASS piping could not be ensured through the use of these conventional UT examination techniques (Sakamoto et al. 2012b).
2017	This NUREG Report	CASS specimen examined with dual-element 1.0 megahertz (MHz) conventional probes; 10% through-wall <u>notch</u> (6.3 mm [0.25 in.]) in equiaxed microstructure not detected
2017	This NUREG Report	Reactor coolant pump carbon steel nozzle-to-CASS safe-end mockup with implanted TFCs examined with two 500 kilohertz (kHz) conventionally-designed probes, fixed refracted angles of 30° and 45°, and two PA probes (500 and 800 kHz). From CASS side of weld, 500 kHz PA outperformed conventional probes in all aspects of the study.
(a) JNES = Japan Nuclear Energy Safety Organization (b) JPEIC = Japan Power Engineering and Inspection Corporation		

<sup>2</sup> The number of international nuclear-related studies using conventional probes for any material have declined. As stated in a German study, "... *phased array technology is widely applied for ultrasonic testing during the construction and operation of nuclear power plants since more than 20 years*" (Pudovikov et al. 2012). Also, an EPRI presentation at the 2<sup>nd</sup> CGI workshop (Doug Kull. June 15, 2009, "NDE of Cast Stainless Steel: PWR Stainless Steel NDE Capability & Performance Demonstration TAC Update," and discussed in Appendix B) indicates that studies to develop and evaluate CASS-related NDE solutions were not started until 2010.

A literature search revealed few studies since 2005 assessing the application of single- or dual-element, fixed-angle probes for the examination of CASS weldments. A Japan Nuclear Energy Safety Organization (JNES) study in 2012 concluded that the structural integrity of CASS piping could not be ensured through the use of the conventional UT examination techniques applied (Sakamoto et al. 2012b). Conventional, encoded UT techniques had not detected flaws approximately 20 mm (0.8 in.) through-wall and smaller. A PNNL study in 2017, described in Chapter 7 of this report, found that a 500 kHz PA outperformed two low-frequency (LF), conventionally-designed probes (fixed-angle, dual-element transmit-receive longitudinal [TRL] probes at 500 kHz) in all aspects of the study when examining a weld through a CASS safe-end.

In the mid-1980s, the NRC had begun to assess the capabilities of data post-processing and imaging methods, such as the synthetic aperture focusing technique (SAFT),<sup>3</sup> for their potential to improve the effectiveness and reliability of component examinations. The NRC tasked PNNL with developing a SAFT-UT system for application to NPP piping and reactor pressure vessels (RPVs), validating the SAFT-UT system through laboratory and field inspections, and generating an engineering database to support ASME Code acceptance of the technology. During the system capabilities investigation, data were collected on a plate used in the second phase of the international Programme for the Inspection of Steel Components (PISC). When the SAFT-UT data were compared to other PISC team performances, the results were better than the average of all teams using advanced UT techniques (Doctor et al. 1987). Based on these results, the NRC sponsored further refinement of the PNNL SAFT system with lower-frequency transducers being developed for use on CASS in the mid- to late-1980s.

PNNL participated in a field exercise at the Seabrook Nuclear Power Station in 1996 aimed at evaluating a LF inspection technique using longer wavelengths for examining thick section, coarse-grained, stainless steel components. The exercise was coordinated with NRC Region I inspectors who were conducting an independent assessment of current industry standard practices for examining CASS components. Analysis of the data indicated that the use of LF probes combined with SAFT post-processing (LF-SAFT technique) was more promising for detecting indications than conventional UT protocols being used by industry (Diaz et al. 1998). For example, the LF-SAFT technique was the only method that provided reliable detection, localization, and sizing data for a 10% deep, 0.318 cm (0.125 in.) wide, 2.54 cm. (1.0 in.) long, circumferentially oriented notch in the CASS calibration block used in the exercise.

The capabilities of the LF work were further demonstrated when PNNL traveled to the EPRI NDE Center in Charlotte, North Carolina, in 1997 to participate in a performance evaluation of the LF-SAFT inspection technique on samples from the inventory of Westinghouse Owner's Group (WOG) CASS and DMW sections (Diaz et al. 2008b). Flaws on the order of 35% through-wall were shown to be readily detected by the LF-SAFT method using an early version of the PNNL system. Later field and EPRI exercises with more advanced LF-SAFT transducers and imaging techniques continued to show that this method was capable of reliably examining CASS piping welds.

The need to improve the effectiveness and reliability of the inspection of CASS weldments was further driven by the NRC's publication of the Generic Aging Lessons Learned (GALL) Report (NUREG-1801), Revision 0 (NRC 2001). The GALL report provides an acceptable approach for a licensee to manage aging effects in the license renewal term. In accordance with the GALL report, a licensee's aging management program must include adequate inspection methods to ensure detection of cracks and a flaw evaluation methodology for CASS components that are susceptible

---

<sup>3</sup> SAFT data processing will be described in more detail in Chapter 6 of this report.



to thermal aging embrittlement. In response to the GALL report, the industry began to assess strategies for the management of aging NPPs and plant license renewal. The results of the industry assessment were published in an EPRI report (EPRI 2008). With respect to CASS, it was determined that, “Current technology may not be adequate for efficiently detecting and characterizing in-service flaws in CASS pipe in the industry.” The report listed several UT techniques for potential study.

Around 2003, PNNL began to experiment with advanced commercially-available ultrasonic phased-array (PA) technologies. The ability to fabricate small piezocomposite elements, along with the increased processing speeds of portable computers, enabled PA-UT to be implemented across several industrial sectors, including commercial nuclear power. In cooperation with other research colleagues and UT equipment manufacturers, PNNL began to acquire laboratory data with LF-PA transducers on CASS weldment specimens. This work built upon the successes of the LF-SAFT methods. The benefit of using PA technology is that it allows for the implementation of multiple propagation angles and beam focusing in near real time. Laboratory experience at PNNL has shown that PA-UT may provide robust, meaningful UT data sets in nearly 1/10th of the scan time required for conventional methods as well as for LF-SAFT (Anderson et al. 2011). The benefits of PA technology have also been noted by industry. As discussed in a report by EPRI (EPRI 2004) it was demonstrated that a PA approach to piping examinations offers improvements in speed, coverage, and reliability. Additional evidence for the speed of PA-UT was presented at the 18<sup>th</sup> World Conference on Nondestructive Testing (Deutsch and Kierspel 2012), which stated that, for the numerous test samples investigated in the study, weld inspection with PA enabled examinations 10 to 20 times faster than for conventional UT.

NRC-sponsored research at PNNL, from the initial LF-SAFT development to the current third-generation LF-PA-UT transducer design and deployment, continues to demonstrate that effective examinations of CASS piping are possible. An initial report (Anderson et al. 2007) provided insights and positive flaw detection results using LF-PA on thick-walled CASS piping weldments, with flaws on the order of 30% through-wall being readily detected and even much shallower flaws (10%–20%) being detected periodically. Later PNNL work (Diaz et al. 2012; Crawford et al. 2015) has shown similar (or better) results, including the current data provided in this report for a thick-walled DMW CASS specimen.

In 2006, PNNL also began to evaluate the capabilities of PA-UT methods applied to CASS pressurizer surge-line piping and associated welds. Whereas thick-wall primary coolant piping is on the order of 65–80 mm (2.6–3.2 in.) thick, thinner CASS pressurizer surge-line piping is approximately 33 mm (1.3 in.) in wall thickness. This research demonstrated that state-of-the-art PA inspection approaches were capable of reliable and effective detection of cracks in CASS pressurizer surge line piping and associated weldments. To further validate the results, PNNL hosted an industry ISI vendor team to conduct an examination of the CASS pressurizer surge-line specimens using an ASME Section XI, Appendix VIII qualified procedure. This team used their equipment to initially perform a blind examination (using encoded PA) as per a Supplement 10 examination procedure for DMWs. An analysis of both PNNL and the industry team’s data showed very good correlation between the results of the techniques used. In fact, both organizations were able to detect 100% of the implanted and thermally induced TFCs on these piping specimens using LF-PA techniques (Diaz et al. 2012).

ASME Code rules have not yet been developed for Supplement 9, “Qualification Requirements for Cast Austenitic Piping Welds,” to Appendix VIII, which continues to be listed as “in the course of preparation.” In the interim, the ASME developed Code Case N-824 *Ultrasonic Examination of Cast Austenitic Piping Welds from the Outside Surface* (ASME Board Approved October 16,

2012) for the examination of piping welds that join CASS material to the same material or to other materials, such as wrought carbon steel, low-alloy steel, or wrought austenitic steel. It should be noted that the NRC final rulemaking (July 18, 2017, 82 FR 32934) approving the use of the Code Case, with conditions, permits voluntary implementation of Code Case N-824. More recently, NRC issued the proposed rulemaking to incorporate Code Case N-824 with conditions into Regulatory Guide 1.147, "Inservice Inspection Code Case Acceptability, ASME Section XI, Division 1," Revision 19 (August 16, 2018, 83 FR 40685). The results of the PNNL research on CASS thick-walled and pressurizer surge-line piping were instrumental in the development of Code Case N-824, as well as the following two NRC-imposed conditions:

- Licensees shall use a phased-array search unit with a center frequency of 500 kHz with a tolerance of  $\pm 20$  percent
- The phased-array search unit must produce angles including, but not limited to, 30 to 55 degrees with a maximum increment of 5 degrees.

As a result of technical engagements between the NRC and L'Institut de Radioprotection et de Sûreté Nucléaire (IRSN), PNNL was introduced to a Commissariat à l'énergie atomique (CEA)-developed software package named CIVA, and began evaluating its capabilities to model probe design, UT capabilities, and weld coverage. In 2012, the NRC requested assistance from PNNL in evaluating the results of three separate examinations where licensees had been unable to obtain full coverage on certain reactor coolant pump (RCP) DMWs that included CASS material. Based on information provided by three separate licensees, PNNL used CIVA to assess the UT that was conducted (PNNL 2013b, c, a). It should be noted that the specific weld configurations, details of the examinations conducted, and modeling results from the analyses of the licensee examinations are not discussed here; however, these details may be found in the references listed above. Among the issues revealed by the modeling were insufficient acoustic energy at the angles required to adequately inspect for inner-diameter (ID) surface-breaking flaws, apparent non-optimization of transducer focal laws, and in one case, the potential to miss flaws on the order of approximately 40% in through-wall extent with flaws having lengths on the order of 25.4 cm (10 in.) was observed.

In 2016, the NRC sponsored PNNL to participate in a CASS round-robin exercise (blind test) coordinated and conducted by the EPRI NDE Center (EPRI 2017; Jacob et al. 2018). EPRI's objectives for this round robin were to assess the current state-of-the-art technologies developed or applied by nuclear NDE vendors, equipment manufacturers, and research organizations. This included an evaluation of crack detection and sizing capabilities of full penetration butt-welded piping components with CASS on one or both sides. It should be noted that no conventional ultrasonic methods were used by any participants; all ultrasonic data acquisition focused on encoded PA techniques. PNNL used LF-PA-UT techniques as the fundamental examination protocol for participation in this round robin. In order to address crack detection and sizing capabilities, PNNL used statistical methods to determine POD versus FCP for the PNNL data set, as well as for the collective set of all participants' data. In addition, the NRC asked PNNL to assess the overall validity of the exercise by determining whether the flaws were reasonable (i.e., too easy or too difficult to detect), whether the specimens accurately represent field conditions (especially in regard to weld root, weld crown, and counterbore), and whether or not a single-sided examination approach is reasonable for CASS components.

The last item in this overview focuses on CASS flaw tolerance evaluations (Griesbach et al. 2014). This topic has influenced nuclear industry reasoning for nearly 20 years and significant resources have been spent as a result. The discovery that CASS was susceptible to thermal

aging embrittlement in conjunction with the need to satisfy the license renewal requirements of the GALL report led the nuclear industry to explore the use of fracture mechanics evaluation techniques (NRC 2001). Studies were conducted to develop inspection screening criteria for evaluating the potential significance of thermal aging embrittlement effects. Initially, some in industry believed that the hardness and tensile strength increases resulting from this degradation may offset the accompanying decreases in ductility, fracture toughness, and impact resistance. Thus, it was hoped that inspection screening criteria might show that many CASS weldments, perhaps all, would not have to be inspected or only rarely inspected. However, the application of deterministic fracture mechanics analyses resulted in allowable piping flaw sizes that were relatively small and mostly below the capabilities of demonstrated examination methods.

Accordingly, a probabilistic fracture mechanics (PFM) model was used to develop a new ASME Code Case N-838, *Flaw Tolerance Evaluation of Cast Austenitic Stainless Steel Piping Components* (ASME 2015). Code Case N-838 was based on a PFM methodology for flaw tolerance evaluation of CASS piping components considering the effects of aging and uncertainties in material properties. The ultimate objectives of the flaw tolerance evaluation are to determine allowable flaw sizes in CASS components and to identify target flaw sizes for NDE that will ensure safe operation considering possible flaw growth. This information will then guide the design of suitable mockups, enabling the development of a qualification program for CASS.

In summary, this section provided a short historical overview of CASS-related highlights beginning with the WEC study in 1976 (the first study with the objective of determining the inspectability of CASS) to the present. Table 1-2 lists the research and events considered to be the most influential with respect to their impacts on subsequent research. Each of these items, along with other historical CASS research, are discussed in more detail later in this report.

Chapter 2 of this report discusses the casting processes and resultant microstructural variation for primary piping in NPPs. Chapter 3 provides inspection requirements, addresses the importance of CASS piping with respect to defense-in-depth, and lists license renewal issues for CASS. Thermal embrittlement and the impact of such degradation is discussed in Chapter 4. The problems encountered during ultrasonic examination of CASS materials along with research aimed at in situ characterization of the currently unknown field microstructures is provided in Chapter 5. Chapter 6 provides results of early research and summarizes important advances and significant results made by PNNL and related industry efforts with respect to developing reliable CASS examinations. A new study to extend PNNL low-frequency results to a thick-walled CASS/DMW specimen is described in Chapter 7. Chapter 8 provides results from additional evaluations of signal drop out and flaw response persistence in CASS, as well as a discussion of pertinent issues impacting the effectiveness and reliability of examinations in CASS piping welds. Chapter 9 provides summary conclusions based upon the body of work presented here, both historically and most recently on CASS examination performance assessments. Full references cited in this report are listed in Chapter 10. Appendices are included to provide further details to support information found in certain sections of this report.

**Table 1-2 Significant Findings or Events that Influenced CASS Research**

<b>Year</b>	<b>Milestone or Event</b>	<b>Result Summary</b>
1976	Westinghouse CASS study	First study with intent to determine inspectability of CASS
1981	German research	Thermal aging embrittlement identified as CASS degradation mechanism
1982	NUREG/CR-2468	Survey of Examiners – global low confidence in ability to inspect CASS
1982	PIRR	No team achieved reliable detection using conventional techniques
1984	PNNL/Westinghouse	Conventional techniques only detected 2 of 29 thermal fatigue cracks
1985	Westinghouse	Established levels of thermal aging embrittlement and effects on fracture of CASS components
1985	ANL	Research confirming German findings and advancing CASS knowledge base
1985	LF-SAFT field demo	Results better than average of teams using advanced techniques
1991	ANL	Research showing thermal aging embrittlement may occur within first 40-year license term
1993	EPRI exercise	LF-SAFT scored higher than all other automated teams
≈1994	ASME Code requirements	Industry proposal to eliminate CASS inspection from Section XI
1996	Seabrook Trial	LF-SAFT only technique to detect and size small (10%) through-wall flaw
1997	EPRI Trial	15% through-wall flaw occasionally detected in CASS specimens
2000	NRC Letter	Defined CASS susceptibility criteria for thermal aging embrittlement
2001	NUREG-1800	Enhanced CASS inspections required for license renewal
2007	NUREG/CR-6933	500 kHz PA probe best detection capabilities
2012	NUREG/CR-7122	PA probe reliably detected 10% through-wall flaw in pressurizer surge piping
2012	Code Case N-824	Developed and approved by ASME as interim measure for CASS examinations
2012	CIVA modeling	Modeling of several licensee examinations revealed technique deficiencies
2014	PNNL-23392	UT CASS beam mapping show poor results > 500 kHz
2014	ANL-14/16	Recommends decreasing ferrite content limits
2015	Code Case N-838	Flaw tolerance evaluation for CASS components
2016	NUREG/CR-4513, Rev. 2	Identifies additional factors with respect to CASS susceptibility to thermal aging embrittlement
2016–2018	EPRI CASS Round Robin	Use of LF-PA-UT resulted in FCPs ≤ 6% and detection rates of 75% to 90%
2017	PVP Paper	Emc2 recommends hybrid model for CASS flaw tolerance

## 2 CASS OVERVIEW AND MICROSTRUCTURAL VARIABILITY

The cast stainless steel piping installed in primary coolant systems of commercial NPPs has provided good corrosion resistance and, compared to the costs of similarly sized vintage wrought piping, was relatively less expensive to fabricate. WEC installed cast stainless steel piping in 27 PWRs in the United States, and practically all WEC-designed plants worldwide contain similar levels of this material (Figure 2-1). Plants designed by Combustion Engineering and Babcock & Wilcox, while typically possessing wrought materials for the main coolant lines, also use cast piping materials as safe ends at RCPs and branch connections to secondary and standby piping systems. In addition, all French-designed PWRs contain cast piping for the primary coolant loop. In boiling water reactors (BWRs), CASS was used only for primary coolant system fittings, and pump and valve bodies. Thus, this material has widespread use in plants that continue to operate—most of them, well beyond their initially projected lifetimes.

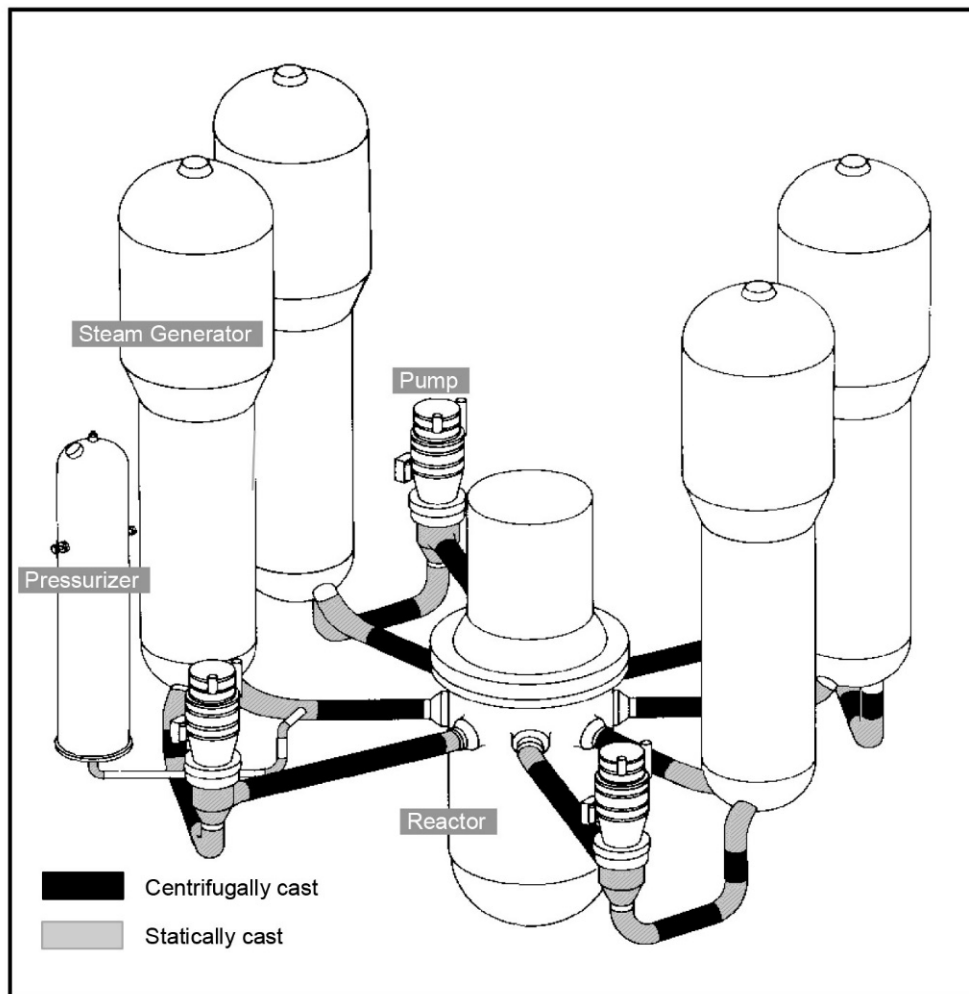


**Figure 2-1** Cast Stainless Steel Material in Primary Coolant System for Westinghouse-Designed Pressurized Water Reactor Four-Loop Plant (based on Westinghouse diagrams; illustration courtesy of A. Chockie, CGI).

Further, there are several locations in certain PWRs where CASS materials are joined to DMWs. These welds have experienced primary water stress corrosion cracking (PWSCC).

In Combustion Engineering plants, the safe ends of medium- and large-bore piping are typically made of CASS—the RCP suction CASS nozzle material on the downstream side of the Alloy 82/182 weld; RCP discharge CASS nozzle material on the upstream side of the Alloy 82/182 weld; the CASS safe-end material on downstream side of the surge nozzle Alloy 82/182 butt weld; CASS safe-end material on upstream side of the safety injection nozzle Alloy 82/182 butt weld; and the CASS safe-end material on the downstream side of the shutdown cooling nozzle Alloy 82/182 butt weld.

There are three major types of weld joints in the primary coolant piping of Westinghouse PWRs. Two of them, the pipe-to-pipe and pipe-to-elbow joints, contain centrifugally cast stainless steel (CCSS). The third joint, safe end-to-elbow does not utilize CCSS. All straight sections of the primary pipe are CCSS. Statically cast stainless steel (SCSS) was typically used in primary coolant system elbows and fittings. An EPRI report (Lapides 1991) provides further information on the 16 locations of circumferential weld joints in the reactor coolant loop piping in Westinghouse PWRs. While these welds are not classified as DMWs, Figure 4-3 in the Lapides report shows, for example, the RCP outlet nozzle and the cold leg piping. This joint configuration results in weldments with a large amount of weld metal. To provide a smooth transition from the nozzle to the piping, a weld overlay is applied for six inches along the cold leg piping. The geometry changes compound the difficulties associated with the inspection of the CCSS base material and associated weld.

Alloying elements of nickel and chromium have positively influenced the corrosion resistance of stainless steel; yet unlike wrought forms of austenitic piping, CASS generally exhibits more complexity to the grain shapes and orientations and significantly coarser microstructures. Cast piping consists of either CCSS or SCSS, with both of these processes producing near-net shaped components upon cooling; only minor surface modification (e.g., machining or grinding) is required to complete the fabrication sequence. Complex geometries such as piping elbows, tees, or nozzles are typically SCSS, while straight tubular piping is primarily CCSS. However, as reported in Ruud et al. (2009), there have been instances where CCSS piping has been mechanically formed (bent) into an elbow shape after cooling.

General process steps for all castings include:

- Mold development or preparation
- Ingot melting and alloying
- Pouring metal into the mold
- Solidification and cooling
- Extracting the casting from the mold.

The microstructure observed for SCSS elbows has typically been that of large, equiaxed grains mainly influenced by ingot chemistry and a slow, static cooling stage, which promotes omnidirectional, volumetric grain growth. The CASS elbows in U.S. commercial nuclear plants were predominantly made by ESCO, a foundry in Portland, Oregon, and the process used an expendable mold made of silica/zircon sand, which would be destroyed to retrieve the elbow after solidification. The sand from the broken mold is normally recycled to make subsequent molds. The only refinements that may have been made to later components over the earliest vintage

elbows appear to be additions of ferro-calcium-silicon mixtures for deoxidation; this may have assisted in forming more nucleation sites, providing slight grain refinement (Ruud et al. 2009). Figure 2-2 provides cross-sectional information for part of a SCSS elbow showing the large, equiaxed grain structure typical of these components.

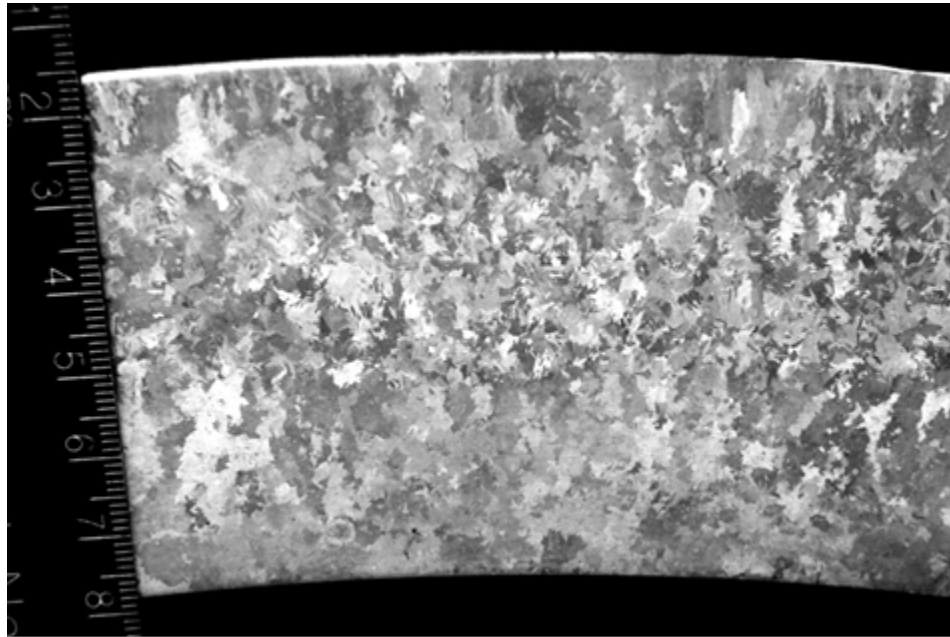


**Figure 2-2 Example of Equiaxed Grain Structure (specimen courtesy of EPRI)**

CCSS piping shows the greatest variability of microstructure. Based on the vintage CASS materials available to historical studies (Good et al. 1991; Anderson et al. 2007; Ramuhalli et al. 2009; Ruud et al. 2009; Diaz et al. 2012), CCSS piping exhibited microstructures that include large equiaxed, smaller equiaxed, large and small dendritic, and mixed/banded layers of multiple types of grains, with certain refinements occurring as the process matured. The oldest examples appear to be the most varied, containing mixed dendritic structures interspersed with finer equiaxed layers, along with some regions of large equiaxed grains (see Figure 2-3). Cross sections of somewhat later vintages of CCSS tend to display more pronounced and larger dendritic grains that may extend from the ID to the outer-diameter (OD) surface of the piping, as exhibited in Figure 2-4.



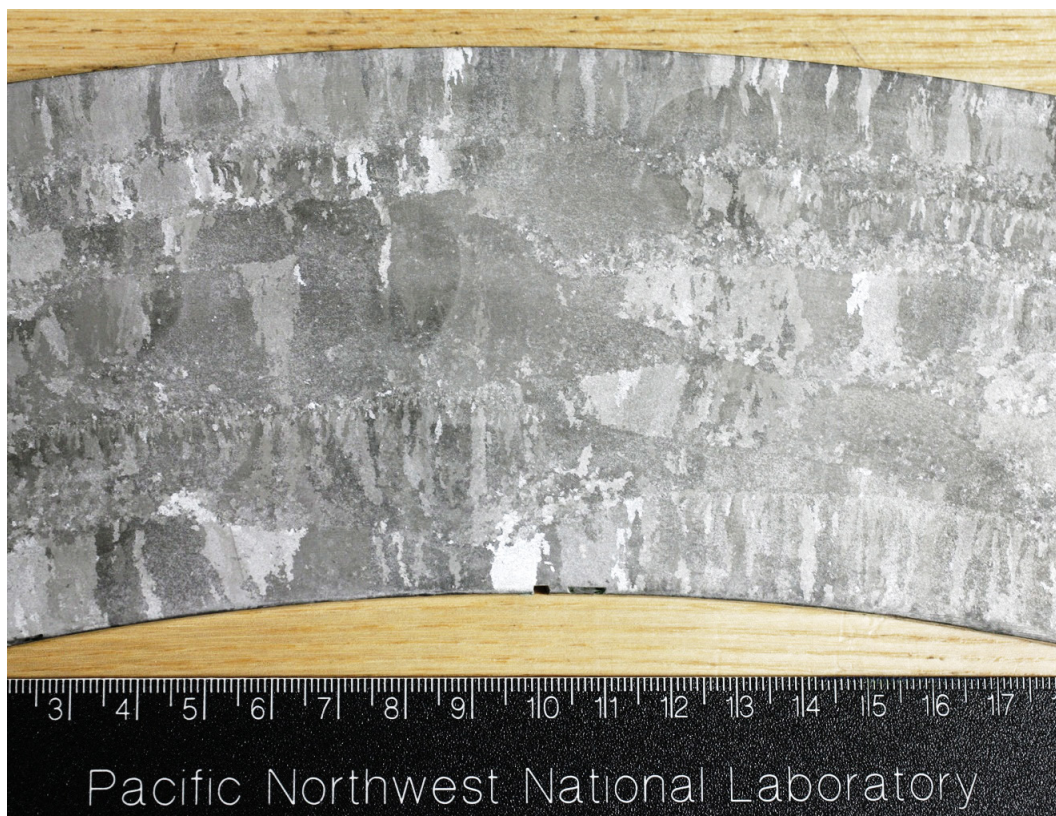


**Figure 2-3 Variation of Grains in Mixed/Banded CCSS Piping from IHI Southwest Technologies, Inc.**

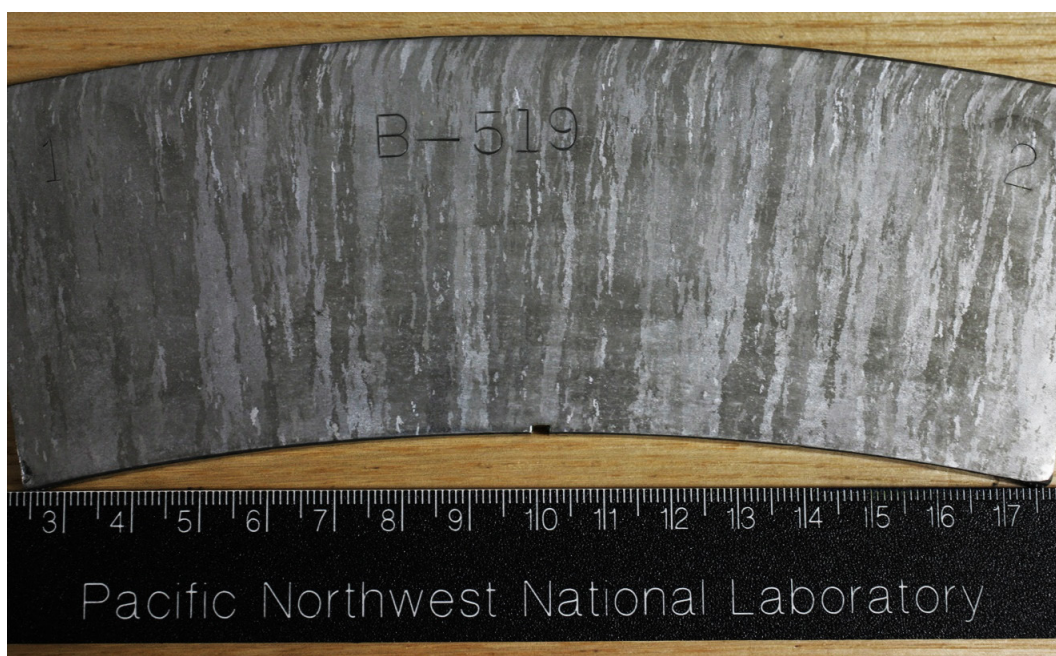


**Figure 2-4 Portion of CCSS Piping Specimen Showing Dendritic Grain Structure Consistent Throughout Circumference**



Finally, for the most recent vintages, likely installed in a few non-U.S. plants constructed in the late-1970s and mid-1980s, the CCSS process was more refined in that a moderately sized equiaxed grain structure appears. An example of a microstructure from a recently constructed (but cancelled) plant of later vintage is shown in Figure 2-5. Based on PNNL (Ruud et al. 2009) and EPRI (Griesbach et al. 2007) research, CCSS piping installed in U.S. plants originated from several fabricators, including U.S. Pipe, Burlington, New Jersey; Sandusky Foundry and Machine, Sandusky, Ohio; and Manoir Foundry, Normandy, France. See Griesbach et al. (2007) and Ruud et al. (2009) for more details and insights into casting processes.



**Figure 2-5 Portion of Later Vintage CCSS Piping Segment Showing Slightly More Refined Equiaxed Grains Throughout**

PNNL conducted an investigation (Ruud et al. 2009) to determine the potential for understanding the grain structures of CASS piping based on variables associated with casting processes, and to identify casting process parameters and their resultant impact on grain structures in LWR CASS piping. The limited amount of information that is available on CASS components relating foundry and heat number to specific grain structures, however, precluded making any firm conclusions. As stated in the Ruud report:

*"It was concluded that columnar grains and banding (layers of significantly different grain structures) were common in [cast] austenitic steels and that such an array of parameters affected their development that control of these casting variables required extraordinary effort. Further, the grain structure cast by a foundry can vary from heat to heat; and within a heat (pipe or component) from one location to another."*

PNNL later conducted an investigation to determine whether, based on experimental measurements, a correlation existed between grain structure in CASS piping and ferrite content of the casting alloy (Ruud et al. 2016). Previous review of the literature indicated that a correlation may exist between CASS microstructures and ferrite concentrations (delta ferrite content of the casting alloy).

Since UT is strongly influenced by CASS grain structure, the probability of detecting flaws could be enhanced by overcoming the deleterious effects of the coarse-grained microstructure on the interrogating ultrasonic beam. Thus, the goal of improving the reliability and effectiveness of ultrasonic inspection of CASS components could potentially be achieved by first characterizing the microstructure of these components. The characterization of CASS microstructures in plant systems must be done in situ. Ferrite can nondestructively be measured in situ, and x-ray fluorescence may be used to nondestructively measure the elemental content of the pipe in situ, thereby allowing the ferrite content of the alloy to be calculated. The 2016 investigation showed that the use of x-ray fluorescence to obtain a volumetric distribution of grain structures (through measurements of elemental composition as a function of spatial location within the volume) is unlikely. In addition, no apparent correlation between Feritscope-measured ferrite levels and grain structure was found. Thus, as revealed by the 2009 investigation, it is not believed possible to determine the microstructure of CASS piping from a review of the constituents via available documents such as chemical material test reports or from the limited amount of casting parameter/process descriptions that can be obtained. However, the 2016 investigation further reinforced the idea that improvements to the reliability of ultrasonic inspection methods could be facilitated by having the ability to characterize the grain structure through the volume of the CASS specimen using various NDE measurement techniques. Evaluations of these techniques to determine the potential for in situ characterization of CASS grain structures have also been performed and documented in several PNNL TLRs (Ramuhalli et al. 2009; Ramuhalli et al. 2010; Ramuhalli et al. 2013). Unfortunately, to date none of the in-situ techniques tested have been able to satisfactorily or reliably determine the volumetric CASS grain structure. Therefore, there are currently no a priori methods of determining how detrimental the grain structure of any given CASS component will be to the UT sound propagation. See Chapter 5.3 for a more in-depth discussion of in situ microstructure assessments.

### 3 INSPECTION REQUIREMENTS FOR CASS WELDMENTS AND REGULATORY BACKGROUND

#### 3.1 Inspection Requirements

GDC 14, *Reactor Coolant Pressure Boundary* (AEC 1971a) of Appendix A to 10 CFR Part 50, General Design Criteria for Nuclear Power Plants, requires that the reactor coolant pressure boundary be designed, fabricated, erected, and tested so as to have an extremely low probability of abnormal leakage, rapidly propagating failure, and gross rupture. GDC 30, *Quality of Reactor Coolant Pressure Boundary* (AEC 1971b), requires that reactor coolant pressure boundary components be tested to the highest quality standards practical.

Provisions for the periodic inspection of primary coolant loop piping, which includes CASS piping and associated weldments (i.e., DMWs), are contained in Section XI, Division 1, *Rules for Inservice Inspection of Nuclear Power Plant Components*, of the ASME Code. The Code is incorporated by reference into 10 CFR, Part 50, *Domestic Licensing of Production and Utilization Facilities*. Thus, licensees are required by law to adhere to the provisions of the ASME Code.

The inspection requirements specific to primary loop piping are contained in Subsection IWB, Article IWB-2500, Table IWB-2500-1, *Examination Categories*. In most cases, Table IWB-2500 states that essentially 100% of the specified portion of selected welds are to be inspected using a volumetric method. UT is the method most commonly employed by the industry to conduct these inspections.

ASME Section XI was first issued in 1968. The authors used operating experience from the oil and gas industries (primarily steam boilers) in developing the examination requirements for NPPs; thus, initial examinations focused on pressure-retaining welds where service-induced degradation had most often occurred in oil- and gas-fired plants. NPP operating experience over the years has reinforced the wisdom of this decision, albeit not the type of service degradation that was initially projected. History in the oil and gas industries indicated that fatigue would be the degradation mechanism most likely to occur in NPPs. The Section XI approach to component examinations was linked to this expectation. However, it was not fatigue, but stress corrosion cracking (SCC) in the weld heat-affected zones of Alloy 82/182 weld materials that has occurred.

As shown in Subsection IWB, Figure IWB-2500-8, Similar and Dissimilar Metal Welds in Components, Nozzles, and Piping, the examination of a pressure-retaining weld extends into the base material. For example, in Figure IWB-2500-8 (c), the examination surface extends 12.7 mm ( $\frac{1}{2}$  in.) beyond the weld into the base metal on both sides of the outside surface of the pipes, and 6.4 mm ( $\frac{1}{4}$  in.) beyond the weld into the base metal on the inside surface of the pipes. The basis for requiring that the examination volume extend beyond the weld is to ensure the heat-affected zone is examined. Operating experience has shown that many of the reported cracks originated in the non-CASS heat-affected zone, especially in cases where welds were repaired during construction.

Meeting the inspection coverage requirements of ASME Code, Section XI is often difficult due to obstructions and materials of construction such as CASS. As an example, Figure 3-1, copied from a June 7, 2012, licensee letter to the NRC (Stanley 2012), shows the configuration of a weld for which the licensee requested approval for an alternative examination because full weld examination coverage could not be obtained. As can be seen in Figure 3-1, significant portions of the weld susceptible to SCC were not examined. The obstruction on the right-hand side of the

weld does not permit the probe to be moved far enough from the weld centerline to properly insonify certain regions of the weld. In addition, portions of the weld were not examined because of weld crown geometry. However, advances in inspection technology have demonstrated that a significant percentage of these regions could be inspected with appropriate techniques. A qualified CASS technique would allow the transducer to be moved further to the left in Figure 3-1 over the CASS safe end to steer acoustic beams through the unexamined weld material at the inside surface of the pipe. Accordingly, to detect any potential defects, a UT method must be effective and reliable in both the base material and weldment. See Chapter 5 with respect to the challenges of inspecting CASS materials and associated DMWs.

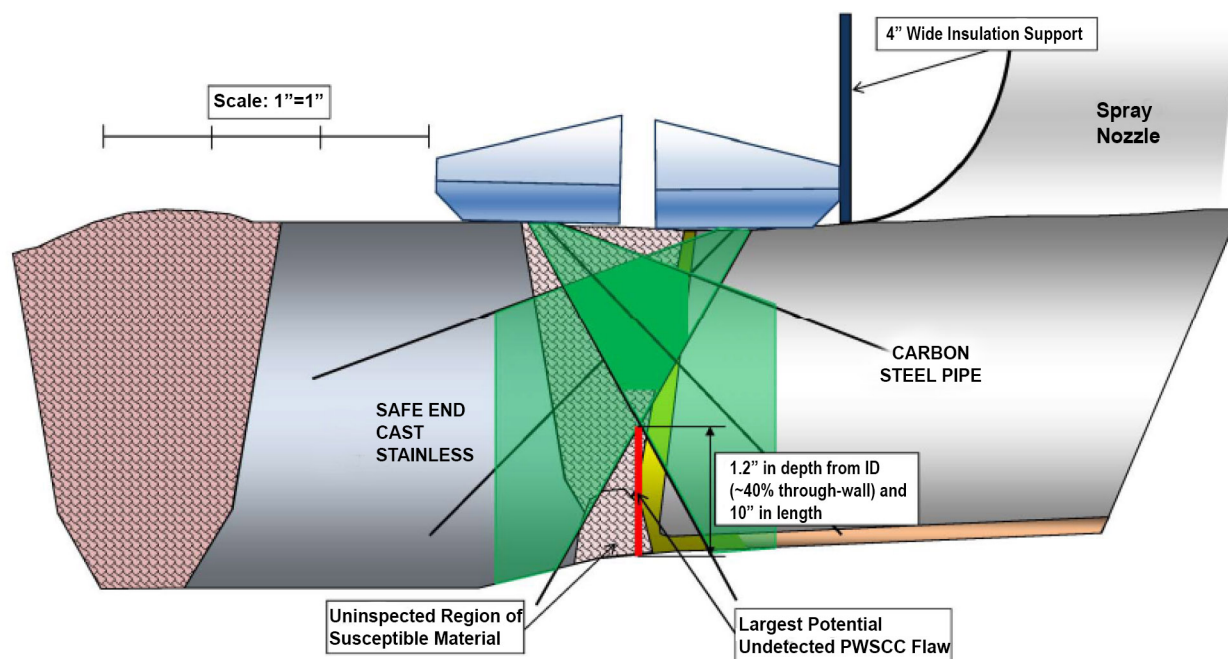


**Figure 3-1 Licensee Calculated Volumetric Coverage and Largest Undetected Flaw for Weld 30-RC-21B-10 (adapted from PNNL 2013b)**

### **3.2 Plant Life Extension Requirements for CASS**

The rules for U.S. licensees applying for extended periods of operation are provided in 10 CFR Part 54, *Requirements for Renewal of Operating Licenses for Nuclear Power Plants*. This part of the CFR defines age-related degradation unique to license renewal and addresses safety-related systems, structures, and components (SSCs) that are relied upon to remain functional during and following design-basis events. Additionally, the NRC published NUREG-1801, Rev. 2, *The Generic Aging Lessons Learned (GALL) Report – Final Report (GALL)* (NRC 2010) in December 2010 (the initial report was published in July 2001), which identifies those aging management programs that were determined by the NRC to be acceptable to manage the aging effects of SSCs in the scope of license renewal. GALL provides the NRC staff's generic evaluation of the existing NPP programs and documents the technical basis for determining whether these programs are adequate or need to be augmented for the proposed period of extended operation. Recommendations are provided in GALL for those specific areas for which existing programs should be augmented for license renewal.

Subsection C2 of GALL, entitled Reactor Coolant System and Connected Lines (Pressurized Water Reactor), addresses the PWR primary coolant pressure boundary. Item IV.C2.R-05 of this Subsection specifically addresses CASS components. This states that for CASS components (1) in systems not subjected to monitoring and control of primary water chemistry, or (2) outside of acceptable carbon and ferrite percentages, a licensee's aging management program must include adequate inspection methods to ensure detection of cracks and a flaw evaluation methodology for those CASS components that are susceptible to thermal aging embrittlement. Industry efforts to develop a generic flaw evaluation methodology are addressed in a later discussion regarding ASME Section XI Code Case N-838.

Criteria to determine the susceptibility of CASS components to thermal aging embrittlement were provided in a NRC May 19, 2000, letter (Grimes 2000). The criteria formed the basis for the CASS aging management program in all revisions of NUREG-1801 (i.e., GALL report). Subsection C2 of the GALL report, "Reactor Coolant System and Connected Lines (Pressurized Water Reactor)," page IV C2-2, specifically addresses CASS components. For the CASS components considered susceptible to thermal aging embrittlement, a licensee's aging management program must include adequate inspection methods to ensure the detection of cracks.



## 4 EXPECTED SERVICE DEGRADATION IN CASS

The relatively low cost and corrosion resistance of CASS piping resulted in this material being used extensively in the primary coolant systems of many PWRs, especially in locations where high strength and creep resistance are required because of elevated temperatures. While CASS piping in primary water conditions has performed well to date with respect to corrosion resistance, it has long been known that degradation due to thermal aging may occur in this material (Trautwein and Gysel 1982; Chopra 1991, 1994).<sup>4</sup> Specifically, hardness and tensile strength increases with accompanying decreases in ductility, fracture toughness, and impact resistance are evident with prolonged exposure to operating temperatures in the range of 280–320°C (≈535–610°F). CASS materials, because they have a duplex structure, are susceptible to thermal embrittlement after extended operation at 288–327°C (550–621°F) for PWR primary coolant piping and 343°C (650°F) for PWR pressurizers (Chopra and Rao 2016).

The early investigations at ANL cited above, as well as research performed elsewhere, have shown that thermal aging embrittlement of CASS components may occur during the initial reactor design lifetime of 40 years. It has been shown that different grades and heats of CASS materials exhibit varying degrees of thermal aging embrittlement. In general, the low-carbon CF3 materials are the most resistant to this degradation, and the molybdenum-bearing, high-carbon CF8M materials appear to be the least resistant. According to these studies, embrittlement of CASS materials may result in brittle fracture associated with cleavage due to twinning of the ferrite phase and/or separation of the ferrite/austenite phase boundary. The critical stress level for brittle fracture is attained at normal PWR operating temperatures. Brittle failure predominantly occurs when the ferrite phase is continuous (e.g., in CASS material with a high ferrite content) or when the ferrite/austenite phase boundary provides an easy path for crack propagation (e.g., in high-carbon grades of CASS with large phase boundary carbides).

In the United States, criteria to determine the susceptibility of CASS components to thermal aging embrittlement of CASS materials were provided by the NRC in 2000 (Grimes 2000). However, a considerable amount of research has been conducted since the NRC letter was issued in 2000. The original criteria have been modified and new ones added based on the research published in Rev. 2 to NUREG/CR-4513 (Chopra and Rao 2016).

The research results clearly demonstrate that CASS primary loop components, such as piping, valve bodies, and pump casings, suffer a loss in fracture toughness due to thermal aging after many years of service at operating PWR primary system temperatures. In the United States, the susceptibility to thermal aging embrittlement of CASS materials has been determined through an assessment of casting method, molybdenum content, and ferrite content, based on the criteria set forth in the May 19, 2000, letter from NRC to industry (Grimes 2000). In France, research has led to the use of different factors to indicate the susceptibility of CASS components to thermal aging embrittlement; that is, chromium, molybdenum, and silicon (Faidy et al. 2003; Faidy 2010).

An extensive amount of research has been conducted since the initial susceptibility methods were established. In May 2016, the NRC published Revision 2 to NUREG/CR-4513 (Chopra and Rao 2016). The procedure and correlations used for predicting changes in fracture toughness and

---

<sup>4</sup> NUREG/CR-4513 was initially published in June 1991 (Chopra 1991) and updated in Rev. 1, published in August 1994 (Chopra 1994). Revision 2 was recently published in May 2016 (Chopra and Rao 2016).

tensile properties for CASS components due to thermal aging were updated in Revision 2 by using a much larger database. Among the notable changes from previous findings:

- The cumulative embrittlement effect is significant for CF8M materials with nickel content of  $\geq 10\%$
- The threshold value of ferrite content for both CCSS and SCSS was decreased
- The latest research suggests is that the level of nickel is a factor with respect to the susceptibility of CASS to thermal aging embrittlement.

Based on the latest research, the criteria for determining the susceptibility of a material to thermal embrittlement have been decreased. In addition, material factors not previously considering for assessing susceptibility have been identified. Another analysis indicates that some aged CASS materials have the potential for exceedingly low toughness (Uddin et al. 2017). Given that research has shown that embrittlement due to thermal aging and neutron exposure of CASS components may occur during the initial licensing period, the need for effective and reliable CASS examination methods is not exclusively an issue related to license renewal and extended operations.



## 5 INTRODUCTION TO ULTRASONIC EXAMINATION ISSUES IN CASS

### 5.1 Implications of Anisotropy

Austenitic stainless steels are anisotropic, meaning that certain properties, such as tensile strength, Young's modulus, and electrical resistivity, and most importantly to the current assessment, ultrasonic velocity, vary within each grain according to the dominant atomic crystalline direction. Stainless materials generally possess a face-centered-cubic crystalline lattice structure, causing the close-packed plane of atoms of each grain to support higher sound velocities than other less densely packed lattice planes. Further complicating volumetric UT propagation is the effect of multi-crystalline structures, where large, individual grains containing lattice orientations in a common direction interfere with sound transmission due to the differing lattice structures of their contiguous neighboring grains. The resulting grain boundaries, or areas of atomic mismatch between grains, present ultrasonic impedance differences and velocity variations. This is not a particularly difficult obstacle for common UT practices in wrought piping (both for ferritic and austenitic materials), as mechanical and thermal processing of these metals produce grains that are typically much smaller than the wavelength of bulk sound being used for volumetric interrogation. Thus, while some attenuation may occur, the longer wavelength-to-grain diameter ratios allow for adequate conventional sound propagation in wrought materials. Note that wrought structural steels, both ferritic and austenitic, have nominal grain diameters on the order of several microns, with typical ultrasonic frequencies ranging from 1.0 to 5.0 MHz being employed for examinations in the field. Based on sound velocities in these materials, at these frequencies one could expect ultrasonic wavelengths ranging from a few hundred to thousands of microns in length, much larger than the grain diameters.

However, in the case of both CCSS and SCSS piping, the process of initial solidification to a near-final shape results in very large, anisotropic grains having diameters as large as several centimeters (Diaz et al. 1998), often on the length scale of the acoustic wavelengths used in traditional or conventional ultrasonic applications. After polishing and etching cross sections of varied CASS microstructures, Anderson et al. (2007) reported grain diameters measuring from 0.44–26.18 mm (0.02–1.06 in.), while median values for SCSS and CCSS were on the order of 12–15 mm (0.47–0.59 in.) and 17–20 mm (0.67–0.79 in.), respectively. Furthermore, various casting process parameters can produce large columnar (dendritic), large and small equiaxed, and/or mixed/banded structures of these microstructures dependent on specific chemistry and solidification heat dissipation. These conditions continue to present significant challenges to ultrasonically examining CASS piping components for detection of potential service degradation.

The nature of these CASS piping microstructures causes severe attenuation, beam redirection (skewing), and scattering of ultrasonic energies at conventional frequencies.<sup>5</sup> As a consequence, certain volumes of material may not be properly insonified, and coherent energy reflected from individual grains may be difficult to distinguish from actual flaw responses. For more detailed information on characterizing the microstructures of available CASS materials, see Anderson et al. (2007).

---

<sup>5</sup> Typical frequencies used for conventional UT are nominally greater than 1.0 MHz with widespread use of probes having center frequencies on the order of 1.5–2.25 MHz for austenitic stainless steels and higher for ferritic steels.

## **5.2 UT Beam Propagation and Sound Field Distortion in CASS**

Some of the earliest assessments of sound field degradation in CASS were performed at PNNL (Good and Van Fleet 1987, 1988; Good and Green 1989). This work involved propagating various sound beams into primarily two distinct CASS microstructures—one fully equiaxed and one fully dendritic (columnar). Longitudinal and shear waves (both vertically and horizontally polarized) were used in frequencies ranging from 500 kHz to 3.0 MHz to insonify CCSS piping specimens with wall thicknesses of approximately 58 mm (2.3 in.) and inside diameters on the order of 700 mm (27.5 in.). Very small microprobes, or “pinducers,” were used to map the transmitted energies on the opposite surface of the specimens. These resultant images were analyzed to evaluate the effect of CASS microstructure on the varied sound fields. A carbon steel wrought specimen of the same thickness was used as a fiduciary for comparison.

Several conclusions were reached in these early studies with respect to applying ultrasonic techniques in CASS. It was observed that only 500 kHz vertically polarized shear waves would sustain a coherent field in this material. It was also found that longitudinal waves at 1.0 MHz, and occasionally at 2.0 MHz, would penetrate the CCSS specimens with varied levels of distortion. It is interesting to note that during this early research, increased use of LF UT was being pursued as higher frequencies (>1.0 to 1.5 MHz) performed poorly on CASS (Pade and Enrietta 1981; Kupperman et al. 1987; Rishel 1988).

More recently, PNNL performed a detailed analysis of the effects of various CASS microstructures on the integrity of sound fields (Crawford et al. 2014). This study applied PA refracted longitudinal waves operating at 500 kHz, 800 kHz, and 1.0 MHz to vintage CCSS specimens having fully equiaxed, fully dendritic, and layered/mixed banded microstructures. Multiple transmitting probes were used to steer and theoretically focus the beam with a small broadband pinducer acting as a receiving element (see Figure 5-1). The sound fields were measured, then material was iteratively removed in slices on the specimens to track variables such as attenuation, scattering, positional error, and sound field partitioning along the sound beam metal path. Several nominal transmitting angles for each frequency were applied along with passive beam skewing to allow those variables to be assessed as well. All data were benchmarked against sound field maps obtained through a fine-grained, wrought stainless steel specimen (Figure 5-2). Examples of the resulting sound field images are shown in Figures 5-3 through 5-6.

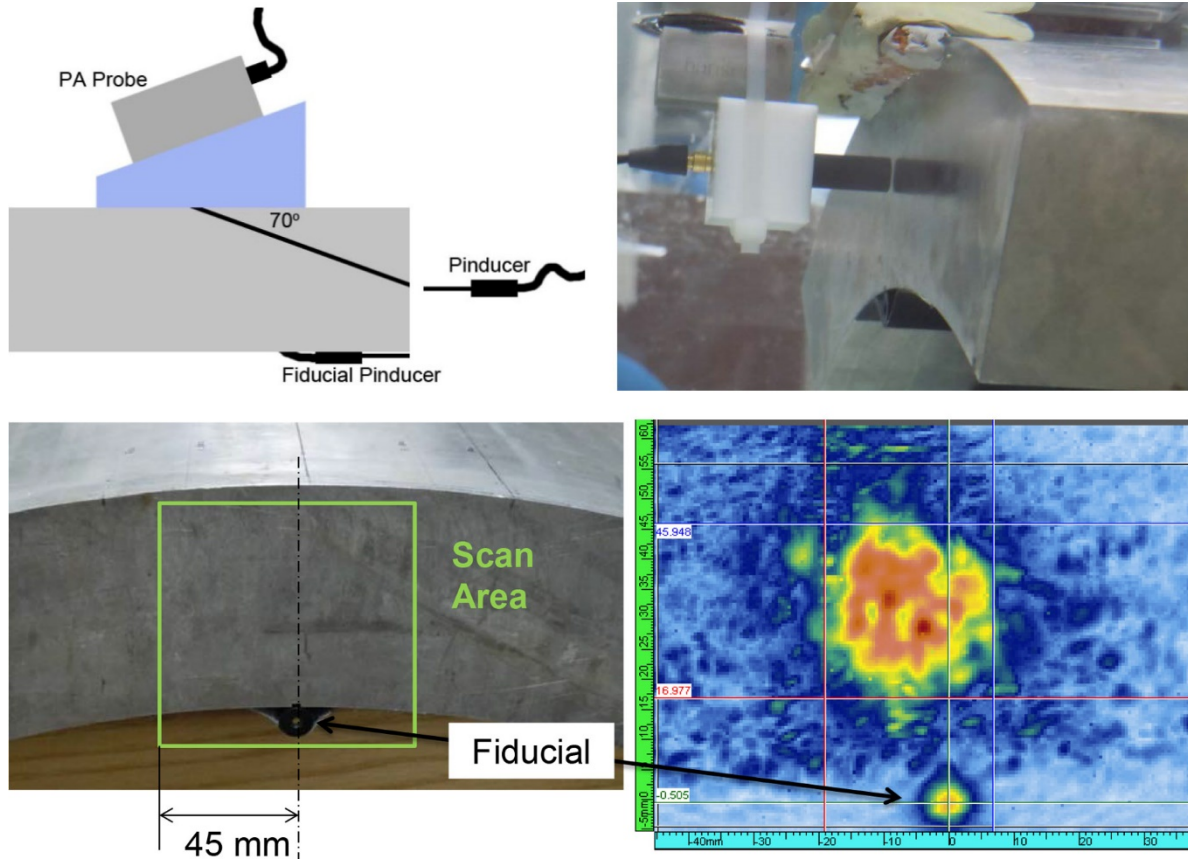


**Figure 5-1** Experimental Set-up for Assessing Sound Fields in CASS Specimens. *Top left* – schematic for experiment, *top right* – photo of receiving pinducer on specimen as seen from side of immersion tank, *bottom left* – axial view showing fiducial emitter used to mark spatial coordinates, and *bottom right* – sample image of as-received sound field and fiducial emitter.

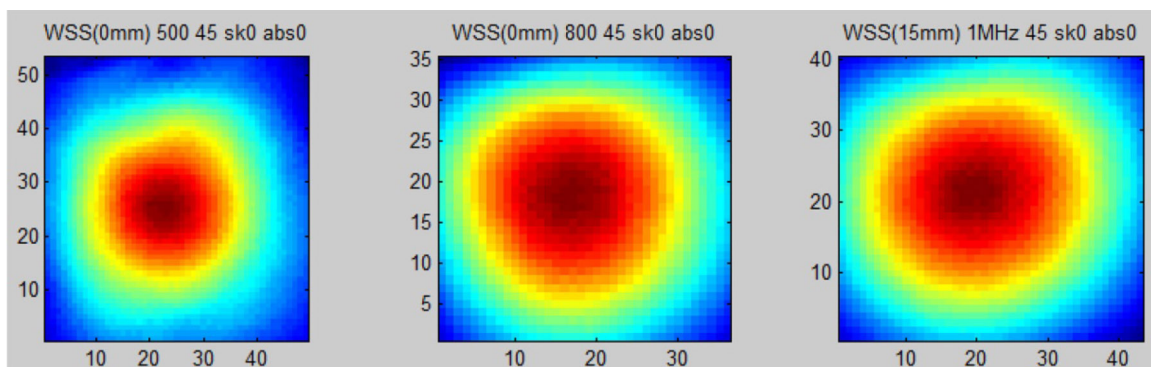


**Figure 5-2** Sound Field Images on Wrought Stainless Steel Specimen at Same Metal Path and 45° Propagation Angle Using 500 kHz (*left*), 800 kHz (*middle*) and 1.0 MHz (*right*) for Benchmarking Purposes.

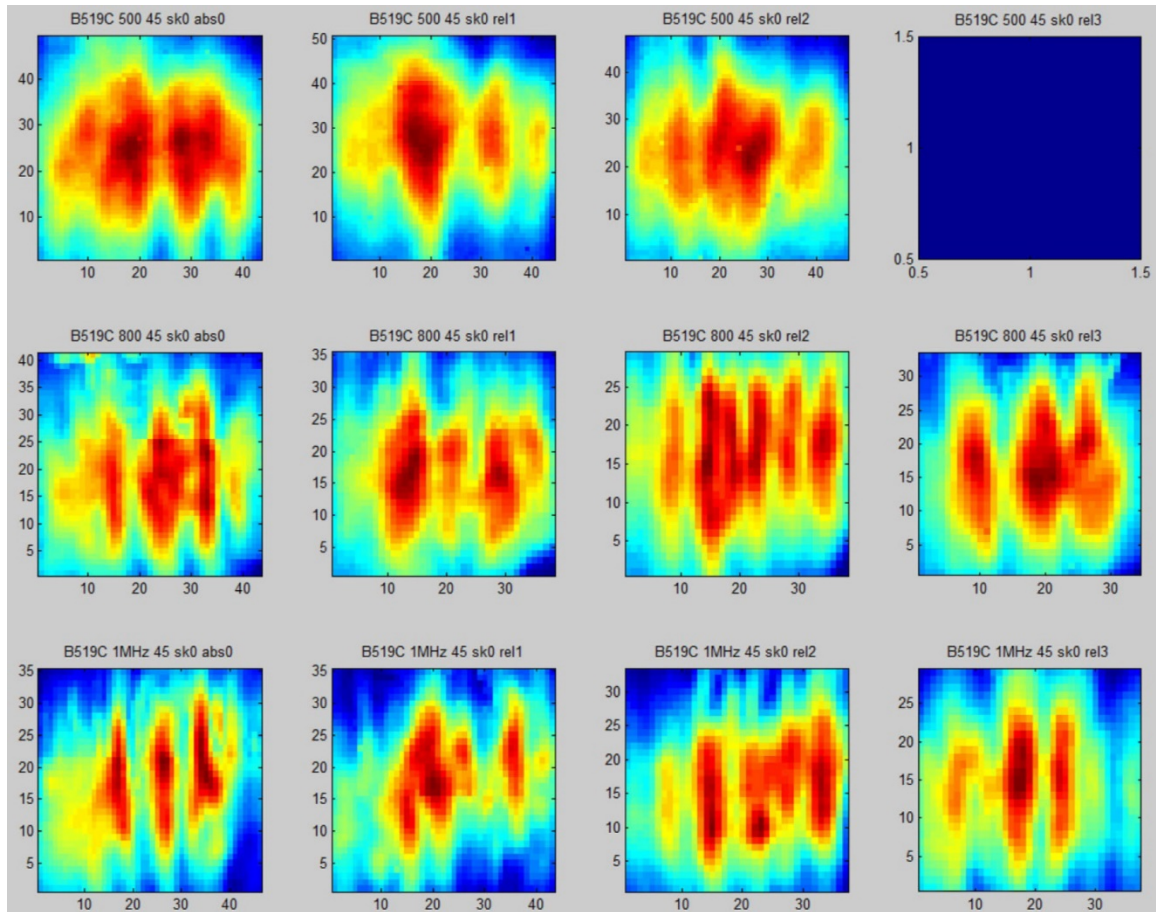


**Figure 5-3** Sound Field in Fully Dendritic Specimen at a 45° Refracted Angle and 0° Beam Skew. In this example, sound fields at 500 kHz (*top row*), 800 kHz (*middle row*), and 1.0 MHz (*bottom row*) probe frequencies are illustrated in slices 0–3, *left to right*. The data file for one 500 kHz scan (*upper right*) was corrupted.



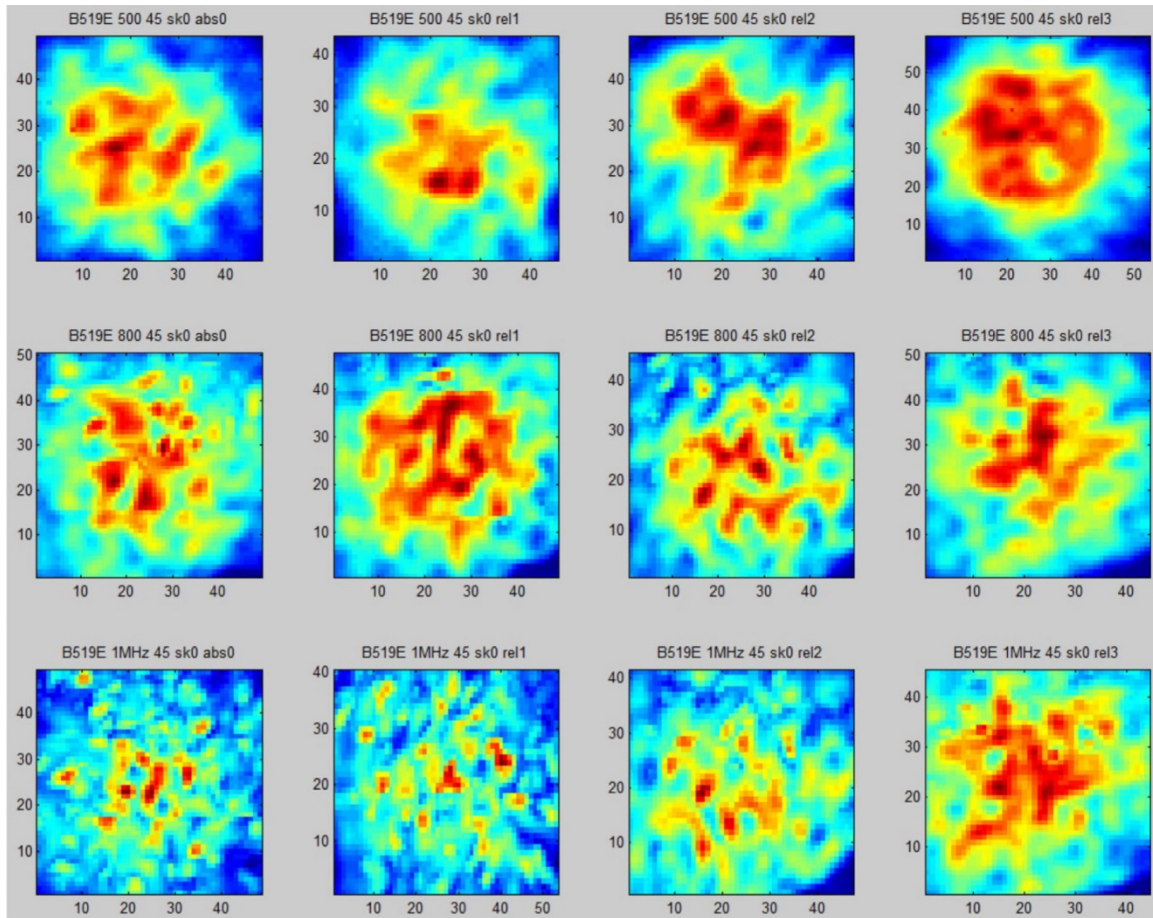


**Figure 5-4** Sound Field in Fully Equiaxed Specimen at a 45° Refracted Angle and 0° Beam Skew. In this example, sound fields at 500 kHz (*top row*), 800 kHz (*middle row*), and 1.0 MHz (*bottom row*) probe frequencies are illustrated in slices 0–3, *left to right*.

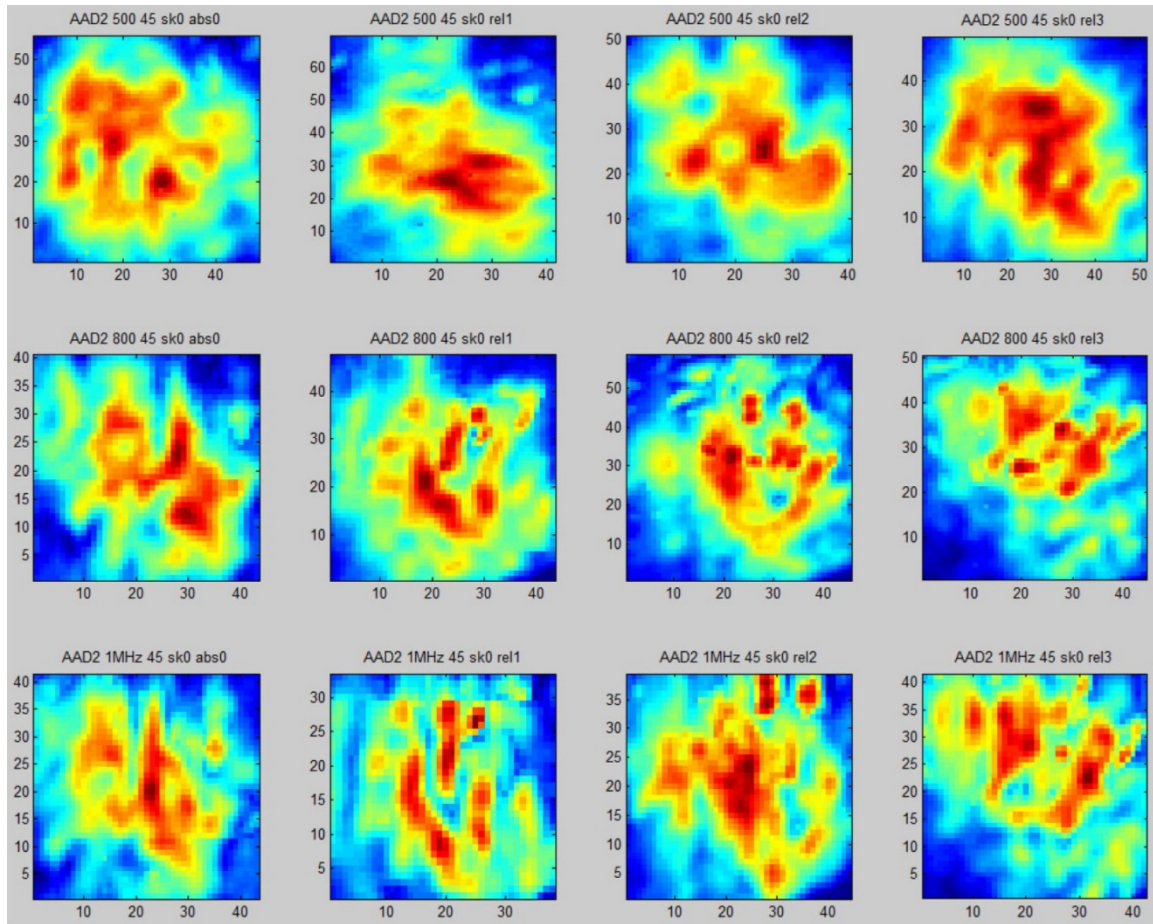


**Figure 5-5** Sound Field in Mixed/Banded Specimen at a 45° Refracted Angle and 0° Beam Skew. In this example, sound fields at 500 kHz (*top row*), 800 kHz (*middle row*), and 1.0 MHz (*bottom row*) probe frequencies are illustrated in slices 0–3, *left to right*.

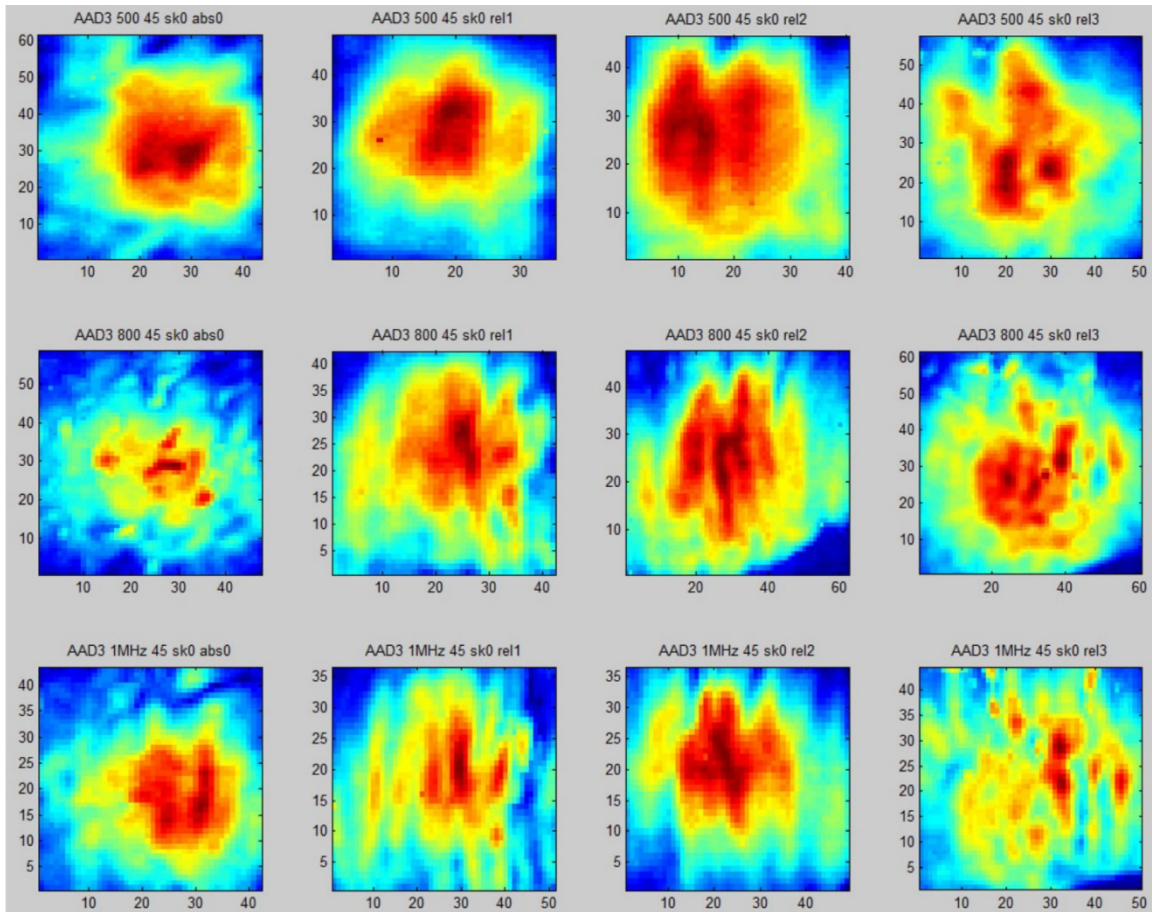


**Figure 5-6 Second Mixed/Banded Specimen at a 45° Refracted Angle and 0° Beam Skew with 0.5, 0.8, and 1.0 MHz Probe Frequencies, *Top to Bottom*, and Slices 0–3, *Left to Right*.**

As expected, the 2014 Crawford study (Crawford et al. 2014) showed that the lowest frequency (500 kHz) produced the least sound beam scattering and partitioning (to a slightly lesser extent), but it also showed the largest positional error, which could provide sizing difficulties when flaws are encountered in the field. Columnar structures produced the greatest partitioning and equiaxed the least; one might intuitively expect such, as each columnar dendrite formed a quasi-waveguide or lens that would tend to cause this effect. A surprising result is that the fully equiaxed microstructure provided the largest scattering of sound as opposed to the mixed/banded or fully dendritic specimens. Refracted angle variation in the primary-steered direction was shown to only be a minor variable with respect to overall scatter and partitioning of sound, as was the case with passive skew angles. Sound beam redirection was also found to be much greater in the CASS versus the wrought specimens; this was expected. Thus, results suggest that flaw responses may inherently be somewhat mis-located and improperly sized when detected in the field.

When compared to the wrought benchmark, peak amplitude responses in the CASS specimens at 500 kHz showed little reduction; however, at 800 kHz and 1.0 MHz, signal-to-noise ratios (SNRs) were observed to be 10–15 decibels (dB) lower than on the wrought material. This again suggests the use of lower frequencies will result in better sound penetration and produce higher flaw responses than higher frequencies, with recommendations that 500 kHz be used for flaw detection in piping larger than approximately 50 mm (2 in.) in thickness.



As stated in Crawford et al. (2014):

*Clearly, the first priority in an ultrasonic examination [of CASS] is the selection of [PA] probe frequency, assuming sufficient probe aperture, element size, and number [of elements] to properly form the beam. The primary objective of the examination is to effectively detect and then [subsequently] characterize relevant flaws in the component.*

### 5.3 In Situ Microstructure Assessments

Initial activities (sponsored by the NRC) to develop NDE techniques for in situ microstructure evaluations at PNNL were performed in the late 1980s and early 1990s. The idea was to assess methods for determining the CASS component microstructure prior to conducting UT examinations in order to choose optimal inspection parameters for the specific microstructure being examined. A UT method using Rayleigh wave critical angle evaluation was pursued with limited success (Hildebrand et al. 1991). This technique involved applying a longitudinal wave in an immersion setup that impacted the CASS specimen's surface at a critical incident angle to generate a Rayleigh surface wave (see Figure 5-7). This wave would propagate along the surface for a finite distance but only penetrate about one wavelength into the material. The critical angle is derived according to the specimen's near-surface elastic constants, which are directly related to the lattice or grain structure in this region. The method is complicated by the anisotropic nature of CASS, but critical angles were experimentally determined, and a relative comparison between two differing CASS microstructures could be ascertained. However, this method was more suitable for a laboratory environment as opposed to application on field CASS piping at operating NPPs.

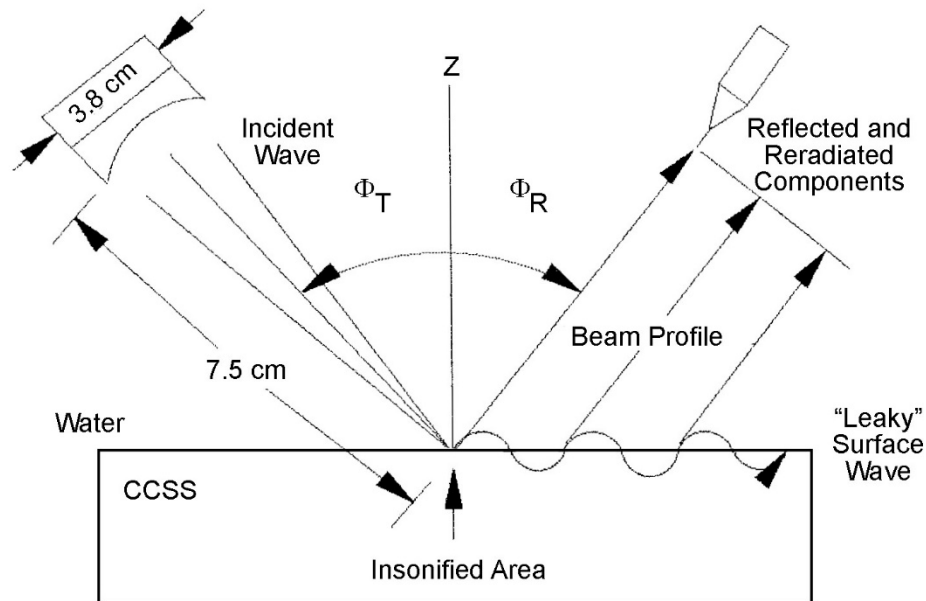


**Figure 5-7 Illustration of the Rayleigh Critical Angle Technique**

Further work on the in situ determination of CASS microstructures was investigated more recently with application of UT longitudinal wave attenuation, and assessing the time-of-flight ratios between normal incidence shear waves and normal incidence longitudinal waves (Ramuhalli et al. 2009). This was followed by longitudinal wave backscatter, monitoring of UT diffuse fields, and a multi-frequency electromagnetic technique (Ramuhalli et al. 2010). Both of these studies were



performed on two sets of CASS specimens, each having homogeneous and distinct microstructures; that is, each set of CASS specimens exhibited either fully dendritic (columnar) or fully equiaxed conditions (see Figure 5-8 as an example of cross-sectional microstructure(s) for the specimens used in these studies).

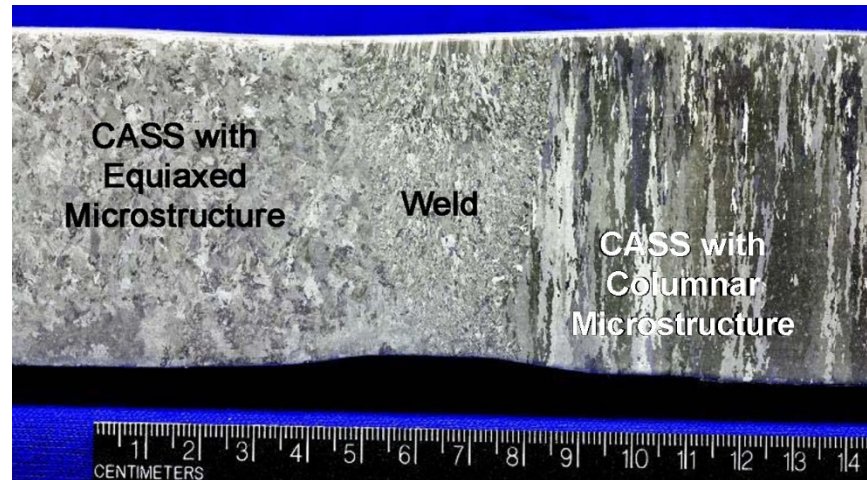


**Figure 5-8 A Representative Axial-Radial Cross Section of a CASS Specimen, Showing Typical Grain Structures on Either Side of the Weld Outside and Inside Diameter Geometry, and Microstructure of a Specimen.**

The time-of-flight shear-to-longitudinal ratio work provided a reliable means to classify material type in this problem set consisting of two distinct microstructures. As shown by the resultant ratio values in Figure 5-9, it was quite straightforward to assess the difference. However, it is cautioned that this is a normal beam ratio (both shear and longitudinal at 500 kHz) and would require specially fabricated electromagnetic acoustic transducers to make measurements in the field. Additionally, it is stated that since this ratio is an average over full specimen thickness, it would be difficult to establish characterization strictly as a function of time or depth.

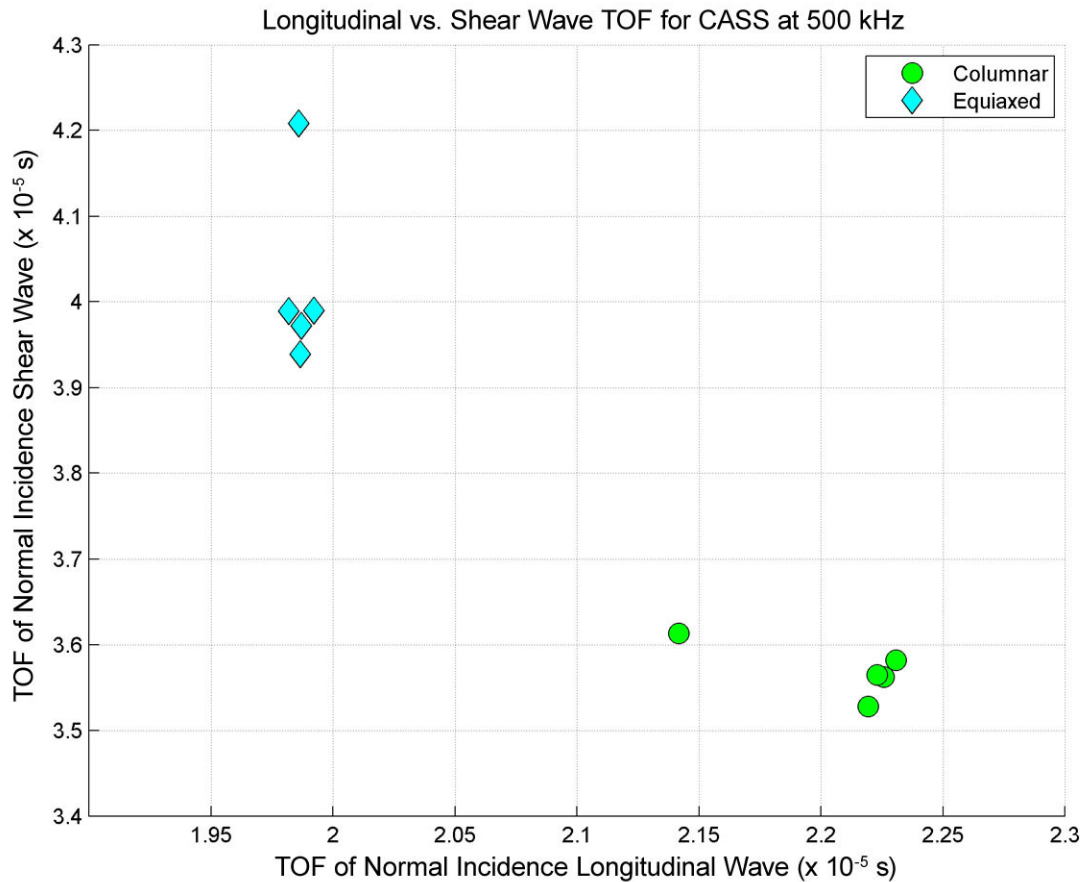


**Figure 5-9 Scatter Plot of Longitudinal Wave against Shear Wave Time-of-Flight (TOF)**

This work led into further investigation (Ramuhalli et al. 2010) using UT longitudinal wave backscatter, UT diffuse fields, and eddy current testing (ET) methods to assess if these applications had potential, with less dependence on wall thickness, to determine the two distinct microstructures (fully columnar or equiaxed). Both of the UT techniques provided data that, after certain algorithmic transformations, exhibited differences between the fully equiaxed and fully dendritic structures; however, these differences were subtle and required data manipulation. In addition, it was stated that specific variables applied during the calculations, such as phase velocity in the backscatter experiments and precise specimen dimensions in the diffuse field work, may not be known for in situ work on piping installed in NPPs.

The ET techniques applied in the aforementioned study also showed promise in the two-variable problem set (purely dendritic or equiaxed) using average magnitude and phase changes that could be precisely measured in the laboratory. However, the ET method was found to be limited in its applicability due to the electromagnetic skin effect, and very low excitation frequencies would be necessary to inspect and characterize typical thick-section CASS components currently used in NPPs (Ramuhalli et al. 2010). Additionally, spatial delta ferrite variances in CASS materials cause significant noise problems when applying an ET technique and could potentially exacerbate the issue of making precise measurements on field piping (Diaz et al. 2007).

More recent research for nondestructively evaluating CASS microstructure was performed to ascertain if an electromagnetic induction technique, coupled with x-ray fluorescence (XRF), might be used in situ to determine the ferrite differences in vintage CASS specimens having columnar, equiaxed, and mixed/banded microstructures (Ruud et al. 2016). If so, the instrumentation for assessing these variations currently exists and is commonly used in the field, for example Feritscope and XRF analyzer. The Ruud report documents research to determine whether, based on experimental measurements, a correlation exists between grain structure in CASS piping and the ferrite content of the casting alloy. The motivation for this research lies in the fact that UT is strongly influenced by size and type of CASS grain structures; knowledge of this grain structure may help improve the ability to interpret UT responses, thereby enhancing the overall reliability of UT inspections of CASS components. A correlation between delta ferrite resulting from ladle chemical composition and casting process parameters and certain CASS microstructures was previously theorized (Ruud et al. 2009). The 2016 research methodology included an assessment (from photomicrographs) of the overall percentage of columnar bands present; these ranged from purely columnar (large grains) at 100%, to small columnar orientations that required a weighted average to assign this percentage, to an arbitrary assignment of 50% for the mixed/banded specimens, and finally to the purely equiaxed specimens that were assigned a 0% for columnar grains present. Seventeen varied specimens were marked with grids on the ID, ID, and through-wall edges available to apply the Feritscope and XRF devices (see Figure 5-10). The analysis of data from the electromagnetic induction technique showed little or no correlation between ferrite measured and grain structure. While it was determined that there are correlations between grain structures and acquired laboratory data, as defined by percent columnar grains and ferrite content calculated from XRF measurements of elemental content, it was determined that the correlation does not adequately capture the volumetric variation of grain structure.

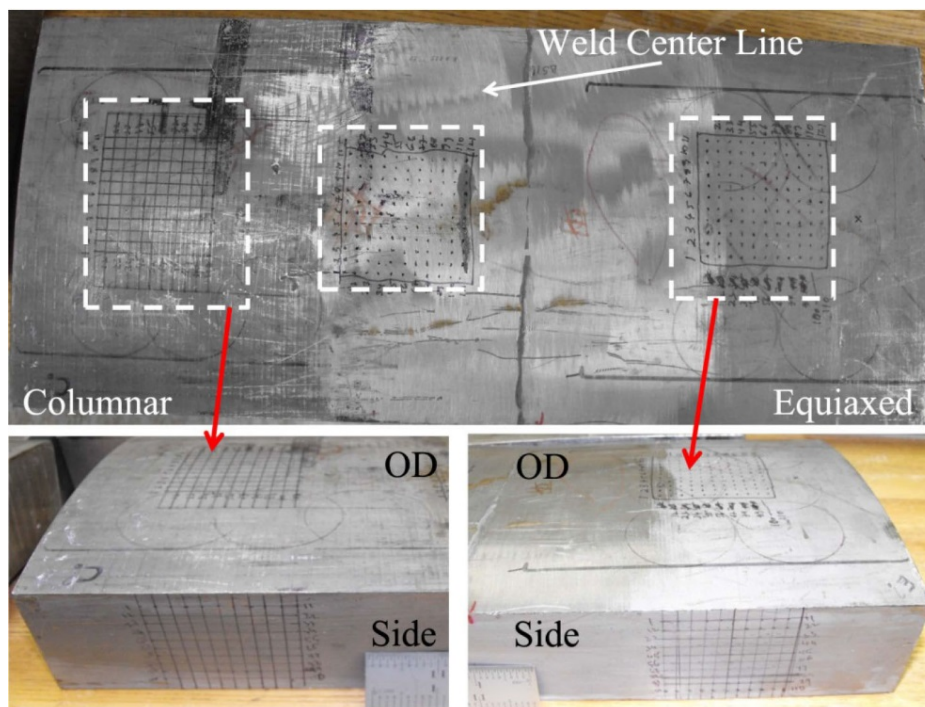


**Figure 5-10 Feritscope and XRF Measurement Grids.** The figure shows the fine-grid scans on the outer-diameter surface and the side (axial-radial cross section) surfaces for the columnar and equiaxed grain sections.

As described above, while certain laboratory methods show promise, no in situ field techniques have accurately provided grain size and orientation data that could be taken into account when developing UT procedures and technique parameters for purposes of ISI. Further, as previously noted, no current evaluation technique, either through data mining or a similar investigative or deductive process, can be used to reliably establish the microstructures existing in nuclear power facilities. When polished and etched, vintage CASS piping materials made available in recent years have continued to show unpredictable microstructural variability along the length of the piping segment as well as circumferentially.

## **6 CASS RESEARCH LEADING TO LOW-FREQUENCY UT**

### **6.1 Early Work, Round-Robin Exercises, and Cooperative Results**

The inherent corrosion resistance, ductility, and relatively lower cost of CASS led WEC to use this material in all PWRs fabricated in the United States as early as the late 1960s. The coarse grain structure and difficulty in ultrasonic examinations was known at this time; however, it was believed that a reliable UT method would be developed prior to the end of the first operating intervals of the early plants being fabricated.

In 1978, WEC pursued a demonstration program using a limited set of welded CASS specimens with purely columnar microstructures having a range of induced mechanical fatigue cracks. Conventional manual UT techniques were applied, and it was reported that all of the flaws greater than 20% through-wall depth were detected with no false calls (Pade and Enrietta 1981). However, it was reported (Taylor 1984) that specimens used in the WEC inspection trial may not be indicative of what was encountered in the field because of the specimen-to-flaw design, type of flaws being used, lack of geometrical reflectors, and use of only one type of microstructure.

PNNL surveys conducted in the early 1980s (Becker et al. 1981; Morris and Becker 1982) suggested that the most common conventional UT techniques being used for CASS materials involved manual, one- or two-element refracted longitudinal waves operating between 1.0 and 1.5 MHz, with theoretical insonification angles between 40° and 45°. Most industry organizations that were surveyed displayed low confidence in these CASS examinations.

The 1978 WEC study results were inconsistent with the PNNL survey results. During this period, NRC sponsored NDE reliability research at PNNL, including the Piping Inspection Round Robin (PIRR) that used welded specimens to simulated field piping. The statistical analysis of the PIRR was reported in NUREG/CR-5068 (Heasler and Doctor 1996). As part of this study, CASS specimens with a variety of microstructures having induced TFC in the presence of blended OD weld crowns and ID counterbores were used. Six commercial inspection teams participated using conventional manual UT techniques in a blind protocol. The results are shown in Figure 6-1. It was clearly evident these methods resulted in poor detection performance and would not form the basis for reliable examinations of CASS (Taylor 1984). This conclusion continues to be validated through more recent NDE research (EPRI 2005b; Anderson et al. 2007; Diaz et al. 2008a; Dennis 2012; Crawford et al. 2014).

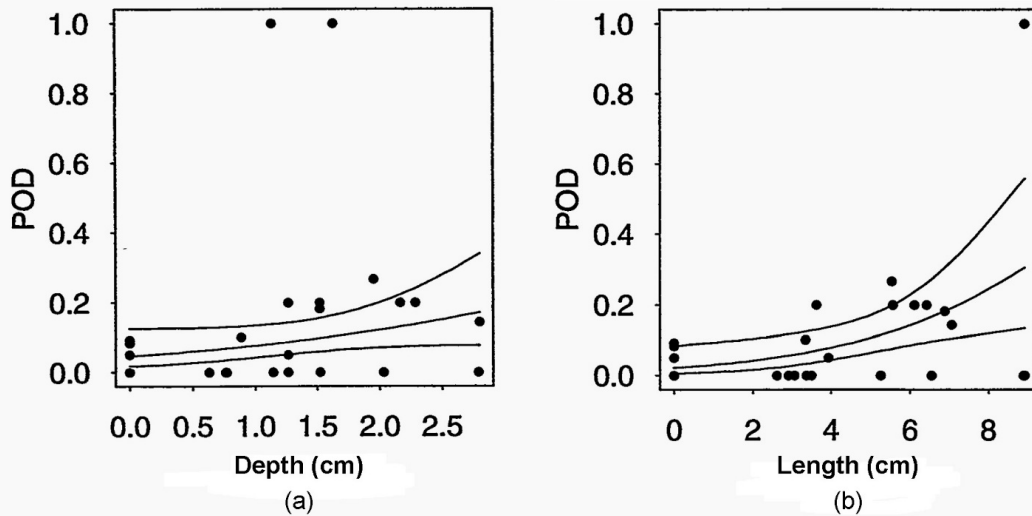


**Figure 6-1 Logistic Curve Fit to Probability of Detection Data with 95% Bounds (cast stainless steel, near-side inspections, all teams): (a) probability of detection versus depth; (b) probability of detection versus length.**

Following the poor results obtained in the PIRR, the international community developed other round robins that included CASS piping weldments (international PISC and the Mini-Round Robin [MRR]). The CASS specimens used in these exercises included fully dendritic, equiaxed, and mixed/banded microstructures having TFCs, mechanical fatigue cracks, and other machined reflectors to assess system capability. Results were consistent in showing that conventional UT methods, some even encoded and automated, continued to provide unreliable results. The poorest results were on the mixed/banded microstructures having TFCs. During this time, the NRC tasked PNNL with developing a prototype LF system coupled with SAFT post-processing to determine if this method showed enough promise to warrant further research.

Extensive laboratory work using “synthetic aperture focusing” coupled with LF (< 1 MHz) ultrasonic probes was performed at PNNL for many years. Synthetic aperture focusing, or SAFT, refers to a process in which the focal properties of a large-aperture focused transducer are synthetically generated from data collected over a large area using a small transducer with a divergent sound field. SAFT was developed to overcome some of the limitations imposed by large physical apertures, such as scanning limitations, and has been successfully applied in the field of UT. The processing required to focus the data has been called beam-forming, coherent summation, or synthetic aperture processing. The resultant image is a full-volume focused characterization of the inspected area (Busse et al. 1984). SAFT-UT technology is able to provide significant enhancements to the inspection of austenitic welds and other anisotropic, coarse-grained materials.

SAFT evolved to focus on inspection problems associated with thick section, reactor coolant piping that are comprised of coarse-grained microstructures exhibiting multi-layered boundary conditions such as centrifugally and statically cast pipe, elbows, and DMWs. Due to the difficulties encountered in these types of examinations, the low-frequency SAFT technique was identified as having potential as a post-processing method to improve detection and discrimination capabilities from ultrasonic signal responses in CASS (Diaz et al. 2008b; Anderson et al. 2011). Additionally, it was anticipated that CASS inspection effectiveness would improve due to the utility of longer wavelengths, thereby reducing the attenuative effects of the weld and parent material.

The reader can refer to previous SAFT algorithm development and testing work at PNNL aimed at developing a real-time flaw detection and characterization SAFT-UT system (Doctor et al. 1987; Doctor et al. 1996), as well as additional PNNL CASS research that employed SAFT-UT (Diaz et al. 1998, 2003 and 2008b). For additional details associated with the historical work in low-frequency SAFT CASS examinations, see Appendix A of this report.

## **6.2 Development of LF-SAFT**

PNNL began to explore the effects of probe frequency in greater depth during the mid-1980s, including the use of probes in the 250–450 kHz range (Diaz et al. 1998; Diaz et al. 2008b). From the mid-1980s through the 1990s, PNNL investigated the potential to examine CASS/DMW components using LF-SAFT. The research indicated that long-wavelength, compressional (longitudinal) waves oriented at appropriate angles with respect to the large grains in CASS showed promise in detecting cracks. PNNL conducted investigations using LF-SAFT with multiple propagation angles because there was no reliable method to determine grain sizes or orientations of CASS in situ. Grain size, orientation, and layering often vary as a function of circumferential and axial locations in piping; *thus, it is highly unlikely there will be a single optimum angle for ultrasonic propagation with respect to CASS microstructure.* (See the discussion in Chapter 8 on applying effective beam propagation angles for a more detailed discussion regarding the need for applying a range of propagation angles in CASS.)

The analytical protocol for crack detection and discrimination was based on the premise that sufficient differences exist between the characteristics of coherently scattered ultrasonic energy from grain boundaries and geometrical reflectors and the scattered ultrasonic energy from ID, surface-breaking cracks in coarse-grained steels. PNNL's empirical approach relied on fundamental acoustic physics, whereby the acoustic impedance variations at the grain boundaries were shown to be reduced by using lower frequencies (longer wavelengths). The degree of coherent energy scattered from these grain boundaries varied as a function of frequency, insonification angle, scan direction, and amplitude of the returning signals.

A LF examination is less sensitive to the effects of the CASS microstructure because the wavelengths are similar, or larger, in size to average grain diameters. This results in better sound field intensities at longer metal paths and less re-direction by the coarse microstructures. The key tradeoff for applying low frequencies is resolution, in that small flaws (with depth values much less than the wavelength) may not be consistently detected. However, with the addition of SAFT signal processing, the examinations were performed at low frequencies while maintaining the capability to detect cracks approximately 35% deep or greater in typical CASS piping components. Therefore, by using multiple examination frequencies and incident angles and by inspecting from both sides of a weld, the LF-SAFT technique invoked a composite approach for detecting, localizing, and sizing of cracks in cast stainless steel material.

While promising results have been achieved with LF-SAFT, its field application presented some significant challenges. This method is time-intensive and requires acquisition and analysis of multiple raster scans over a range of specific incident angles, on both near- and far-side orientations, and at multiple frequencies; typically, 250, 350, and 450 kHz. Further, if the weld crown permits, 0° raster scans are also acquired over this area. The research clearly indicated that a multiple-angle, multiple-frequency data acquisition method was necessary if reliable examinations were to be undertaken on CASS weldments, and this approach proved to be effective in detecting cracks during blind testing.



In March 1993, EPRI invited PNNL to participate in an exercise to determine the reliability of the data obtained from ultrasonic examinations of CASS components (Diaz et al. 1998). The intent was to determine realistic expectations for flaw detection by experienced vendors and researchers using their most current technology. The results were encouraging as the PNNL team scored higher than all other automated inspection teams, with an FCP of 30% and a POD and correct interpretation of 70%.

The LF-SAFT approach required multiple steps to post-process the data files and results in a sizeable amount of data generated for each weldment. It became very challenging to study the ultrasonic responses and determine a comprehensive meaning between the various data sets. Hence, there was a need to develop and test a set of software tools for effective data fusion and analytical capabilities to reduce the time for analysis, improve consistency of the process, and enhance the ability to discriminate between coherent ultrasonic responses from material structure (e.g., grain boundaries) and targeted cracks.

As a result of the large data sets produced by LF-SAFT, PNNL focused on implementing a semi-automated analysis method for combining the data sets in a reliable and consistent fashion. The new software and interactive tools, called the Multi-Parameter Analysis Tool Set (MPATS), provided a means for more effectively combining data sets taken at multiple angles and frequencies. MPATS addressed the issues of accurate registration (positional information) between data sets, overlaying and fusing multiple independent data sets, and included interactive application of specific crack identification and sizing criteria developed during the mid-1990s. The goal of MPATS was to facilitate discrimination of coherent ultrasonic signal responses from grain boundaries and those from cracks.

Inputs to MPATS included LF-SAFT data sets from multiple probe frequencies, from several probe angles and, if possible, from both sides of a specimen's weld. As many as 21 separate data scan files (all longitudinal wave and obtained with LF dual-element probes) were processed and fused together to assist in analyzing CASS weldments. These included propagation angles of 0°, 30°, 45°, and 60° at 250, 350, and 450 kHz from both sides and across the weld (if the weld crown permitted). For more details on this work, refer to Diaz et al. (2003).

The software tool was tested on several CASS WOG practice specimens on loan from the EPRI NDE Center. The specimens consisted of CCSS pipe welded to SCSS elbow material, ranged in wall thickness at the weld centerline from 55.9 mm (2.2 in.) to 71.1 mm (2.8 in.), and contained either a thermal or mechanical fatigue crack introduced after welding.

Figure 6-2 presents an example of data filtering in MPATS. The application controls are on the left side of the figure. A C-scan of the LF-SAFT-processed data file is displayed in the upper left and a low-pass filtered version of this data in the lower left. Low-pass filter parameters are adjusted by the slider bars in the left control panel. An amplitude threshold is applied to the filtered data with results displayed in the upper right. Six areas of interest were identified, targeted for further analysis with MPATS, and labeled as signal amplitude anomalies (SAAs). The SAA concept was developed in preparation for a blind round-robin test conducted at EPRI (Diaz et al. 2008b). A full list of criteria for identifying relevant SAAs used for LF-SAFT CASS detection analyses are provided in Appendix D. Finally, in the application shown in Figure 6-2, the image is filtered for a minimum response length (11 pixels as determined from the slider bar input). After applying this filter only one SAA remains. This processed result can then be saved and used as input during data fusion. The data could also be filtered for width of the SAA or the skeleton of the SAA. A skeleton of a response is calculated and then represented as a line along the points that are equidistant from the edges of the response and represent the full composite data fusion of all



SAAs. This is illustrated by the lines in the upper right corner of Figure 6-3, which shows an example of full data fusion for multiple data sets.

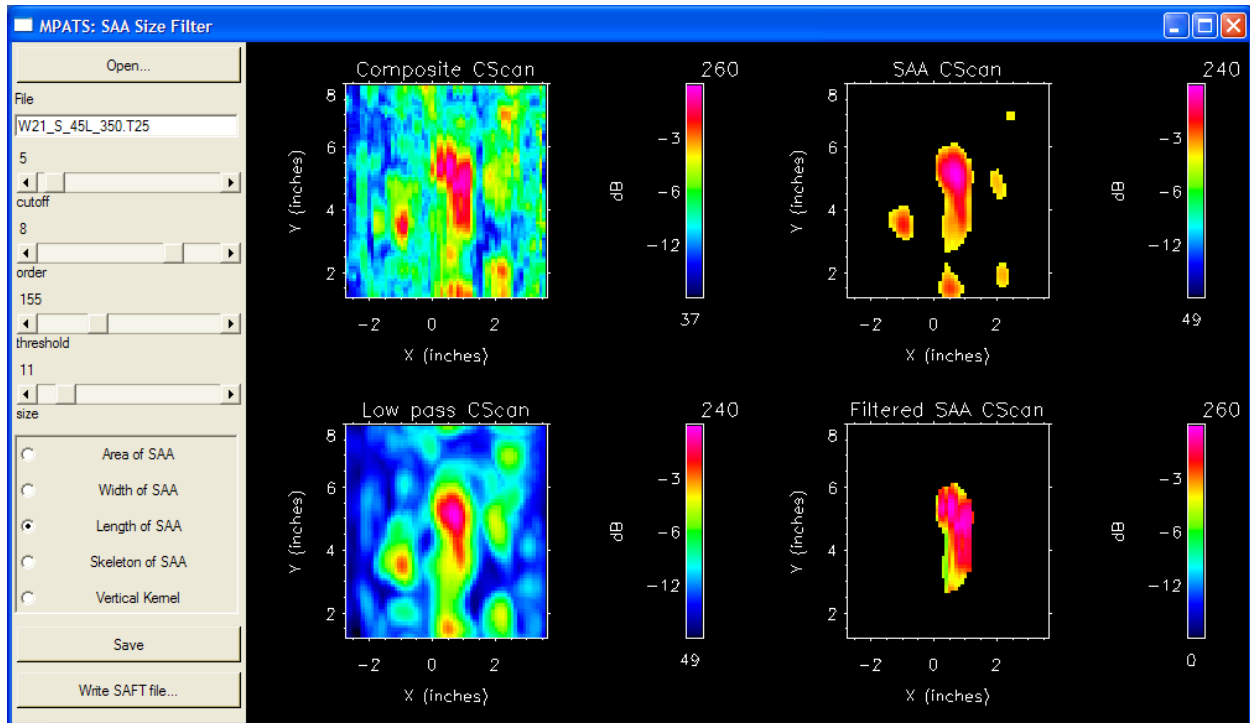


**Figure 6-2 Application Window and Controls for SAA Size Filter**

All 21 input data sets are typically displayed if all data are available for acquisition. The three probe frequencies are represented in rows and the seven probe angles in columns. The right-most image is a fusion of all data as represented by a skeleton. This image shows a counterbore signal on the left and three SAAs, or possible flaw signals, to the right. Test results from the WOG specimens compared favorably to reported true state and required considerably less time to compile than if one individually analyzed all data sets for a particular specimen.

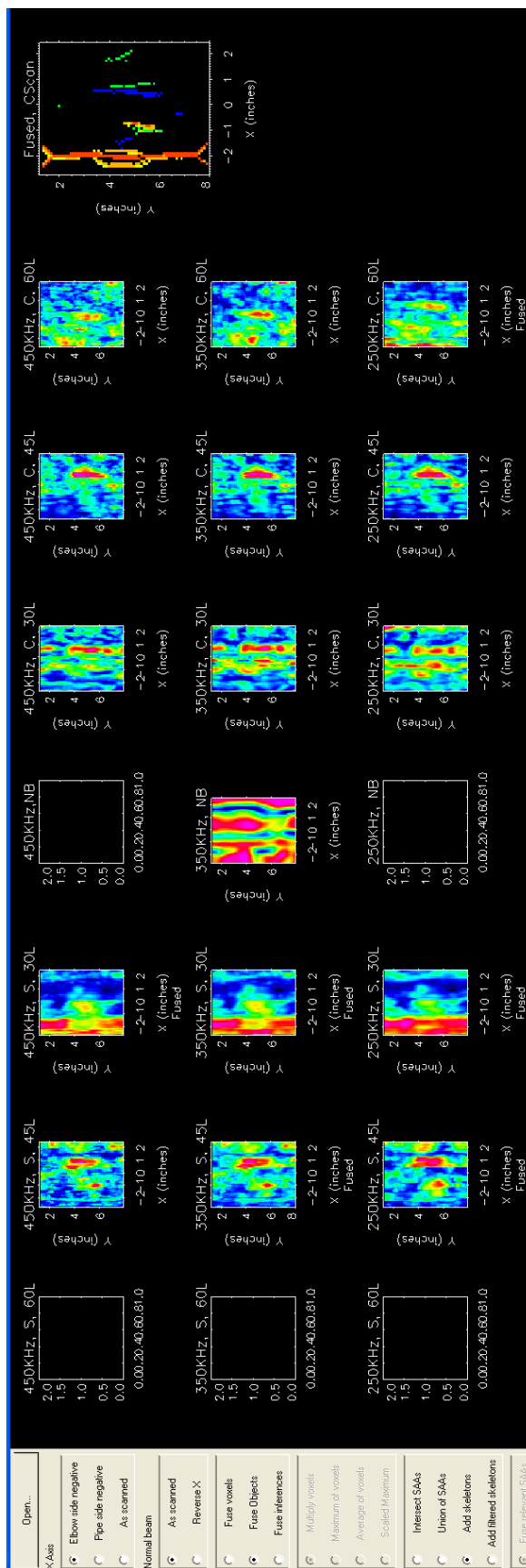
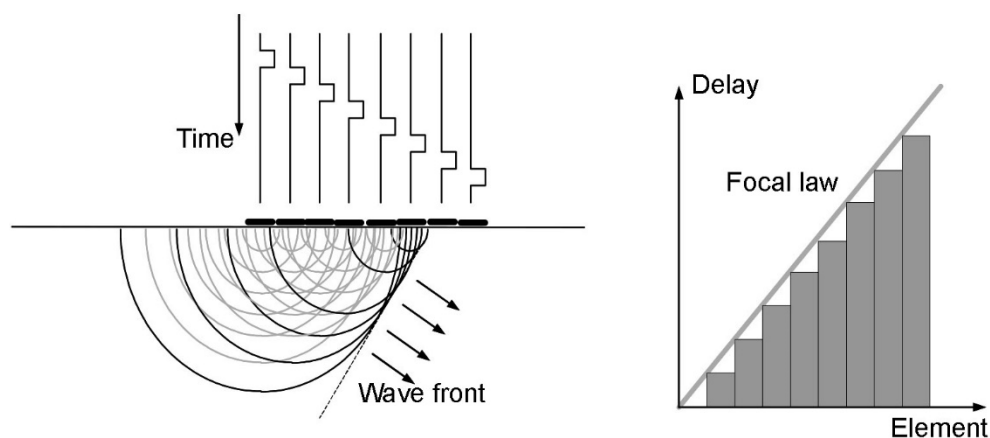


Figure 6-3 Application Window and Controls for Fuse All Tool

### 6.3 Transition to Low-Frequency Phased Array UT

With the speed of personal computers increasing and the ability of ultrasonic equipment manufacturers to make small piezo-composite transducer elements, the use of ultrasonic PA technology gained traction in commercial industrial applications in the early 2000s. The basic premise for all PA transducers involves a set of small, individual piezoelectric elements that are independently driven. These elements may be pulsed individually or in groups, and the real strength of this technique lies in the capability of the system to electronically delay signals to and from each of these elements during both generation and reception of ultrasonic sound fields. The wave fronts produced by subsets of elements interfere within the inspected component to produce a resultant, phase-integrated ultrasonic wave. This is commonly referred to as beam forming (see Figure 6-4). The PA system can therefore nearly simultaneously steer and focus the integrated ultrasonic beam within the component.



**Figure 6-4 Beam Forming Using PA (courtesy of R/D Tech, Inc.)**

The advent of PAs meant that the concept of combining LF ultrasonic energy with multi-angle scanning and multi-side access was achievable. This also meant that effective and reliable examination of CASS components could be possible in field settings and within examination times similar to or even better than conventional UT. PAs allow data to be rapidly acquired using beam focusing and beam steering algorithms that provide high-resolution merged images in near real time. The ultimate result is similar to LF-SAFT but at greatly reduced processing and analysis times.

Because industrial applications of PA were typically implemented using probes having very small elements to allow optimum beam forming in wrought materials, the frequencies used were typically 2.25 MHz or higher. The concept of developing PA to operate at low frequencies (<1.0 MHz, which required much larger elements) for coarse-grained CASS structures was generated in the early 2000s as the product of brainstorming sessions between PNNL, vendor representatives from R/D Tech (now Zetec, Inc., a PA equipment manufacturer), AIB-Vinçotte (a Belgium array designer and manufacturer), and a research colleague at Electricité de France.

The first PA system at PNNL consisted of a Tomoscan III (Figure 6-5) produced by R/D Tech. This was a standard piece of equipment used for PA applications in several industrial sectors. This type of system was being used by General Electric to inspect reactor internals and at the EPRI NDE Center for a variety of applications, including far-side inspection procedure development and initial true-state characterization of the industry's Performance Demonstration

Initiative specimens. The instrument was programmable (by development of focal laws in software) to control up to 32 channels for transmission and reception of ultrasonic signals at a typical frequency range of 1–5 MHz. For the early LF work, R/D Tech modified a Tomoscan III to operate at 500 kHz. Instruments with extended frequency ranges can now be routinely ordered, such as the Zetec DYNARAY class of PA equipment (Figure 6-6).



**Figure 6-5 Modified Tomoscan III with Typical Acquisition Data Station**



**Figure 6-6 Zetec DYNARAY Off-the-Shelf Phased Array Instrument with Low-Frequency Capabilities**

The design of LF arrays was similar to conventional TRL transducers at these frequencies, with separate, discrete sections of the search unit being used for transmitting the longitudinal ultrasonic wave while other sections are only for reception. Additionally, although housed as a single unit, transmit and receive sections were mounted on integral wedges and acoustically separated. The general design, including contact footprint and wedge angles of these arrays, was consistent with conventional mono-element transducers being used throughout industry for inspecting austenitic and DMWs. The primary difference is that matrices of individually controlled elements were used for each transmit and receive section as opposed to a single piezoelectric crystal and, of course, the elements are made to operate at 500 kHz. Therefore, instead of being able to generate only a single angle of sound within the component, the arrays allow steering sound beams through multiple angles in near real time. In addition, focusing of sound at the proper depths within the material can also be accomplished with the array. This means that a single *line scan* adjacent to

the weld can be made while data are collected for many angles simultaneously. This is similar to performing multiple scans at many angles with a conventional transducer, which, along with spatial encoding, enables production of detailed UT images with only a single pass from the array along each weld (Anderson et al. 2011). Additional support for this approach can be found in industry publications. For instance, (Davis and Moles 2007) described differences between manual conventional and encoded PA methods, where they state, "Linear scanning offers significant advantages in speed, maybe up to a factor of five or ten times over monocrystalline inspections. Besides collecting and displaying all the defects, some encoded PA units can perform multiple scans simultaneously, i.e., they can fulfill the code requirements in a single pass, with arrays [located] on either side of the weld."

Given appropriate acquisition and digitization rates, line scan times are very fast, with normal operating scan speeds at approximately 50 mm/s (2 in./s). Control software allows angles of transmitted sound to be performed in segments of degrees. However, raster scanning, where the probe is translated in one axis and incrementally stepped in the orthogonal axis, can require several hours to complete for a large-diameter piping weld. While PA line scans can be accomplished in a fraction of the time to that for raster scans, they do not provide a means to acquire the echo dynamic response from reflectors nor do they accommodate the potential for significant beam skewing or partitioning that may occur in CASS microstructures. In contrast, PA raster scans result in much larger data files and take longer to interpret/analyze. Thus, while there are benefits and limitations to both scanning methods, the application of PAs in the field can significantly reduce ISI outage time needed for examinations and decrease the amount of absorbed radiation dose. It is important to note that line scans would only be used to provide an initial screening of a weld configuration, where a full raster scan would be needed to fully detect and characterize any flaws within the examination volume.

Of primary importance with respect to the examination of CASS, DMWs, and coarse-grained materials in general, is that the PA method allows for multiple angles of inspection in a single scan. CASS material properties can change significantly from location to location within the material. Correspondingly, investigations at PNNL have shown that the large-grained structure and anisotropic nature of CASS results in certain sound angles propagating more efficiently (Crawford et al. 2014). Thus, the use of PAs increases the probability that an optimum inspection angle will be applied, even as the grain structure changes as a function of circumferential/axial position.

Another advantage of spatially encoded PAs is that all data are stored digitally during each scan, allowing offline processing and interpretation in an environment better suited for analysis than one usually encounters during ISI data acquisition. The raw ultrasonic data received from the transducer are stored digitally as an array of amplitude (intensity) versus time values that can be plotted and viewed in what is known as an A-scan view. The A-scan represents information at one angle and at one circumferential location. A single A-scan can be difficult to interpret, so advanced software is used to compile all the data based on position, time, and intensity. The compiled data are then displayed visually in a color-coded format. The most common view for displaying compiled line scan data is the sectoral view, which displays all depth and angle information at a specific circumferential location, and the end view, which displays depth and scan (circumferential) information, at a single angle (Cinson and Crawford 2010). Several image channels of the data can be displayed, depending on the preference of the analyst. As discussed in NUREG/CR-6933 (Anderson et al. 2007), PNNL staff used the volume-corrected B-, C-, and S-scan images, along with supplemental A-scans, to assist their understanding of the data.

For the TomoView and UltraVision PA software used during the study (Anderson et al. 2007), the B-scan image is a 2D, maximum-intensity projection of the sound field through the component, oriented as if looking along the direction of sound propagation, displaying a circumferential cross section of the weld (right pane in Figure 6-7). The S-scan (upper left pane), or sector view, provides a projection of the sound fields (from initial to final angle being used, i.e., 30°–60° for the TRL arrays). The black line in the S-scan shows which angle is currently selected. Finally, the A-scan (lower left pane) represents the electronic responses for reflectors based on x-y axes of time and amplitude, respectively. A typical composite analysis screen showing the scan images described above is included as Figure 6-7.

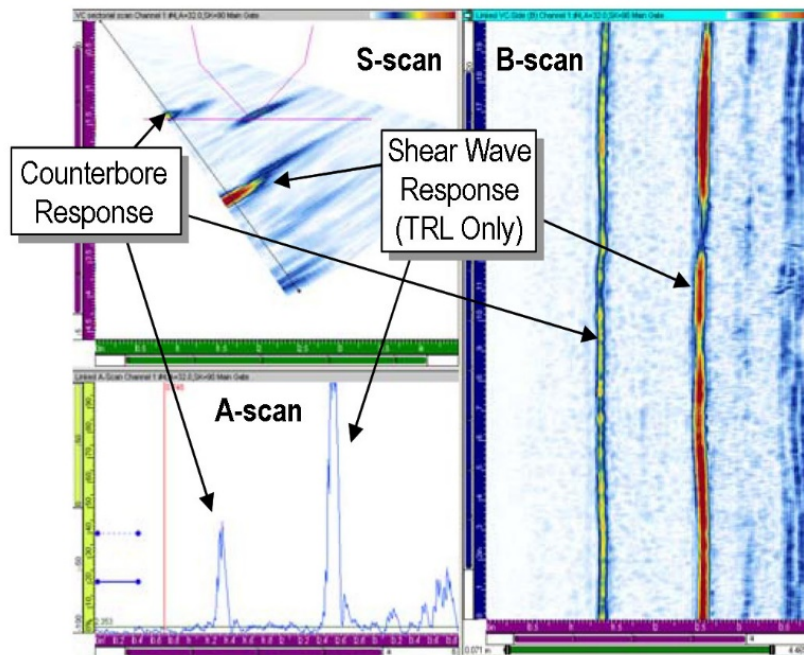


**Figure 6-7 Typical Analysis Images Used for Phased-Array Inspection**

Measurement, gating, and sound field cursors are used to provide slices of material to view along the projected sound beam, and discrete beam angle responses are shown in the A-scan. By manipulating these cursors, the analyst is able to “walk through” cross sections of the material along each spatial direction. An important analysis tool of the PA system is the ability to examine each angle individually. This allows the NDE examiner to view the different response images in a given scan and discriminate between the various features in a specimen. Using the location of geometrical responses from ID counterbore and weld root (if these exist), one can ensure the sound is penetrating to the ID surface, and these aid in locating flaw responses, particularly in coarse-grained materials where spurious echoes from grain boundaries may appear as flaws.

Within PA data there often will be a baseline level of intensity that is caused by the reflection of ultrasonic energy from the component material itself. Signals above this noise level must be taken into consideration as possible flaws. One must keep in mind there can be multiple signal regions that stand out that are not necessarily flaw related. Frequently, there are ID geometrical reflections from the counterbore in a pipe. These signals are fairly uniform, strong, and constant near the ID region within the scan, unlike typical flaw characteristics that tend to be localized and may exhibit some through-wall extent.



Volumetric merging is a common analysis procedure performed on PA line scan data that allows the inspector to rapidly review the entire section of data for signals and flaws. This merging of the data results in composite images, in which the signals from echo responses combine additively while noise and spurious from grain boundaries signals mix with the background. The sectoral and end views display the images made from all data collected in the scan. Time gates can be used to isolate specific regions of interest. Image resolution may be compromised or blurred with volumetric merging, but in general the technique works well for rapid flaw detection screening. Volumetric merging of PA data is a very similar fusion technique to what was employed with MPATS for conventional LF-SAFT data sets at PNNL but requires much less processing and analytical time (Figure 6-8).

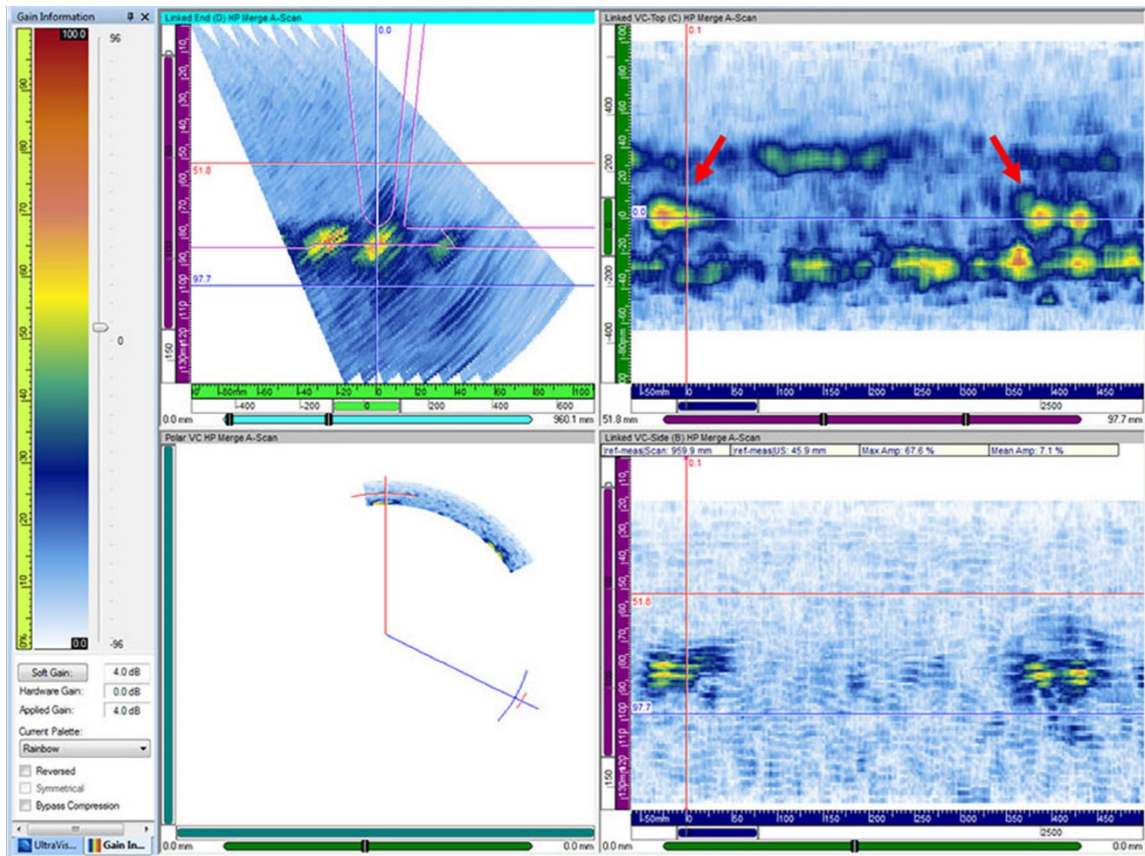


**Figure 6-8 Example of Volumetrically Merged PA Data**

Post-acquisition images afforded by PA analysis software provide fundamentally important capabilities for discrimination of responses in the coarse-grained materials. The images produced via off-line analyses through automated scanning and data storage are powerful tools with respect to the discrimination of signal responses. For example, Figure 2.6 in NUREG/CR-6933 (reproduced below as Figure 6-9) displayed the results for an inspection angle of 35°. At that angle, reflections from the counterbore of the examined pipe were seen to dominate the reflection. When a higher angle of 53° was displayed (Figure 2.7, Figure 6-10 below), other features such as weld root also become visible. At an angle of 65° (Figure 2.8, Figure 6-11 below), only the targeted flaws became visible. It was found that this angular discrimination was a very useful tool when linked with A-, B-, and C-scans.

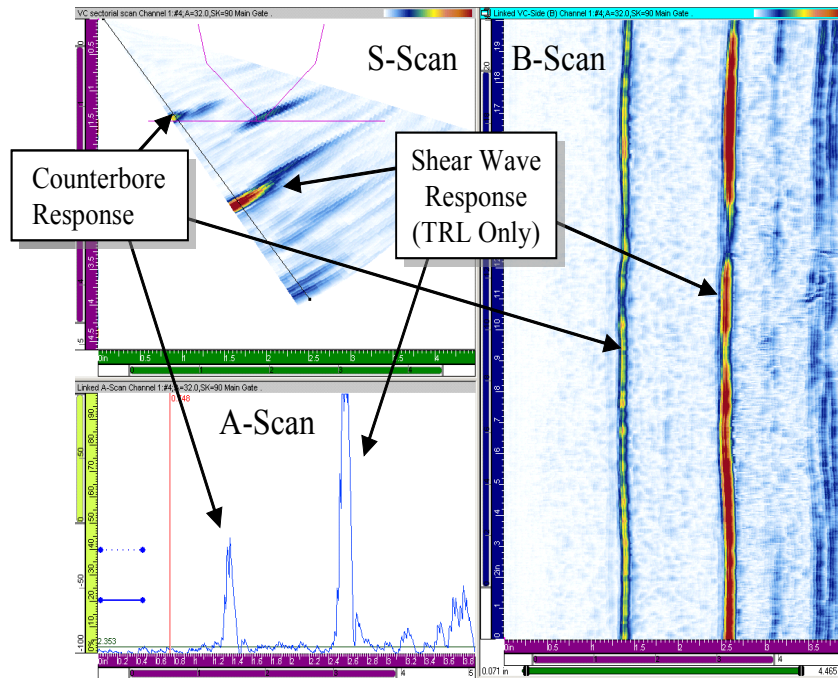


**Figure 6-9 Typical Analysis Images Used for Phased Array Inspection (Figure 2.6, NUREG/CR-6933)**

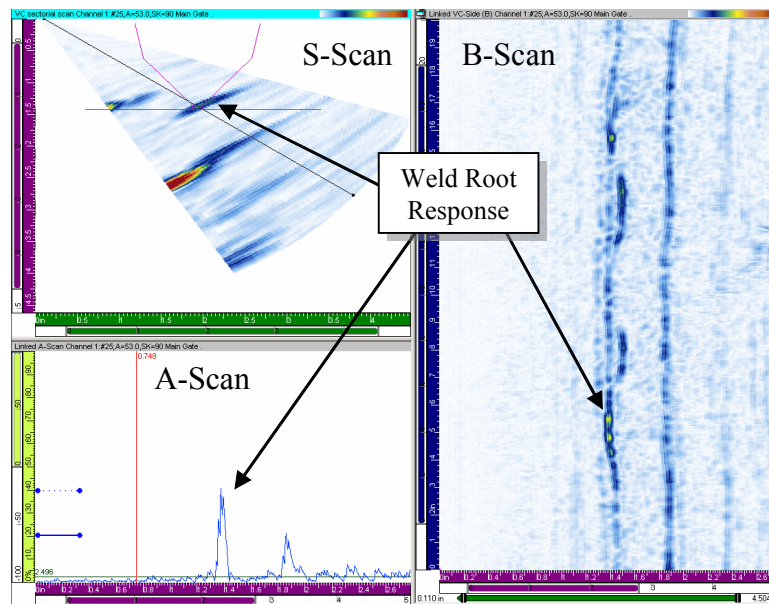


**Figure 6-10 Typical Analysis Screen with Mid-Range Angle (53°) Selected, Showing Weld Root with TRL Array (Figure 2.7, NUREG/CR-6933)**



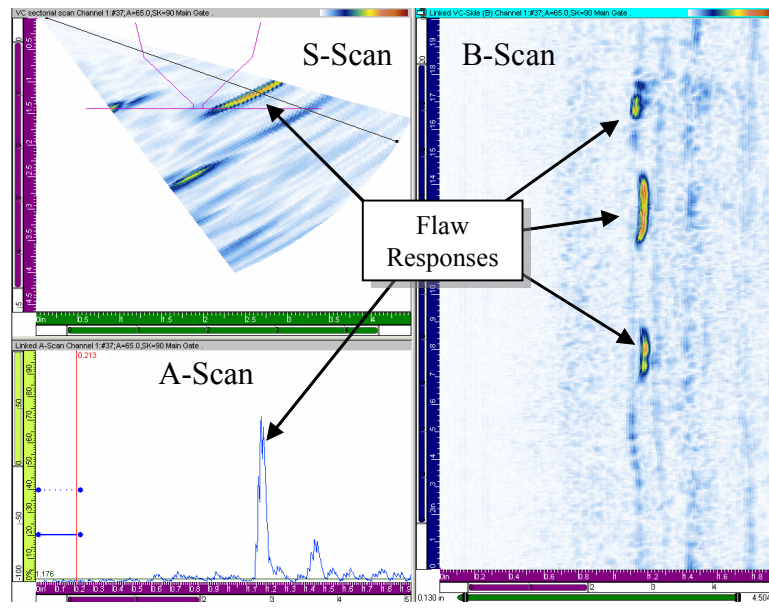


**Figure 6-11 Typical Analysis Screen with High Angle (65°) Selected, Showing Flaws with TRL Array (Figure 2.8, NUREG/CR-6933)**

In the early 2000s, the NRC asked PNNL to apply and evaluate advanced NDE methodologies for far-side inspection of wrought stainless steel piping with austenitic welds (Anderson et al. 2011). The study employed both the LF-SAFT and PA technologies in a comparative assessment of detection performance. From this and subsequent work that has included the use of LF-PA methods for CASS materials, the effective but relatively cumbersome LF-SAFT methodology has given way to the streamlined performance of the PA approach using 500 kHz refracted longitudinal waves.

The initial LF-PA work was performed with a first-generation, or prototype, transducer developed at AIB-VINÇOTTE in Belgium. Under contract to Electricité de France, the prototype was designed and constructed with piezoceramic elements, as these were the only LF transducer materials available in late 2003. The prototype had a very large footprint ( $115 \times 115$  mm [ $4.5 \times 4.5$  in.]) because of the active aperture length needed for sound field focusing, the radiating area of each element required for beam steering in the 500 kHz domain, and an integral wedge to enable steered beams up to  $70^\circ$  in stainless steel. The plastic housing and insulating materials also contributed to this large overall footprint (Figure 6-12). Electricité de France subsequently loaned this prototype LF-PA to PNNL for tests on WOG (now called PWROG – Pressurized Water Reactor Owners Group) and NRC-owned CASS specimens at PNNL.

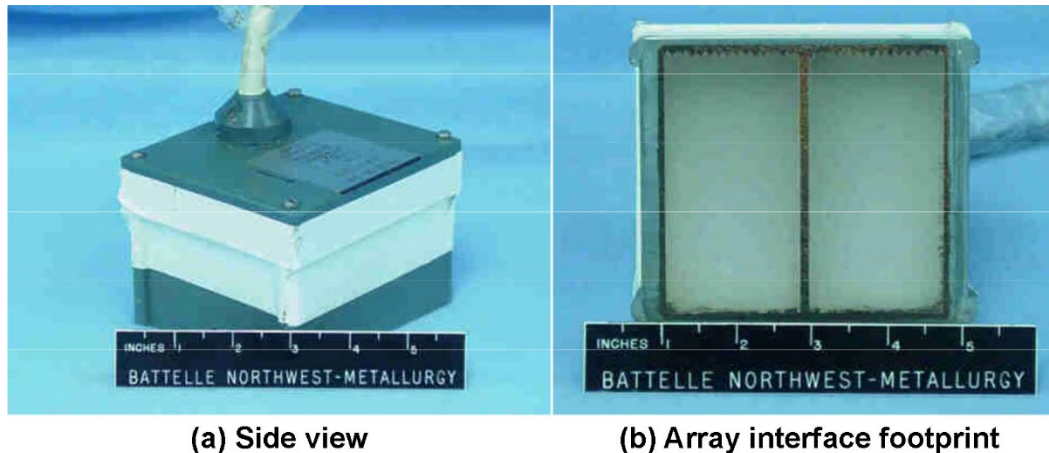


**Figure 6-12 500 kHz Prototype Phased Array**

The preliminary results obtained in 2005 with this prototype design were encouraging in that many of the mechanical and TFC in the WOG and PNNL CASS specimens examined were detected quite easily (Anderson et al. 2007). With respect to certain cracks not being detected, several WOG specimens have OD surface features, such as tapers, base-to-weld metal transitions, and short axial surface regions that severely limit access to perform proper scanning, especially for the low-angle beams using this prototype probe. The large footprint of the probe in combination with the surface features of the WOG specimens precluded the array from being located near enough to the weld on some specimens to acquire data through the entire range of steered beams ( $30^{\circ}$ – $70^{\circ}$ ). This resulted in potential flaw responses not being peaked, providing only reduced SNRs, often on the order of 2:1 or less, and made flaw detection more problematic. In addition, the piezoceramic elements produced a narrower bandwidth (BW) than current piezocomposite elements and required high gain settings for sound generation, which effectively lowered the dynamic range of the system.

Much was learned from the use of the prototype PA probe. For example, it was noted that in cast materials, use of lower angles ( $30^{\circ}$ – $50^{\circ}$ ) provided better flaw responses in most of the available specimens. Therefore, the footprint of the array would need to be minimized for use on challenging OD surface geometries to allow the active array to be placed closer to the weld/flawed region. Also, the probe geometry was designed with an insufficient number of elements in the passive direction to enable lateral beam skewing, thus requiring a wedge roof angle to produce a transmit-to-receive crossover point that was too shallow for detecting very small flaws, although this probe feature actually enhanced responses from flaws on the order of 30% through-wall and greater. Because specular reflections from the flaw face dominate the responses detected in CASS, a probe that can focus at varied depths would be more effective in detecting flaws. PNNL noted that most of the flaws, especially those made by thermal fatigue, exhibited significant branching, or portions of the flaw face were oriented at oblique angles to the sound field. Thus, the ability to detect flaws may be improved with an array that can steer the beam through multiple angles and can also skew the beam in the passive direction. Finally, it was felt that by using piezocomposite elements, one could increase the frequency response via a broader bandwidth and improve dynamic range, as piezocomposites require less excitation energy (instrument gain) to produce sound fields as compared to conventional piezoceramics. This would increase the dynamic range of the system and provide better images for data analysis. The insights gained were used to design an improved 500 kHz array.

The second-generation, integral 500 kHz probe was designed to allow an inspector to skew the beam to enhance the detection of branched cracks, such as those generally observed for TFCs. Several rows of piezocomposite elements were used in the passive direction, while the active dimension of the probe was made shorter to allow the array closer proximity to the welds (see Figure 6-13). Simulations were performed using Zetec beam simulation software (described below) to determine the range of skew angles possible and the beam profile at the skew angles of interest. The simulations showed that the 500 kHz probe was capable of skewing the beam in the lateral axis  $\pm 20^\circ$ . This skewing is helpful in detecting branching cracks that may not reflect sound directly back to the probe when no skewing is used.



**Figure 6-13 Improved Design of 500 kHz Phased Array Probe**

The third-generation 500 kHz PA probe, which is the latest design, was produced to overcome issues with integral wedges and optimize the matrix design for improved steering, focusing, and skewing in CASS (Crawford et al. 2011). PNNL used lessons learned from application of previous generation probes and minor changes suggested by Zetec (formerly R/D Tech), based on their experience with arrays, in the design of the third-generation LF probe. The Crawford report documents the evolution of the 500 kHz PA probe, associated electronics, and the scanning protocol that PNNL has been investigating for application to coarse-grained materials.

The third-generation probe exhibits significant improvements over previous generations. For instance, piezocomposite elements were used instead of the piezoceramic material, allowing a reduction in system gain of nearly 30 dB and greatly reducing electronic noise. The matrix has enough elements in the passive direction to allow for significantly improved beam skewing, and the element sizes were optimized for directivity while still allowing the smallest active direction footprint that could be obtained. The latest probe has a much better dynamic range, which produces higher SNRs, adding to its flaw discrimination capability. It is designed with detachable wedges, so that multiple diameters of piping can be accommodated by using matching surface contouring. This enables beam forming to operate more efficiently. The system electronics for the latest probe were fully optimized for a 500 kHz center frequency (Figure 6-14). This PNNL probe design continues to be applied by multiple industry vendors as well as EPRI to examine large-

bore CASS piping specimens. It should be noted that the probe design is not proprietary; that is, PNNL specifically left it “open market” so that others could take advantage of its capabilities without seeking permission.



**Figure 6-14 Current (latest) Generation of 500 kHz PA Probe**

With enhanced scanner capabilities, smaller step sizes can be used to achieve improvements in data quality for both line and raster scans. The small step sizes produce high-resolution images that improve flaw discrimination and, along with the increased SNR inherent in the latest probe design, enhance detection of the upper regions of the flaw, making depth sizing more plausible. Finally, the physical sizes of the successive generations of probes have progressively decreased, allowing better access to the area of interest on specimens with weld crowns.

The sound fields for all probes used in the above research were simulated using the Zetec 3-D Ray Tracing Beam Simulation and UT Data Visualization software package to ensure that the probe designs were capable of providing full insonification of the areas of interest. The sound fields that this software generates assume the material has a constant ultrasonic velocity (i.e., the material is isotropic). Thus, the software does not accurately simulate the significant velocity variations (as high as 20%) (Kupperman et al. 1981; Doctor et al. 1989) caused by the large grain sizes found in CASS. However, the software provides information as to whether the probes are capable of producing a useful sound field at the angles and depths required in isotropic material (Figure 6-15).

In summary, it was determined early in the research that low frequencies were required to penetrate CASS grain structures and post-processing of encoded data was also needed to allow off-line imaging for effective signal discrimination and detection of flaws. The LF-SAFT methodology, coupled with MPATS data fusion protocols, proved sufficient for reliable detection of significant cracks (30% through-wall and greater) in multiple field-simulated mock ups; however, the process was tedious and time consuming. The transition to LF-PA allowed these barriers to be overcome by providing quick scanning and built-in imaging with merged (fused) data capabilities using off-the-shelf equipment and software. It is unlikely that conventional techniques could perform to this level of success, as indicated by several historical domestic and international exercises, and as suggested during a recently performed EPRI CASS round-robin (EPRI 2017),

where no participants elected to employ conventional, non-encoded approaches. Further discussion on the subject of conventional non-encoded examinations is provided in Chapter 8.

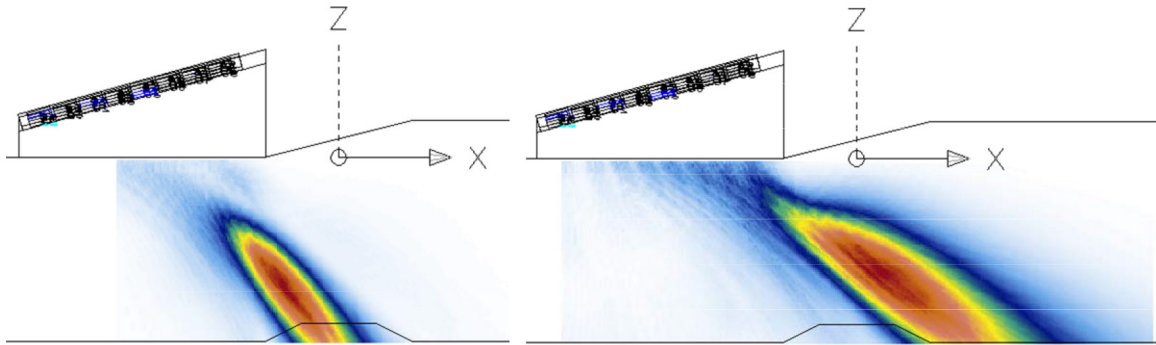


**Figure 6-15 Side View of Sound Profile Generated in Zetec UltraVision Software to Assess Beam Intensity and Coherence of 500 kHz Phased Array for 45° (*left*) and 60° (*right*) Propagation Angles in Isotropic Stainless-Steel Media.**





## 7 UT FLAW DETECTION OF A CASS TO CARBON STEEL DISSIMILAR METAL WELD

Over the past decade, the challenge of volumetric examination of thick-walled cast stainless steel piping has been a focus of work at PNNL (Anderson et al. 2007; Crawford et al. 2014; Crawford et al. 2015). Studies have been conducted at PNNL on flaw detection in base metal (heat affected zones) and weld joints of thick-walled cast stainless steel mockups using PA probes with center frequencies ranging from 500 kHz to 1.0 MHz. Results have consistently shown that encoded, LF (i.e., 500 kHz) PA methods provide the most reliable means of flaw detection. This section is a continuation of the LF-PA work to further demonstrate the necessity of LF-PA-UT in examination of thick-walled CASS piping. The specimen described below is a DMW (carbon steel-to-Alloy 82/182-to-CASS) mockup with five implanted flaws ranging from 10% to 40% through-wall. Automated scanning and spatial encoding were used to detect the flaws from the CASS side of the weld with LF-PA probes. Results are consistent with previous studies and confirm the importance of utilizing LF, encoded PA for flaw detection in CASS.

### 7.1 Wrought Stainless Steel Spatial and Depth Resolution and Probe Spot Size Summary

Understanding the resolution limits of the UT system and how they are affected by CASS materials is important to recognizing the detection and sizing limitations of examinations in CASS. Prior to scanning a CASS dissimilar metal weld specimen, spatial and depth resolution were measured for a variety of PA probes in a wrought stainless-steel specimen. This was done to characterize the ideal resolution in a specimen with minimal scattering. Following this, resolution measurements were made on a CASS specimen from the Manoir Foundry to demonstrate how spatial resolution may be degraded by coarser-grained, austenitic material.

#### 7.1.1 Specimen Description

A fine-grained, wrought stainless steel specimen, 304L, with a 914.4 mm (36.0 in.) OD and a wall thickness of 63.5 mm (2.5 in.) had two identical rows of four flat-bottomed holes. The holes had varying separation distances between them and were machined into the specimen ID surface, one row circumferentially and the other axially (see Figure 7-1). This geometry allows for a probe's forward, or primary, resolution to be determined by scanning the axially oriented holes and lateral, or secondary, resolution to be assessed by scanning the circumferentially oriented holes. Holes were separated by edge-to-edge distances of  $\lambda/2$ ,  $\lambda$ , and  $2\lambda$  (as measured from the specimen OD), where  $\lambda$  is the L-wave wavelength at 500 kHz (see Table 7-1). The holes were 4.76 mm (0.1875 or 3/16 in.) in diameter and were drilled to a depth of 12.7 mm (0.5 in.).

**Table 7-1 Hole Separation Values for Probe Spatial Resolution Measurements**

Edge-Edge Separation mm (in.)	Edge-Edge Separation – Wavelength at 500 kHz
5.7 (0.22)	$\lambda/2$
11.3 (0.45)	$\lambda$
22.7 (0.89)	$2\lambda$

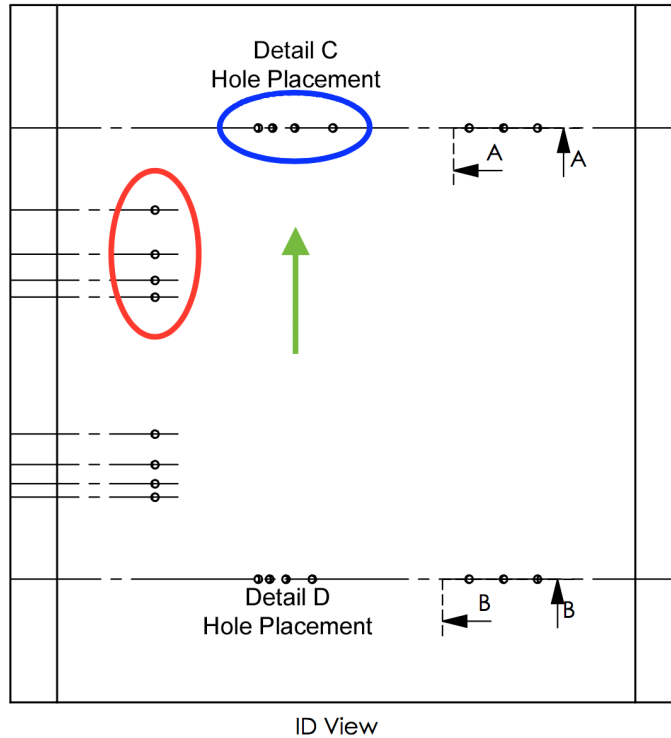


**Figure 7-1 Wrought Stainless-Steel Resolution Specimen. The axial holes for spatial resolution (primary) and circumferential holes for lateral resolution used in this study are encircled by the red and blue ovals, respectively. The green arrow indicates the scan direction for both sets of holes.**

#### 7.1.1.1 Data Acquisition

The holes were scanned from the OD surface with four PA probes operating at nominal center frequencies of 500 kHz, 800 kHz, 1.0 MHz, and 1.5 MHz in a side-by-side, pitch-catch mode. The probes are shown in Figures 7-2 through 7-5. Table 7-2 shows the number and size of elements in each probe, the overall probe apertures, and the bandwidths. An ATCO scanner was interfaced to a Zetec DYNARRAY controller via a Zetec motor control drive unit MCDU-02 (see Figure 7-6). All data acquisition parameters were accessed through UltraVision. Probes were driven by a 200 V square pulse of width equal to one-half the wave period. For example, the 1000 kHz probe was driven with a pulse width of 500 ns.

**Table 7-2 Phased Array Probe Specifications**

Frequency, kHz	Number of Elements		Element Size, mm (in.)		Aperture Size, mm (in.)		BW at -6 dB
	Primary	Secondary	Primary	Secondary	Primary	Secondary	
500	10×5		5.5 (0.22)	6.0 (0.24)	64.0 (2.52)	34.0 (1.34)	>45%
800	10×5		3.6 (0.14)	3.6 (0.14)	43.2 (1.70)	21.2 (0.84)	>50%
1000	10×5		3.5 (0.14)	3.5 (0.14)	39.5 (1.56)	19.5 (0.77)	>55%
1500	10×3		3.3 (0.13)	5.6 (0.22)	35.0 (1.38)	17.5 (0.69)	>60%



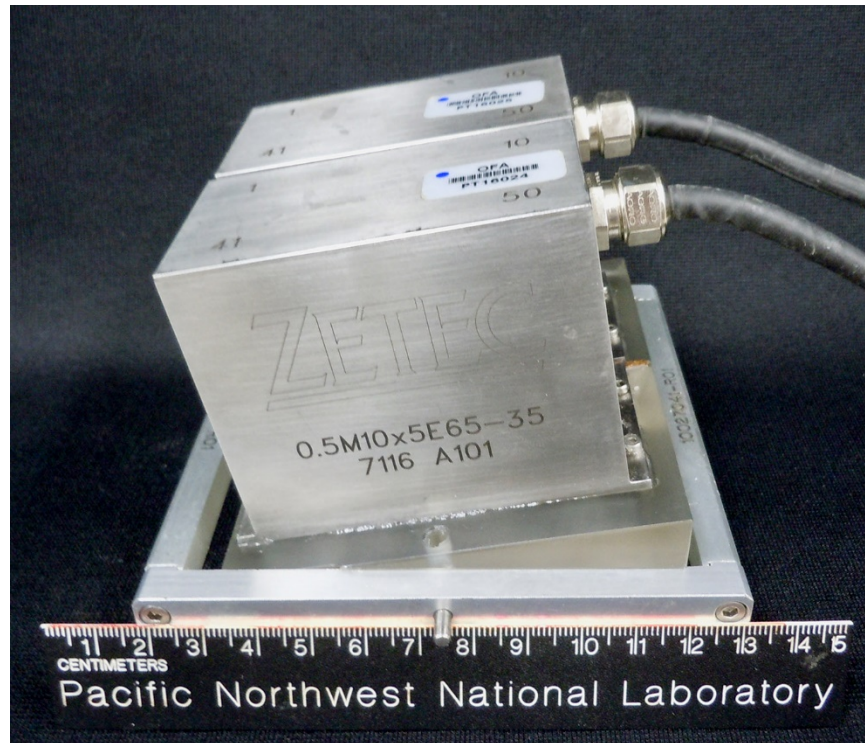


Figure 7-2 500 kHz PA Probe

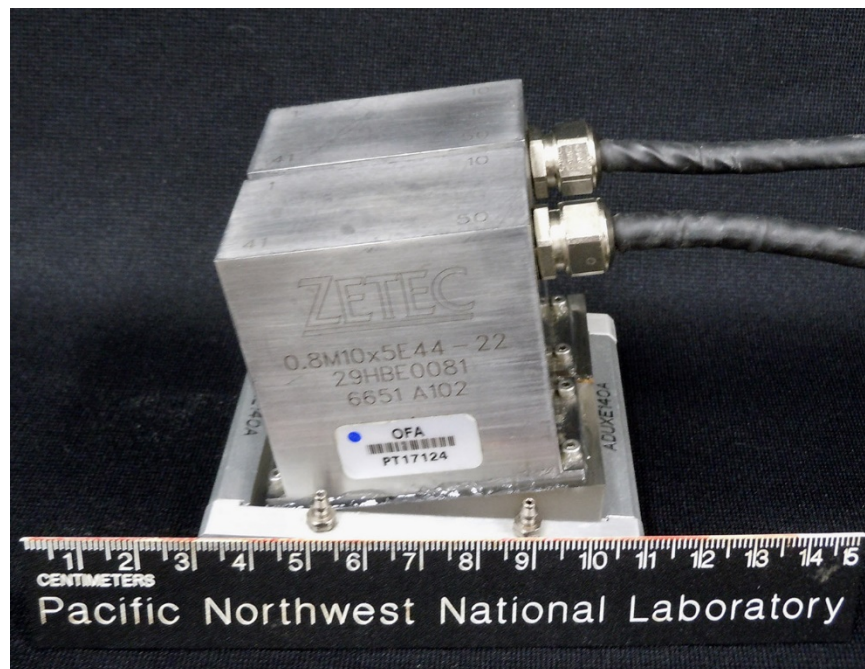


Figure 7-3 800 kHz PA Probe

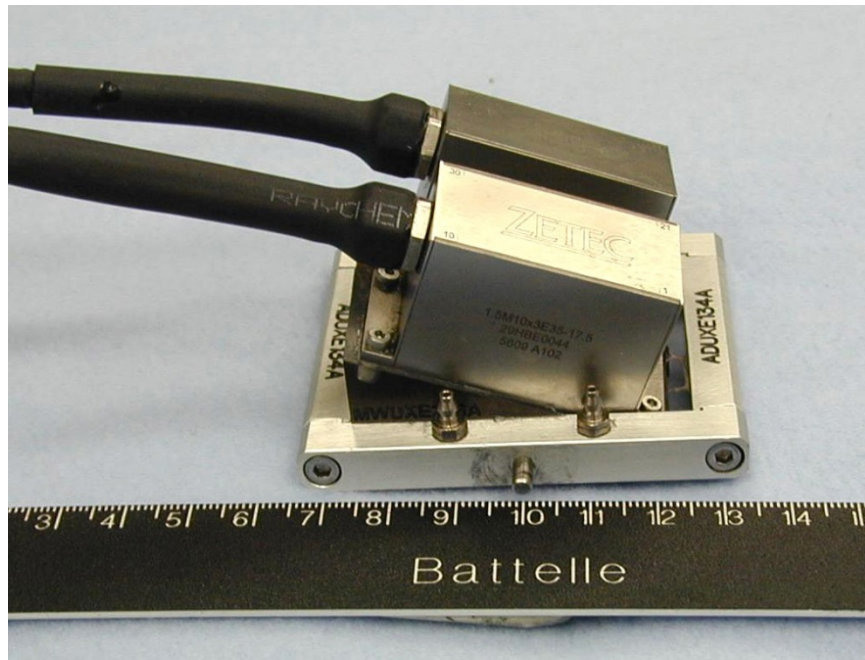


Figure 7-4 1.5 MHz PA Probe

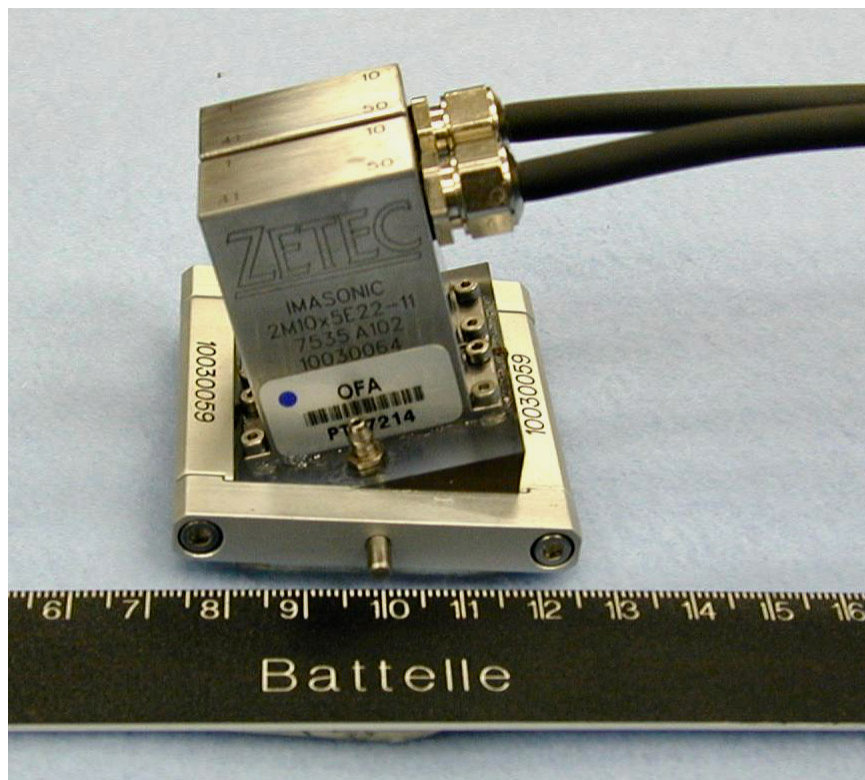
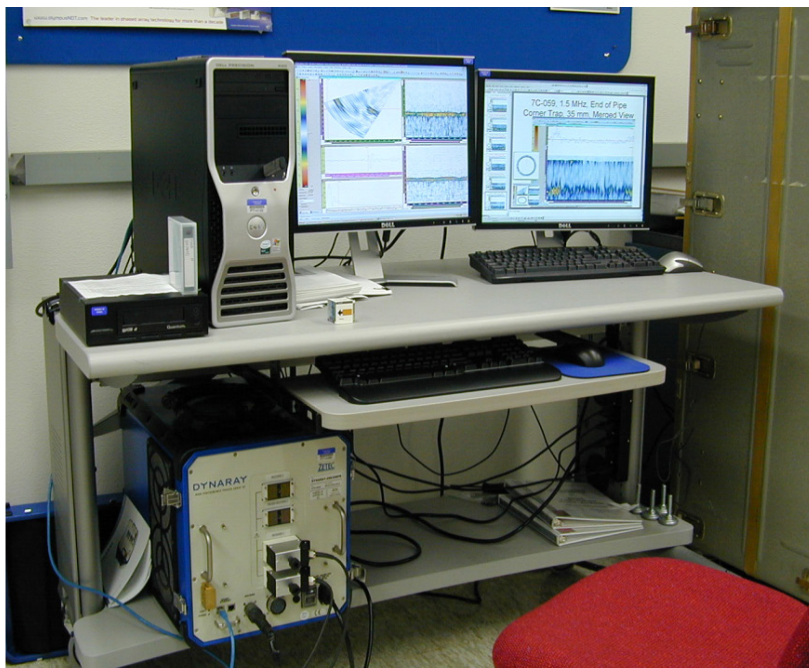


Figure 7-5 2.0 MHz PA Probe





**Figure 7-6 Data Acquisition System and Laboratory Workstation.** *Left:* DYNARAY PA data acquisition system (courtesy of Zetec). *Right:* Laboratory workstation for both data acquisition and data analysis, with the DYNARAY system on the lower shelf.

Data were collected by scanning both sets of holes in the axial direction (green arrow in Figure 7-1), thus allowing the resolution of both the forward and lateral axes of the beam spot to be measured. Scans were made using true-depth (TD) and half-path (HP) focusing. TD focuses the beam at a constant depth for all refraction angles (Figure 7-7, *left*), while HP focuses the beam at a constant distance from the probe for all refraction angles (Figure 7-7, *right*).

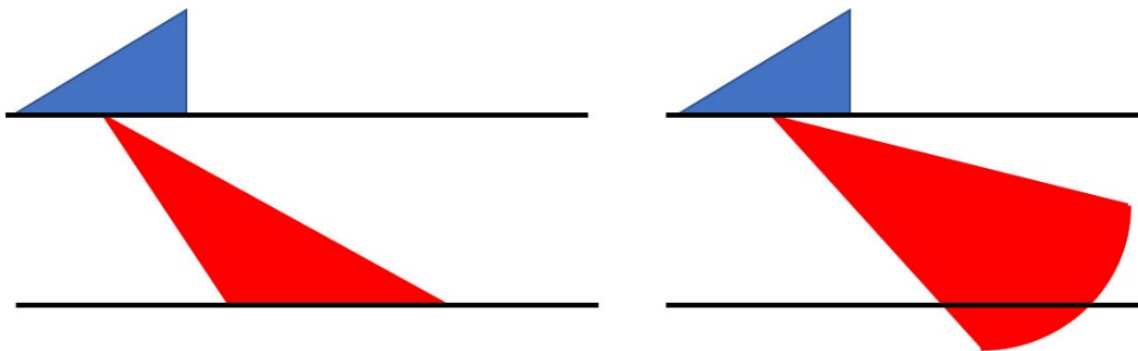


**Figure 7-7 True Depth and Half Path Focusing.** Illustration of true depth focusing, where the ultrasonic beam is focused at the ID surface for all refraction angles (*left*) and half path focusing, where the beam is focused at a constant distance from the probe (*right*).

### 7.1.1.2 Data Analysis

The following method was used to determine whether a hole was resolved or not. For a focused circular probe, the Rayleigh resolution ( $\Delta X$ ) is defined as:

$$\Delta X = 1.22(\lambda f/a)$$

where:  $\lambda$  = wavelength,  $f$  = focal length,  $a$  = probe aperture. In this scenario, the center of an Airy disk (maximum) generated by one-point source is coincident with the first zero or minimum of an Airy disk generated by the second point source. The image intensities are defined to be resolved if they show a 19% dip between maximum points, as shown in Figure 7-8 (Busse et al. 1984). While the imaging system used in the PNNL evaluation is not a circular disk but rather a focused beam as generated by a PA probe and specific focal laws, for the data analyses conducted in this assessment the 19% dip (or -1.8 dB) criterion was used to determine spatial resolution. In cases where the peaks were of unequal height, the 19% dip was measured from the lower of the two peaks.

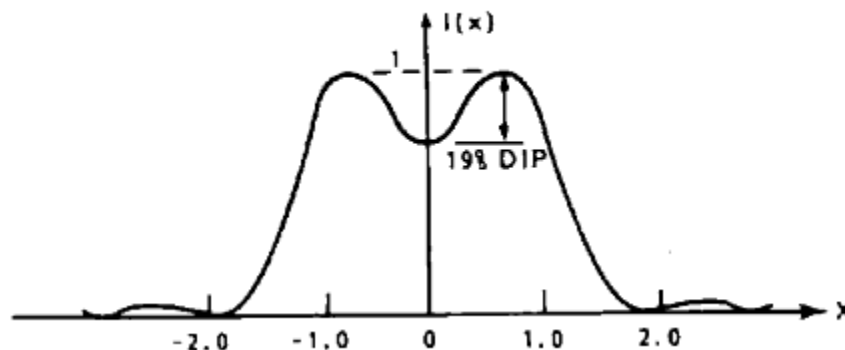


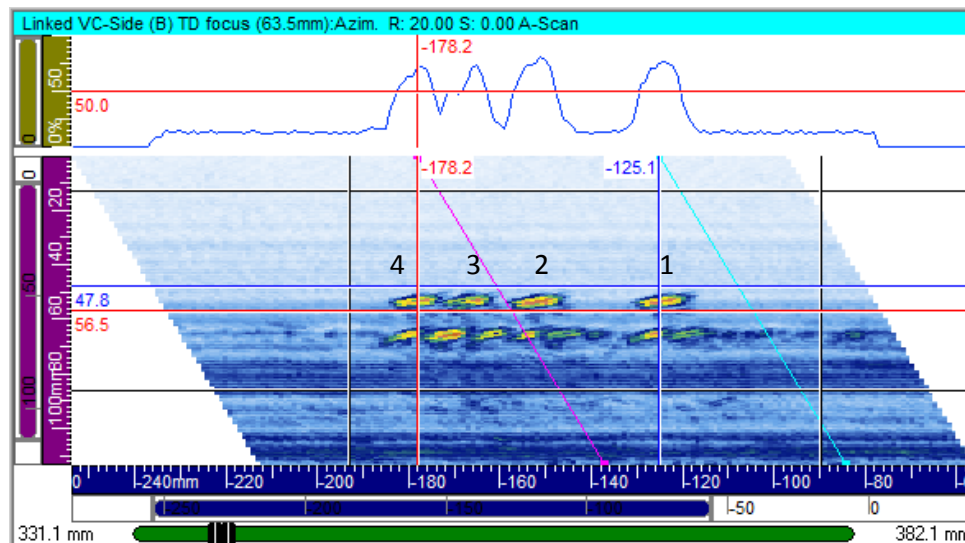
**Figure 7-8 Rayleigh Resolution for a Focused Circular Probe. Peaks are resolved if a 19% dip is realized.**

### 7.1.1.3 Results and Observations

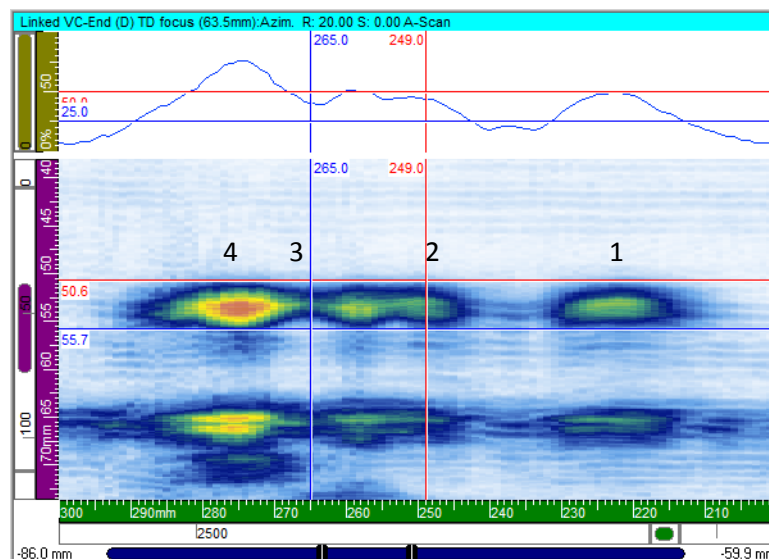
The four axially-oriented holes were resolved at the four probe frequencies for TD and HP focusing. Figure 7-9 shows an example of B-scan data acquired with the 1.5 MHz probe at a 20° refracted angle and TD focusing. The blue and red vertical lines mark Holes 1 and 4, respectively. The blue echo-dynamic curve above the B-scan is a contour of the signal from the bottoms of the holes taken from the area between the red and blue horizontal lines in the image. The echo-dynamic curve can be used to measure the amplitude dip between the responses of the holes and therefore determine the probe's spatial resolution. In summary, all four probes were able to resolve holes separated by 5.7 mm (0.22 in.) or more in probe's forward direction.

Figure 7-10 shows an example of data acquired with the 1.5 MHz probe of the circumferentially oriented holes. Holes 1, 2, and 4 were correctly identified, but Hole 3 was not detected. Therefore, only Holes 1 and 2 are resolved. Hole 2 is coincident with the red vertical line in Figure 7-10 and the blue vertical line represents the position where the Hole 3 response should be located. Note the considerably "brighter" (higher amplitude) response from Hole 4 compared to that in Figure 7-9, where all four holes had comparable responses. This may be from a merged Hole 3 and Hole 4 reflection. Similar results were found in the 800 kHz and 1.0 MHz data; however, in the 500 kHz data, the Hole 2 response was also not detected. In summary, the 800 kHz, 1.0 MHz,

and 1.5 MHz probes were able to resolve holes separated by 22.7 mm (0.89 in.) or more in the probe's lateral direction, while the 500 kHz probe's lateral resolution was greater than 22.7 mm (0.89 in.).



**Figure 7-9 A Series of Axially Oriented Spatial Resolution Holes at 1.5 MHz, True Depth Focus. All holes were resolved.**



**Figure 7-10 A Series of Circumferentially Oriented Spatial Resolution Holes at 1.5 MHz, True Depth Focus. Only Holes 1 and 2 were resolved in this example.**

#### 7.1.1.4 Spot Size

For an ultrasonic probe, a primary determinant of spatial resolution is the probe's beam spot size. In this assessment, the spot size for a given probe and focal style were measured both in the empirical and modeled data as calculated from Zetec UltraVision software. The spot sizes were measured at the half amplitude, or -6 dB level (50%), and also at the -3 dB level (71%). To empirically measure the beam, a hole with a diameter less than a wavelength was scanned

(ASTM E2491-13 2013, Annex A.1). The holes in this specimen met this criterion for frequencies up to 1.2 MHz. The hole diameters, however, were approximately 25% larger than ideal for the 1.5 MHz probe, resulting in an overestimation of the empirical spot size. The spot size results, as averaged from HP and TD focal styles, are presented in Table 7-3. Modeled results were within 20% of the empirical spot size values for all but two data points in the 500 kHz set, where the difference was below 30%.

Note that the lateral spot sizes are consistently larger than the forward spot sizes, sometimes by a factor of two. This is because of the design of the phased-array probes. As indicated above, the probes have 10 elements in the forward direction and only three or five in the lateral direction. The additional forward elements provide additional beam focusing ability and therefore a smaller spot size.

**Table 7-3 Average Beam Spot Size in mm (in.)**

Probe Frequency, MHz	Empirical (-3 dB)		Modeled (-3 dB)		Empirical (-6 dB)		Modeled (-6 dB)	
	Forward	Lateral	Forward	Lateral	Forward	Lateral	Forward	Lateral
0.5	7.5 (0.30)	14.0 (0.55)	9.3 (0.37)	16.9 (0.67)	11.0 (0.43)	22.5 (0.89)	14.1 (0.56)	24.2 (0.95)
0.8	6.8 (0.27)	12.3 (0.48)	8.0 (0.31)	14.9 (0.59)	9.8 (0.39)	22.3 (0.88)	11.0 (0.43)	20.9 (0.82)
1.0	6.7 (0.26)	12.3 (0.48)	7.6 (0.30)	13.0 (0.51)	10.1 (0.40)	21.0 (0.83)	10.7 (0.42)	18.8 (0.74)
1.5 <sup>(a)</sup>	7.3 (0.29)	10.8 (0.26)	6.5 (0.26)	11.3 (0.44)	9.3 (0.37)	17.0 (0.67)	9.3 (0.37)	16.3 (0.64)

(a) Empirical measurements may not be accurate at this frequency.

It is desirable to estimate spatial resolution in terms of beam spot size, so that the expected resolution can be estimated directly from the spot size, which is easily obtained. Table 7-4 presents the ratio of the edge-to-edge separation distances to the empirical -3 dB beam spot sizes. For example, if the hole separation was 11.3 mm (0.44 in.) and the spot size was 7.5 mm (0.3 in.), then the table entry would be 11.3/7.5 (0.44/0.3), or 1.5, indicating that the hole separation was 1.5 times the spot size. Larger hole spacing results in larger ratios (smaller spot size relative to the hole spacing) and therefore a greater chance that the holes will be resolved. As described above, all holes were resolved in the forward direction for the three separation distances. Correspondingly, the separation distances were  $\geq 0.8$  of the forward direction beam spot size. That is, holes closer together than the spot size were resolved in the forward direction.

In the lateral direction, on the other hand, the holes with separation distances of 5.7 and 11.3 mm (0.22 and 0.45 in.) were not resolved by any of the probes. Furthermore, the 500 kHz probe did not resolve the holes with the largest separation distance, 22.7 mm (0.89 in.), which was 1.6 times the spot size. For edge-to-edge separation distances greater than the spot size, it was anticipated that the holes would be readily resolved. The range of data in Table 7-4 is limited, but results indicate that the holes were resolved in the probe's primary or forward direction if they were separated by distances that were at least 80% of the beam -3 dB spot size. However, lateral resolution was degraded and required separation distances of approximately two times the beam's lateral spot size.

**Table 7-4 Ratio of Edge-to-Edge Separation to the -3 dB Spot Size (Wrought Stainless Steel)**

Freq., MHz	Forward, E-E Separation, mm (in.)			Lateral E-E Separation, mm (in.)		
	5.7 (0.22)	11.3 (0.45)	22.7 (0.89)	5.7 (0.22)	11.3 (0.45)	22.7 (0.89)
0.5	0.8	1.5	3.0	0.4 <sup>(a)</sup>	0.8 <sup>(a)</sup>	1.6 <sup>(a)</sup>
0.8	0.8	1.7	3.4	0.5 <sup>(a)</sup>	0.9 <sup>(a)</sup>	1.9
1.0	0.9	1.7	3.4	0.5 <sup>(a)</sup>	0.9 <sup>(a)</sup>	1.8
1.5	0.8	1.6	3.1	0.5 <sup>(a)</sup>	1.1 <sup>(a)</sup>	2.1
E-E = edge to edge						
<sup>(a)</sup> Holes not resolved						

Similar to Table 7-4, Table 7-5 presents data for edge-to-edge separation distances as a function of the -6 dB beam size. The -6 dB beam size is larger than the -3 dB beam size, so the ratios are generally smaller than those in Table 7-4. The data suggest that holes were resolved in the forward direction if the separation distance was approximately 0.5 of the -6 dB beam spot size, while lateral resolution requires a separation distance nominally equal to the -6 dB spot size.

**Table 7-5 Ratio of Edge-to-Edge Separation to the -6 dB Spot Size (Wrought Stainless Steel)**

Freq., MHz	Forward, E-E Separation, mm (in.)			Lateral E-E Separation, mm (in.)		
	5.7 (0.22)	11.3 (0.45)	22.7 (0.89)	5.7 (0.22)	11.3 (0.45)	22.7 (0.89)
0.5	0.5	1.0	2.1	0.3 <sup>(a)</sup>	0.5 <sup>(a)</sup>	1.0 <sup>(a)</sup>
0.8	0.6	1.2	2.3	0.3 <sup>(a)</sup>	0.5 <sup>(a)</sup>	1.0
1	0.6	1.1	2.3	0.3 <sup>(a)</sup>	0.5 <sup>(a)</sup>	1.1
1.5	0.6	1.2	2.5	0.3 <sup>(a)</sup>	0.7 <sup>(a)</sup>	1.3
E-E = edge to edge						
<sup>(a)</sup> Holes not resolved						

Tables 7-4 and 7-5 show that the PA probes are better able to resolve the holes in the forward direction than in the lateral direction, with all of the holes resolved in the forward direction, but only the most widely-spaced holes resolved laterally. This is expected in light of the fact that the forward spot size was smaller than the lateral spot size, as described above. The results also indicate that the spot size for a given probe, whether measured at -3 dB or -6 dB, did not play an important role in the ability to resolve the holes. Thus, a probe's spot size and expected performance can be estimated at whatever level the user finds convenient. In practice, the user should be aware of a probe's limitations, since the ability to resolve features is a direct result of probe performance. Furthermore, the ability to resolve features depends on the scan direction, so measuring the spot size in one dimension may not be sufficient to understand a probe's resolution limits.

#### 7.1.1.5 *Depth Resolution*

Through-wall depth resolution was assessed on a probe's ability to resolve an ID corner response from the hole bottom on machined flat-bottom holes. These holes were in the same WSS specimen and are represented on Figure 7-1 as indicated by the "A." Three holes, with diameters of 4.76 mm (0.1875 or 3/16 in.) and an edge-to-edge separation of 20.6 mm (0.81 in.), were machined to depths of 2.83, 5.66, and 11.33 mm (0.112, 0.223, and 0.446 in.) corresponding to  $\lambda/4$ ,  $\lambda/2$ , and  $\lambda$  for 500 kHz longitudinal waves, respectively. The diameters were chosen such that the holes would be large enough to provide a significant signal for all probes used. The responses were evaluated over TD and HP focusing at three refracted angles and at a normal incidence. The general findings were that the tip, or upper specular reflection, was resolved from the ID corner response when the hole depth was one wavelength or greater. At 500 kHz, tip signals were detected for the shallower two holes, but a 19% dip in amplitude between the corner and tip responses was not evident, meaning that the tip was not resolved from the corner. Flaw height RMSE were 0.50, 1.17, 1.52, and 1.93 mm (0.020, 0.046, 0.060, and 0.076 in.) for probe frequencies of 1.5 MHz, 1.0 MHz, 800 kHz, and 500 kHz, respectively. All values would meet the ASME Section XI performance demonstration depth sizing criterion of 3.18 mm (0.125 in.).

### 7.1.2 **CASS Manoir Ring Spatial and Depth Resolution Summary**

#### 7.1.2.1 *Specimen Description*

The spatial and depth resolution of 500 and 800 kHz PA probes in TRL mode was also evaluated on resolution holes machined into a CASS Manoir ring specimen (see Figure 7-11). The specimen has a 914 mm (36.0 in.) OD and a 75 mm (3.0 in.) wall thickness. A section of the specimen was polished and etched to reveal an equiaxed grain structure with typical grain sizes of ~2 mm (~0.08 in.). Three rows of five flat-bottom holes were machined into the ID surface of the specimen. One of the rows was oriented axially, one oriented circumferentially, and another also oriented circumferentially but with the holes machined at a 30° angle from the surface normal. Each hole was 15.01 mm (0.591 in.) deep and 4.78 mm (0.188 or 3/16 in.) in diameter.

Holes were spaced such that the distance between holes decreased from one hole to the next, with Hole 1 being the most isolated in each set; the edge-to-edge values are shown in Table 7-6 in units of millimeters, inches, and wavelength ( $\lambda$ ) at the two probe frequencies. Note that the speed of L-waves in this specimen was measured to be 5770 m/s, but the spacing of the holes was designed for an assumed 5660 m/s velocity.



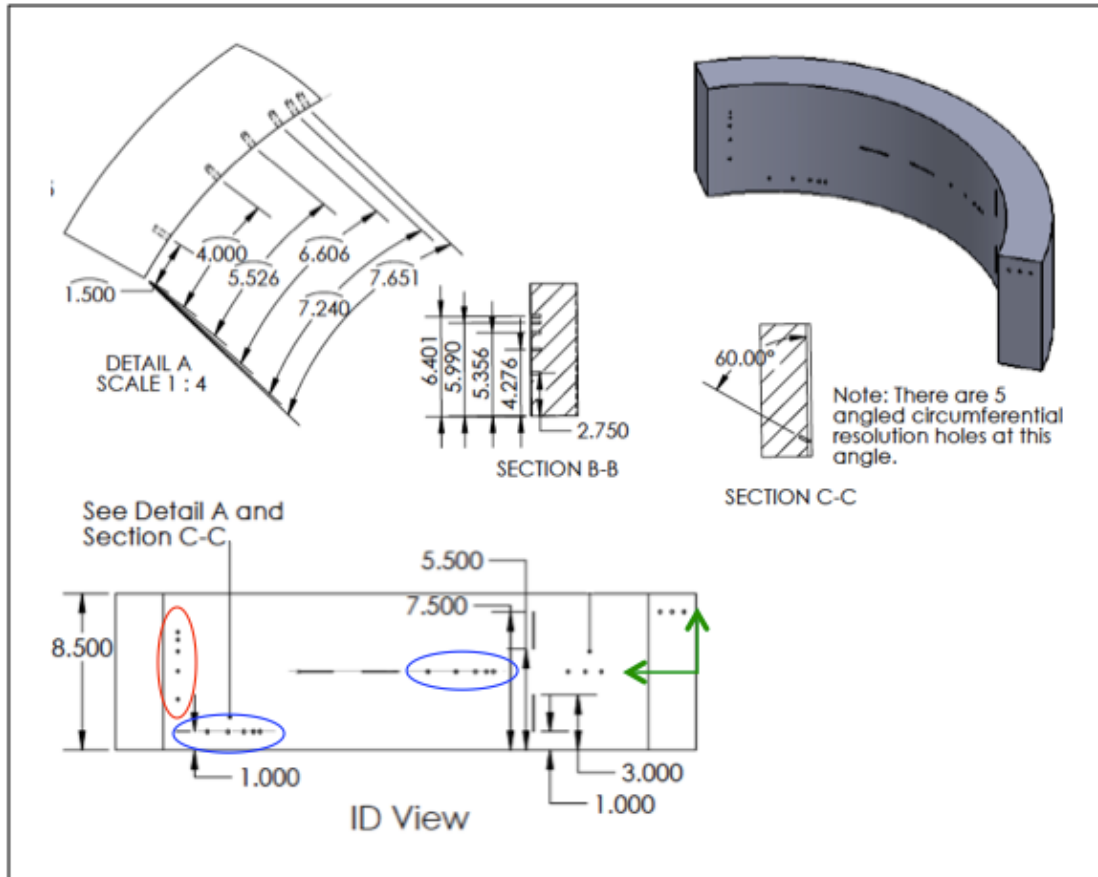


**Figure 7-11 Manoir Ring Specimen.** Sets of resolution holes were machined axially (red oval) and circumferentially (blue ovals). The circumferential holes at the center of the specimen are straight and those at the edge are angled. The scan origin is indicated by the green arrows.

**Table 7-6 Spacing of Holes**

Holes	Edge-Edge Spacing, mm	Edge-Edge Spacing, in.	Number of $\lambda$ s at 500 kHz	Number of $\lambda$ s at 800 kHz
1-2	34.0	1.34	2.9	4.7
2-3	22.7	0.89	2.0	3.1
3-4	11.3	0.45	1.0	1.6
4-5	5.7	0.22	0.5	0.8

#### 7.1.2.2 Data Acquisition

Data were collected from the OD surface of the specimen with 500 and 800 kHz PA probes by scanning each set of holes in the direction normal to each set's orientation; therefore, only the probes' lateral resolutions were assessed. Scans were made using TD and HP focusing at focal distances of 74 mm (2.91 in.) and 105 mm (4.13 in.), respectively. The focusing distances were chosen to maximize energy at the reflectors, based on beam models performed in UltraVision.

The refraction angle was incremented in 4° steps from 25–45° in the TD scans and from 25–65° in the HP scans. Data were acquired at beam skews of –10°, 0°, and +10° for all scans. These angle parameters assured full coverage of the reflectors while maintaining manageable data file sizes. For the circumferential straight holes, data were acquired at 0° and 180° probe skews; for the axial and circumferential angled holes there was only sufficient axial space for 0° probe skew scans. Figure 7-12 shows an example of the straight circumferential holes scanned with the 800 kHz probe. Note that the noise level in this CASS specimen is considerably higher than that in the wrought stainless-steel specimen.

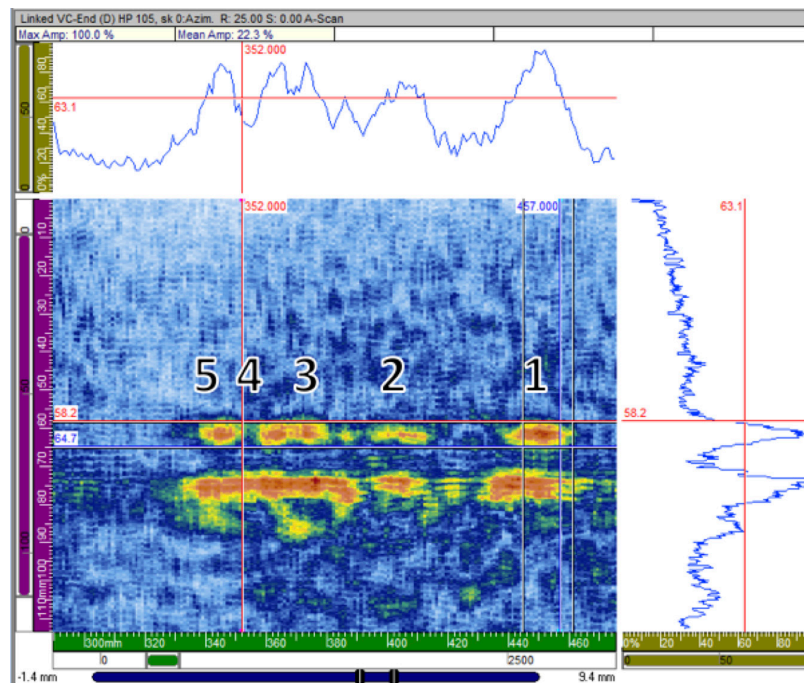


**Figure 7-12 A Series of Circumferentially Oriented Resolution Holes at 800 kHz, Half Path Focus, 0° Beam Skew. The hole true-state positions correspond to the label positions. Only Holes 1 and 2 were resolved.**

### 7.1.2.3 Data Analysis

As with the wrought stainless-steel specimen, the probe spot size was determined by measuring the signal response from Hole 1. The spot size was measured by isolating the hole in the C-scan and measuring the –6 dB and –3 dB levels in the lateral (index) and forward (scan) directions.

The positions of the peak responses from each hole were determined, and the amplitudes of the peaks and troughs were measured. As described above, a trough was considered significant if it was at least a 19% dip (–1.8 dB) from the lower of the two surrounding peaks. A hole was considered to be resolved if: (1) a significant trough was found on both sides of the peak in question (except for Holes 1 and 5, which only had one neighboring hole); and (2) the location of the peak in question was found to be ≤3.0 mm (0.125 in.) from its known true-state location. Criterion 2 was implemented to help account for potential beam redirection from the coarse-grained material.

Comparing the locations of the peaks to the known locations of the holes was straightforward for scans with beam skew of 0°. For each set of holes, the peak location of Hole 1 (the most isolated and easiest to measure) consistently matched well with the known hole location; therefore, it was assumed that the other holes and peak locations should also match for beam skew 0°. Beam skews of ±10° were more complicated. In circumferential scans, hole locations were deflected by approximately the amount predicted for beam skews of ±10°:  $D \cdot \sin(\theta)$ , where  $D$  is the thickness of the specimen and  $\theta$  is the beam skew. However, for beam skews of ±10° in axial scans, peaks were not in the locations expected, showing considerably less deflection. Reasons for this are unclear but may be related to the non-isotropic grain structure of the specimen. Therefore, to account for the discrepancy, an empirical correction was made in each circumferential and axial scan with non-zero beam skew. For Hole 1 in each image, the average peak location of the ±10° beam skews was calculated and the difference was defined as a “skew offset.” This offset was then applied to all the peaks in the scan to find the difference between the observed peaks and known hole locations.

#### 7.1.2.4 Results and Observations

Overall, results showed that the holes tended to be better resolved using the 800 kHz probe versus the 500 kHz probe, the TD focus versus the HP focus, and non-zero beam skew versus the zero-beam skew.

Table 7-7 shows the percentage of the time that each hole was resolved for each beam skew and probe frequency, considering all the analyzed data (scan orientations, refraction angles, etc.). Hole 1 was consistently resolved from Hole 2, but the ability to resolve the holes decreased with the decreasing distance between the holes. Resolution also decreased with decreasing probe frequency, while non-zero beam skews may improve resolution. Holes 2 to 3 and 3 to 4 were resolved at least 50% of the time with the 800 kHz probe and at non-zero skew angles. Holes 4 and 5 were not well resolved. The 500 kHz probe resolved Holes 2 and 3 at 75% or greater for non-zero skew angles and did not resolve Hole 3 from Hole 4 nor Hole 4 from Hole 5.

**Table 7-7 Percentage of Time that Holes are Resolved in Relation to Probe Frequency and Beam Skew**

Probe Frequency	Separation, mm	Separation, in.	Holes	Beam Skew		
				-10°	0°	+10°
500 kHz	34.0	1.34	1–2	100	100	100
	22.7	0.89	2–3	100	33	75
	11.3	0.45	3–4	0	0	0
	5.7	0.22	4–5	0	0	0
800 kHz	34.0	1.34	1–2	100	100	100
	22.7	0.89	2–3	90	73	50
	11.3	0.45	3–4	60	18	60
	5.7	0.22	4–5	10	0	0

Spatial resolution as a function of flaw orientation, as well as beam skew and probe frequency, is considered in Table 7-8. As shown above, non-zero beam skews can provide better resolution. At 500 kHz the axial flaws showed slightly better resolution, but at 800 kHz the circumferentially oriented flaws had better resolution.

**Table 7-8 Percentage of Time that Holes are Resolved in Relation to Flaw Orientation as well as Probe Frequency and Beam Skew**

Probe Frequency	Separation, mm	Separation, in.	Holes	Axial		Circ.	
				-10, 10°	0°	-10, 10°	0°
500 kHz	34.0	1.34	1-2	100	100	100	100
	22.7	0.89	2-3	100	50	75	25
	11.3	0.45	3-4	0	0	0	0
	5.7	0.22	4-5	0	0	0	0
800 kHz	34.0	1.34	1-2	100	100	100	100
	22.7	0.89	2-3	67	25	80	100
	11.3	0.45	3-4	50	0	70	29
	5.7	0.22	4-5	0	0	10	0

#### 7.1.2.5 Spot Size

As with the wrought stainless-steel specimen, average spot sizes were measured using the first, most isolated hole as the reflector. A single average spot size for each probe was determined from the average values for both focal styles at -10°, 0°, and 10° beam skew for the 0° probe skew orientation; see Table 7-9. The spot sizes for the circumferential scans were consistently larger than those for the axial scans. This was possibly due to the longer part path and the anisotropic nature of the CASS material, as the inhomogeneous and anisotropic nature of the CASS material affects the spot size due to scattering. Spot sizes of the axial scans are also given in the table. For purposes of comparison, the axial values from the WSS specimen are reprinted in the last two rows in the table. The percent difference in measured spot sizes between wrought stainless steel and CASS material ranges from -5.8% to 25.5%. The spot size in the WSS specimen was consistently smaller than in CASS for the 500 kHz probe but not for the 800 kHz probe. This is likely because the lower frequencies are less affected by the CASS grains, so there is less beam spread and scattering at 500 kHz than at 800 kHz.

**Table 7-9 Average Probe Spot Sizes, in mm (in.)**

Scan Orientation	Probe Frequency	-6 dB		-3 dB	
		Forward	Lateral	Forward	Lateral
Circ.	500 kHz	18.6 (0.73)	29.7 (1.17)	12.8 (0.50)	16.7 (0.66)
	800 kHz	18.1 (0.71)	27.2 (1.07)	10.3 (0.41)	14.2 (0.56)
Axial	500 kHz	12.8 (0.50)	23.2 (0.91)	8.5 (0.33)	14.7 (0.58)
	800 kHz	10.7 (0.42)	20.7 (0.81)	6.4 (0.25)	12.7 (0.50)
WSS Axial	500 kHz	11.0 (0.43)	22.5 (0.89)	7.5 (0.30)	14.0 (0.55)
	800 kHz	9.8 (0.39)	22.3 (0.88)	6.8 (0.27)	12.3 (0.48)

#### 7.1.2.6 Spatial Resolution in Terms of Spot Size

The relationship between spot size and the ability to resolve holes was examined for spot sizes measured at the -3 dB level (see Table 7-10). As with Tables 7-4 and 7-5, data are presented as the ratio of the hole separation to the spot size. These data are for a probe's lateral resolution.

Table 7-10 indicates, in general terms, that holes were resolved if the separation between holes was 1.5–2.0 times the beam size or greater. Results can be compared to those for the wrought stainless steel in Table 7-4, where results similarly show that the holes were resolved if the separation was about 1.8 times the beam size or greater in the lateral direction. Here, the ability to resolve laterally was somewhat better, with some holes resolved with a separation-to-spot size ratio as small as 0.8. However, not all of the holes with this ratio were resolved, and the ability to consistently resolve the holes was not realized until the hole separation was at least twice the spot size. It is likely that the grain structure of the CASS material scatters and redirects the beam unpredictably, sometimes aiding in hole resolution but more often hindering.

**Table 7-10 Ratio of Edge-to-Edge Separation to the –3 dB Spot Size (CASS)**

Frequency (kHz)	Lateral E-E Separation, mm (in.)			
	5.7 (0.22)	11.3 (0.45)	22.7 (0.89)	34.0 (1.34)
500 circ.	0.3 <sup>(a)</sup>	0.7 <sup>(a)</sup>	1.4 <sup>(b)</sup>	2.0
800 circ.	0.4 <sup>(a)</sup>	0.8 <sup>(b)</sup>	1.6	2.4
500 axial	0.4 <sup>(a)</sup>	0.8 <sup>(a)</sup>	1.5 <sup>(b)</sup>	2.3
800 axial	0.4 <sup>(a)</sup>	0.9 <sup>(a)</sup>	1.8 <sup>(b)</sup>	2.7
E–E = edge-to-edge (a) Not resolved or resolved ≤50% of the time (b) Resolved for non-zero skews, >65% of the time				

Table 7-11 shows the edge-to-edge separation as a function of the –6 dB beam or spot size. These data indicate that the holes were nominally resolved if the separation was approximately equal to or greater than the beam size. Results can be compared to those for the wrought stainless steel in Table 7-5. Similar to the discussion above, some holes in the CASS material were resolved when the separation was only 0.4 times the spot size, but this was not typical. Overall, resolution in the CASS was lower than in the WSS, again mostly likely due to the beam scattering and redirection from the grain structures.

**Table 7-11 Ratio of Edge-to-Edge Separation to the –6 dB Spot Size (CASS)**

Frequency (kHz)	Lateral E-E Separation, mm (in.)			
	5.7 (0.22)	11.3 (0.45)	22.7 (0.89)	34.0 (1.34)
500 circ.	0.2 <sup>(a)</sup>	0.4 <sup>(a)</sup>	0.8 <sup>(b)</sup>	1.1
800 circ.	0.2 <sup>(a)</sup>	0.4 <sup>(b)</sup>	0.8	1.3
500 axial	0.2 <sup>(a)</sup>	0.5 <sup>(a)</sup>	1.0 <sup>(b)</sup>	1.5
800 axial	0.3 <sup>(a)</sup>	0.5 <sup>(a)</sup>	1.1 <sup>(b)</sup>	1.6
E–E = edge-to-edge (a) Not resolved or resolved ≤50% of the time (b) Resolved for non-zero skews, >65% of the time				

#### 7.1.2.7 Depth Resolution

Three additional flat-bottomed holes were machined into the Manoir CASS specimen for an assessment of depth resolution. Measurement of depth resolution is important for understanding the minimum crack depths that can be resolved when a tip signal is detected. Through-wall depth differences between responses from the top of the hole and its corner were measured to determine flaw height, or through-wall depth. The depths of the holes were 5.7, 11.3, and 22.7 mm (0.22, 0.45, and 0.89 in.). These depths represented  $\lambda/2$ ,  $\lambda$ , and  $2\lambda$  at 500 kHz and  $0.8\lambda$ ,  $1.6\lambda$ , and  $3.1\lambda$  at 800 kHz. The deeper two holes were resolved with the 500 and 800 kHz probes, and flaw tips were detected but not resolved for the shallowest hole. Therefore, in this CASS material, flaw tips, or upper specular reflectors, as shallow as one wavelength were detected and resolved with the 500 kHz probe. While the shallowest hole was detected, it had a large sizing error. The 500 kHz probe exhibited a 54% sizing error and the 800 kHz probe had a 52% sizing error for a 25° refracted angle, zero beam skew, and half-path focusing. RMSE values from all three holes were 1.71 and 1.63 mm (0.067 and 0.064 in.) for the 500 and 800 kHz probes, respectively, with a HP focus. TD focusing showed similar RMSE at 500 kHz (1.69 mm or 0.066 in.) but improved at 800 kHz with 0.72 mm (0.028 in.). All values would meet the ASME Section XI performance demonstration depth sizing criterion of 3.18 mm (0.125 in.). These RMSE values are comparable to those measured in the WSS specimen.

#### 7.1.3 Conclusions

Understanding the resolution limits of the UT system and how they are affected by CASS materials is important to recognizing the detection and sizing limitations of examinations in CASS. In the wrought stainless-steel specimen, it was shown that the PA probe forward resolution was about twice that of the lateral direction. It was further observed that the beam spot size and resulting lateral resolution were only somewhat degraded by the CASS material as compared to the wrought stainless-steel material. It was expected that coarse-grained materials would have a negative impact on resolution for a given probe and scan parameters. Unfortunately, the CASS material used in this comparison was relatively fine grained when compared to other CASS materials, implying that results are a best-case scenario of sorts for CASS materials. The grain structure was unknown prior to data acquisition. Resolution is expected to be diminished by coarser grained CASS materials as sound dispersion, redirection, and noise levels increase. Depth resolution was not appreciably different in the two specimens; however, the arrays of hole depths in the sets of depth resolution holes were limited.

### 7.2 Dissimilar Metal Weld Specimen

A thick-walled RCP carbon steel nozzle-to-CASS safe-end mockup was fabricated with implanted TFCs. Cracks were detected and characterized with both ET and UT.

#### 7.2.1 Specimen 14C-146

Specimen 14C-146 was fabricated by FlawTech under contract to PNNL as a carbon steel nozzle-to-CASS safe-end mockup (similar in design to a CE RCP) with three circumferentially-oriented flaws and two axially-oriented flaws located in the weld/butter region. PNNL supplied the carbon steel spool piece and the vintage CASS material that had been acquired from the Manoir Foundry to FlawTech for fabrication welding and flaw implantation. The completed specimen was received by PNNL as shown in Figure 7-13. Oxidation and mill scale on the carbon steel side were removed to ensure a smooth scanning surface for best flaw signature analysis. Hoist rings (eye bolts) were added to the CASS side for safe handling.



**Figure 7-13 DMW Mockup as Received by PNNL**

The weld profile for this mockup is depicted in Figure 7-14, with a detailed view of the weld region in Figure 7-15. The carbon steel nozzle section is SA-516 Gr 70, while the CASS pipe section is SA-351 CF8M. The cladding material is 308/309 stainless steel and the weld and butter material is Inconel 82/182. The mockup has an OD of 930.5 mm (36.63 in.) and an ID of 760.9 mm (29.96 in.) for a through-wall thickness of 84.8 mm (3.34 in.). Figure 7-16 shows a schematic of an end view of the specimen illustrating the implanted flaws and a preexisting cut-out section in approximately one-third of the CASS piece, also visible in Figure 7-13. This cut-out section was made at Manoir for certain mechanical and chemical tests.

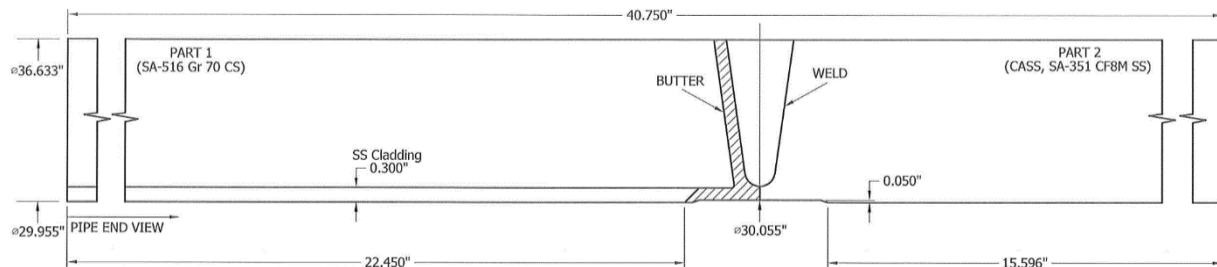


**Figure 7-14 Axial Schematic of the Mockup.** This figure shows the general construction of the mockup, with the carbon steel end on the left and the CASS end on the right.

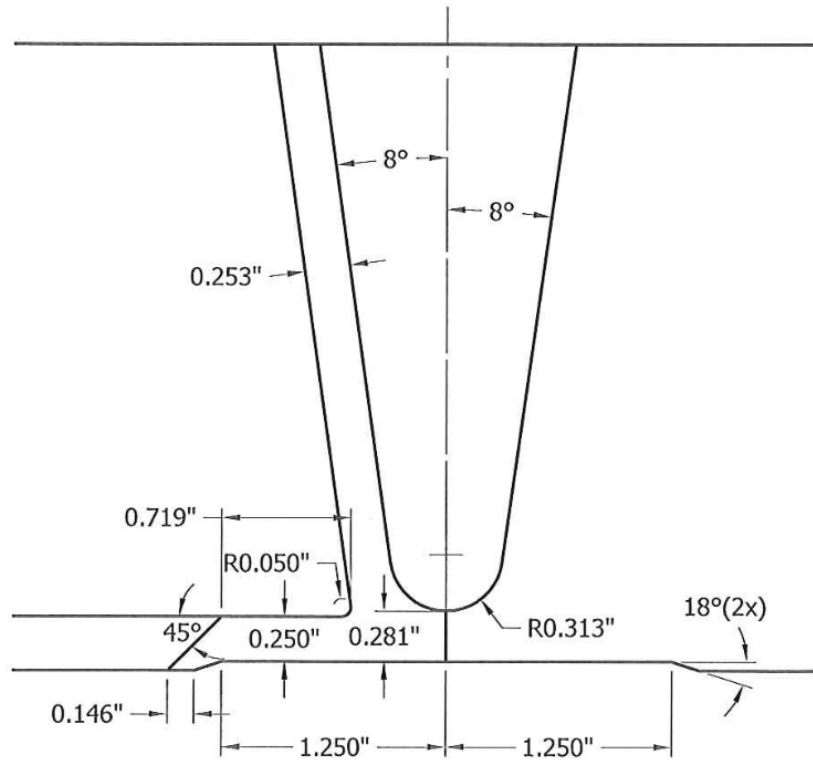


**Figure 7-15 Axial Detail of the Weld Joint**



PIPE END VIEW (SEE SHEET 1)  
SCALE - 1:5

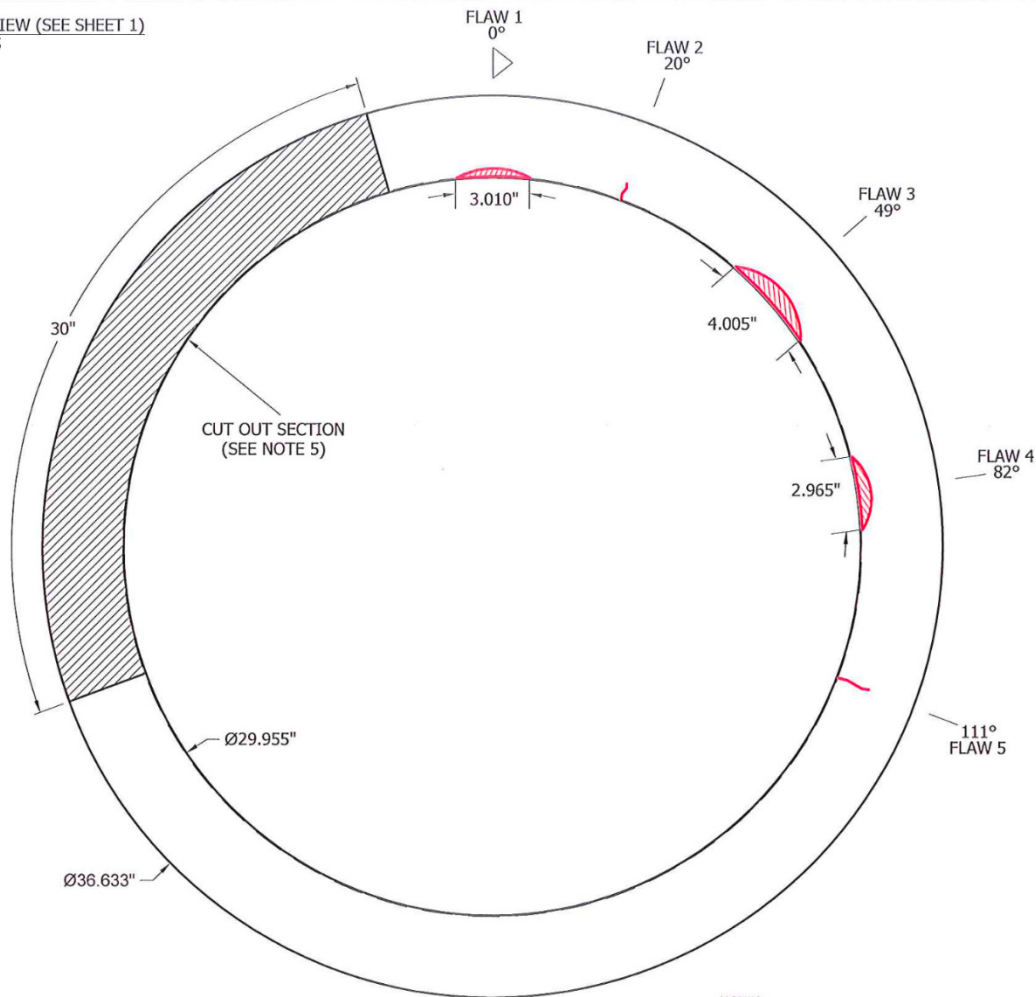


**Figure 7-16 End Schematic of the Mockup.** This view shows the flaw placement, the specimen circumferential origin (center of Flaw 1), and the cutout region.

### 7.2.1.1 Grain Structure

Photographs of the grain structure of this CASS material were taken from polished and etched pieces cut from the specimen. Figure 7-17 shows the portion of CASS material that was removed, as indicated by the red line drawn on the mockup. Thin slices (~6 mm or ~0.25 in.) were cut from both the axial and circumferential faces for polishing and etching. Figure 7-18 illustrates the respective orientations of each slice. Figure 7-19 and Figure 7-20 are detail photographs showing axial and circumferential views of the grain structure, respectively. The grains appear to be columnar near the OD and somewhat columnar near the ID, with relatively larger grains near the ID. Equiaxed grains are present in the mid-wall region with a wide range of grain sizes. Figure 7-20 shows a particularly striking heterogeneity in grain structure, size, and distribution toward the right side of the section. Note that the grain structures in Figure 7-19 and Figure 7-20 may appear slightly different from those in Figure 7-18; this is due to the different ways that the grain faces reflect light in the different photographs.

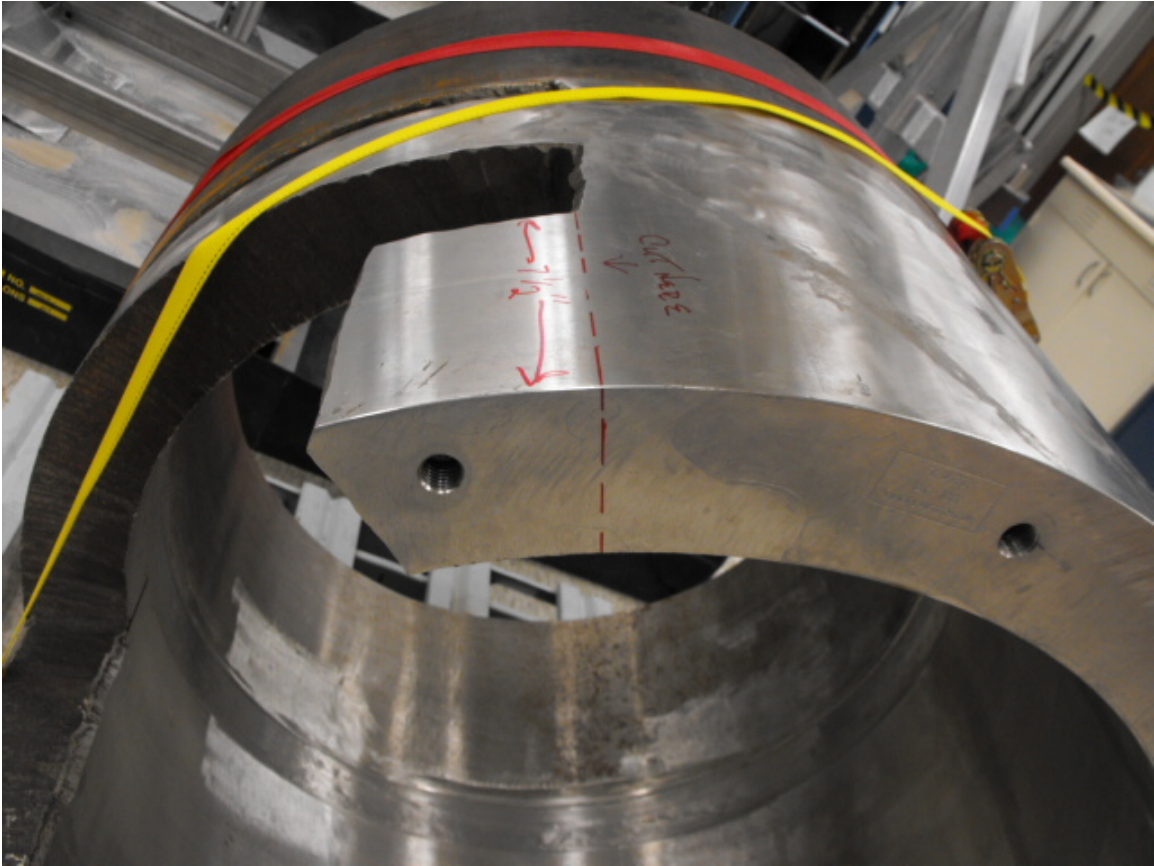


**Figure 7-17 Section of the Mockup Cut for Grain Size Measurements. The mockup came with a section in the cutout region that was removed (see red dashed line). The section was cut, polished, and etched axially and circumferentially.**

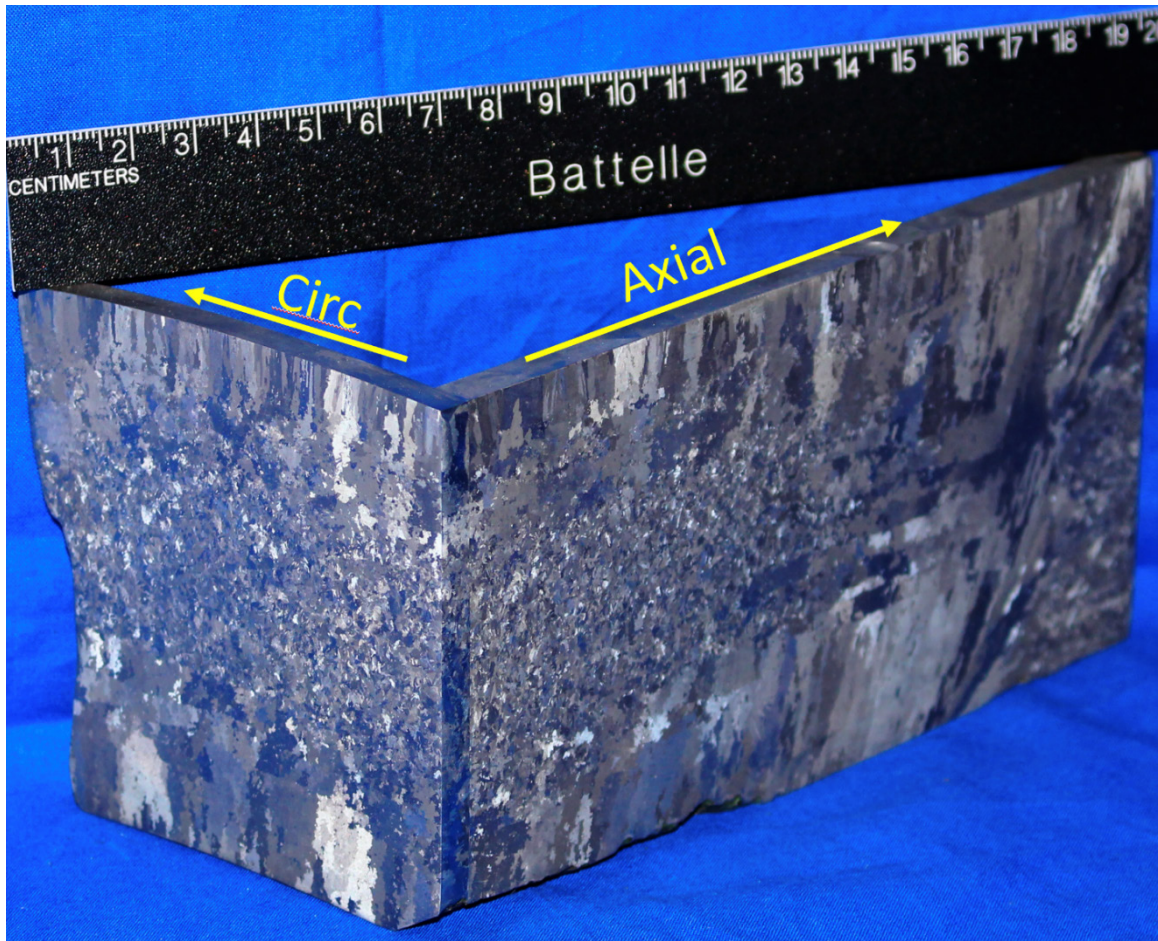


**Figure 7-18 Cut and Polished Axial and Circumferential Sections.** This figure shows the cut sections in the orientation as they were on the original specimen. The sections are sitting with the OD upward.



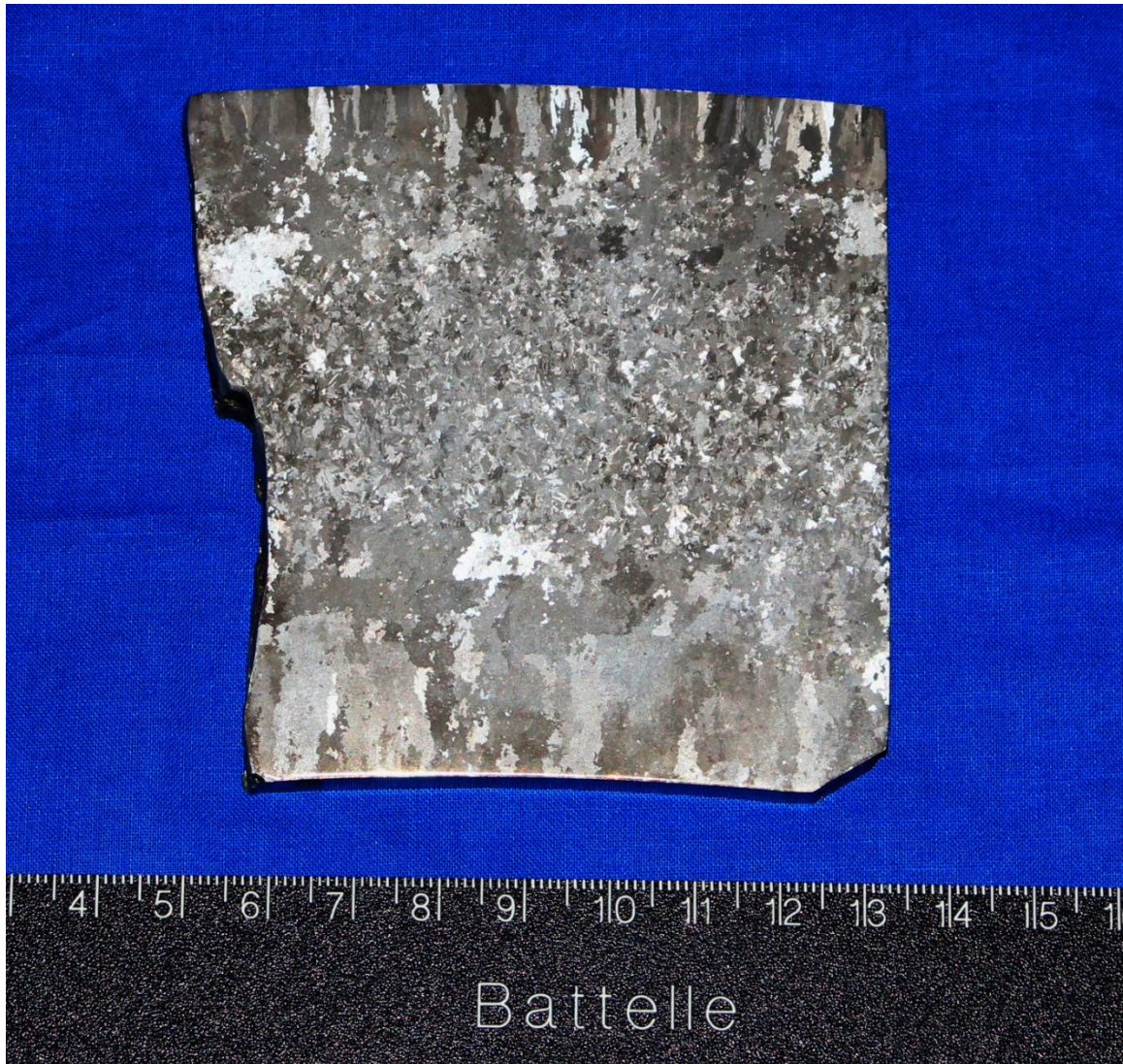


**Figure 7-19 The Polished and Etched Axial Section.** This figure shows the axial grain structure of the removed section. Note the heterogeneity in grain size and structure. The OD is at the top of the figure.





**Figure 7-20 The Polished and Etched Circumferential Section.** This figure shows the circumferential grain structure of the removed section, revealing considerable heterogeneity in grain structure type, size, and distribution. The OD is at the top of the figure.

Regions with predominantly similar grain geometries were delineated so that the average grain size and orientation could be measured in each region. This was done using a linear intercept method described in Anderson et al. (2007). Figure 7-21 and Figure 7-22 show the different regions that were delineated and categorized (color coding was added to aid in visualization).



**Figure 7-21 False Color Image of the Different Grain Regions Identified in the Axial Section**



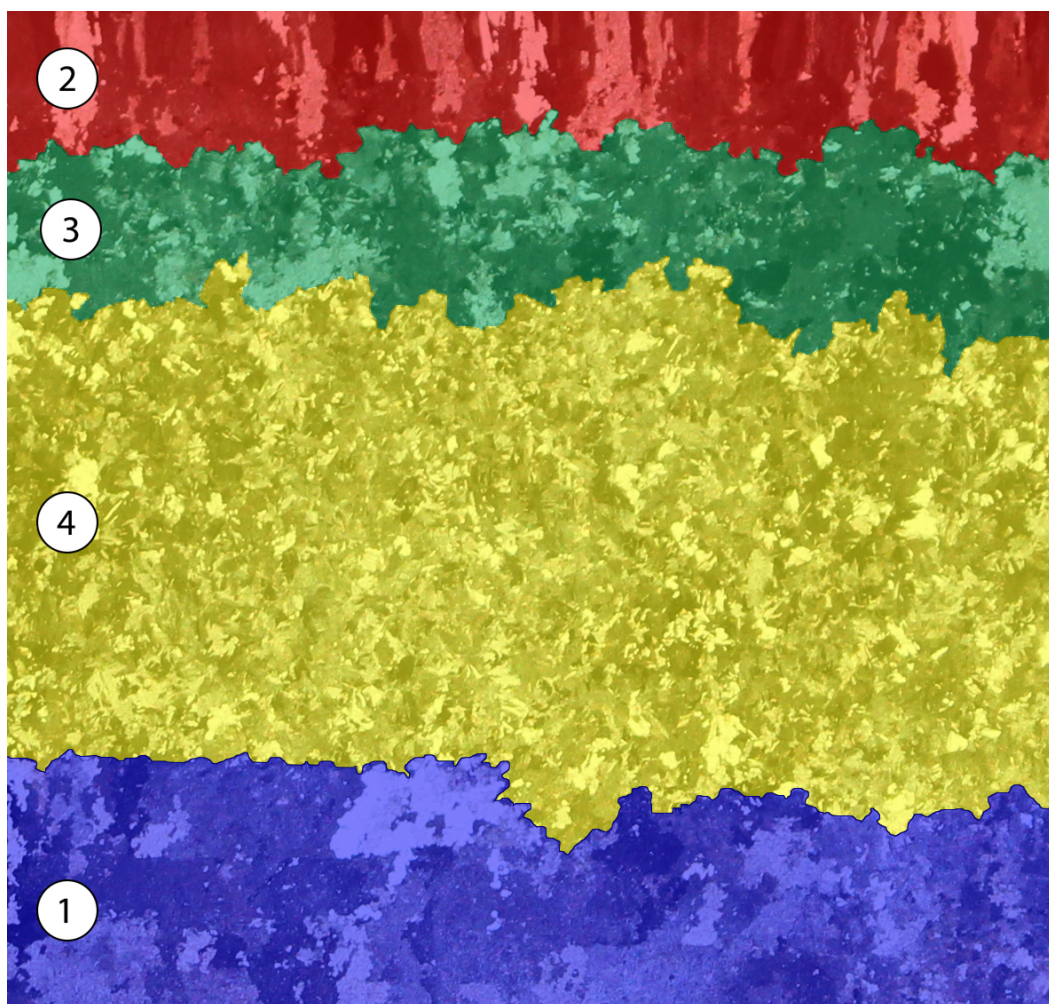


**Figure 7-22 False Color Image of the Different Grain Regions Identified in the Circumferential Section**

Table 7-12 shows the results of measurements made of grain sizes in each of the identified regions. The ratio of the average radial extent to the average circumferential or axial extent shown in the tables (R/C or R/A, respectively) is an indication of the elongation of each grain; larger ratios indicate more columnar grains. Overall, heterogeneity in grain size distribution is high, with the average grain size measuring 1–2 mm (0.04–0.08 in.) across, though the largest grains measure as large as 40 mm (1.6 in.). This range of grain sizes is comparable to other CASS specimens examined previously (Anderson et al. 2007; Crawford et al. 2014). The wide variation in grain sizes and high degree of spatial heterogeneity indicate that beam scattering and redirection will likely not be consistent across the mockup. While all CASS materials will have unique microstructures not represented by this mockup, this mockup is characteristic of the types of issues common to all CASS.

**Table 7-12 Grain Size Measurements Made from the Axial and Circumferential Cut Sections. Boldface and italic type indicate average grain extents that exceed  $0.2\lambda$  for at 800 kHz and 500 kHz, respectively.**

Grain Type	Region Number	Average Axial Extent, mm (in.)	Average Radial Extent, mm (in.)	Maximum Axial Extent, mm (in.)	Maximum Radial Extent, mm (in.)	R/A
Equ (S)	1	0.88 (0.03)	0.85 (0.03)	9.27 (0.37)	7.10 (0.28)	0.96
Equ (S)	2	0.82 (0.03)	0.75 (0.03)	6.34 (0.25)	5.93 (0.23)	0.92
Col	3	<b>1.85 (0.07)</b>	<b>2.11 (0.08)</b>	13.73 (0.54)	9.27 (0.37)	1.14
Col	4	<b>2.60 (0.10)</b>	<b>3.06 (0.12)</b>	16.90 (0.67)	27.17 (1.07)	1.18
Equ (L)	5	<b>4.33 (0.17)</b>	<b>3.72 (0.15)</b>	40.90 (1.61)	24.00 (0.94)	0.86
Equ (M)	6	<b>2.38 (0.09)</b>	<b>2.30 (0.09)</b>	28.87 (1.14)	16.14 (0.64)	0.97
		Average Circ. Extent, mm (in.)	Maximum Circ. Extent, mm (in.)		R/C	
Equ (L)	1	<b>2.48 (0.10)</b>	<b>2.42 (0.10)</b>	24.11 (0.95)	13.27 (0.52)	0.98
Col	2	<b>1.60 (0.06)</b>	<b>2.04 (0.08)</b>	12.08 (0.48)	9.17 (0.36)	1.27
Equ (M)	3	<b>1.86 (0.07)</b>	<b>1.18 (0.07)</b>	18.15 (0.71)	10.18 (0.40)	0.97
Equ (S)	4	0.90 (0.04)	0.85 (0.03)	7.38 (0.29)	6.85 (0.27)	0.95
R/A = Ratio of Average Radial Extent to the Average Axial Extent R/C = Ratio of Average Radial Extent to the Average Circumferential Extent Equ = Equiaxed Col = Columnar S, M, L = Small, Medium, Large						

Smaller grain sizes ( $d$ ) relative to the UT wavelength ( $\lambda$ ) are necessary to minimize beam redirection and scattering, with a desired  $d/\lambda$  ratio of approximately 0.2 or lower being a common *rule of thumb* (Anderson et al. 2007; Diaz et al. 2007; Diaz et al. 2012; Wan et al. 2017). In brief, the grain size-to-wavelength ratio describes the relationship of how scattering and redirection increase or decrease as the grain size varies relative to the wavelength. The longitudinal wavelength was measured in this mockup to be about 11.3 mm (0.44 in.) at 500 kHz and about 7.1 mm (0.28 in.) at 800 kHz (see Chapter 8.1.2.2). In Table 7-12, cases where average grain size extents exceeded  $0.2\lambda$  for 800 kHz (i.e., 1.4 mm, or 0.06 in.) are shown in boldface, and cases that exceeded  $0.2\lambda$  for 500 kHz (i.e., 2.3 mm, or 0.09 in.) are in italic. Note that all maximum grain extents exceed the  $0.2\lambda$  levels of both frequencies. Results suggest that 500 kHz is a more desirable frequency for detection in this material in both axial and circumferential directions, since the average grain sizes are more often below the  $0.2\lambda$  level.

#### 7.2.1.2 Flaws

Five flaws were implanted in the weld region. FlawTech employs a proprietary process for introducing TFCs in a coupon. The flaw coupon is precisely measured and placed during the welding and fabrication process so the true state of the flaw size, position, and orientation can be documented. Figure 7-16 and Figure 7-23 show the placement and dimensions of the five implanted flaws, and flaw lengths and depths are given in Table 7-13. The column “Depth %” is the flaw depth as a percentage of through-wall thickness. PNNL further characterized the flaws by using 1.5 and 2.0 MHz PA-UT probes from the carbon steel side of the weld. Data were collected

from the carbon steel side to provide the best signal responses for “true state” characterization, as beam distortion, even at lower frequencies, would be expected to affect signals and not provide similarly accurate dimensions from the CASS side of the weld. Tip signals were observed on all the flaws, and the mean flaw depth as measured by PA-UT is also reported in Table 7-13. Results of the UT scans show good agreement with the FlawTech-reported fabrication true states. Further validation of true-state lengths and locations using ET is reported below in Chapter 7.3.

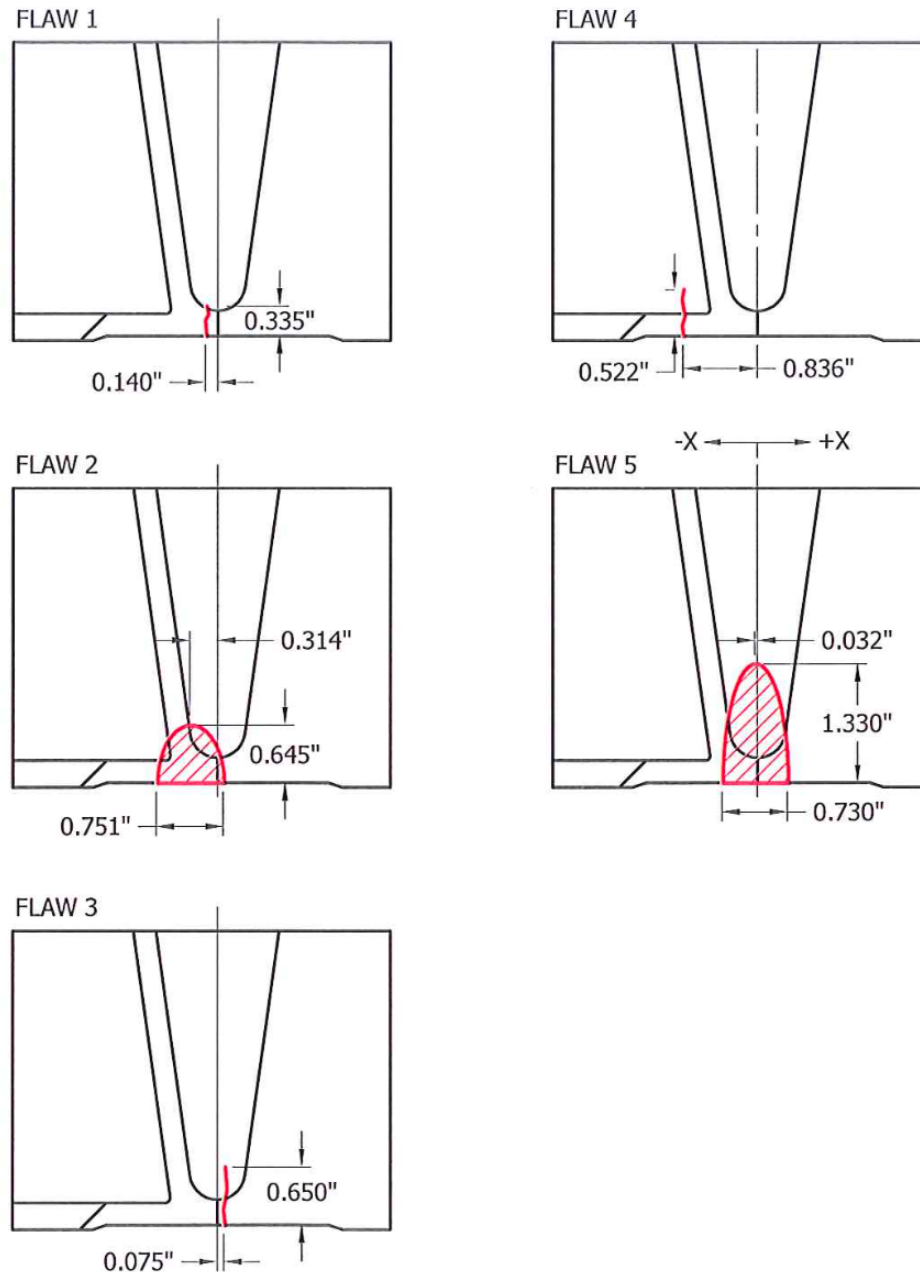


**Figure 7-23 Details of the Five Implanted Flaws.** The through-wall depths and positions relative to the weld centerline of the five implanted flaws are shown in axial views as reported by FlawTech.



**Table 7-13 FlawTech-reported True-state Flaw Orientations, Lengths, and Depths. Depth % is the percentage of through-wall thickness. Measured depth results of UT scans from the carbon steel side are included in the last column.**

Flaw	Orientation	Length, mm (in.)	Depth, mm (in.)	Depth, %	Mean UT Depth, mm (in.)
1	Circumferential	76.5 (3.01)	8.5 (0.34)	10.1	8.4 (0.33)
2	Axial	19.1 (0.75)	16.4 (0.65)	19.4	15.8 (0.62)
3	Circumferential	101.7 (4.01)	16.5 (0.65)	19.6	17.5 (0.69)
4	Circumferential	75.3 (2.97)	13.3 (0.52)	15.7	10.6 (0.42)
5	Axial	18.5 (0.73)	33.8 (1.33)	40.1	31.4 (1.24)

The flaws were all ID-connected and vertically oriented (no tilt). The flaws were placed in about one-third of the specimen, leaving ample space between flaws so UT scans could sufficiently exceed the flaw bounds and obtain base material responses to facilitate SNR measurements. Approximately one-third of the specimen was unaltered, to be used for baseline scans and possible future in situ grown TFCs.

Figures 7-24 through 7-28 are photographs of the flaw locations on the ID surface of the weld region. In all photos, the CASS side is upward, and any position markings (in blue) indicate ID distance from the origin. The red ovals encircle the flaw locations. Flaws 1 and 2 were not discerned visually and may not be fully open at the surface due to grinding or surface preparation. Notice in Figure 7-23 that circumferential Flaw 4 is placed in the butter region on the carbon steel side of the weld near the counterbore, offset by 21.2 mm (0.84 in.) from the weld centerline. Therefore, an inspection of this flaw from the CASS side of the weld is considered a far-side examination. It should be noted that the FlawTech method of implanting flaws does not lend itself to placing TFCs in the CASS or carbon steel base materials unless after-welding heat treatment is applied. This type of heat treatment (above the austenitic temperature) to remove base material-to-flaw implantation welding interfaces could significantly affect the microstructure of the base materials, so no flaws were implanted in these areas.

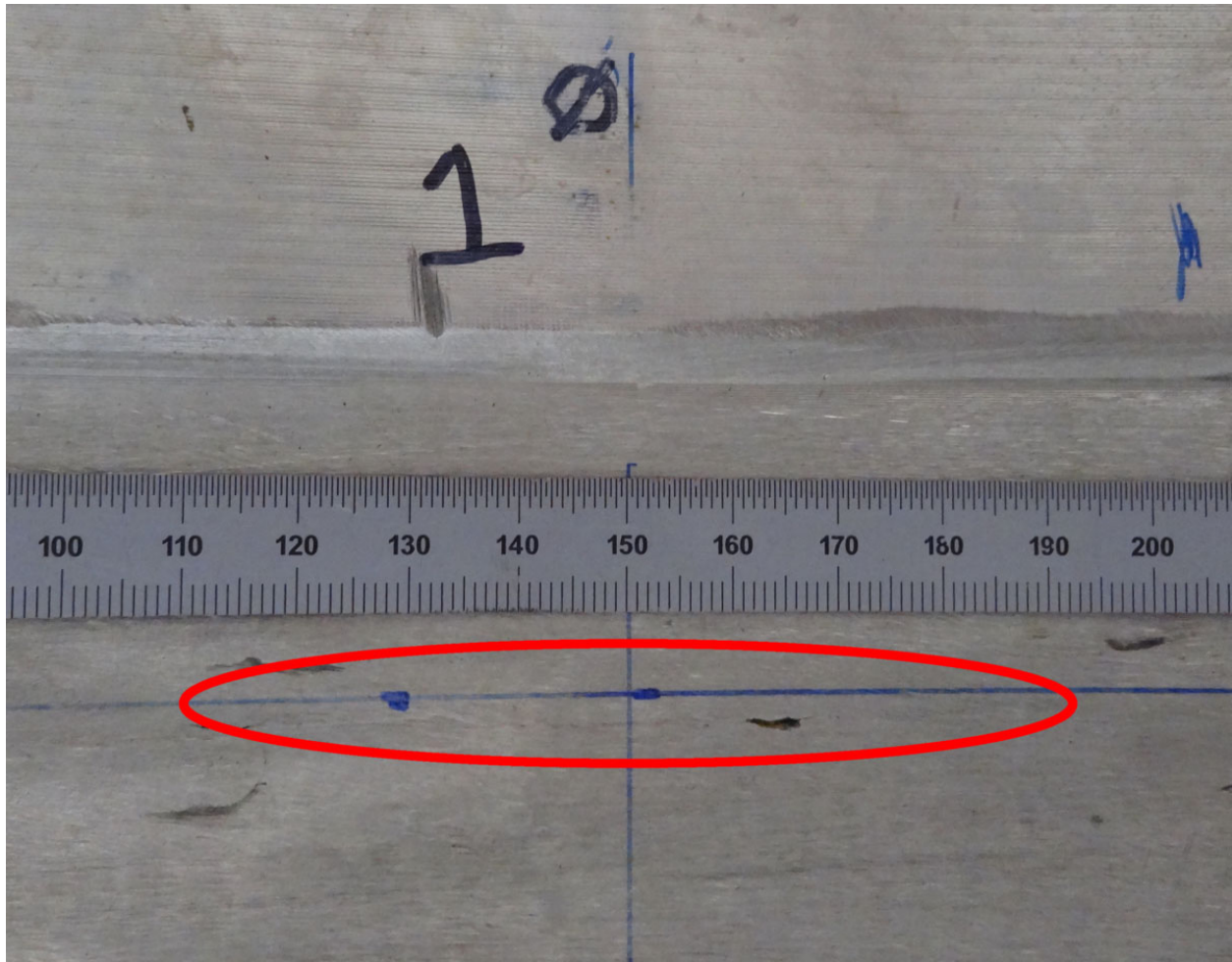


**Figure 7-24** Photograph of Flaw 1 (10% circ). The red oval encircles the flaw location. This flaw is not readily visible, and it is unclear whether imperfections on the inner-diameter surface are flaw-related. The CASS end is upward.

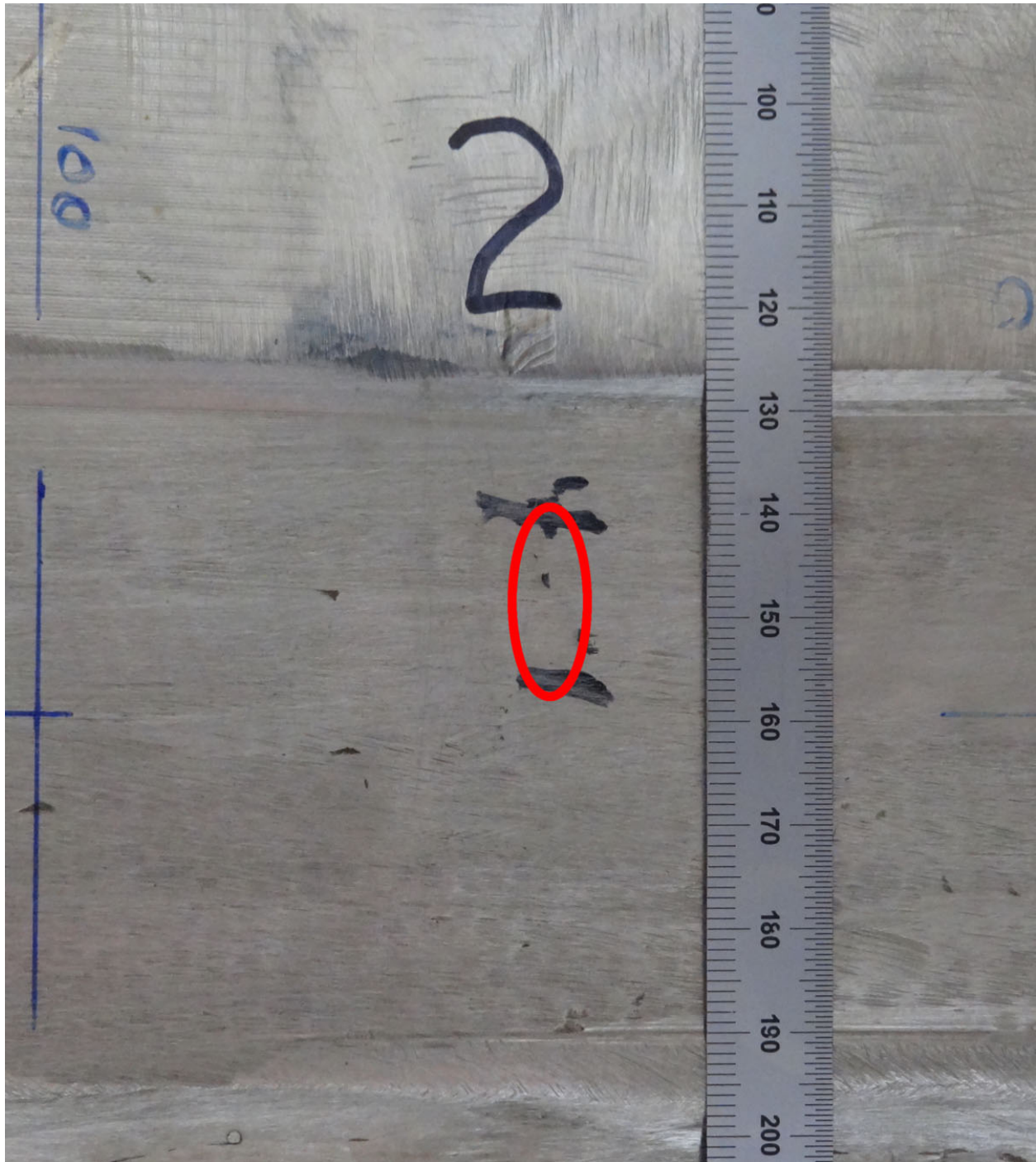


**Figure 7-25** Photograph of Flaw 2 (20% axial). The red oval encircles the flaw location. Imperfections visible on the inner-diameter surface may be flaw-related, but the whole flaw is not visible. The CASS end is upward.

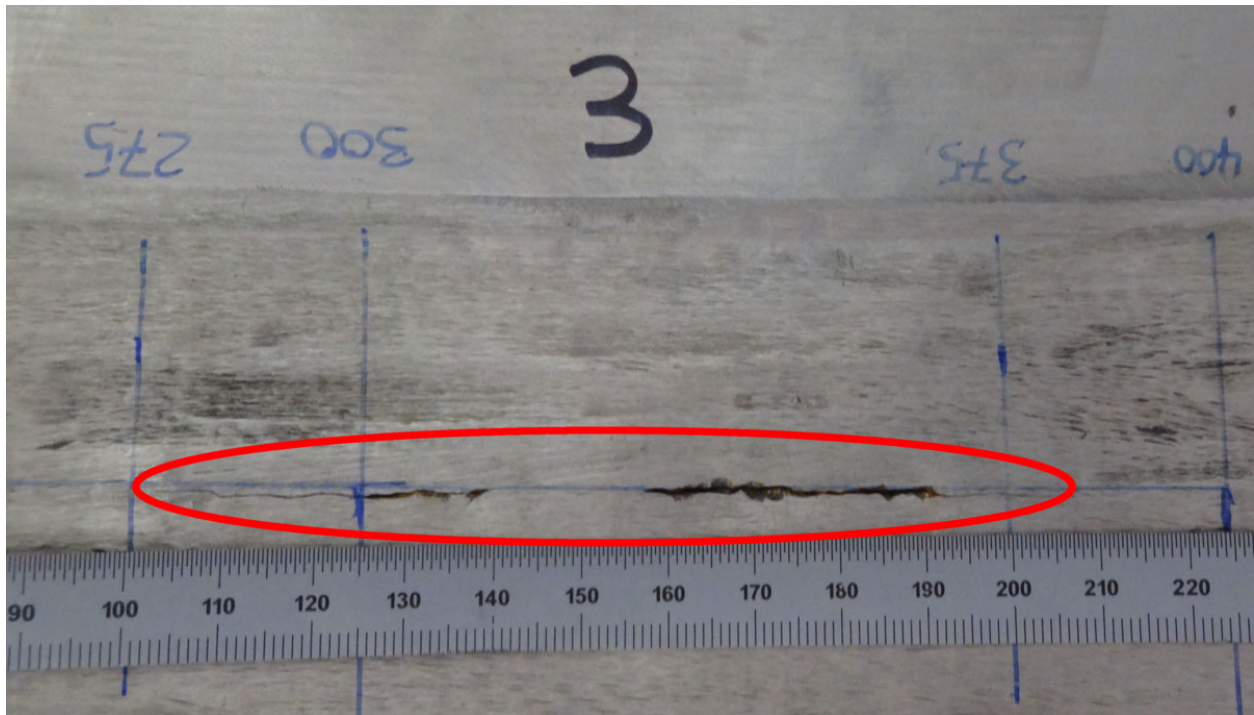


**Figure 7-26** Photograph of Flaw 3 (20% circ). This flaw is visible within the red oval, approximately spanning the region between 105–205 mm on the ruler. The CASS end is upward.





**Figure 7-27** Photograph of Flaw 4 (16% circ). This flaw is in the butter region on the carbon steel side of the weld. It is visible below the ruler within the red oval and spans from approximately 110–190 mm on the ruler. The CASS end is upward. Some grind marks are visible above the ruler.

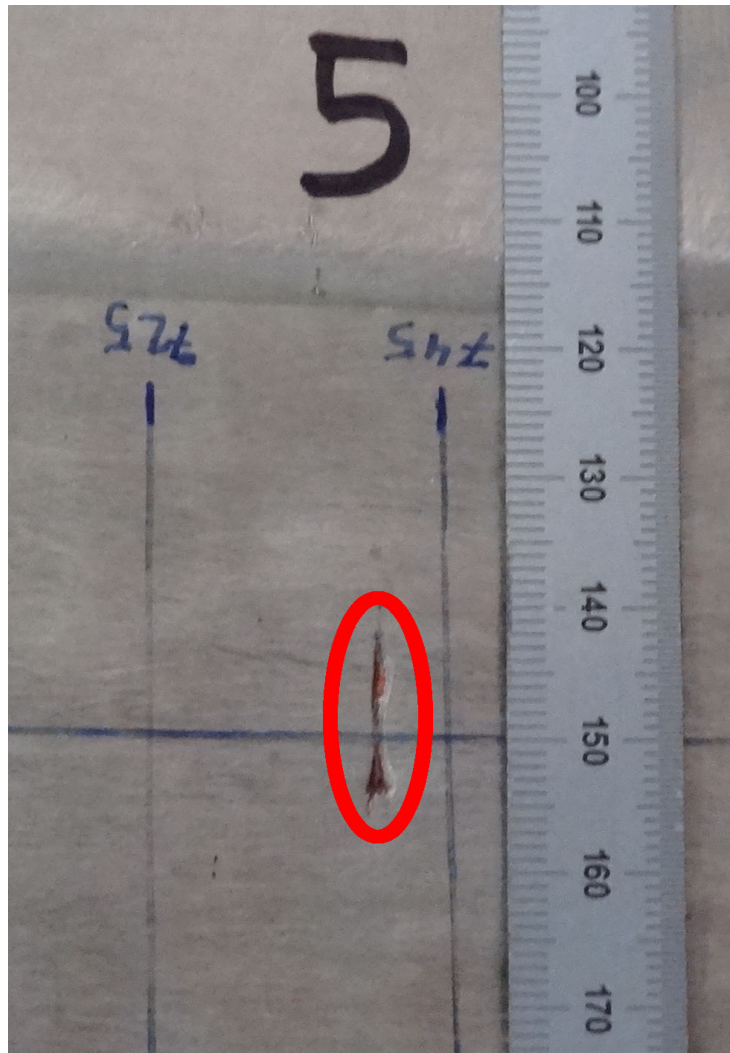


**Figure 7-28** Photograph of Flaw 5 (40% axial). This axially-oriented flaw is visible within the red oval, spanning from approximately 140–155 mm on the ruler. The CASS end is upward.

### **7.3 Eddy Current Validation of Flaw True State**

ET was used to validate the FlawTech-reported true-state length and position information. This testing method has been used extensively in the nuclear industry for surface and near-surface examinations of components, such as SG tubing, heat exchanger components, and other thin-walled tubing (ASNT 2012). The eddy current technique has also been effective at inspection of cast stainless steel components (Diaz et al. 2007) from the ID.

Fundamentally, ET relies on the principle of electromagnetic induction. Alternating currents are applied to a coil resulting in a magnetic field. When the coil is in close proximity to an electrically conductive test surface, eddy currents are generated in the test material. These eddy currents induce magnetic fields that consequently change the impedance of the coil. Changes in conductivity in the test material, such as the presence of defects, will perturb the eddy currents. These perturbations are sensed by measuring the impedance of the coil (Libby 1971; ASNT 2004, 2012).

### 7.3.1 ET Data Acquisition

An automated scanning system was used to acquire ET data on the DMW specimen. The system consisted of a WesDyne ET data acquisition system, a Zetec MCDU-02 motor controller, an ATCO GPS-1000 two-axis scanner, and a Stanford Research Systems Digital Delay Pulse Generator. The WesDyne system acquired phase and magnitude data for each point in a two-axis raster scan and was also used to analyze the data. The motor controller was used to control the ATCO scanner and provide trigger pulses for each position of the raster scan. The pulse generator conditioned the output trigger of the motor controller to a 5 V square wave pulse for triggering the WesDyne system. The ATCO scanner used magnetic wheels placed on a ring track, concentric with the curvature of the specimen, for motion in the index (circumferential) direction. Motion in the scan (axial) direction was accomplished with a chain-drive arm aligned with the axis of the specimen. The weld centerline was used as the origin for the scan axis, and a reference stamp on the OD of the specimen was used as the index direction origin. Data were collected on a 0.5 mm (0.020 in.) interval in the scan and index directions.

A UniWest pencil probe (model# US-3228, serial # 62106) and Zetec Spot Probe (model # Z0000857-1, serial # 455562) were used to acquire data (see Figures 7-29 and 7-30). The pencil probe is similar to the spot probe, but its smaller diameter is better suited for ID examinations of components with counterbore transitions (Diaz et al. 2007). The pencil probe had a diameter of 4.75 mm (0.187 in.) and was operated between 100 and 500 kHz. The spot probe had a coil diameter of 3.05 mm (0.12 in.), a case diameter of 12.7 mm (0.50 in.) and was operated between 100 and 500 kHz. Both probes had cross-wound coils that were used in a differential approach to reduce artifacts caused by surface roughness; thus, systematic signal artifacts were greatly reduced. In this study, examinations were conducted with the probes in a plus-point configuration (0° rotation) and a cross-point configuration (45° rotation) for improved detection sensitivity of off-axis defects.

Polytetrafluoroethylene (or PTFE) tape with a thickness of 0.094 mm (0.0037 in.) was placed over the scan region of each flaw for the pencil probe examinations, as shown in Figure 7-31. The tape provided a consistent liftoff (offset from the specimen surface) and also protected the wear-face of the probe. The spot probe was placed in a machined Delrin fixture, shown in Figure 7-32, such that the probe face was 0.13 mm (0.005 in.) from the examination surface. This configuration provided a consistent liftoff throughout the examination and protected the probe wear-face.

A calibration reference standard featuring notches within weld material was not available, so a flat reference standard made of 304 stainless steel was used. This standard had four notches with depths ranging from 0.25 to 1.02 mm (0.010 to 0.040 in.) and openings of 0.13 mm (0.005 in.). A 1.6 mm (0.063 in.) long notch with a depth of 0.4 mm (0.016 in.) met the ASME Code Section XI requirements for a “qualification” notch; it was used as a detection (or sensitivity) notch for this activity. A 25.4 mm (1.00 in.) long notch with a depth of 1.0 mm (0.040 in.) was used as a reference notch.



**Figure 7-29 UniWest US-3228 Pencil Probe**

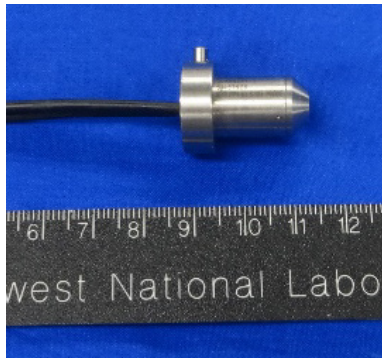


**Figure 7-30 Zetec Spot Probe**



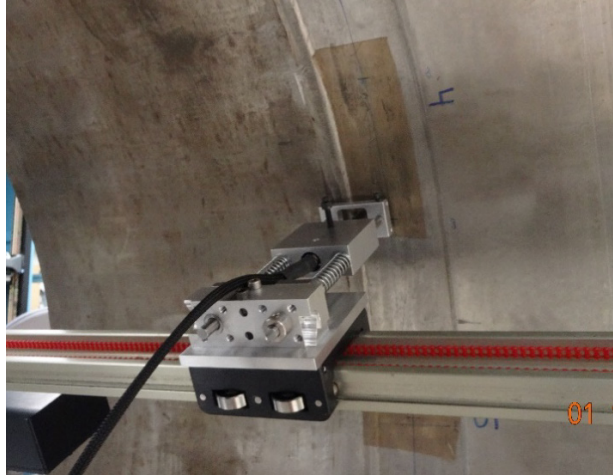


**Figure 7-31 Data Acquisition Using the US-3228 Probe**



**Figure 7-32 Data Acquisition Using the Zetec Spot Probe**

## **7.3.2 Eddy Current Testing Results**

### **7.3.2.1 Reference Standard and Length Sizing Technique**

Figure 7-33 shows an example of reference standard calibration data. A threshold equal to the maximum amplitude response of the detection notch in the reference standard (far right in the figure) was used for length sizing. Once the threshold was set, pixels with amplitude at or above the threshold were colored pink, as shown with the reference notch bounded by the red and white horizontal lines in Figure 7-33. Length sizing cursors were placed one pixel (0.020 in.) over from the threshold amplitude response. In addition, it was confirmed that the amplitude response from the detection notch was greater than twice the background noise of the weld response from the

DMW specimen, in accordance with requirements of ASME Code Section XI Mandatory Appendix IV Supplement 2 Acceptance Criteria.

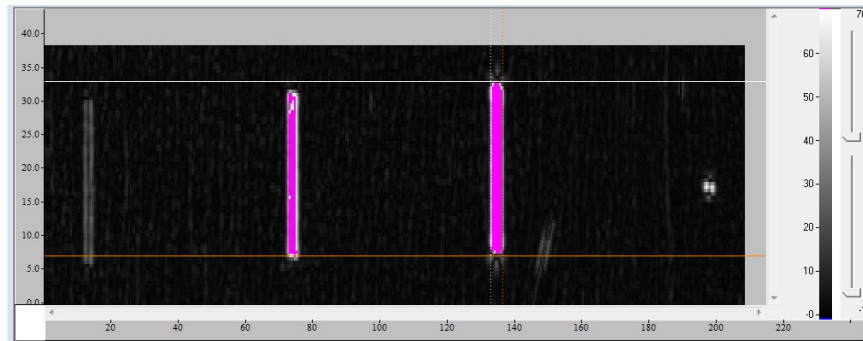


**Figure 7-33 UniWest US-3228 Plus-Point 400kHz Calibration Data. Pink pixels are at or above the maximum amplitude of the detection notch, seen at the far right.**

The reference notch length was independently measured using a precision optical technique and determined to be 25.20 mm (0.992 in.) long. Both ET probes at 400 kHz measured the reference notch as 25.9 mm (1.02 in.) and 26.4 mm (1.04 in.) in plus- and cross-point configurations, respectively.

#### 7.3.2.2 Flaws

Figures 7-34 and 7-35 show the results for Flaws 1 and 2 and are representative of the ET images for all the flaws. The horizontal axes correspond to the axial direction of the specimen and the vertical axes correspond to the circumferential direction. The plus-point configuration consistently resulted in higher amplitude responses compared to the cross-point configuration. In general, noise tended to be higher on the CASS side of the weld. The compiled sizing and location information are shown in Figure 7-36, which also include FlawTech-reported true-state information for comparison. The UniWest probe was able to detect all five flaws in the DMW specimen using both plus- and cross-point configurations. The spot probe detected all of the flaws in both configurations except Flaw 4, which was located too close to the taper of the counterbore for the probe to access it.

Overall, the ET-measured lengths and locations of all five implanted flaws agreed well with the provided FlawTech true-state information. The greatest discrepancies were in the circumferential positions of Flaws 2 and 4, where the actual circumferential positions differed from the reported true-state positions by about 7 mm (0.28 in.). Note, however, this corresponds to only  $\sim 1^\circ$  angular (circumferential) difference from the true state.

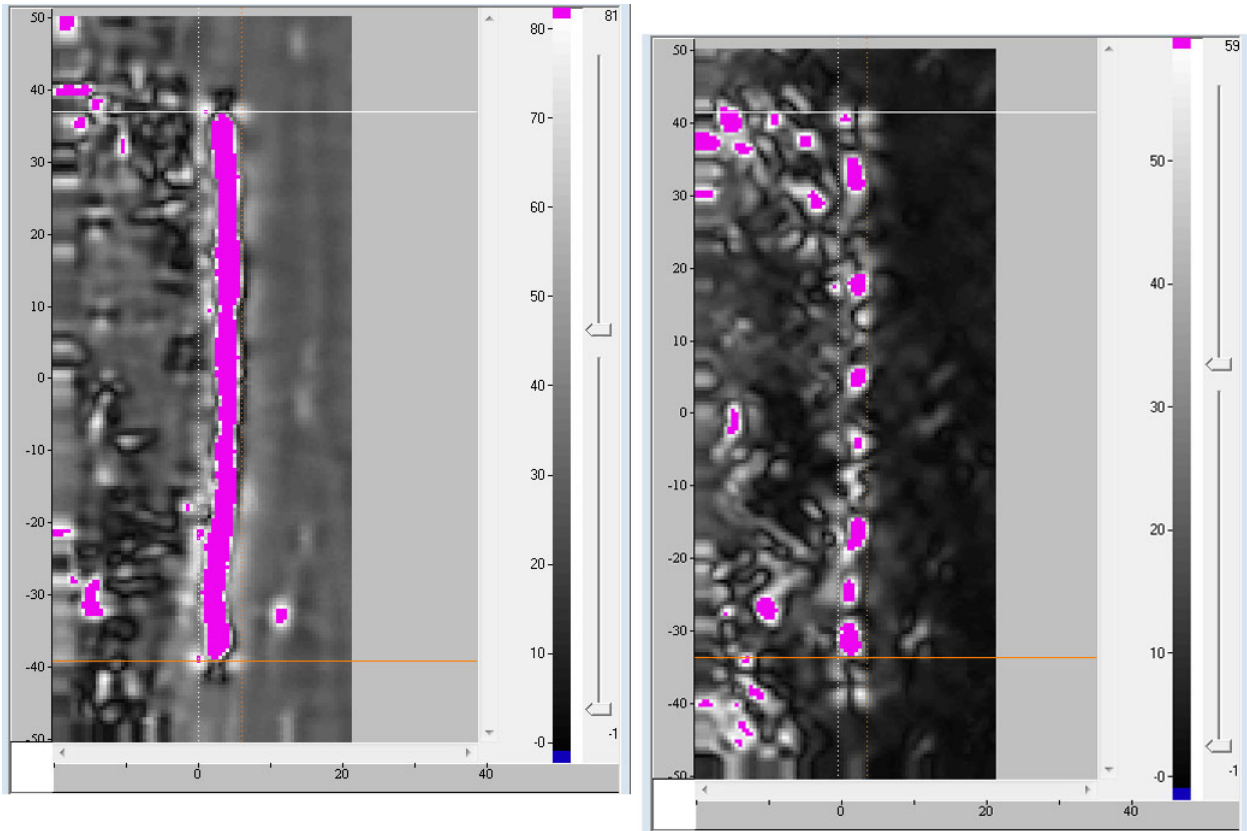


**Figure 7-34 Flaw 1 Results Acquired with the Zetec Spot Probe in Plus-point (*left*) and Cross-point Configurations (*right*)**

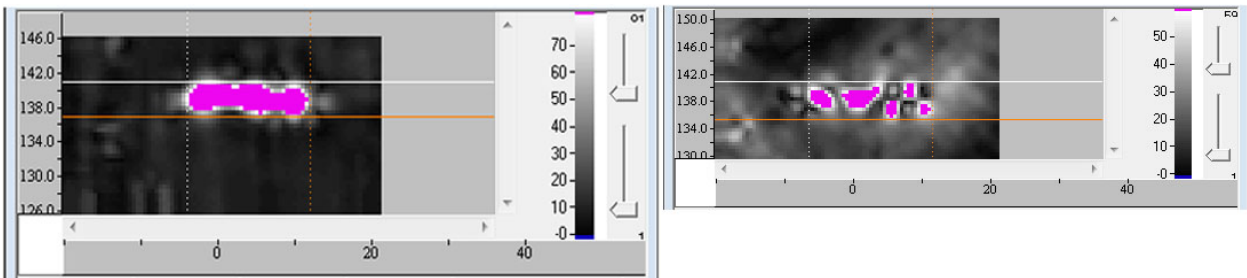


**Figure 7-35 Flaw 2 Results Acquired with the Zetec Spot Probe in Plus-point (*left*) and Cross-point Configurations (*right*)**

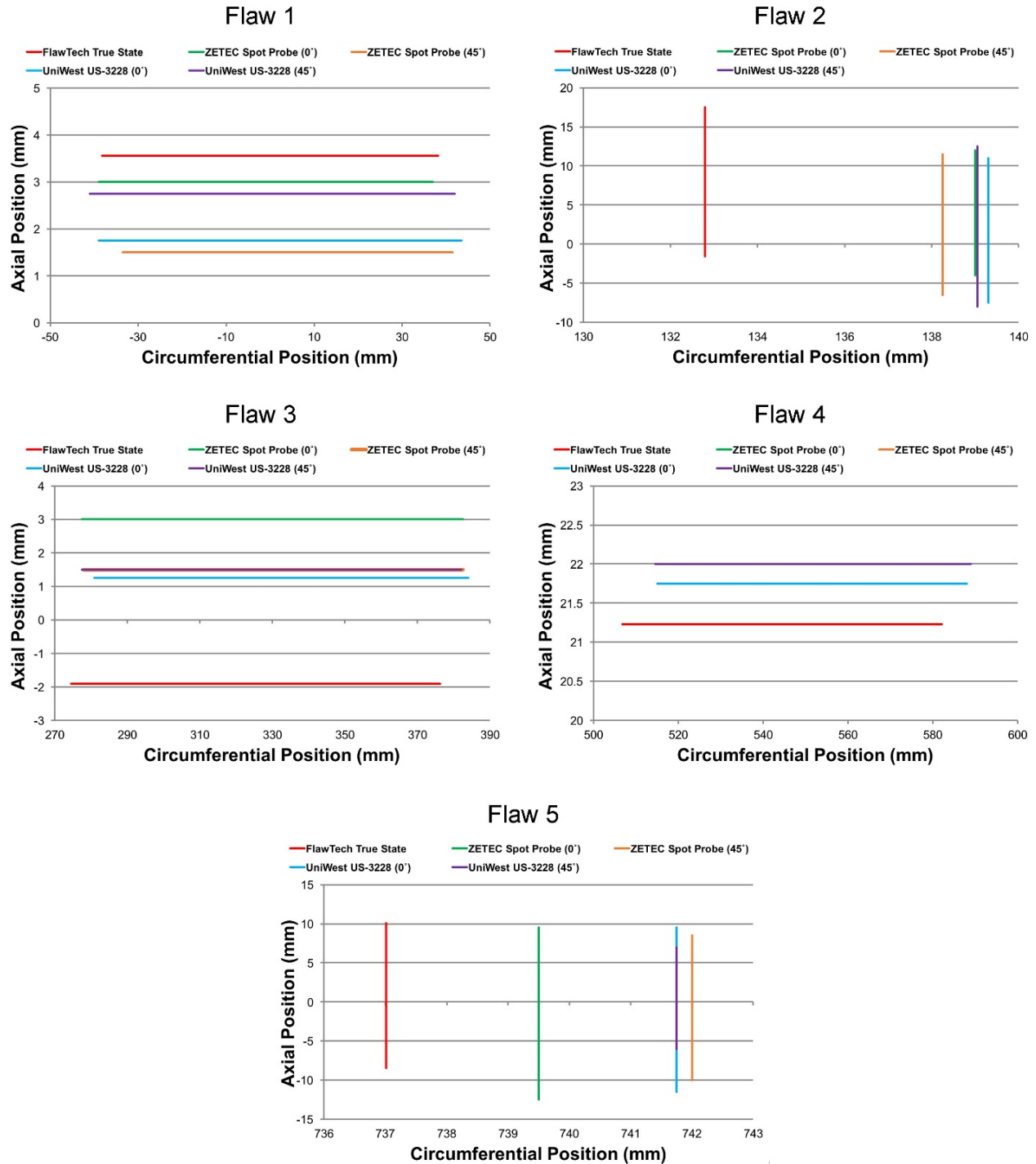


**Figure 7-36 Comparison of FlawTech-reported True-state and ET-measured Flaw Lengths and Positions. Results for both probes in plus-point configuration (0° rotation) and cross-point configuration (45° rotation) are shown.**

### **7.3.3 Eddy current testing conclusions**

Both probes performed well at detecting and sizing the five flaws in the mockup. The only exception was that the Zetec Spot probe was unable to collect data over Flaw 4 due to flaw placement and ID geometry. Flaw 4 is located near the counterbore and this taper on the ID precluded the Zetec Spot probe from collecting data in this region while keeping compliance with the ID surface. The smaller diameter of the UniWest pencil probe made it better suited accessing this region.

The measured length and locations of all five implanted flaws in the DMW specimen correlated well with the provided true-state information. The largest discrepancy of length sizing was observed to be 6.6 mm (0.26 in.) on Flaw 1 where the true-state information stated 76.5 mm (3.0 in.) and the measured length using the UniWest probe was 83 mm (3.3 in.). The greatest circumferential position discrepancy was 7.3 mm (0.3 in.), which occurred on Flaw 4 using the pencil probe. This small discrepancy is approximately 1° different from the FlawTech-reported true state.

Overall, ET results show that surface-breaking cracks can be readily detected and length-sized in a carbon steel-to-CASS DMW. If the inner surface is accessible, then ET may be a reliable and effective method for crack detection. This supports the conclusions of previous work at PNNL using ET for crack detection in cast stainless steel piping components (Diaz et al. 2007).

### **7.4 UT Hardware, Setup, and Data Acquisition**

UT data were acquired from the CASS side of the weld with 500 and 800 kHz PA TRL probes and two 500 kHz Applus+ RTD TRL probes with fixed refracted angles of 30° and 45°. The RTD probes were designed especially for this study in order to optimize the chances for success in CASS for the single angle, L-wave, LF, dual/TRL approach and then compare this to the performance of our LF-PA-UT techniques. The RTD probes were designed to have large apertures, comparable to those of the LF-PA-UT probes. Note that, because the RTD probes had a TRL design and operated at a frequency below 1 MHz, they are not considered “conventional” UT probes. Data from the carbon steel side were acquired with higher frequency PA TRL probes operating at 1.5 and 2.0 MHz. All probes operated in a side-by-side pitch-catch mode. The probes are shown in Figures 7-2 through 7-5 and Figure 7-37. Table 7-14 provides the number of elements, element sizes, and bandwidths of the PA probes.

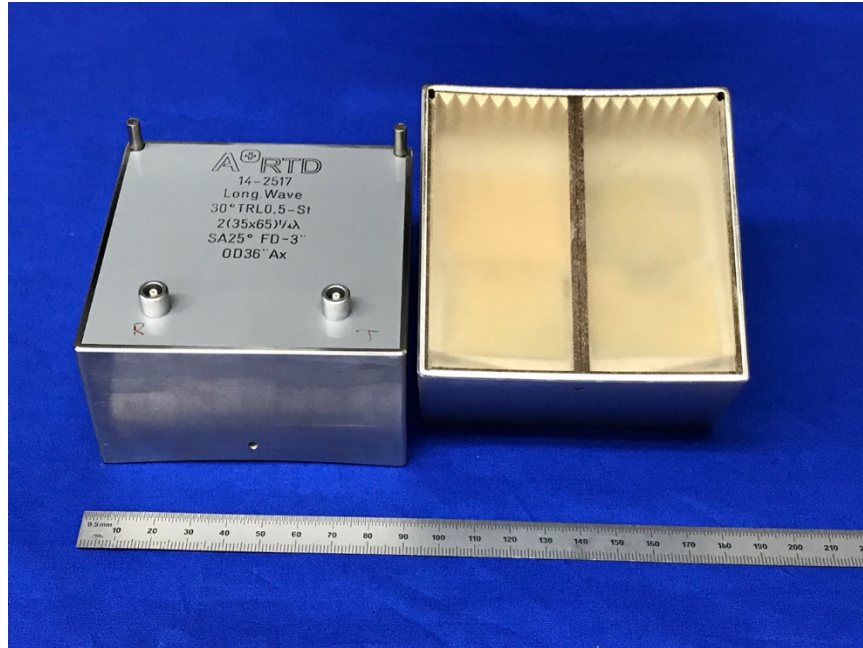


**Figure 7-37 500 kHz RTD Probes. 30° probe (*left*) and 45° probe (*right*), inverted. The bottom of the 45° probe shows the cork damping medium between the elements and provides an example of wedge contouring required for adequate coupling of probes of this size.**

**Table 7-14 Phased Array Probe Specifications (includes 2 MHz probe)**

Frequency, kHz	Number of Elements	Element Size, mm (in.)		Aperture Size, mm (in.)		Bandwidth at -6 dB
	Primary × Secondary	Primary	Secondary	Primary	Secondary	
500	10×5	5.5 (0.22)	6.0 (0.24)	64.0 (2.52)	34.0 (1.34)	>45%
800	10×5	3.6 (0.14)	3.6 (0.14)	43.2 (1.70)	21.2 (0.84)	>50%
1500	10×3	3.3 (0.13)	5.6 (0.22)	35.0 (1.38)	17.5 (0.69)	>60%
2000	10×5	2.0 (0.08)	2.0 (0.08)	21.8 (0.86)	10.8 (0.43)	>60%

The two RTD probes have element sizes of 65 × 35 mm (2.56 × 1.38 in.) and a footprint of 90 × 90 mm (3.54 × 3.54 in.). Both probes were designed for an effective focal depth of 76.2 mm (3.0 in.). Their wedges were contoured for axial scanning of 914.4 mm (36.0 in.) OD pipes. The probes have -6 dB bandwidths of nominally 56%, which is typical for UT probes. Additional RTD probe parameters are shown in Table 7-15.

**Table 7-15 RTD Probe Specifications**

Angle in Material, degrees	30	45
Wedge Angle, degrees	12.03	17.15
Roof Angle, degrees	5.15	3.97
Squint Angle, degrees	25	13
Focal Depth, mm (in.)	76.2 (3.0)	76.2 (3.0)
-6 dB Bandwidth	56%	56%

Beam modeling produced an approximate idea of how spot sizes of the RTD probes compare to the spot size of the 500 kHz PA probe. PNNL modeled the PA probe using UltraVision and the RTD probes were modeled in CIVA by the manufacturer and the results were provided to PNNL. The PA probe was modeled at 30° and 45° for both TD focusing (at the distance necessary to focus at the ID surface of a specimen thickness of 84 mm [3.3 in.]) and HP focusing (at a fixed distance of 110 mm [4.3 in.]); see Figure 7-7. The RTD probes were modeled at a depth of 76 mm (2.9 in.) at their fixed angle. Results show that the effective spot size of the RTD probes is approximately twice as large as that of the 500 kHz PA probe; see Table 7-16.

**Table 7-16 Spot Sizes of the 500 kHz PA and RTD Probes**

Probe	Angle, degrees	Focus/Depth, mm (in.)	-6 dB Spot, mm	-6 dB Spot, in.
500 PA	30	TD84/84 (3.3)	19.5×29.5	0.77×1.16
500 PA	30	HP110/84 (3.3)	19.5×29.4	0.77×1.16
30 RTD	30	75 (2.95)	52.0×43.2	2.05×1.70
500 PA	45	TD84/84 (3.3)	29.4×33.5	1.16×1.32
500 PA	45	HP110/84 (3.3)	29.4×33.5	1.16×1.32
45 RTD	45	75 (2.95)	54.1×50.3	2.13×1.98

The PA probes were mounted side by side on Rexolite wedges that were contoured to match the specimen outer surface. Wedge properties are shown in Table 7-17. Wedges oriented axially were for scanning circumferential flaws and vice versa. Wedges had a 0° roof angle, except those for the 1.5 MHz probe had a 4.3° roof angle. This was to aid in beam steering, as the 1.5 MHz probe had only three elements along the secondary axis (the other PA probes had five secondary axis elements). All wedges, including the RTD probe wedges, had a cork layer between the transmit and receive housings for effective signal isolation.



**Table 7-17 Wedge Specifications. Axial wedges are used to detect circumferentially oriented flaws and vice versa.**

Frequency, kHz	Orientation	Angle, degrees	Dimensions (L×W), mm (in.)
500	Axial	16.5	89×102 (3.50×4.02)
500	Circumferential	15	88×102 (3.46×4.02)
800	Axial	17.5	63×63 (2.48×2.48)
800	Circumferential	15	65×63 (2.56×2.48)
1500	Axial	15	53×50 (2.09×1.97)
1500	Circumferential	15	53×50 (2.09×1.97)
2000	Axial	16.5	37×47 (1.46×1.85)
2000	Circumferential	15	37×48 (1.46×1.89)

#### 7.4.1 Data Acquisition

Ultrasonic data were acquired in two phases. During Phase 1, the specimen was oriented vertically; see Figure 7-38. During Phase 2, the specimen was oriented horizontally; see Figure 7-39. The vertical orientation was initially used as a matter of safety and convenience as it allowed the specimen to sit stably on its carbon steel end while providing access to the entire weld and CASS corner circumference. Typically, PA probes are held in a frame containing water ports for coupling to the specimen. However, with this mockup orientation the water ports often did not provide sufficient coupling because the large footprint of the probes and the slightly uneven surface of the mockup sometimes resulted in gaps between the probe and mockup. Thus, additional water was pumped above the PA probe to cascade down the specimen. Even so, vigilance was required to assure that water filled the gap between the wedge and the specimen at the weld position, which at times was several millimeters. Furthermore, the repeated vertical motion of the relatively heavy 500 and 800 kHz probes caused stress to the mechanical motor arm (scanner) and occasionally resulted in slipping of the motor arm drive belt. These problems motivated the move to the horizontal orientation in Phase 2 for which a stable support mechanism was designed and assembled to safely hold the specimen horizontally.





**Figure 7-38 Corner Scan on the Vertically Oriented Specimen. This scan is being done with the 800 kHz PA probe.**

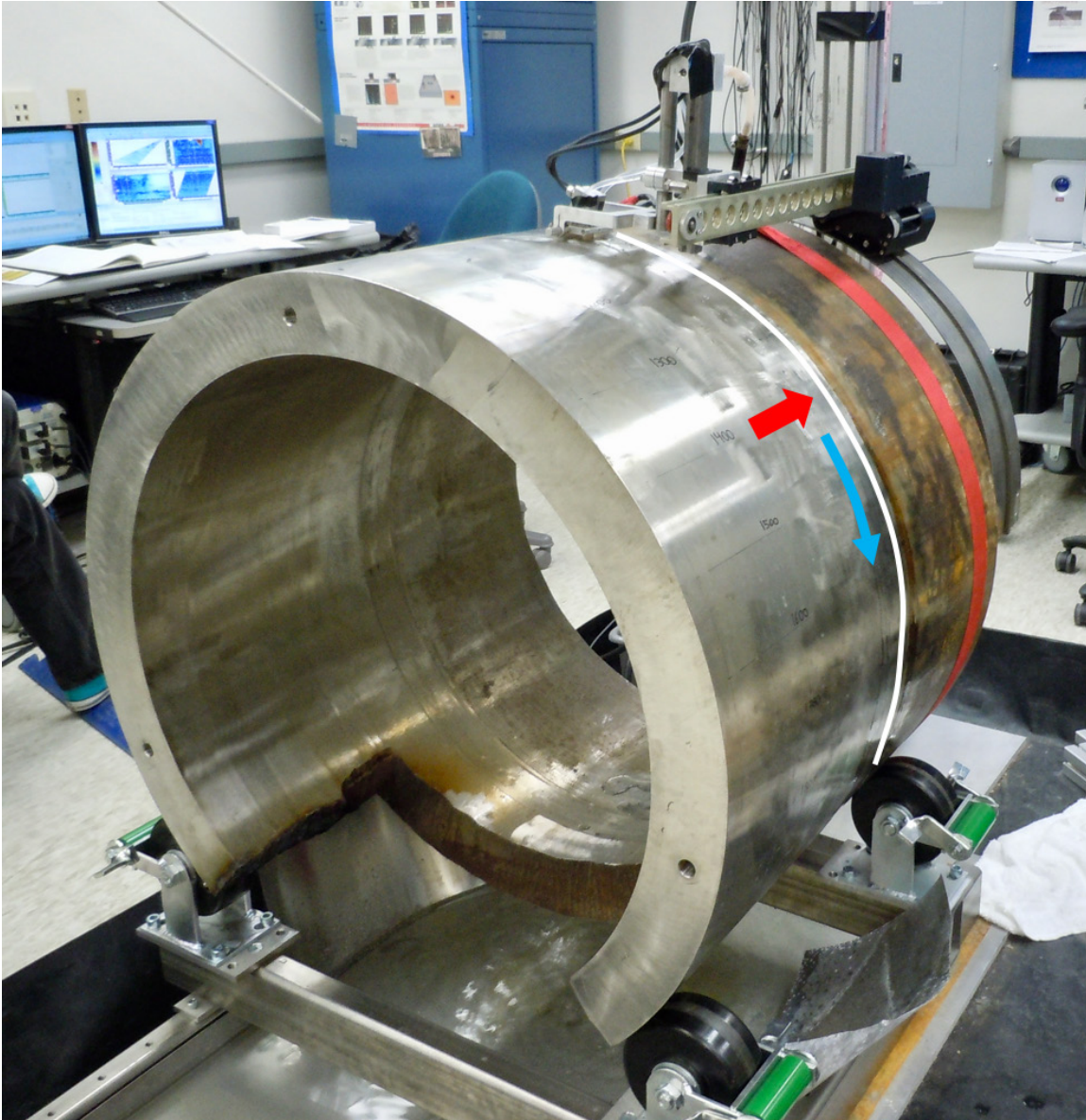


**Figure 7-39 Scanning the Horizontally Oriented Mockup. The red arrow is the positive axial direction, and the blue arrow is the positive circumferential direction. The weld centerline (WCL) is indicated by the white line.**

The resulting improved coupling was at the expense of having to rotate the specimen to access different flaw emplacements. Note that many large-bore CASS-to-piping DMWs in the field are oriented horizontally, as illustrated in Figure 2-1. All scans from Phase 1 were closely examined for quality issues, such as poor coupling. Phase 2 included scans that had not been completed in Phase 1. Also, scans that were found to have coupling issues during acquisition in Phase 1 were repeated in Phase 2. Table 7-18 shows the scans that were completed with each probe and the corresponding specimen orientation.

**Table 7-18 Scan Matrix. This table shows the completed scans for each probe and the mockup orientation.**

Scan Type	Probe Orientation	0.5 MHz PA	0.8 MHz PA	1.5 MHz PA	2.0 MHz PA	0.5 MHz RTD-30	0.5 MHz RTD-45
RASTER							
CASS Corner	Axial	V	V	–	–	V	V
Flaw 1	Axial	V	V	H	V	V	V
Flaw 2, Skew 0	Circumferential	H	H	H	H	–	–
Flaw 2, Skew 180	Circumferential	H	H	H	H	–	–
Flaw 3	Axial	V	V	H	V	V	V
Flaw 4	Axial	V	V	H	V	V	V
Flaw 5, Skew 0	Circumferential	H	H	H	H	–	–
Flaw 5, Skew 180	Circumferential	H	H	H	H	–	–
Blank (no flaws)	Axial	V	V	H	V	V	V
Blank, Skew 0	Circumferential	H	V	V	H	–	–
Blank, Skew 180	Circumferential	H	V	V	H	–	–
LINE							
Flaw 1	Axial	H	H	H	H	–	–
Flaw 3	Axial	H	H	H	H	–	–
Flaw 4	Axial	H	H	H	H	–	–
Blank	Axial	H	H	H	H	–	–
H = Horizontal specimen V = Vertical specimen – = not scanned All 0.5 and 0.8 MHz axial raster scans (including RTD): skew 0 All 1.5 and 2.0 MHz axial raster scans: skew 180 All 0.5 and 0.8 MHz line scans: skew 90 All 1.5 and 2.0 MHz line scans: skew 270							

The circumferential flaws were scanned from the CASS side with the 500 and 800 kHz probes (four total – RTD and PA) and from the carbon steel side with the 1.5 MHz and 2.0 MHz probes (two total). The axial flaws were scanned from both directions with the PA probes only. The contour of the integral wedge in the RTD probe housing did not allow scanning of the axial flaws. Acquired data also included no-flaw regions for baseline material and noise characterization.

An ATCO scanner was interfaced to a Zetec DYNARAY controller via a Zetec motor control drive unit MCDU-02 (see Figure 7-6). These are off-the-shelf devices and are commercially available. All data acquisition parameters were accessed through UltraVision 3.6R5. Probes were driven by a 200 V square pulse of width equal to one-half the wave period. For example, the 800 kHz probe was driven with a pulse width of 625 ns.

#### 7.4.1.1 UT Setup

The mockup origin was defined as the weld centerline (0 axial position) and a 0 circumferential position that was stamped on the specimen OD. Circumferential markings at successive 100 mm (3.9 in.) increments were made to assist in locating the probe relative to the origin. A scanner track ring was centered with respect to the mockup. PA probes were held in a frame containing water ports for coupling to the specimen.

The mean longitudinal velocity in the CASS material was measured to be  $5640 \pm 120$  m/s or  $5.64 \pm 0.12$  mm/ $\mu$ sec ( $0.222 \pm 0.004$  in./ $\mu$ sec). This was measured on the corner response using the 500 kHz 45° RTD probe at 11 locations around the specimen. This velocity was entered into the specimen settings of the UltraVision software and was subsequently used in the conversion of ultrasonic signals from the time domain ( $\mu$ sec) to mockup space (i.e., units of length). A typical book value for longitudinal velocity in stainless steel is 5770 m/s (0.227 in./ $\mu$ sec). However, in CASS, material velocities routinely vary from position to position and with refracted angle due to heterogeneities in grain microstructure. Indeed, the measurements made on this specimen varied by as much as about 7%, ranging from 5466 to 5829 m/s (0.215 to 0.229 in./ $\mu$ s).

A corner response was used to set the nominal receiver gain, or hard gain. Receiver gain was initially set to bring the specimen peak corner response at ~80% of full screen height with 6 dB added to account for typically weaker flaw responses. In practice, hard gain was adjusted as needed to accommodate the flaw response, i.e., gain was reduced and scans were repeated if a flaw response saturated the receiver. Soft gain was added as needed during analysis to enhance visualization.

#### 7.4.1.2 UT Scan Protocol

The coordinate system used for data collection is depicted in Figure 7-39. By convention, the direction of the ultrasonic beam during a raster scan defines a probe skew of 0° when the probe is facing the positive direction. The weld center line (white line) was the axial zero position, and the positive axial direction was chosen as pointing toward the weld center line (red arrow). Note that this gives line scans of the weld from the CASS side a probe skew of 90°, as the scan direction is perpendicular to the positive axial direction. The blue arrow represents the positive circumferential direction for all scans, i.e., all skews.

Line and raster scans were performed on the weld region. Line scans were acquired of the entire flaw-containing region (approximately -70 to 950 mm [-2 to 37 in.] in circumferential range) and were used initially for circumferential flaw detection and noise measurements. Raster scans were acquired of each flaw individually and were intended for measuring flaw parameters, such as SNR, length, and through-wall depth. Additionally, the following data were acquired: raster scans of the corner response from the CASS edge to evaluate signal consistency and drop out (i.e., loss of signal), and line and raster scans in a non-flawed weld region for determination of baseline noise and signal. Refer to Table 7-18 to see the probes used for the various scans.

For raster scans, the index increment (or index resolution) was 1.0 mm (0.04 in.) and the scan axis resolution was 0.5 mm (0.02 in.). The scan range was typically 130–200 mm (5.1–7.9 in.), and the index range was typically 100–275 mm (3.9–10.8 in.), depending on the length of the flaw. The index range was set to exceed the overall flaw length by as much as one to two times on each side of the flaw to assure an adequate proximal range for noise measurements, and the scan range was set to be large enough to assure that the flaw signal was not truncated at any

refraction angle. For line scans, the index increment was 10 mm (0.4 in.), and the scan resolution was 0.5 mm (0.02 in.). Similar measures were taken to avoid flaw signal truncation, with a typical index range of 70 mm (2.8 in.) used.

PA-UT raster data were acquired with both TD and HP focusing. TD focuses the beam at a constant depth for all refraction angles (Figure 7-7 *left*), while HP focuses the beam at a constant distance from the probe for all refraction angles (Figure 7-7 *right*). The hypothesis was that TD focusing would be better suited for flaw corner response detection at the ID surface and HP focusing would result in better specular and tip detection. To assure full volumetric coverage of the region containing the flaws, the TD focal depth was set to match the specimen thickness (T) of 84 mm (3.3 in.) for all refraction angles, or TD84, and the HP focus was set to  $T/\cos(40^\circ) = 110$  mm (4.3 in.) for all refraction angles, or HP110, as the nominal peak response occurs at  $\sim 40^\circ$ . The TD84 focal distance therefore ranged from 89–130 mm (3.5–5.1 in.), while the HP focal distance was fixed at 110 mm (4.3 in.). For scans of the circumferential flaws, TD84 data were acquired over a 20–50° refracted angle range and HP110 data were acquired over a 30–51° range, both with 3° increments. These parameters allowed for sufficiently high-resolution scans without unduly large data files that are time-consuming to analyze. Line scans used the same sweep of angles but with 1° resolution (the coarser index increment of line scans allowed for a finer refracted angle increment). Note that it would be ideal to increase spatial resolution and capture all angles, but the result would be increased scan times and unwieldy file sizes. For this work, file sizes were held to below 10 GB each.

For scans of the axial flaws, the curvature of the pipe increased the angle at which the sound beam interacted with the ID surface, or the impingement angle; an illustration of this is shown in Figure 7-40. Note that the impingement angle, like the refraction angle, is measured from the surface normal.

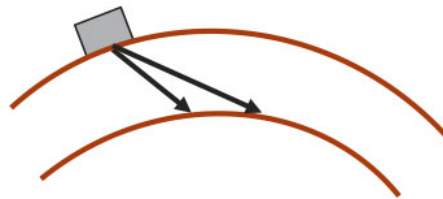


**Figure 7-40 Illustration of How Circumferential Scanning Affects Impingement Angle.** Circumferential scanning results in a higher impingement angle due to the curvature of the pipe. At higher refraction angles, a beam that might otherwise interact with the ID surface might miss the surface altogether if pipe curvature is not accounted for in the focal laws.

The result is that the impingement angle increases with increasing refraction angle by the following equation:

$$\sin \alpha_I = \left( \frac{OD}{ID} \right) \sin \alpha_R$$

where  $\alpha_R$  is the refracted angle,  $\alpha_I$  is the impingement angle, and OD and ID are the outer and inner diameters, respectively. Figure 7-41 shows the result of this equation. There are two important considerations in this situation: (1) eventually, the impingement angle will reach 90°, at which point the sound would fail to interact with the ID surface altogether; and (2) to maintain a TD



focus, as depicted in Figure 7-42, the path length of the beam for higher refraction angles must increase compared to that for a non-curved ID surface, resulting in more scatter and reduced ability to focus the beam. Therefore, it is important to carefully consider the focal laws when scanning for axial flaws. To account for pipe curvature, the minimum HP110 angle was reduced to 20° (with the same focal distance), and the TD84 focal distance increased to a range of 91–165 mm (3.6–6.5 in.). All probe and angle parameters were verified using beam modeling in UltraVision prior to data collection. Note that UltraVision does not automatically correct focal laws to account for pipe curvature.

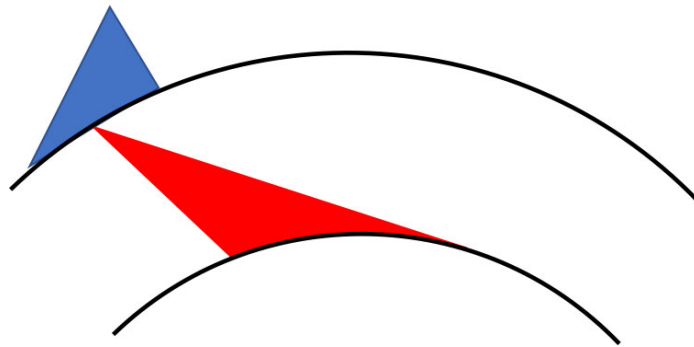


**Figure 7-41 True-depth Focusing during Circumferential Scanning of Axial Flaws. The curvature of the pipe forces the focal distance and angle of impingement to increase at higher angles.**

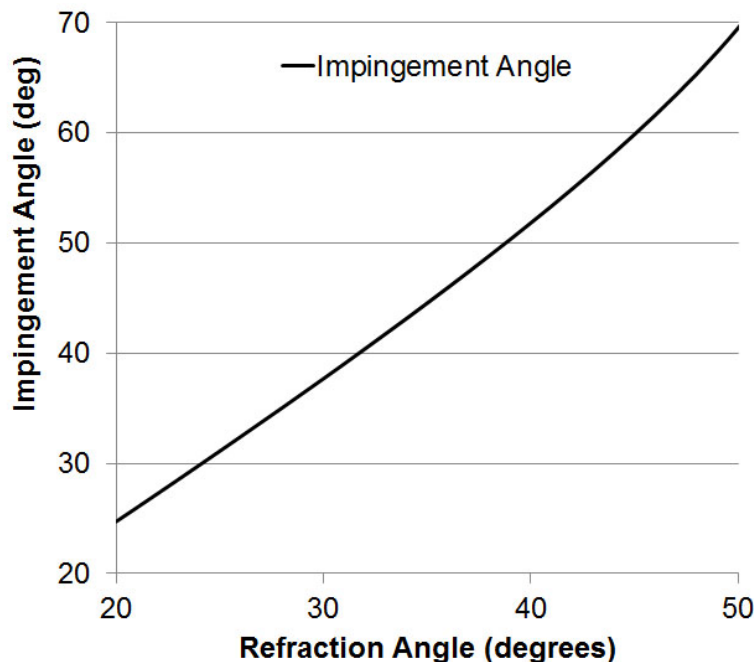


**Figure 7-42 Impingement Angle versus Refraction Angle**

In addition to TD and HP focusing, the beam was skewed in the passive direction in three increments: -10°, 0°, and +10° (note that a 0° beam skew is the primary beam direction). This covered a relatively large 20° sweep of angles, which was well within the steering capability of the PA probes, while maintaining manageable file sizes. Principal flaw detection and sizing was done

with 0° skew data while  $\pm 10^\circ$  skew data were considered supplemental. The experimental setup files for data acquisition were therefore created with four data channels: (1) TD84 with 0° beam skew; (2) HP110 with 0° beam skew; (3) TD84 with  $\pm 10^\circ$  beam skew; and (4) HP110 with  $\pm 10^\circ$  beam skew.

## **7.5 Data Analysis and Results**

### **7.5.1 UT Line Scans**

According to PNNL CASS examination protocol, line scan data were acquired as a screening tool for flaw detection of the circumferentially oriented flaws. This is because line scans can be acquired rapidly and can be used to determine areas of the specimen where more time-consuming raster scans should be acquired for flaw characterization. For the scans reported herein, line scans were typically  $\leq 10\%$  of the duration for raster scans over a larger section of the specimen. For line scans, the probe was oriented toward the weld centerline as in a raster scan, but the scan direction was circumferential, and the index direction was axial.

For analysis, all lines and angles were merged together for a single, overall view and then angles in individual lines were merged for discrete views of each line. Spatial interpolation (implemented using UltraVision 3.8R7) was used during merging to aid in visualization. Examples of merged line scans are shown in Figure 7-43 with the locations of flaws indicated. It should be noted that PNNL did not acquire or analyze the data in this Chapter in a blind fashion; true-state was known prior to the initiation of scanning. This scan, performed from the CASS side of the horizontal specimen at 500 kHz using HP focusing, covered the circumferential region encompassing Flaws 1, 2, and 3. The top image shows the full merge (all angles and all lines) and the middle image shows a single line merge (all angles, one line) of line -40 (i.e., the front of the wedge was 40 mm [1.6 in.] from the weld centerline on the CASS side). Note that the circumferential flaws are visible in the full merge (indicated by red arrows), but they are more readily isolated from the counterbore signals in the single-line merge. Note that Flaw 2 was axially oriented and therefore was not detected in these scans. The bottom image of Figure 7-43 shows the full merge of the line scan that encompassed Flaws 4 and 5. The red arrow indicates Flaw 4. Note that other signals, likely originating from the counterbore, were detected at the same axial position (such signals were also observed in the top image). However, Flaw 4 presented with higher signal intensity and was more discrete than the counterbore signal. Note that Flaw 5 was not visible because it was axially oriented. Figure 7-44 shows a similar view from the carbon steel side at 1.5 MHz, also using half-path focusing. Flaws 1 and 3 are indicated by red arrows and the tip of Flaw 3 is clearly visible as indicated by the blue arrows.

Although the line scans were not intended for flaw characterization, a few measurements were made to gain insight into expected accuracy. These results are shown in Table 7-19. Overall, the RMSE of both length and depth (when tip diffracted responses were evident) were within the ASME Code performance demonstration sizing acceptance criteria for wrought austenitic piping welds (Section XI, Appendix VIII, Supplement 2(3.2)(a) and (3.2)(b)) and DMWs (Section XI, Appendix VIII, Supplement 10(3.2)(d) and (3.3)(c)) of 19.05 mm and 3.81 mm (0.75 in. and 0.15 in.), respectively. Note that such criteria are not yet established for CASS materials, so these criteria are shown as surrogates.



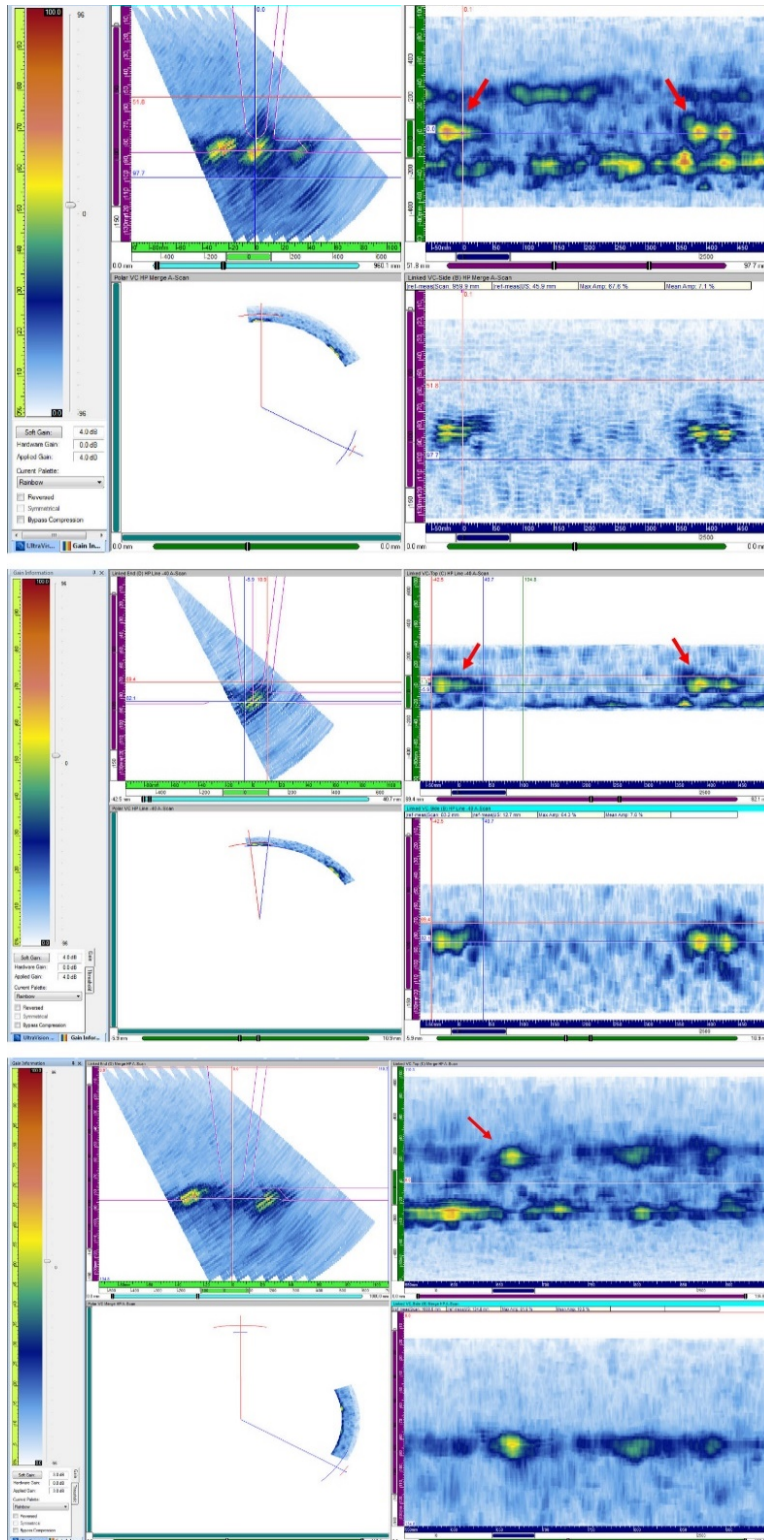


**Figure 7-43** Line Scan with the 500 kHz PA Probe. Multi-line merge with all lines and all angles (*top*) and single-line merge with all angles from one line (*middle*) of Flaws 1 and 3 (red arrows). Multi-line merge of Flaw 4 (red arrow) (*bottom*). Flaws 2 and 5 were axially oriented and not visible in these scans.

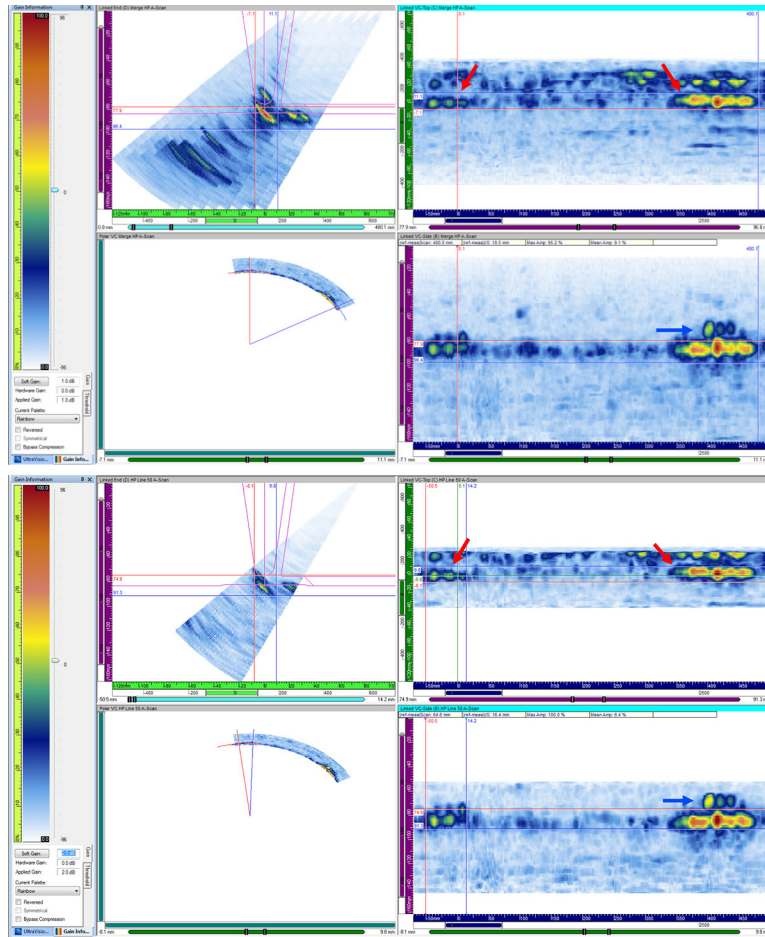


**Figure 7-44** Line Scan with the 1.5 MHz PA Probe. Multi-line merge with all lines and all angles (*left*) and single-line merge with all angles from one line (*right*). This scan covers the region containing Flaws 1 and 3 (red arrows). Flaw 2 is axially oriented and was not visible in this scan. The tip of Flaw 3 is indicated by the blue arrows. The tip of Flaw 1 was visible but not well resolved.

**Table 7-19 Flaw Characteristics as Measured from the Line Scans.** The table shows the measured length, depth, and SNR of the three circumferential flaws with all four PA probes in comparison to the FlawTech-reported lengths and depths. The length RMSE value is given. There was insufficient data for a depth RMSE value.

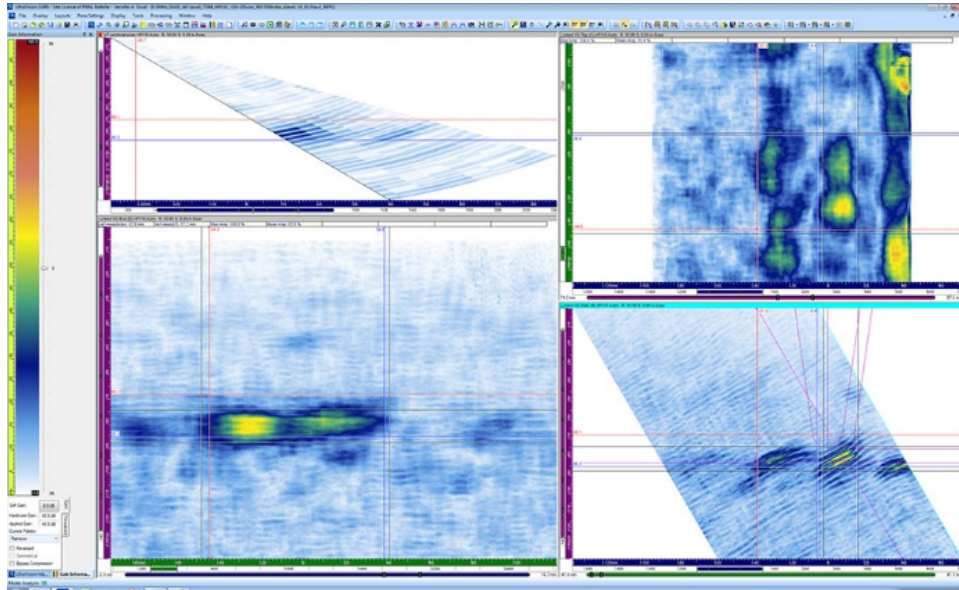
Flaw	Frequency, kHz	Focus	Measured			Measured			Difference, mm (in.)	SNR P-P	SNR P-M
			True Length, mm (in.)	Length, mm (in.)	Difference, mm (in.)	True Depth, mm (in.)	Depth, mm (in.)				
1	500	TD	76.45 (3.01)	83.7 (3.30)	7.25 (0.29)	8.51 (0.34)	nd	nd	7.82	14.54	
1	500	HP	76.45 (3.01)	83.2 (3.28)	6.75 (0.27)	8.51 (0.34)	nd	nd	7.07	14.15	
3	500	TD	101.73 (4.01)	82.6 (3.25)	-19.13 (-0.75)	16.51 (0.65)	20.2 (0.80)	3.69 (0.15)	7.85	14.28	
3	500	HP	101.73 (4.01)	84.2 (3.31)	-17.53 (-0.69)	16.51 (0.65)	20.6 (0.81)	4.09 (0.16)	8.1	14.95	
4	500	TD	75.31 (2.96)	41.1 (1.62)	-34.21 (-1.35)	13.26 (0.52)	nd	nd	1.71	10.43	
4	500	HP	75.31 (2.96)	55.1 (2.17)	-20.21 (-0.80)	13.26 (0.52)	nd	nd	1.77	10.32	
4	800	TD	75.31 (2.96)	51.6 (2.03)	-23.71 (-0.93)	13.26 (0.52)	nd	nd	0.5	9.89	
4	800	HP	75.31 (2.96)	59.1 (2.33)	-16.21 (-0.64)	13.26 (0.52)	nd	nd	0.11	9.36	
RMSE: 13.67											
nd = no tip response											
P-M = peak to mean											
P-P = peak to peak											

#### 7.5.1.1 UT Raster Scans

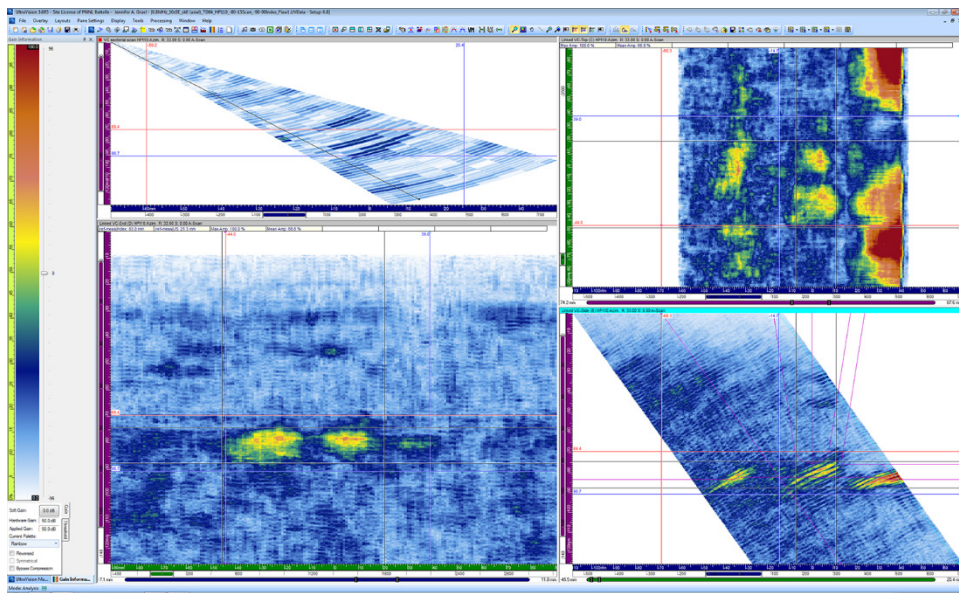
Raster scans were used as a characterization tool. As described above, all flaws were raster scanned from the CASS side of the weld with the 500 and 800 kHz probes (including the RTD probes) and from the CS side with the 1.5 and 2.0 MHz PA probes. No data merging was done with raster scan data. The analysts inspected the data for each refraction angle to help determine a flaw's location, length, and depth (when a tip signal was visible). Recall that the angular steps for raster scans were larger than those for line scans due to the constraints of the encoded data file sizes.

##### 7.5.1.1.1 Example Images: Flaw 1

Figure 7-45 shows examples of the detection of Flaw 1, the 10% through-wall flaw, with each of the four probes. For the 500 kHz PA probe at 30°, the flaw is well defined and easily gated, resulting in relatively high SNR with low background clutter. The 800 kHz probe showed a similar response but had a relatively weaker SNR. With the 30° RTD probe, on the other hand, the flaw is not as well defined and there is considerably more background signal, resulting in an overall lower SNR. The 45° RTD probe shows an improvement over the 30° RTD probe with lower background signal, but the flaw is noticeably oversized. Note that there is an apparently stronger signal response with the RTD probes than with the PA probes; however, the background noise is also considerably higher with the RTD probes, resulting in much lower SNR values. There was no sound field normalization in the images shown in Figure 7-45, so direct quantitative comparisons of absolute signal intensities between the different probe responses is not possible. From the carbon steel side, both the 1.5 and 2.0 MHz probes easily detected the flaw and resolved the tip (most clearly visible in the B-scans). The 2.0 MHz probe, however, also picked up appreciable echoes from the stainless steel cladding and the weld region, which reduced the SNR.



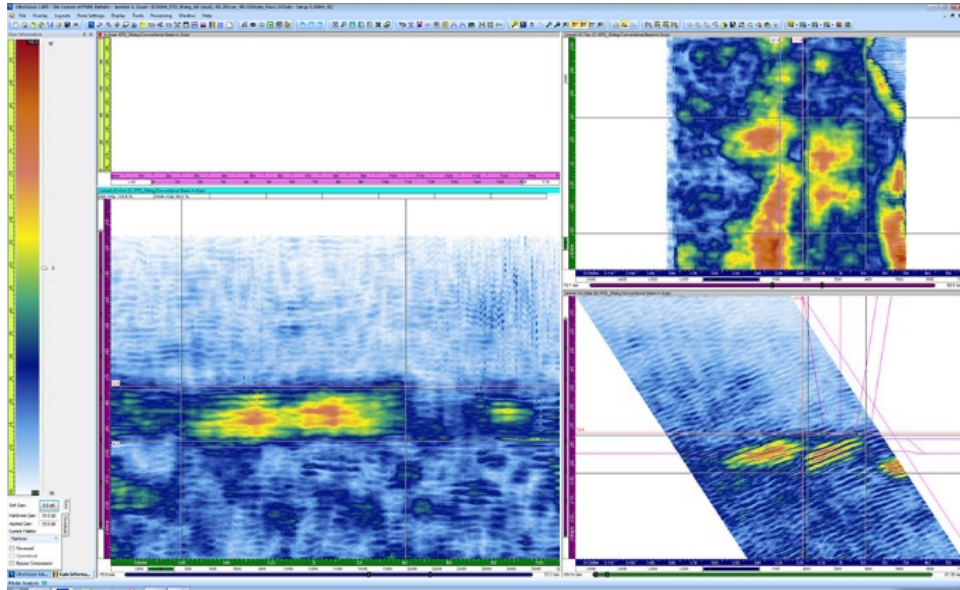
(a) 500 kHz PA at 30° from CASS



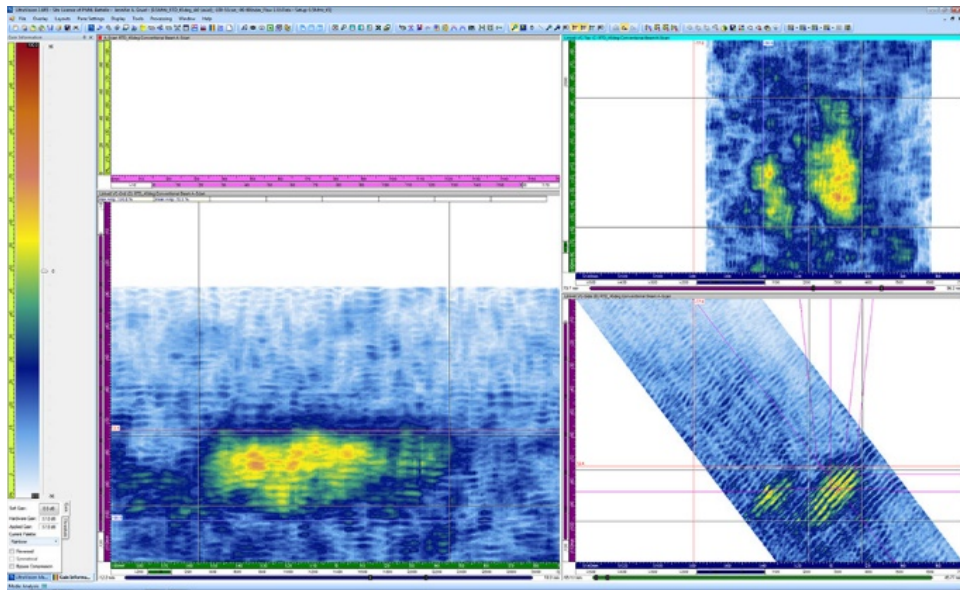
(b) 800 kHz PA at 39° from CASS

**Figure 7-45 Flaw 1 (10% through-wall) as Visualized with the Six Different Probes. This illustrates an example of how visualization of a single flaw varied with the different probes. Clockwise in each panel: sectoral view, C-scan, B-scan, and D-scan.**



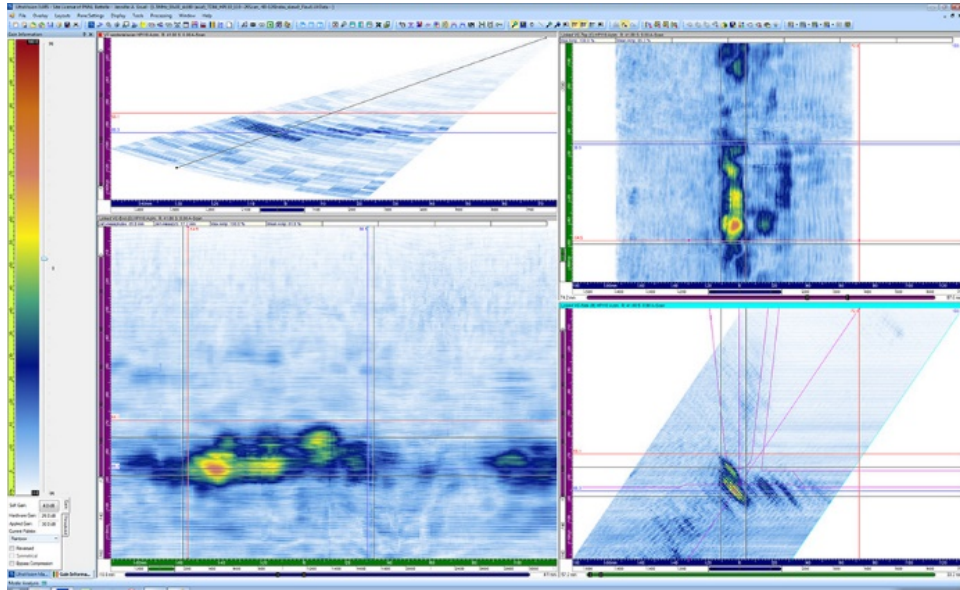


(c) 500 kHz RTD at 30° from CASS

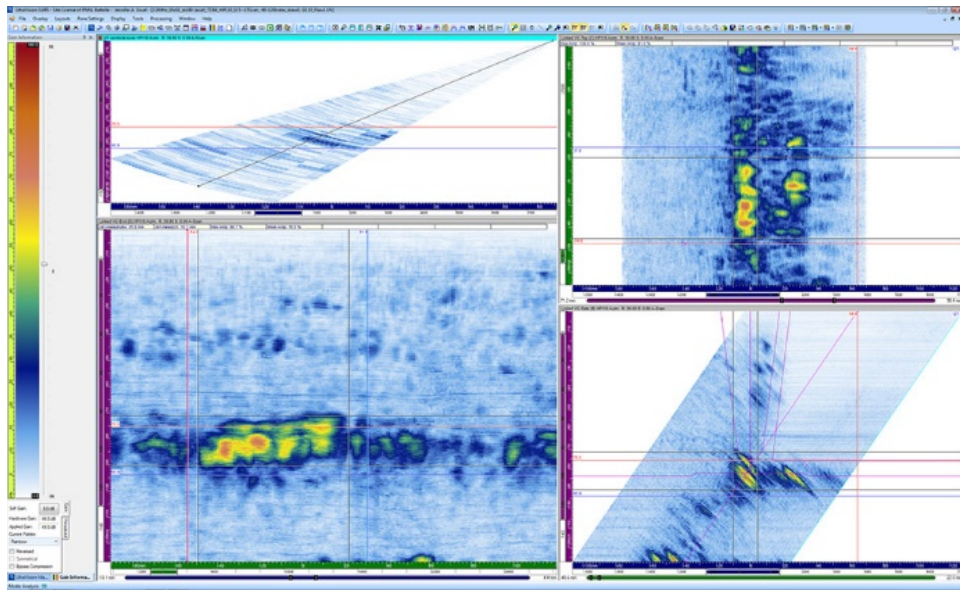


(d) 500 kHz RTD at 45° from CASS

**Figure 7-45 (continued)**



(e) 1.5 MHz PA at 41° from CS



(f) 2.0 MHz PA at 39° from CS

**Figure 7-45 (continued)**



#### 7.5.1.1.2 *TD and HP Focusing Comparison*

Data were collected with both TD and HP focusing. At the onset of data collection, it was uncertain which beam focusing would be more effective at detecting the corner and tip responses of the flaws. To directly compare results, the tip response, flaw length, through-wall depth, and SNR were examined using a subset of the analyzed data. Data were used for this analysis if the TD and HP refraction angles were within 1° of each other. A sampling of data for all flaws and all probes was included. Table 7-20 shows the measurement results and the differences between TD and HP, including RMSE for flaw length and depth. Results showed that there were no statistically significant differences between TD and HP focusing for any of the parameters measured. Overall, the TD channel had a slightly stronger tip signal by less than 0.5 dB on average. The HP channel had a slightly higher SNR ratio by less than 0.5 dB on average. The average flaw length differed by 0.8 mm (0.03 in.), which is below the raster resolution of the scan. The average through-wall depth differed by only 0.2 mm (0.01 in.), which is considerably smaller than the beam spot size or wavelength for any of the probes. Indeed, these differences are small enough to be considered inconsequential. Therefore, for this specimen and the scan parameters used, the data acquired by one focusing type was representative of the other focusing type and can be used interchangeably. Thus, for clarity and simplicity, the data below will be presented only for HP focusing unless otherwise noted.

The small differences between TD and HP focusing are illustrated in Figure 7-46, which shows an example comparison between the TD and HP channels of the 800 kHz scan of Flaw 4 (16% through-wall) at 38° TD and 39° HP. This corresponds to the eighth line in Table 7-20 (emphasized with boldface), which was chosen because it showed some of the largest differences between TD and HP. Even so, close examination of the figure shows only very subtle, visually distinguishable differences between the scans.

#### 7.5.1.1.3 *Beam Skew Comparison*

To determine the effectiveness of the non-zero beam skews (i.e., beam steering in the passive direction), comparisons were made in analyzed data for the five flaws using the 500 and 800 kHz probes. As with the TD/HP comparison, flaw tip response, length, depth, and SNR were examined. Figure 7-47 shows an example of the beam skew -10°, 0°, and +10° for Flaw 3 (20% through-wall) measured with the 500 kHz probe at 39° refraction angle and HP focusing. This 39° angle was chosen because the measurements at this angle were closest to providing an optimum perpendicular reflection for the true condition of the flaw; note that this angle is consistent with the range of angles shown to give the least end-of-block signal dropout (see Chapter 8). The figure reveals that some qualitative differences are visible in the presentation of the flaw for the different beam skews. Table 7-21 shows the results for the 500 and 800 kHz probes, including flaw length and depth RMSE. There are a few differences to note. For example: in the 500 kHz data, beam skew +10° results had a much poorer length measurement RMSE of 25.4 mm (1.0 in.) compared to 14.7 mm (0.6 in.) for the other skews; the tip of Flaw 2 (20% through-wall, axial) was detected with the beam skew -10° scan in the probe skew 180° data where it was missed otherwise; and beam skew -10° missed the tip of Flaw 3 (20% through-wall) at 41° refraction angle while it was detected for 0° and +10° beam skews. The 800 kHz data show smaller differences in flaw length RMSE between the skews than the 500 kHz data. While varying the beam skew appeared to have greater effect than varying the focusing between HP and TD, for simplicity, only beam skew 0° data will be presented hereafter.

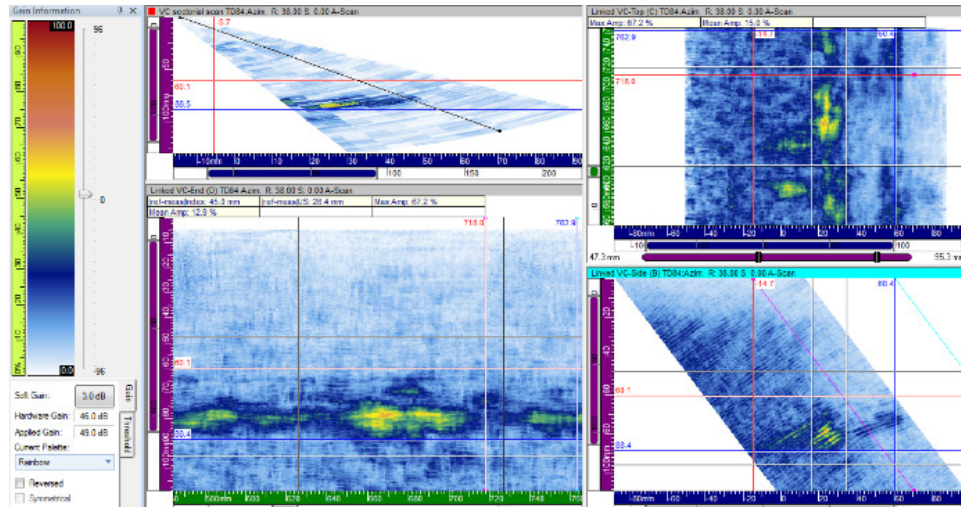
Table 7-20 Comparison of TD and HP Focusing

Flaw	Freq., kHz	Angle <sup>(a)</sup> (TD/HP) [Impinge.]	Length, <sup>(b)</sup> mm (in.)			Depth, <sup>(c)</sup> mm (in.)			P-M SNR, <sup>(d)</sup> dB		
			TD <sup>(e)</sup>	HP <sup>(f)</sup>	Diff <sup>(g)</sup>	TD	HP	Diff	TD	HP	Diff
1	500	29/30	81 (3.19)	81 (3.19)	0 (0.00)	na	na		14.8	14.1	-0.7
1	800	29/30	60 (2.36)	60 (2.36)	0 (0.00)	na	na		11.5	11.3	-0.2
1	800	38/39	80 (3.15)	80 (3.15)	0 (0.00)	na	na		8.7	8.8	0.1
2	500	35 [45]	23 (0.91)	24 (0.94)	1 (0.04)	12.1 (0.48)	11.5 (0.45)	-0.6 (-0.02)	10.9	11.2	0.3
2	800	26 [32]	16 (0.63)	16 (0.63)	0 (0.00)	21.6 (0.85)	20.6 (0.81)	-1 (-0.04)	8.8	8.2	-0.6
3	500	29/30	109 (4.29)	106 (4.17)	-3 (-0.12)	na	na		12.3	12.8	0.5
3	800	38/39	85 (3.35)	85 (3.35)	0 (0.00)	19.6 (0.77)	19.7 (0.78)	0.1 (0.00)	11.8	11.9	0.1
4	800	38/39	66 (2.60)	61 (2.40)	-5 (-0.20)	9.3 (0.37)	10.7 (0.42)	1.4 (0.06)	8.8	9.9	1.1
4	800	41/42	69 (2.72)	67 (2.64)	-2 (-0.08)	10.9 (0.43)	12.5 (0.49)	1.6 (0.06)	8.7	9.4	0.7
5	800	26 [32]	24 (0.94)	23 (0.91)	-1 (-0.04)	30.0 (1.18)	30.6 (1.20)	0.6 (0.02)	14.6	16.6	2
5	500	35 [45]	38 (1.50)	37 (1.50)	-1 (-0.04)	28.1 (1.11)	27.6 (1.09)	-0.5 (-0.02)	15.6	15.2	-0.4
5	800	26 [32]	16 (0.63)	16 (0.63)	0 (0.00)	30.1 (1.19)	30.4 (1.20)	0.3 (0.01)	12.4	13.6	1.2
5	800	26 [32]	15 (0.59)	15 (0.59)	0 (0.00)	30.8 (1.21)	30.9 (1.22)	0.1 (0.00)	14.3	14.8	0.5
Average:			-0.85			0.22			11.78	12.14	0.35
RMSE:			8.5	8.7		3.3	3.1				
(a)			“Angle” is the refraction angle. For circumferential scans of axial flaws, the calculated impingement angle is reported in square brackets.			(c) Depth is the flaw through-wall depth in mm.					
(b)			Length is the flaw length measured at the -6 dB level in mm, ignoring any signal gaps.			(d) P-M SNR is the peak-to-mean signal-to-noise ratio in dB.					
						(e) TD = true depth					
						(f) HP = half path					
						(g) Diff = difference					
						na = not applicable					

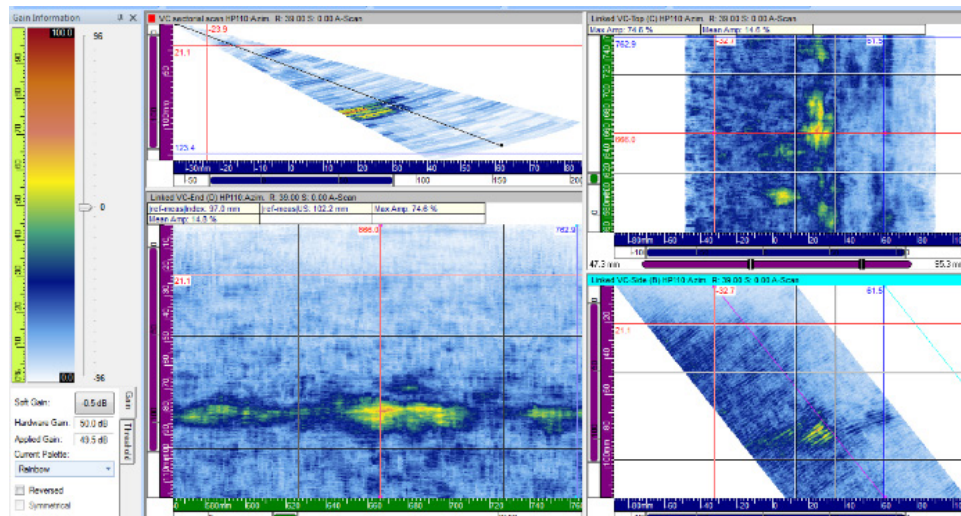
**Table 7-21 Comparison of Beam Skews at 500 and 800 kHz. The table shows the ratio of the corner to tip signal in dB, length, depth, and SNR of the five flaws.**

Flaw	Angle <sup>(a)</sup> [Impinge.] (probe skew)	C:T Ratio, <sup>(b)</sup> dB			Length, <sup>(c)</sup> mm (in.)			Depth, <sup>(d)</sup> mm (in.)			P-M SNR, <sup>(e)</sup> dB			
		Skew -10	Skew 0	Skew +10	Skew -10	Skew 0	Skew +10	Skew -10	Skew 0	Skew +10	Skew -10	Skew 0	Skew +10	
500 kHz														
1	29	na	na	na	85 (3.35)	81 (3.19)	80 (3.15)	na	na	na	14.26	14.82	14.72	
1	41	na	na	na	93 (3.66)	89 (3.50)	71 (2.80)	na	na	na	14.85	14.46	12.77	
2	26 [32] (0)	na	na	na	26 (1.02)	29 (1.14)	22 (0.87)	na	na	na	10.26	9.79	9.63	
2	35 [45] (0)	1.06	1.53	2.49	38 (1.50)	23 (0.91)	51 (2.01)	12.4 (0.49)	12.1 (0.48)	16.1 (0.63)	11.23	10.87	12.04	
2	26 [32] (180)	11.84	na	na	27 (1.06)	30 (1.18)	42 (1.65)	14.5 (0.57)	na	na	18.14	16.48	14.02	
2	35 [45] (180)	na	na	na	28 (1.10)	31 (1.22)	38 (1.50)	na	na	na	18.05	18.71	16.96	
3	29	na	na	na	109 (4.29)	109 (4.29)	105 (4.13)	na	na	na	11.19	12.27	11.35	
3	41	na	7.38	7.01	106 (4.17)	90 (3.54)	42 (1.65)	na	17.3 (0.68)	16.7 (0.66)	12.21	14.78	14.35	
4	32	na	na	na	68 (2.68)	65 (2.56)	43 (1.69)	na	na	na	10.24	11.55	10.76	
4	41	na	na	na	41 (1.61)	41 (1.61)	36 (1.42)	na	na	na	8.75	10.99	11.11	
5	26 [32] (0)	4.12	2.27	2.77	21 (0.83)	24 (0.94)	34 (1.34)	30.2 (1.19)	30 (1.18)	29.9 (1.18)	15.2	14.6	14.99	
5	35 [45] (0)	1.46	1.24	0.23	29 (1.14)	27 (1.06)	38 (1.50)	31.7 (1.25)	31 (1.22)	30.9 (1.22)	14.77	13.8	12.08	
5	26 [32] (180)	2.24	1.48	1.83	39 (1.54)	41 (1.61)	29 (1.14)	27.6 (1.09)	28.1 (1.11)	28.5 (1.12)	11.82	11.54	12.37	
5	35 [45] (180)	2.4	1.54	1.14	36 (1.42)	38 (1.50)	31 (1.22)	28.8 (1.13)	28.1 (1.11)	27.1 (1.07)	14.07	15.57	15.91	
Average:		3.85	2.57	2.58							13.22	13.59	13.08	
RMSE:					14.7 (0.58)	14.7 (0.58)	25.4 (1.00)	4.1 (0.16)	4.2 (0.17)	4.0 (0.16)				
800 kHz														
1	29	na	na	na	68 (2.68)	60 (2.36)	71 (2.80)	na	na	na	11.7	11.5	10.1	
1	38	na	na	na	66 (2.60)	80 (3.15)	52 (2.05)	na	na	na	8.9	8.7	10.4	
2	26 [32] (0)	1.79	2.53	na	21 (0.83)	16 (0.63)	17 (0.67)	21.4 (0.84)	21.6 (0.85)	na	8.62	8.79	7.73	
2	26 [32] (180)	na	na	na	22 (0.87)	20 (0.79)	21 (0.83)	na	na	na	11.8	12.9	11.83	
2	35 [45] (180)	na	na	na	30 (1.18)	21 (0.83)	20 (0.79)	na	na	na	12.18	14.11	13.73	
3	39	5.7	6.09	6.21	62 (2.44)	85 (3.35)	111 (4.37)	20 (0.79)	19.7 (0.78)	18.7 (0.74)	11.9	11.9	10.8	

Flaw	Angle <sup>(a)</sup> [Impinge.] (probe skew)	C:T Ratio, <sup>(b)</sup> dB			Length, <sup>(c)</sup> mm (in.)			Depth, <sup>(d)</sup> mm (in.)			P-M SNR, <sup>(e)</sup> dB		
		Skew -10	Skew 0	Skew +10	Skew -10	Skew 0	Skew +10	Skew -10	Skew 0	Skew +10	Skew -10	Skew 0	Skew +10
4	45/42/45	4.7	4.47	3.65	68 (2.68)	67 (2.64)	59 (2.32)	14 (0.55)	12.5 (0.49)	11.4 (0.45)	9.4	9.4	9.3
5	26 [32] (0)	5.47	4.68	5.72	19 (0.75)	16 (0.63)	25 (0.98)	30.8 (1.21)	30.1 (1.19)	29.2 (1.15)	13.09	12.44	14.36
5	35 [45] (0)	-0.51	-3.33	-5.19	23 (0.91)	19 (0.75)	14 (0.55)	29.8 (1.17)	31 (1.22)	31.9 (1.26)	12.07	11.05	8.41
5	26 [32] (180)	4	6.33	6.61	16 (0.63)	25 (0.98)	18 (0.71)	30.5 (1.20)	28.7 (1.13)	30.7 (1.21)	13.78	14.54	14.6
5	35 [45] (180)	-1.71	0.08	1.53	34 (1.34)	22 (0.87)	22 (0.87)	29.3 (1.15)	28.9 (1.14)	30.4 (1.20)	11.92	11.46	14.41
Average:		2.78	2.98	3.09							11.40	11.45	11.42
RMSE:					14.2 (0.56)	8.0 (0.32)	9.8 (0.39)	3.7 (0.14)	3.9 (0.16)	3.0 (0.12)			
<p>(a) "Angle" is the refraction angle. Probe skew is given in parentheses. For circumferential scans of axial flaws, the calculated impingement angle is reported in square brackets.</p> <p>(b) C:T ratio is the signal ratio between the corner and the tip responses (if a tip was detected), reported in dB. A lower C:T value indicates a relatively stronger tip signal.</p> <p>(c) Length is the flaw length measured at the -6 dB level in mm, ignoring any signal gaps.</p> <p>(d) Depth is the flaw through-wall depth in mm.</p> <p>(e) P-M SNR is the peak-to-mean signal-to-noise ratio in dB.</p> <p>na = no tip detected</p>													

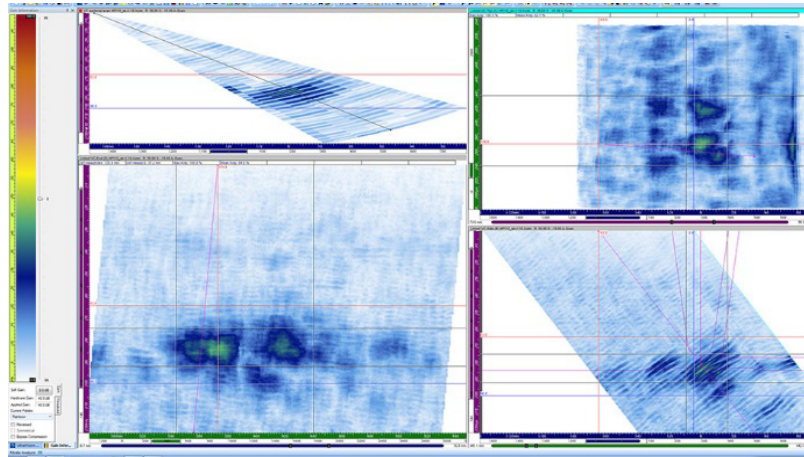


TD 800 kHz Flaw 4 at 38°

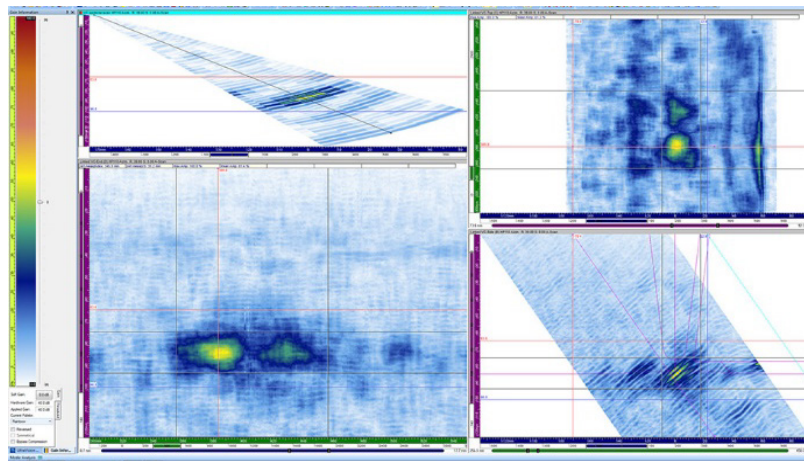


HP 800 kHz Flaw 4 at 39°

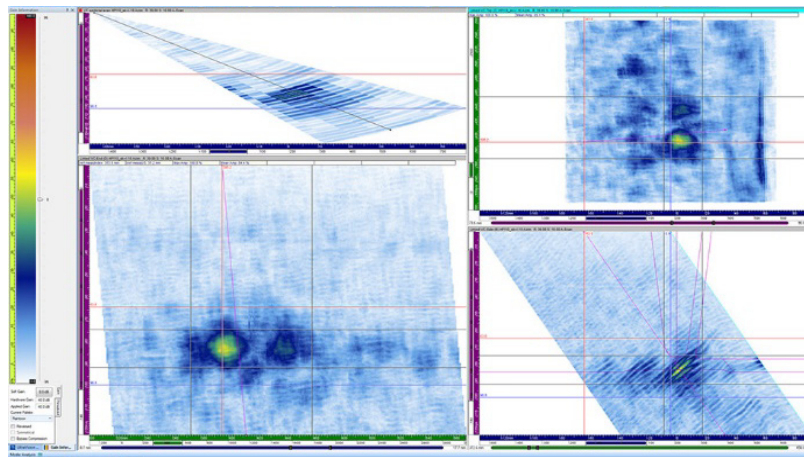
**Figure 7-46 Example Comparison of TD and HP Focusing. Minimal differences are visible between the two focusing types. Clockwise in each panel: sectoral view, C-scan, B-scan, and D-scan.**



Skew -10



Skew 0

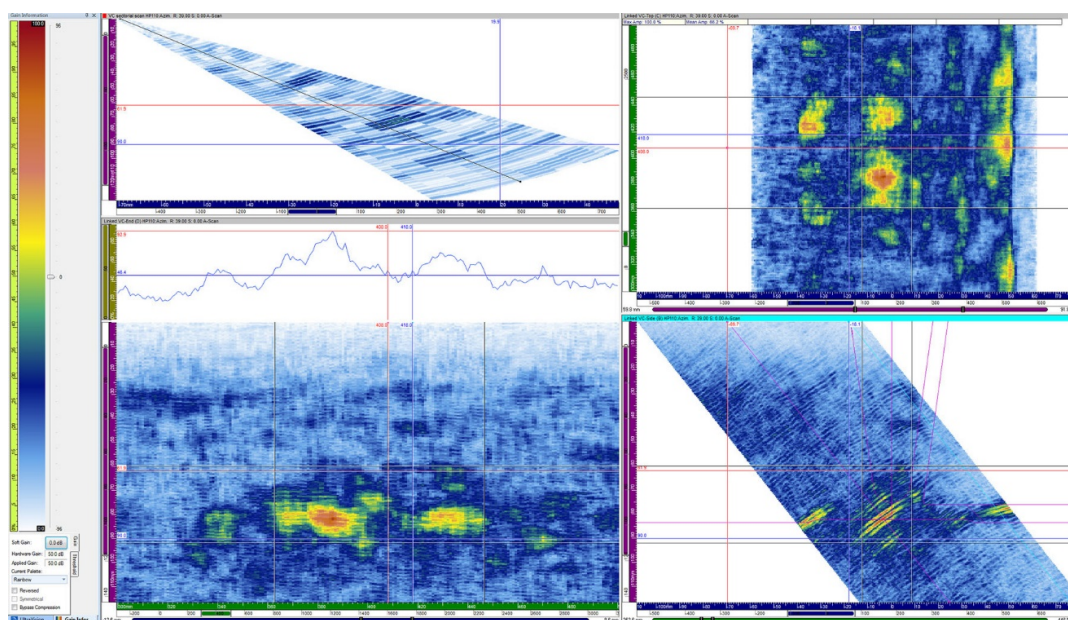


Skew +10

**Figure 7-47 Example Comparison of Different Beam Skews. Images show scans of Flaw 3 (20% through-wall) with the 500 kHz PA probe at 41°. Clockwise in each panel: sectoral view, C-scan, B-scan, and D-scan.**



Flaw length was measured at the  $-6$  dB signal level after identifying and gating the flaw corner response. At the strict  $-6$  dB level, discontinuous signal responses, or sections of dropout, were sometimes present in the flaw response measured with the 800 kHz probe. For example, Figure 7-48 shows Flaw 3 (20% through-wall) as measured by the 800 kHz probe at  $39^\circ$ . The graph above the D-scan is an echo dynamic curve, which shows the peak signal intensity of the selected region (between the cursors) of the D-scan. The red and blue vertical lines in the D-scan and echo dynamic curve mark the dropout edges and the black vertical lines mark the flaw  $-6$  dB end points. The blue horizontal line in the echo dynamic curve was placed at the  $-6$  dB level. Although the  $-6$  dB length with and without the dropout was measured, only the single planar flaw length (without dropout) is reported herein. It is important to note that no signal dropout was observed in any flaw detection with the 500 kHz PA probe. This again underscores the advantage of using lower frequencies (i.e., 500 kHz) for flaw detection in CASS material.



The SNR was measured as peak-to-mean (P-M) noise. Noise was calculated at the same metal path as the flaw but on each side of the flaw signal in the D-scan end view image. Figure 7-49 shows results of length RMSE and SNR measurements for the probes used. Recall that the RTD probes were only used to scan the circumferential flaws, whereas the PA probes were used on all the flaws, including from both directions on the axial flaws. The plot shows that the PA probes provided the lowest RMSE results, and the 500 kHz PA probe provided the highest SNR. The tabular results shown in Table 7-22 and Table 7-23 use HP focusing, beam skew  $0^\circ$ , and the refraction angle that gave the best results (i.e., closest to true state); the angle shown is the refraction angle, and for circumferential scans of axial flaws, the impingement angle is shown in square brackets. For blind measurements, an analyst may choose to use the angle that gives the highest SNR or, to be conservative, the largest flaw length. A blind analysis was not done for this work.

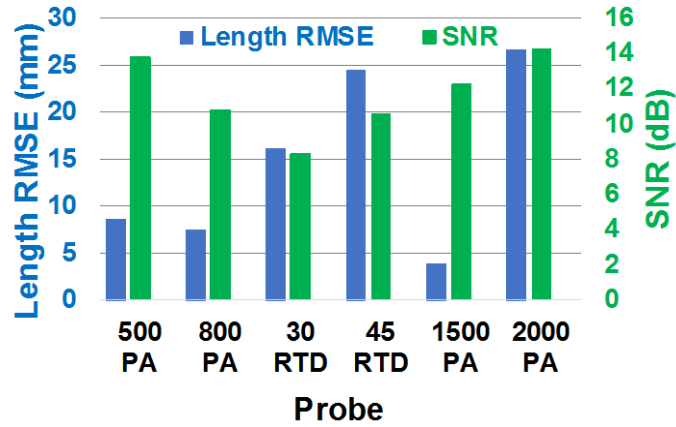


**Figure 7-49 Length RMSE and SNR.** The length RMSE (blue) for the PA probes is much lower than that of the 500 kHz RTD probes while the SNR (green) for the PA probes is higher. The 500 kHz PA probe had the highest SNR overall with length RMSE comparable to that of the 800 kHz PA probe. Note: data acquired at 1500 and 2000 kHz were scanned from the carbon steel side of the mockup. The probe labels refer to the PA probes in kHz and RTD probes in refracted angle.

**Table 7-22 Length Sizing and SNR Measured by the 500 and 800 kHz PA Probes and the 500 kHz RTD Probes. Length RMSE and mean SNR are also shown. Recall that the axial flaws (Flaw 2 and Flaw 5) were not scanned with the RTD probes.**

Flaw	Probe Skew, degrees	Angle [Impinge.], degrees	True Length, mm (in.)	Measured Length, mm (in.)	Difference, mm (in.)	P-M SNR, dB
500 kHz PA Probe						
1	0	30	76.5 (3.01)	81 (3.19)	4.5 (0.18)	14.1
2	0	35 [45]	19.1 (0.75)	24 (0.94)	4.9 (0.19)	11.2
2	180	35 [45]	19.1 (0.75)	31 (1.22)	11.9 (0.47)	19.1
3	0	30	101.7 (4.00)	106 (4.17)	4.3 (0.17)	12.8
4	0	48	75.3 (2.96)	76 (2.99)	0.7 (0.03)	10.4
5	0	26 [32]	18.5 (0.73)	23 (0.91)	4.5 (0.18)	16.6
5	180	26 [32]	18.5 (0.73)	36 (1.42)	17.5 (0.69)	12.4
			RMSE: 8.7 (0.34)		Average SNR: 13.8	
800 kHz PA Probe						
1	0	39	76.5 (3.01)	80 (3.15)	3.5 (0.14)	8.8
2	0	26 [32]	19.1 (0.75)	16 (0.63)	−3.1 (−0.12)	8.2
2	180	26 [32]	19.1 (0.75)	20 (0.79)	0.9 (0.04)	12.3
3	0	39	101.7 (4.00)	85 (3.35) <sup>(a)</sup>	−16.7 (−0.66)	11.9
4	0	42	75.3 (2.96)	67 (2.64)	−8.3 (−0.33)	9.4
5	0	26 [32]	18.5 (0.73)	16 (0.63)	−2.5 (−0.10)	13.6
5	180	35 [45]	18.5 (0.73)	22 (0.87)	3.5 (0.14)	11.6
			RMSE: 7.5 (0.29)		Average SNR: 10.8	
500 kHz RTD Probes						
1	0	30	76.5 (3.01)	95 (3.74)	18.5 (0.73)	9.5
1	0	45	76.5 (3.01)	101 (3.98)	24.5 (0.96)	10.3
3	0	30	101.7 (4.00)	113 (4.45)	11.3 (0.44)	6.8
3	0	45	101.7 (4.00)	107 (4.21)	5.3 (0.21)	11.9
4	0	30	75.3 (2.96)	93 (3.66)	17.7 (0.70)	8.6
4	0	45	75.3 (2.96)	41 (1.61)	−34.3 (−1.35)	9.7
			RMSE: 20.8 (0.82)		Average SNR: 9.5	
(a) A −6 dB gap was ignored.						

**Table 7-23 Length Sizing and SNR Measured by the 1.5 and 2.0 MHz PA Probes. Length RMSE and mean SNR are also shown. Length measurements in boldface indicate that a -6 dB gap was present but ignored.**

Flaw	Probe Skew, degrees	Angle [Impinge.], degrees	True Length, mm	Measured Length, mm	Difference, mm	P-M SNR, dB	P-P SNR, dB
<b>1.5 MHz PA Probe</b>							
1	180	41	76.5	<b>76</b>	-0.5	12.2	4.8
2	0	26 [32]	19.1	20	0.9	9.0	1
2	180	23 [28]	19.1	20	0.9	9.4	1.4
3	180	38	101.7	111	9.3	16.4	7.3
4	180	38	75.3	<b>80</b>	4.7	15.5	5.3
5	0	26 [32]	18.5	18	-0.5	11.8	1.5
5	180	26 [32]	18.5	18	-0.5	11.8	3.6
			RMSE:	4.0	Average:	12.3	3.55714
<b>2.0 MHz PA Probe</b>							
1	180	39	76.5	64	-12.5	11	3.9
2	0			Flaw not detected			
2	180			Flaw not detected			
3	180	42	101.7	<b>100</b>	-1.7	16.5	7.3
4	180	42	75.3	<b>31</b>	-44.3	15.2	3.4
5	0			Flaw not detected			
5	180			Flaw not detected			
			RMSE:	26.6	Average:	14.2333	4.86667

PNNL generally considers the minimum P-M SNR needed for unambiguous flaw detection in CASS to be approximately 9.5 dB (3:1) (Anderson et al. 2014). The 500 kHz PA probe was able to detect all of the flaws above the 9.5 dB SNR level without signal dropout while consistently exceeding the SNR levels of the 800 kHz probe, which fell below the 9.5 dB level on several occasions and showed some dropout. This type of information corroborates earlier CASS thick-walled research (Anderson et al. 2007), and was, therefore, expected, as transmission of higher frequencies is hindered in coarse-grained materials due to scattering and refraction. In particular, the 10% through-wall flaw (Flaw 1) was detected by the 500 kHz PA probe at nearly two times the SNR level (5.3 dB higher) of the 800 kHz probe.

The SNR of the 30° RTD probe was consistently lower than that of the 45° probe, and every measurement with the 30° probe was at or below the 9.5 dB level. Figure 7-50 shows an example of poor SNR realized by the 30° RTD probe on Flaw 3 (20% through-wall), where the P-M SNR was only 6.8 dB. The 30° RTD probe signal was routinely plagued by surface noise due to the relatively steep refraction angle and lack of true beam focusing. By comparison, the same figure shows Flaw 3 as captured by the 500 kHz PA probe at 30°. Note that the signals from the two probes are not normalized. The P-M SNR with the PA probe was about 7.0 dB higher (2.2 times)

than that of the 30° RTD probe. The PA probe outperformed the RTD probe at the same refraction angles due to the better focusing capabilities of the PA probe.

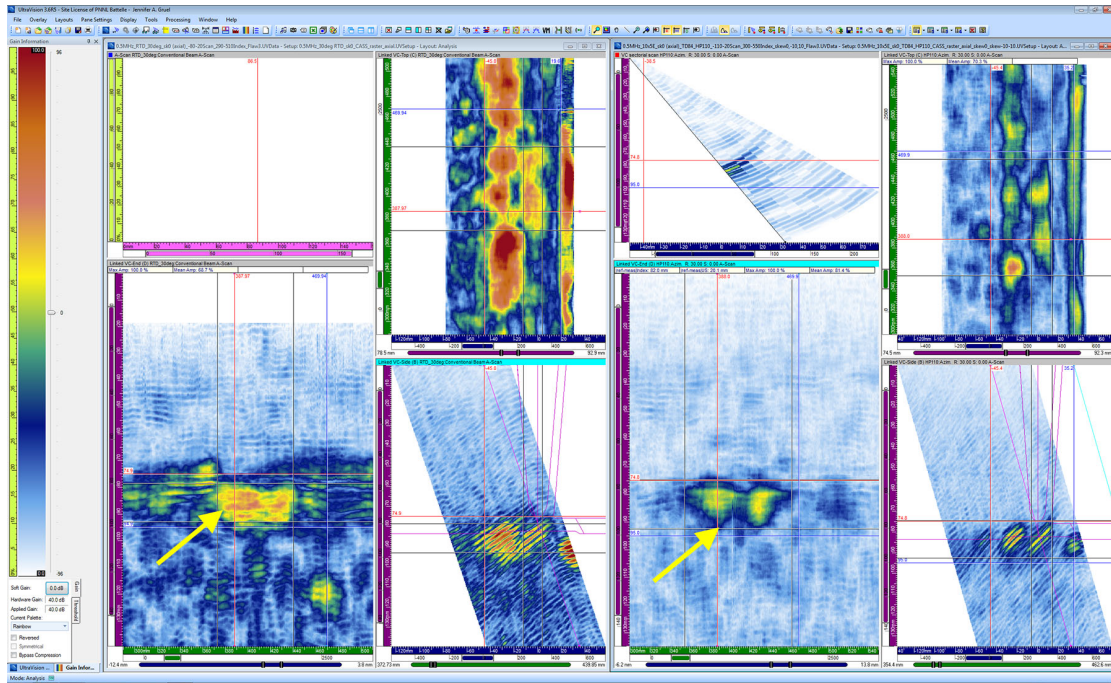


**Figure 7-50 Comparison of the 30° RTD Probe and the 500 kHz PA Probe. Flaw 3 (20% through-wall) is shown as scanned with the 30° RTD probe (left) and the 500 kHz PA probe at 30° refraction angle (right). The SNR of the RTD probe is 6.8 dB while the SNR of the PA probe is 13.8 dB. Note that the signal intensities are not normalized.**

In addition to poorer performance for flaw detection in this specimen, the 800 kHz probe had a length RMSE that was not appreciably better than that of the 500 kHz PA probe. The RMSE of the 800 kHz probe was lower by about 1 mm (0.04 in.), indicating only slightly better average sizing accuracy. However, note that if the strict -6 dB length sizing was used, the RMSE for the 800 kHz probe would have been higher due to the signal dropout observed in Flaw 3. It is important to note that the detection of Flaw 3 by the 500 kHz probe showed no signal dropout. Although length sizing acceptance criteria for performance demonstration have not yet been established for CASS components in the ASME Code, such criteria are defined for DMWs and wrought austenitic stainless steel as an RMSE tolerance of 19.05 mm (0.75 in.); see Section XI, Appendix VIII, Supplement 10(3.2)(d) and Supplement 2(3.2)(a). Both the 500 and 800 kHz PA probes were well within this tolerance. The 500 kHz RTD probes, on the other hand, showed a considerably higher RMSE for length sizing and were outside the tolerance.

Note in Table 7-22 that axial Flaw 2 (20% through-wall, axial) was observed with higher SNR at 500 kHz and 800 kHz in the skew 180° scans than in the skew 0° scans. Figures 7-51 and 7-52 highlight the differences between the two skews for the 500 and 800 kHz probes, respectively. For a given gain setting, the figures show that Flaw 2 was strikingly more visible in the skew 180° scans (right side of the figures). Also note from the tables that the Flaw 5 SNR values at skew 0° were stronger than at skew 180°. There were no observed issues with coupling or noise levels between the different skews. It was unknown if this phenomenon was due to a misaligned flaw, grain structure causing different beam redirection in the weld region, or another effect.



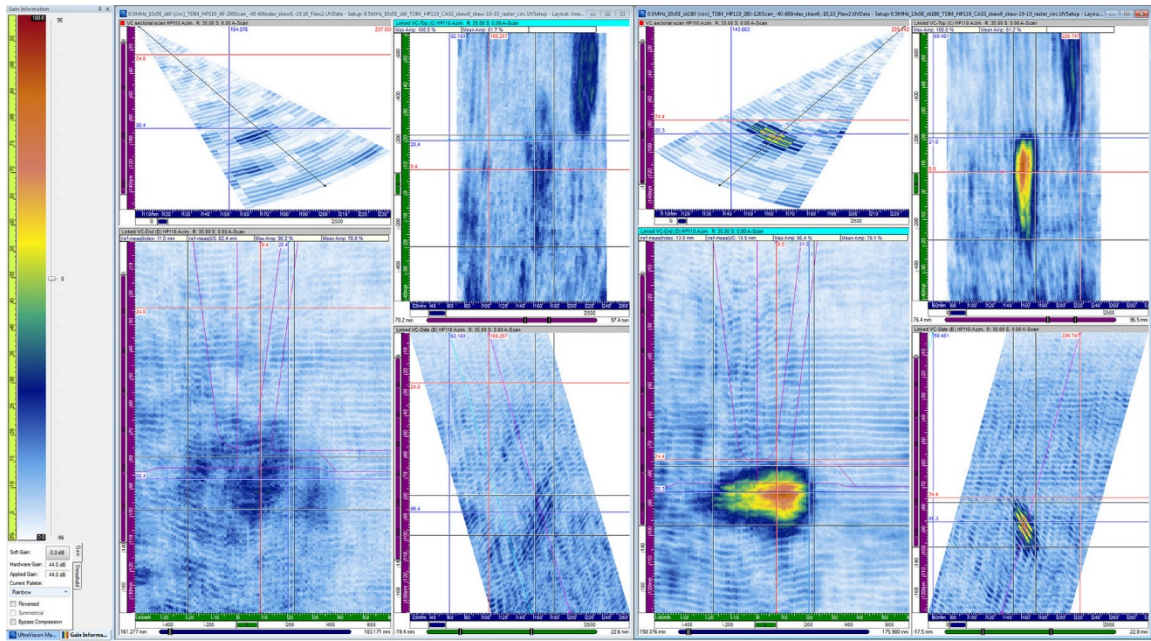


**Figure 7-51** Flaw 2 (20% through-wall, axial) as Scanned by the 500 kHz PA Probe. The skew 0° scan is on the left and the skew 180° scan is on the right. The refraction angle is 35°, and the impingement angle is 45°. Clockwise in the panels: sectoral view, C-scan, B-scan, and D-scan.

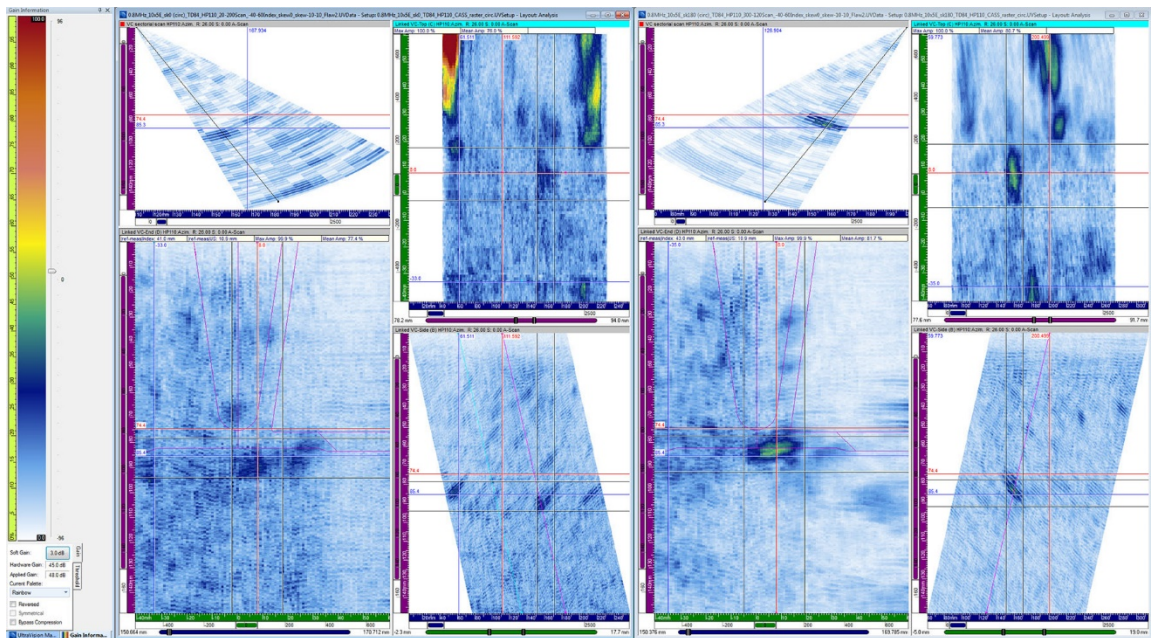


**Figure 7-52** Flaw 2 (20% through-wall, axial) as Scanned by the 800 kHz PA Probe. The skew 0° scan is on the left and the skew 180° scan is on the right. The refraction angle is 26°, and the impingement angle is 32°. Clockwise in the panels: sectoral view, C-scan, B-scan, and D-scan.



From the carbon steel side of the weld, both the 1.5 and 2.0 MHz probes were able to detect the circumferential flaws. The 2.0 MHz probe did not detect the axial flaws; this was anticipated as exams for axial flaws require the sound to transit through weld metal and at these frequencies, beam redirection and attenuation is prevalent. For example, Figure 7-53 shows the scan of Flaw 5 with the 2.0 MHz probe at 26° (32° impingement angle). There is no readily identifiable corner or tip response. A possible corner response in the skew 180° scan is overshadowed by a brighter artifact at the same metal path on the carbon steel side (i.e., to the right of the corner response). A possible tip signal near the fusion plane was visible from the skew 0° side of the flaw but was at the wrong depth to be the actual tip signal; this signal may have been a fabrication artifact. For comparison, a scan of the no-flaw region is also shown (Figure 7-54). Note the considerable echo responses from within the weld region at approximately mid-wall depth. The length RMSE of the flaws detected by the 2.0 MHz probe was 26.6 mm (1.0 in.), higher than the 19.05 mm (0.75 in.) tolerance discussed above. Two of the detected circumferential flaws had gaps at the -6 dB level, and Flaw 4 was greatly undersized. The SNR of the 2.0 MHz probe was high, but this was inflated through the exclusion of the non-detected axial flaws. The 1.5 MHz probe, by comparison, had the lowest length RMSE of all the probes but still had an average P-M SNR above the 9.5 dB mark (note that SNR below 9.5 dB from Flaw 2 dragged down this average). Flaw 4 had a -6 dB gap with the 1.5 MHz probe. Flaw 4 was located near a counterbore that produced a strong reflection when viewed from the carbon steel side (see Figure 7-23). This may have complicated flaw detection and sizing.

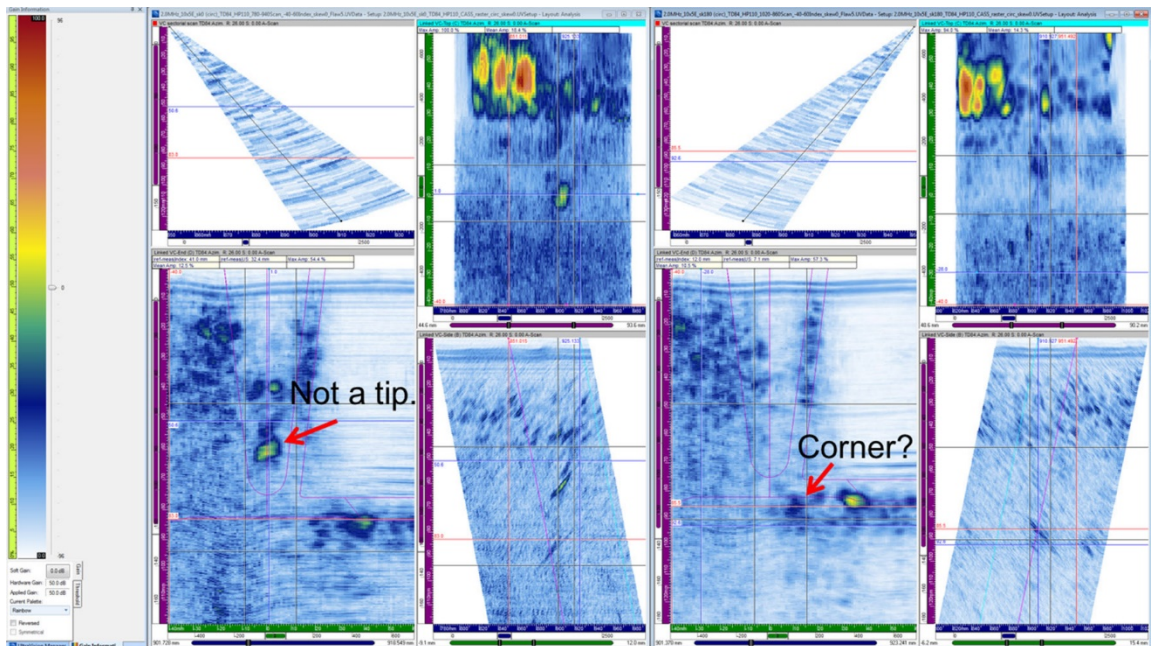


**Figure 7-53** Flaw 5 as Scanned by the 2.0 MHz PA Probe. The refraction angle is 26° and the impingement angle is 32°. Spurious signals and strong background signals complicate flaw detection. Clockwise in the panels: sectorial view, C-scan, B-scan, and D-scan.

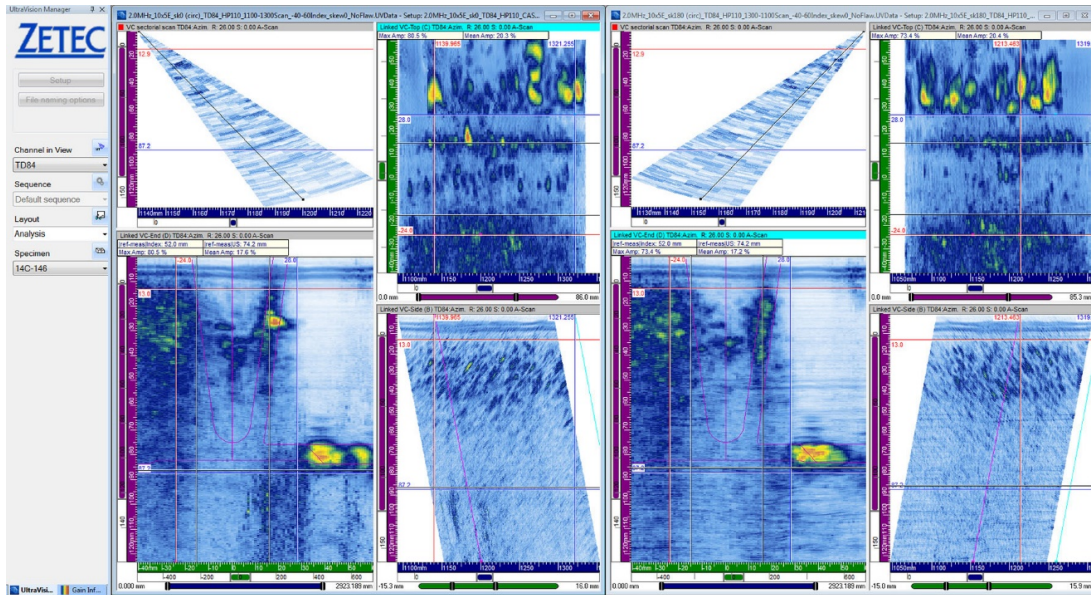


**Figure 7-54 No-Flaw Region as Scanned by the 2.0 MHz PA Probe. The refraction angle is  $26^\circ$  and the impingement angle is  $32^\circ$ . Spurious signals and strong background signals persist in and near the weld region. Clockwise in the panels: sectoral view, C-scan, B-scan, and D-scan.**

An example of a far-side detection of Flaw 4 (16% through-wall) with the 500 kHz PA probe is shown in Figure 7-55. This flaw had the lowest SNR (10.4 dB) of the flaws detected with the 500 kHz PA probe; nevertheless, the P-M SNR was still above 9.5 dB mark, and it sized within 5 mm (0.20 in.) of the true-state length.

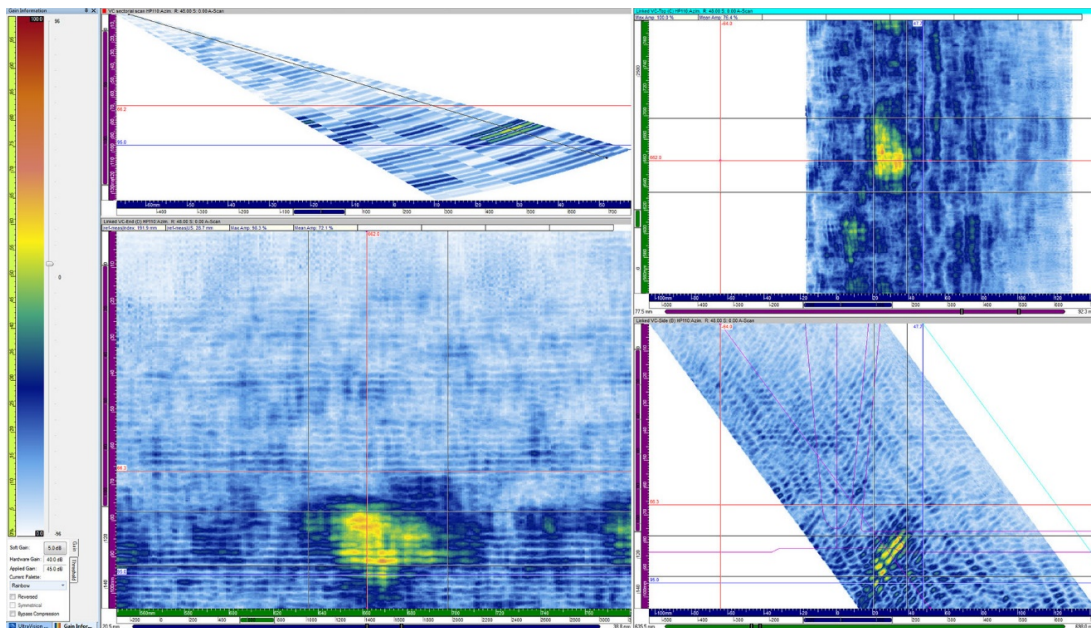


**Figure 7-55 Example of a Far-Side Detection. This figure shows Flaw 4 (16% through-wall) as detected by the 500 kHz PA probe at  $48^\circ$ . Clockwise in the image: sectoral view, C-scan, B-scan, and D-scan.**

### 7.5.1.3 Flaw Depth Sizing

Data were analyzed for flaw depth when a tip signal was observed by the analyst. Flaw depth was determined by the difference between radial (through-wall) positions of the tip and main specular responses. Tables 7-24 and 7-25 show the flaw depth results for HP focusing, beam skew 0°, and, as with the length measurements, the refraction angle that gave the best results (i.e., closest to the FlawTech reported values). These angles are expected to vary from frequency to frequency; see Chapter 8.2. Note that these angles may vary from those used to measure flaw lengths. No tip responses were seen from either of the fixed-angle 500 kHz RTD probes, so these data are excluded from the tables.

The magnitude of the corners-to-tip signal ratio is presented in tables 7-26 through 7-29 to give an indication of the relative visibility of the tips. Note that this ratio is given in dB, so a negative value indicates a stronger tip response than corner response. In practice, many factors can affect the amplitude of the tip response, including local grain structure, sound field characteristics, probe frequency (wavelength), crack opening displacement, flaw morphology, dimensions, and orientation to the sound field. As shown in the data, diffracted tip responses can be detected with a wide range of signal amplitudes, from no detectable tip signal to a tip signal that is stronger than the corner signal. There is no threshold or rule-of-thumb in CASS for determining whether a tip is detected based on the relative amplitude of the tip diffraction signal to the corner signal. Experience at PNNL indicates that tip signals are generally found to be lower in amplitude from the specular reflected flaw response by as much as 20 dB, although there is significant variability. Therefore, care and vigilance should be used when examining CASS data for tip diffracted signals.

**Table 7-24 Flaw Depth Sizing with the 500 kHz PA Probe. The measured depth, depth RMSE, and the corner-to-tip signal ratio (in dB) are shown.**

Flaw	Probe Skew, degrees	Angle [Impinge.], degrees	FlawTech True Depth, mm (in.)	Measured Tip Depth, mm (in.)	Difference, mm (in.)
1	0		No tip observed		
2	0	35 [45]	16.4 (0.65)	11.5 (0.45)	-4.9 (-0.19)
2	180		No tip observed		
3	0	45	16.5 (0.65)	16.5 (0.65)	0.0 (0.00)
4	0		No tip observed		
5	0	35 [45]	33.8 (1.33)	31.0 (1.22)	-2.8 (-0.11)
5	180	26 [32]	33.8 (1.33)	28.2 (1.11)	-5.6 (-0.22)
RMSE: 4.0 (0.16)					

**Table 7-25 Flaw Depth Sizing with the 800 kHz PA Probe. The measured depth, depth RMSE, and the corner-to-tip signal ratio (in dB) are shown.**

Flaw	Probe Skew, degrees	Angle [Impinge.], degrees	FlawTech True Depth, mm (in.)	Measured Tip Depth, mm (in.)	Difference, mm (in.)
1	0		No tip observed		
2	0	26 [32]	16.4 (0.65)	20.6 (0.81)	4.2 (0.17)
2	180		No tip observed		
3	0	39	16.5 (0.65)	19.7 (0.78)	3.2 (0.13)
4	0	42	13.3 (0.52)	12.5 (0.49)	-0.8 (-0.03)
5	0	35 [45]	33.8 (1.33)	30.9 (1.22)	-2.9 (-0.11)
5	180	26 [32]	33.8 (1.33)	30.9 (1.22)	-2.9 (-0.11)
RMSE: 3.0 (0.12)					

**Table 7-26 Flaw Depth Sizing with the 500 kHz PA Probe. The measured depth, depth RMSE, and the corner-to-tip signal ratio (in dB) are shown. . A C:T ratio <0 indicates a brighter tip signal than corner signal.**

Flaw	Probe Skew, degrees	Angle [Impinge.], degrees	True Depth, mm (in.)	Measured Tip Depth, mm (in.)	Difference, mm (in.)	C:T Ratio, dB
1	0		No tip observed			
2	0	35 [45]	16.4 (0.65)	11.5 (0.45)	-4.9 (-0.19)	2.0
2	180		No tip observed			
3	0	45	16.5 (0.65)	16.5 (0.65)	0.0 (0.00)	3.6
4	0		No tip observed			
5	0	35 [45]	33.8 (1.33)	31.0 (1.22)	-2.8 (-0.11)	1.4
5	180	26 [32]	33.8 (1.33)	28.2 (1.11)	-5.6 (-0.22)	2.5
RMSE:				4.0 (0.16)		

**Table 7-27 Flaw Depth Sizing with the 800 kHz PA Probe. The measured depth, depth RMSE, and the corner-to-tip signal ratio (in dB) are shown. A C:T ratio <0 indicates a brighter tip signal than corner signal.**

Flaw	Probe Skew, degrees	Angle [Impinge.], degrees	True Depth, mm (in.)	Measured Tip Depth, mm (in.)	Difference, mm (in.)	C:T Ratio, dB
1	0			No tip observed		
2	0	26 [32]	16.4 (0.65)	20.6 (0.81)	4.2 (0.17)	3.1
2	180			No tip observed		
3	0	39	16.5 (0.65)	19.7 (0.78)	3.2 (0.13)	6.1
4	0	42	13.3 (0.52)	12.5 (0.49)	-0.8 (-0.03)	4.5
5	0	35 [45]	33.8 (1.33)	30.9 (1.22)	-2.9 (-0.11)	-3.5
5	180	26 [32]	33.8 (1.33)	30.9 (1.22)	-2.9 (-0.11)	6.0
RMSE:				3.0 (0.12)		

**Table 7-28 Flaw Depth Sizing with the 1.5 MHz PA Probe. The measured depth, depth RMSE, and the corner-to-tip signal ratio (in dB) are shown. A C:T ratio <0 indicates a brighter tip signal than corner signal.**

Flaw	Probe Skew, degrees	Angle [Impinge.], degrees	True Depth, mm (in.)	Measured Tip Depth, mm (in.)	Difference, mm (in.)	C:T Ratio, dB
1	180	41	8.5 (0.33)	9.6 (0.38)	1.1 (0.04)	2.5
2	0	26 [32]	16.4 (0.65)	15.8 (0.62)	-0.6 (-0.02)	1.5
2	180			No tip observed		
3	180	38	16.5 (0.65)	16.1 (0.63)	-0.4 (-0.02)	6.8
4	180	38	13.3 (0.52)	9.0 (0.35)	-4.3 (-0.17)	1.5
5	0	35 [45]	33.8 (1.33)	32.6 (1.28)	-1.2 (-0.05)	-1.4
5	180	26 [32]	33.8 (1.33)	30.1 (1.19)	-3.7 (-0.15)	2.7
RMSE:				2.4 (0.10)		



**Table 7-29 Flaw Depth Sizing with the 2.0 MHz PA Probe. The measured depth, depth RMSE, and the corner-to-tip signal ratio (in dB) are shown. A C:T ratio <0 indicates a brighter tip signal than corner signal.**

Flaw	Probe Skew, degrees	Angle [Impinge.], degrees	True Depth, mm (in.)	Measured Tip Depth, mm (in.)	Difference, mm (in.)	C:T Ratio, dB
1	180	39	8.5 (0.33)	7.1 (0.28)	-1.4 (-0.06)	1.6
2	0			Flaw not detected		
2	180			Flaw not detected		
3	180	42	16.5 (0.65)	18.8 (0.74)	2.3 (0.09)	6.7
4	180	45	13.3 (0.52)	12.1 (0.48)	-1.2 (-0.05)	-3.1
5	0			Flaw not detected		
5	180			Flaw not detected		
RMSE:				1.7 (0.07)		

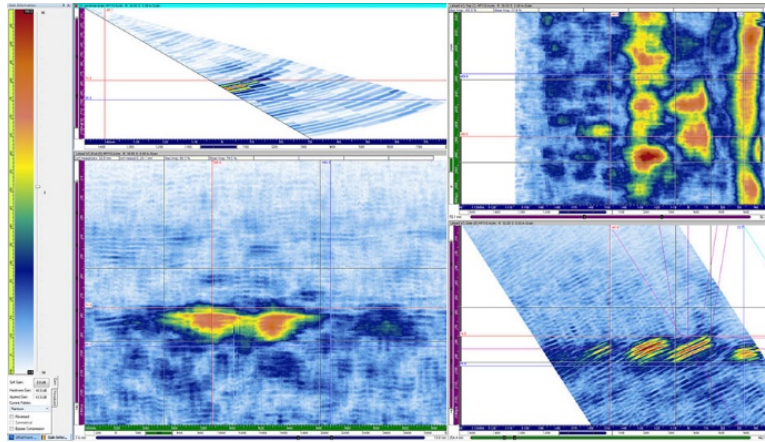
Tip signals were not seen from the CASS side for Flaw 1, which was 10% through-wall. Tip signals were also not seen with the 500 kHz PA probe for Flaw 4, which was 16% through-wall and on the far side of the weld. Flaw 2 (20% through-wall, axial) showed a tip signal from the skew 0° side but not the skew 180° side with both the 500 and 800 kHz probes. Note that from the previous discussion on SNR for the axial flaws and Figure 7-51, the skew 0° signals were much weaker for Flaw 2 than the skew 180° signals. Nevertheless, it was the skew 0° data that showed apparent flaw tip signals. Overall, and as expected, the 800 kHz probe performed better than the 500 kHz probe in both the number of tips observed and the resulting depth RMSE. This is not surprising because of the smaller spot size of the 800 kHz probe (see Chapter 7.1.1.4). Although depth sizing acceptance criteria in performance demonstration have not yet been established for CASS components in the ASME Code, such criteria are defined for DMWs and wrought austenitic stainless steel as an RMSE tolerance of 3.0 mm (0.125 in.); see Section XI, Mandatory Appendix VIII, Supplement 10(3.3)(c) and Supplement 2(3.2)(b). This tolerance was exceeded by the 500 kHz probe but was met by the 800 kHz probe when tips could be observed. Note that, due to the small number of measurements, RMSE may not be a good indicator; the comparison to acceptance criteria is illustrative only.

Figure 7-56 shows an example of detecting the tip of Flaw 3 (20% through-wall) with the 500 kHz probe. The tip was not visible at the lowest refraction angle of 30°, but it came into view as the angle was increased to 39° and 45°, as indicated by red arrows. This demonstrates a key advantage of PA-UT: the main flaw response and the tip response may be best visualized at different refraction angles, which can be acquired with a single probe in a single scan.

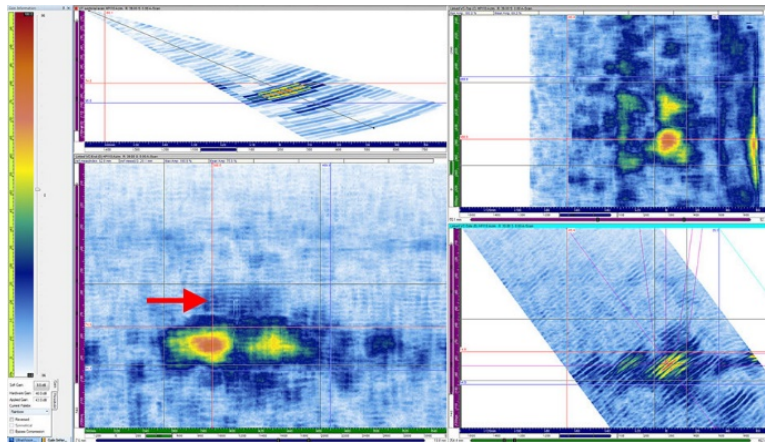
Figure 7-57 illustrates a situation with axial Flaw 5 (40% through-wall) where the tip signal is visible at a low refraction angle, but it became brighter than the main corner response at higher angles. Note that an artifact (red arrow) complicated length sizing of this flaw. The relative consistency of the artifact signal at the different refraction angles compared to that of the corner response helped reveal that it was not part of the flaw, although it did reduce the measured SNR.

Figure 7-58 shows an example of a far-side tip detection of Flaw 4 (16% through-wall) with the 800 kHz probe. The material and grain structure changes through the weld can reduce SNR in far-side examinations; however, the tip is still visible, albeit faintly. Note that the tip of this flaw was not visible with the 500 kHz probe.

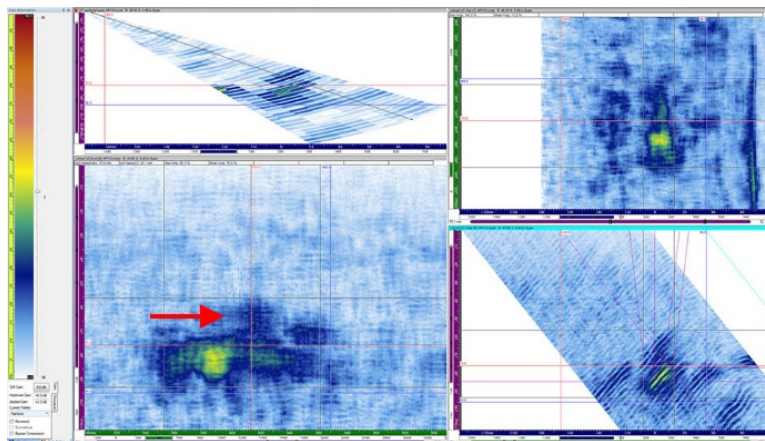




30°

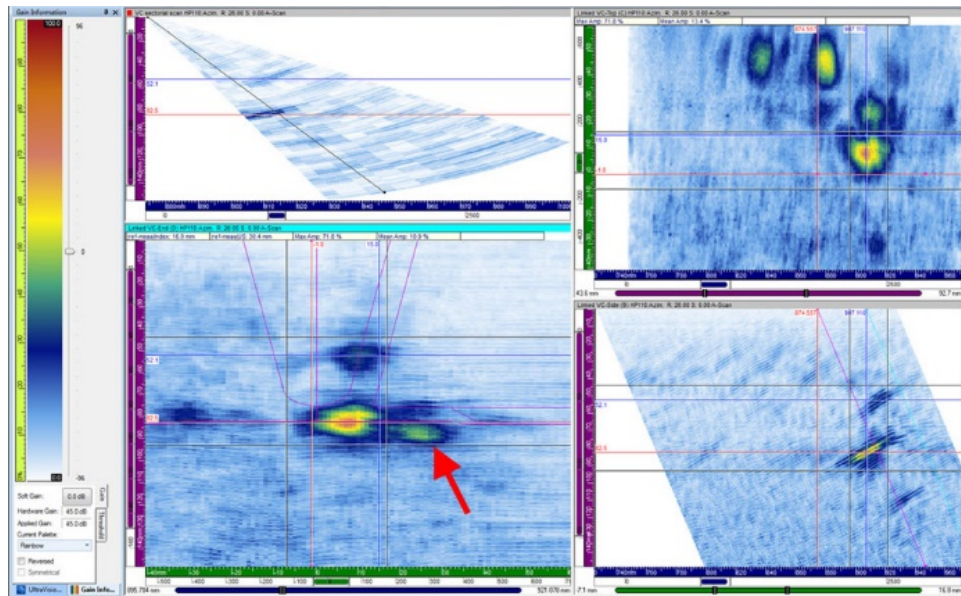


39°

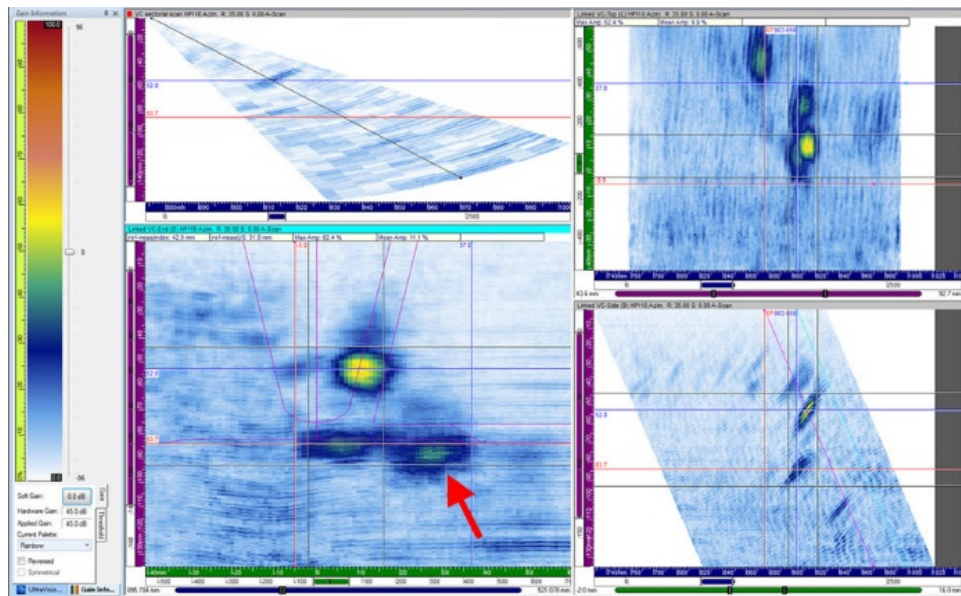


45°

**Figure 7-56 An Example of Improved Tip Visualization with Increasing Refraction Angle.** Shown are scans of Flaw 3 (20% through-wall) with the 500 kHz PA probe. The tip, best visualized in the B-scan and D-scan, begins to appear at 39° and is stronger (compared to the corner response) at 45° (red arrows). Clockwise in the panels: sectoral view, C-scan, B-scan, and D-scan.



26° (32° impaction angle)



35° (45° impaction angle)

**Figure 7-57 Example of a Tip Signal that is Stronger than a Corner Response. This figure shows Flaw 5 (40% through-wall, axial) as scanned with the 800 kHz PA probe. The tip, visible in the B-scans and D-scans, becomes brighter than the corner at 35°. An artifact, whose signal intensity remains relatively consistent, is indicated by the red arrow. Clockwise in the image: sectoral view, C-scan, B-scan, and D-scan.**



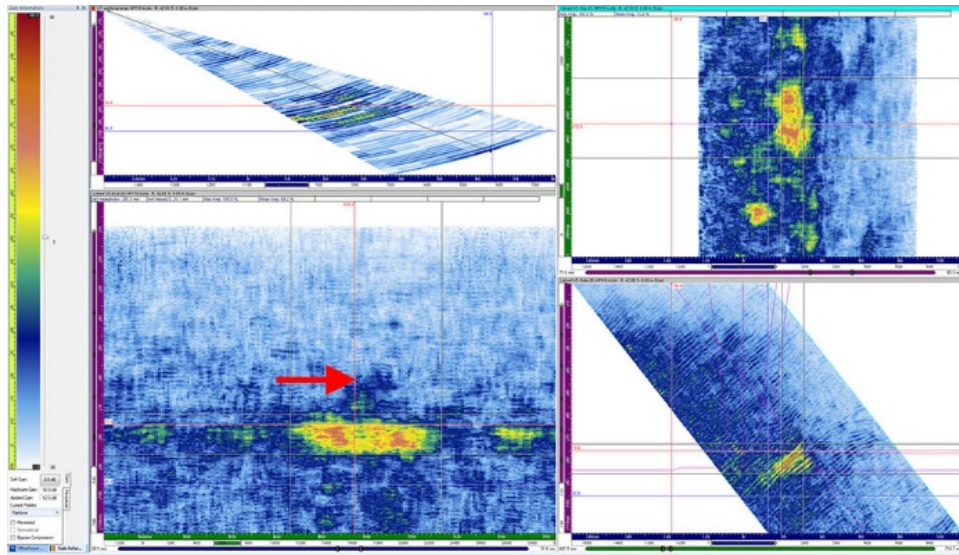


**Figure 7-58 Example of a Tip Signal in a Far-Side Detection. This figure shows Flaw 4 (16% through-wall) as detected by the 800 kHz PA probe at 42°. The flaw tip is indicated by the red arrow. Clockwise in the image: sectoral view, C-scan, B-scan, and D-scan.**

Tips of all three circumferential flaws were detected from the carbon steel side with the 1.5 and 2.0 MHz probes. Figure 7-59 shows an example of a tip response from Flaw 1 (10% through-wall). The tip is not as clearly resolved on the D-scan, but the B-scan shows a distinct separation between the tip (red arrow) and the crack corner. The height RMSE results for both probes were below the 3.0 mm (0.125 in.) ASME code limit (see Tables 7-28 and 7-29). It is important to note that the work in this Chapter was not a blind study, and that detection and measurement of the axial flaws with the 1.5 and 2.0 MHz probes particularly benefited from the analysts' a priori knowledge of true state. For example, Figures 7-52 and 7-60 show the detection of Flaw 5 from both probe skews with the 2.0 and 1.5 MHz probes, respectively. Artifactual echoes make the corner difficult to isolate and obscure the tip signals. Figure 7-61 shows a comparable scan of a no-flaw region with the 1.5 MHz probe; although the image is cleaner, some artifact signals persist. See also Figure 7-54, the 2.0 MHz scan of a no flaw region.

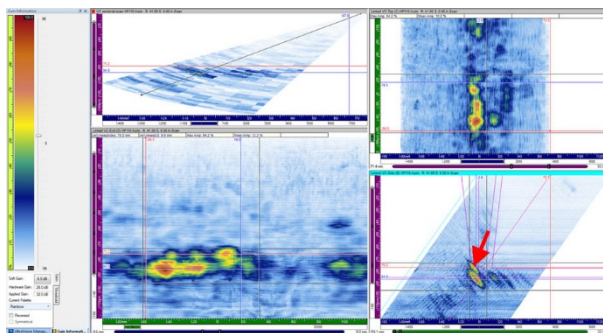


**Figure 7-59 Example of a Tip Signal in a 10% Through-Wall Flaw showing Flaw 1 as Detected by the 1.5 MHz PA Probe at 41°. The red arrow indicates the tip signal, which is better resolved in the B-scan than in the D-scan. Clockwise in the image: sectoral view, C-scan, B-scan, and D-scan.**

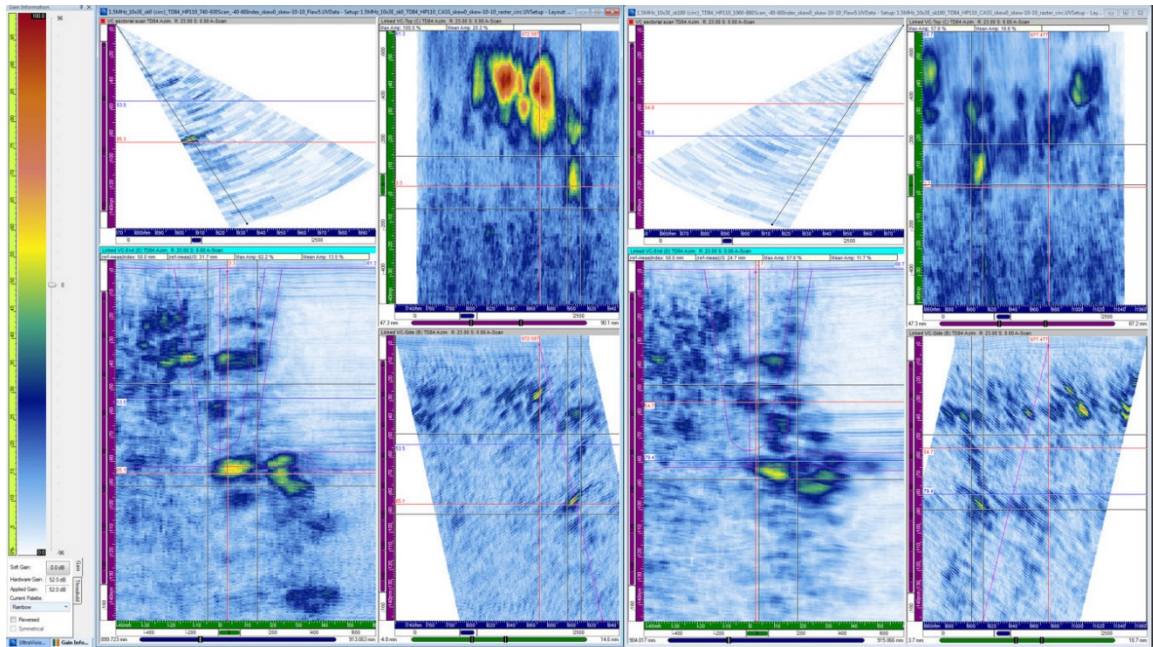


**Figure 7-60** Detection of an Axial Flaw at 1.5 MHz. Spurious signals in and around the weld region complicate detection and measurement of the flaw. Clockwise in the panels: sectoral view, C-scan, B-scan, and D-scan.

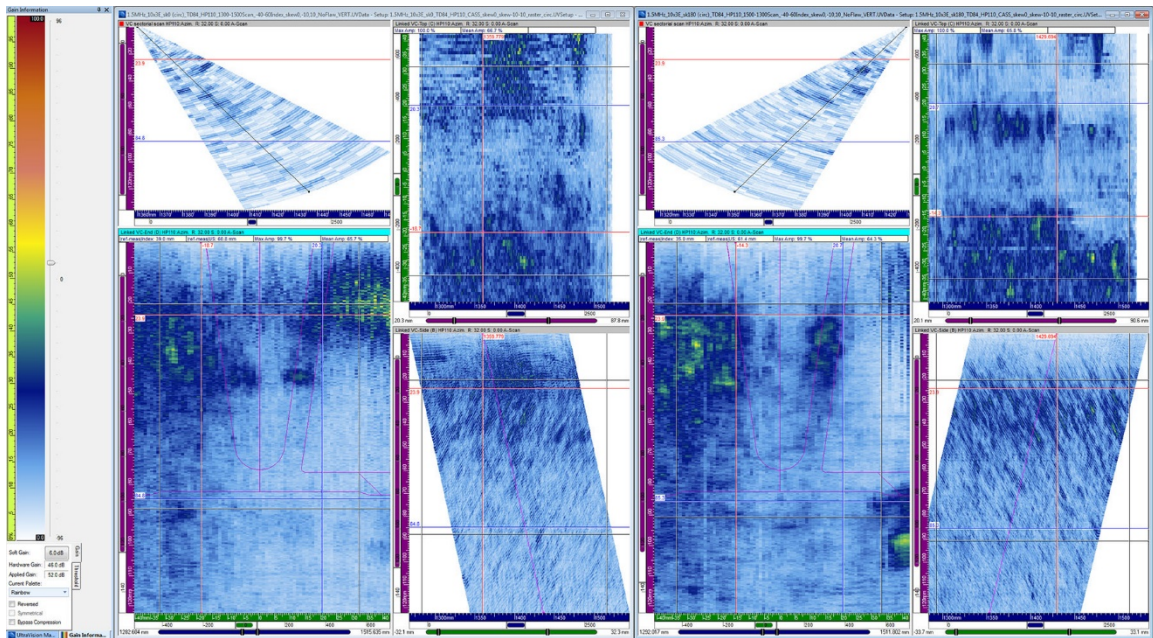


**Figure 7-61** The No-Flaw Region as Scanned by the 1.5 MHz PA Probe. Clockwise in the panels: sectoral view, C-scan, B-scan, and D-scan.



#### 7.5.1.4 Artifacts

Artifact analysis was possible in this study because implanted flaw positions and lengths were known from ET and approximate flaw depths were provided by FlawTech; otherwise, in blind studies, artifacts could be mistaken as flaws or flaw tips. Here, artifacts are defined as signal responses that originate from a source other than an implanted flaw or a known geometrical feature (such as counterbore). Potential sources of artifacts may be weld fabrication flaws or imperfections around an implanted flaw coupon. The response depth and circumferential location of detected signals, in light of targeted flaw locations, helped identify signals as artifacts. For example, Figure 7-62 shows the TD, 800 kHz scan of Flaw 3 at 29°. The artifact responses in this figure (circled in red) approximately form an arc shape in the circumferential direction above the flaw response. However, these responses did not occur at a depth from the OD that would correspond to a tip response (Flaw 3 was 20% through-wall, so the tip would be approximately 68 mm or 2.7 in. from the OD), nor did they appear as ID connected flaws. Indeed, these signal response depths were shallower, with depths from the OD surface of 43–57 mm (1.7–2.2 in.). These signal responses were therefore interpreted as implantation artifacts. For comparison, an artifact signal response in a no-flaw scan, encircled in red in Figure 7-63, were even closer to the OD surface and had no indication of ID connectedness; thus, they appeared to be embedded flaws, likely welding fabrication flaws. Therefore, in specimens with implanted flaws, the shape of the circumferential extent of an artifact response and the proximity to an implanted flaw corner response could provide important clues to the nature of artifacts. Note that with in situ grown cracks, implantation artifacts would not be expected, but welding fabrication flaws may still be present. Artifacts pose a significant problem if they are mistaken for actual flaws in field examinations. Action taken to further investigate, or even initiate repairs, can be very costly in terms of both time and money. Experienced field examiners are able to use information from the scans to differentiate between actual flaws and artifacts, such as SNR, flaw location (e.g., is the flaw ID surface breaking or is it within the weld material), and sizing. Although it is important to understand the source of potential artifacts, false calls cannot be entirely avoided.

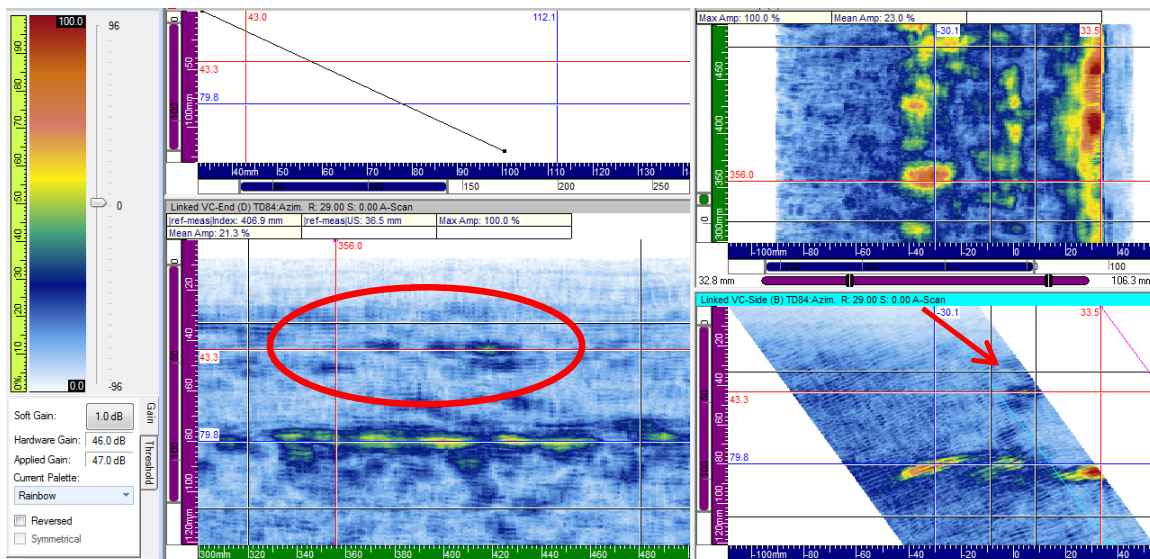


**Figure 7-62 Possible Implantation Artifact. Scan of Flaw 3 (20% Through-wall) at 800 kHz, 29° refracted angle, TD84. Circled in red are artifacts that approximately form an arc above the flaw corner response, possibly indicating the edges of the implanted flaw coupon.**

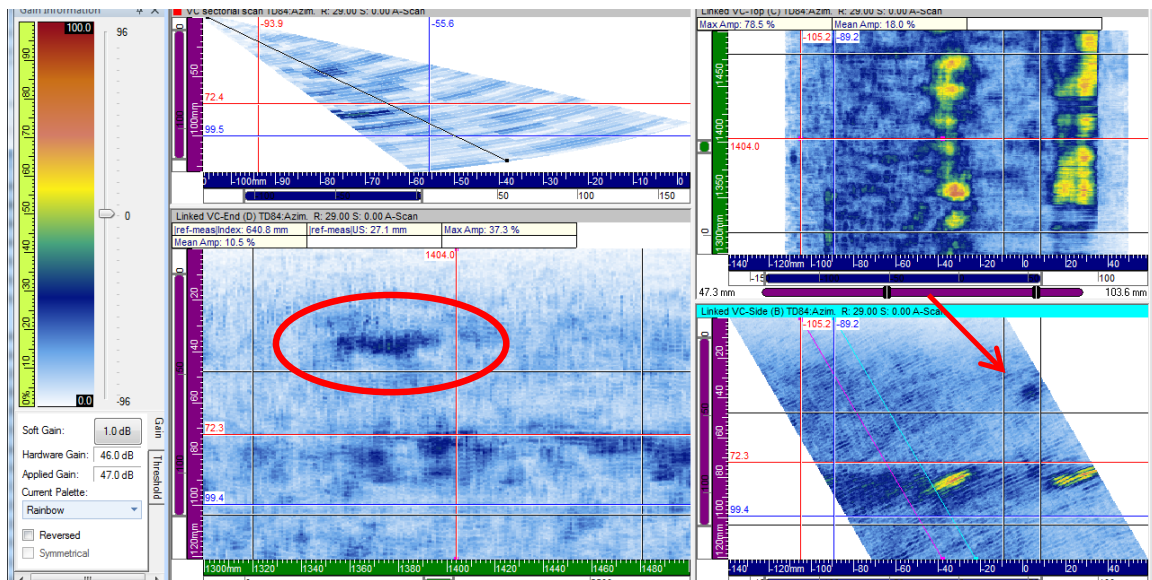


**Figure 7-63 Possible Fabrication Artifact. Scan of a no-flaw region at 800 kHz, 29° refracted angle, TD84.**

## 7.6 Summary and Discussion

PA and conventional UT methods were used to examine five implanted TFCs in a CASS-to-carbon steel DMW mockup from the CASS side of the weld. LF (500 kHz) TRL probes and 500 and 800 kHz PA TRL probes were used to examine both circumferentially- and axially-oriented flaws, and 1.5 and 2.0 MHz PA probes were used from the carbon steel side. All of the implanted flaws in this specimen were detected; however, the axial flaws were not detected with the highest frequency probe (2.0 MHz).

The 500 kHz PA method outperformed the two conventional 500 kHz probes in all aspects of the study, including SNR, flaw depth sizing accuracy, and flaw length sizing accuracy. Detection and characterization benefits from assimilation of responses using multiple refraction angles (i.e., produced using multiple focal laws), giving advantage to PA technology. In particular, line scan data can be merged to simultaneously show all angles and all lines, allowing for a full view of the entirety of the scan data. Raster scan data can be reviewed angle-by-angle, which is facilitated by all the data being collected in one scan into a single data file. In this specimen, however, detection did not further benefit from either of the two different PA focusing types (TD vs. HP) and only marginally benefited from PA beam skews at  $\pm 10^\circ$  off-normal. This is most probably because the flaws are very planar.

Length sizing, completed at the -6 dB (half amplitude) level, was within the ASME Code Section XI, Appendix VIII performance demonstration standard (for wrought materials) of 19 mm (0.75 in.) RMSE using the 500 and 800 kHz PA probes. Note that the Appendix VIII value for sizing accuracy was used herein only as a guideline, as there were only a statistically limited number of data points in this study and performance demonstration standards for CASS flaw characterization have yet to be written. The 30° conventional probe was also within the Code-acceptable length-sizing range, but the 45° conventional probe was not. Dropout in the flaw response signals were observed with the 800 kHz PA probe but not with the 500 kHz PA probe; however, length sizing overall was more accurate with the 800 kHz probe when dropout was ignored. It should be emphasized that the lack of dropout observed at 500 kHz along with an



overall higher SNR (compared to 800 kHz) is consistent with previous work showing that 500 kHz is best for flaw detection in CASS while higher frequencies can be used for flaw characterization (Anderson et al. 2007; Diaz et al. 2012). Overall, it was observed that the 500 kHz PA probe displayed higher sensitivity and less signal dropout, with an average SNR advantage over the 800 kHz PA probe of about 3 dB, or about 40%. The 500 kHz PA probe also revealed fewer artifacts that may result in false calls. The 800 kHz probe performed better at length and depth sizing. From the carbon steel side, the 1.5 MHz probe was within the ASME standard, but the 2.0 MHz probe was not.

Flaw depth measurements were made based on flaw tip responses, if detected. More flaw tips were visible with the 800 kHz PA probe than with the 500 kHz PA probe. No tips were visible with the conventional probes, and tips were not visible from the shallow 10% through-wall flaw (Flaw 1) from the CASS side with any probe. Flaw depth sizing was within the ASME Code Section XI, Appendix VIII performance demonstration standard (for wrought materials) of 3.2 mm (0.125 in.) for all the PA probes (when tips were observed) but not for the 500 kHz conventional probe. From the carbon steel side, tips were readily visible.

Overall, it was observed that the 500 kHz PA probe displayed higher sensitivity and less corner signal dropout, with an average SNR advantage over the 800 kHz PA probe of about 3 dB. The 500 kHz PA probe also revealed fewer artifacts that may result in false calls. However, the 800 kHz probe performed better at length and depth sizing. Therefore, it may be most appropriate to use the 500 kHz PA probe for flaw detection and identification and the 800 kHz PA probe for flaw characterization while avoiding the use of conventional probes in CASS material.



## 8 CONDUCTING EFFECTIVE AND RELIABLE EXAMINATIONS IN CASS PIPING WELDS

Results and conclusions from domestic and international research, including investigations conducted by nuclear regulatory agencies, research and development laboratories, NPP design organizations, and utilities with operating plants, have been reviewed in the development of this report. An objective assessment of this research highlights certain issues in regard to performing reliable UT field examinations for CASS weldments. These include:

- Selecting appropriate UT frequencies, propagation angles, and beam forming methods for establishing effective sound fields to detect, then characterize, flaws in varied coarse-grained CASS microstructures
- The importance of using encoded data with off-line analyses for the discrimination between cracks, geometrical reflectors, and material noise inherent in CASS
- The use of UT modeling to optimize examinations, providing preliminary validation of search unit design, theoretical sound field intensities, and potential for adequate volumetric coverage
- Training examiners through specialized instruction in CASS microstructures that may be encountered, resultant sound field effects, and methods to discriminate between flaws, geometry, and other coherent noise in CASS configurations.

The following subsections discuss and summarize the bases for PNNL technical positions in these areas.

### 8.1 Applying Adequate Sound Fields for CASS Examinations

#### 8.1.1 Optimizing Frequency

Early research pointed to the use of low frequencies for CASS examinations (Good and Van Fleet 1987, 1988; Good and Green 1989) to generate the longer wavelengths needed for penetration in these coarse-grained microstructures. The use of longer wavelengths was corroborated during several follow-on studies and round-robin trials (Bates et al. 1987; Dau et al. 1991; Heasler and Doctor 1996; Diaz et al. 2008b) in which LF-SAFT was shown to be effective, given the protocols employed, including application of multiple angles and directions, along with encoded data analytical techniques. Longer wavelengths allowed the methodology to gain traction among the CASS NDE research community. The work was performed in the 200–400 kHz domain with unique adjustable TRL wave transducers that enabled propagation angles to be changed between separate raster scans (Diaz et al. 1998). The LF-SAFT work continued to evolve and to be shown effective on a larger set of CASS microstructures. However, it had a shortcoming in implementation; the level of effort and duration for data acquisition was considerable, and thorough post-processing and data imaging analyses took longer than desired. Thus, while the time to acquire data could not be significantly reduced, a computer-based *data fusion method* (MPATS – see Chapter 6 and Appendix D) was developed to allow these analyses to proceed more efficiently.

The successful LF-SAFT approach was further extended with the development of advanced LF-PA ultrasonic techniques in the mid-2000s. Arrays operating at 500 kHz with appropriate active apertures for beam formation (steering and focusing) were applied, exhibiting promising results on CASS piping specimens with geometries that could accommodate probes with larger footprints (Anderson et al. 2007). The LF-PA methods significantly reduced data acquisition time for flaw

detection over LF-SAFT techniques, with imaging and data fusion (via merged data) capabilities being readily available as part of the PA off-the-shelf software. Over time, the PNNL LF-PA work has been corroborated by other research entities (Dennis 2012; Sakamoto et al. 2012a). Thus, the use of 500 kHz PA gained wider acceptability and has to-date been shown to exhibit the best overall detection for CASS piping welds with wall thickness greater than approximately 41 mm (1.6 in). As a result, this LF approach has been incorporated into ASME Code Case N-824, with the NRC imposing a condition to require 500 kHz PA methods for flaw detection in all thick-walled CASS examined under this Case. Recent evidence showing improved performance using low frequencies for CASS has also been observed during PNNL preliminary analyses of participants' detection and false call data collected during an EPRI-sponsored CASS round robin (EPRI 2017). As can be seen in Figure 8-1, data show that detection performance (as quantified by POD) is significantly improved for LF (500 kHz) PA-UT applications versus teams that employed PA-UT at 1.0 MHz and above. In addition, the preliminary assessment indicates that FCP was also reduced with the use of lower frequencies. An initial PNNL analysis of the data has been completed (Jacob et al. 2018). PNNL's full analysis will remain unpublished for the present in order to maintain security of the specimens.

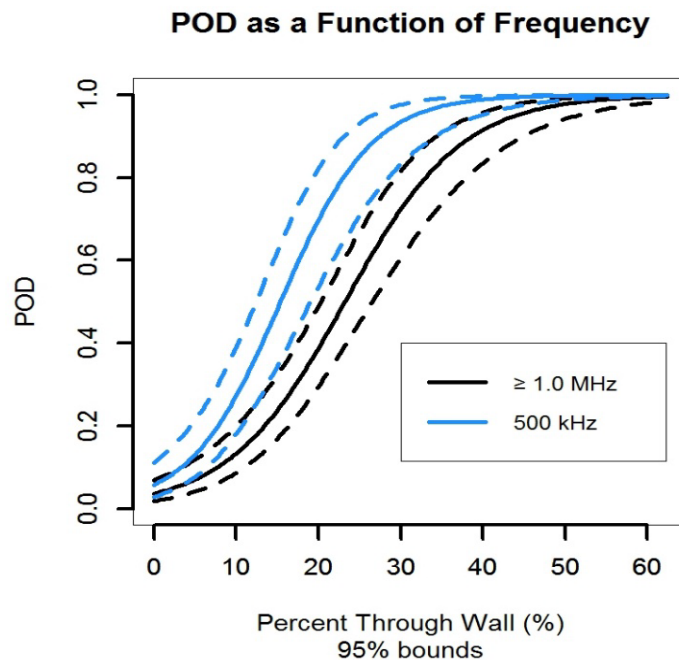


**Figure 8-1 POD Curves for 500 kHz versus 1.0 MHz and Greater Frequencies Applied During EPRI CASS Round Robin Exercise. Note the improved POD for the lower frequency application.**

PNNL has also performed research into CASS weldments for thinner-walled piping [41 mm (1.6 in) or less in wall thickness] (Diaz et al. 2012). It was shown that 800 kHz PA performed better for overall detection, exhibiting higher SNRs than similar PA transducers operating at 1.0 MHz and above on pressurizer surge line specimens as well as on thin-walled calibration specimens loaned to PNNL by EPRI. It was concluded that 800 kHz should be applied for components with these wall thicknesses for initial flaw detection. Higher frequencies (up to 2.0 MHz) are recommended, along with raster scanning techniques, only after detection to better characterize these flaws. In many cases, flaw tip responses were detected in these thin-walled specimens which allows for acceptable through-wall depth-sizing.

Thus, one key to reliable examinations has always been to apply an optimum frequency, and in the vast majority of CASS microstructures that have been observed, LF (less than 1.0 MHz) PA-UT methods allow for coherent sound field penetration while maintaining sufficient resolution for effective flaw detection. Since it is not currently feasible to predict or otherwise identify component field microstructures (type, orientation, and sizes of grains) prior to examination, and because these microstructures typically change as a function of spatial location on the component, it is necessary to apply the lowest frequency that has been demonstrated to be most effective for initial detection of flaws in all microstructures. In certain cases or areas/ microstructures of piping, a LF application may be superfluous, but it would be imprudent to assume reliable applications can be achieved, and to risk flaws going undiscovered, by applying higher frequencies for initial detection screening. Based on the literature reviewed, the data compiled at PNNL over the past 40 years, and recent observations in the EPRI CASS round robin, 800 kHz would ensure the appropriate wavelength for optimal detection performance in components under 41 mm (1.6 in.).

Therefore, as supported by the discussion above, it is paramount that 500 kHz be used for thicker-walled CASS [greater than or equal to 41 mm (1.6 in.)] and it is highly recommended that lesser wall thicknesses [less than 41 mm (1.6 in.)] employ only a slightly higher (800 kHz) examination frequency for purposes of initial flaw detection.

### **8.1.2 Applying Effective Beam Propagation Angles**

Another important aspect supporting reliable CASS examinations is the use of an effective range of propagation angles. As previously noted, a large body of work conducted at PNNL has shown that it is not feasible to predict microstructural variability as a function of spatial location on the piping, and since certain angles appear to be more effective for various microstructures, the use of multiple angles may allow for these “windows” of CASS materials to be accessed in order to facilitate beam propagation with less overall distortion and signal loss (Diaz et al. 1998; Anderson et al. 2007; Diaz et al. 2012; Crawford et al. 2014). The resulting effect on the ultrasonic beam can be significant enough to cause a loss of detected signal even with a perfect reflector, such as a smooth, machined block end, which approximates an ideal 100% through-wall reflector. This multi-angle approach has also been observed by other NDE research organizations, both domestic and international (Kurozumi 2004; Dennis 2012; Sakamoto et al. 2012b).

Further work to specifically assess whether certain dominant angles of propagation could be expected to perform well in multiple CASS microstructures has been recently completed at PNNL and is detailed below. The work was conducted using LF-PA techniques on a set of CASS specimens that exhibited a relatively wide range of microstructural variation; these specimens included grain sizes that are believed to be in a range typical of those present in field installations. An additional fine-grained, wrought stainless steel (WSS) specimen was included as a control. In order to normalize the results for all specimens, a machined, end-of-block reflector was used as a target, which represents an ideal, 100% through-wall reflecting source. A set range of propagation angles (as determined by incremental focal laws in the operating software) was used for each specimen and end-of-block response.

#### **8.1.2.1 Description of Specimens**

Seven CASS specimens and one WSS specimen were selected for this study. The specimens consisted of pipe sections that ranged in wall thickness from approximately 61 to 85 mm (2.4 to 3.3 in.). Table 8-1 lists the different specimens used, the microstructure along with the average and maximum grain sizes. Microstructures included equiaxed, columnar, and mixed types. These

different grain sizes and structures can be seen in figures 8-2 through 8-8, which show polished and etched ends for each specimen. The revealed grain structure was taken to be representative of the entire specimen. Note that the grain structures can vary throughout a specimen, so the revealed grain structures may not truly represent the actual grain structures at the locations where data were acquired. However, to reduce costs of destructive testing and to preserve the specimens, only one section of each specimen was polished and etched. These polished ends were used to characterize the grain sizes and structures using a linear intercept method previously described (Anderson et al. 2007; Crawford et al. 2014). Most of these specimens have been examined and reported on previously; references that may include additional information about the specimens are provided in the figure captions. Note that specimen 14C-146 is discussed at length in Chapter 7 of this NUREG/CR.

**Table 8-1 Description of Specimens**

	<b>Outer Diameter mm (in.)</b>	<b>Wall Thickness mm (in.)</b>	<b>Grain Structure</b>	<b>Mean Grain Size, mm (in.)</b>	<b>Max Grain Size, mm (in.)</b>	<b>Single/ Dual Corner Access</b>
B-519E	845.8 (33.3)	58.4 (2.3)	Equiaxed/small	1.6 (0.06)	14.9 (0.59)	Single
Manoir	914.4 (36)	75 (3.0)	Equiaxed/small	*	*	Dual
ONP-D-5	914.4 (36)	63.5 (2.5)	Equiaxed/coarse	3.9 (0.15)	20.3 (0.80)	Single
B-519C	845.8 (33.3)	61 (2.4)	Columnar	5.5 (0.22)	48.5 (1.91)	Single
Westinghouse	711.2 (28)	64 (2.5)	Columnar/banded	3.1 (0.12)	16.3 (0.64)	Dual
IHI SW	914.4 (36)	84 (3.3)	Mixed/banded	2.0 (0.08)	25.0 (0.98)	Dual
14C-146	914.4 (36)	84.8 (3.34)	Mixed/banded	2.1 (0.08)	40.9 (1.61)	Single**
WSS	914.4 (36)	63.5 (2.5)	Fine	*	*	Dual
*Mean grain size not measured.						
**Scanned across two different regions.						





**Figure 8-2 Specimen B-519E.** This specimen from PNNL has a smaller-to-medium grain equiaxed microstructure. Figure adapted from PNNL-23393 (Crawford et al. 2014).



**Figure 8-3 Manoir Ring.** This pipe segment from the Manoir Foundry exhibits a small-grained equiaxed microstructure.



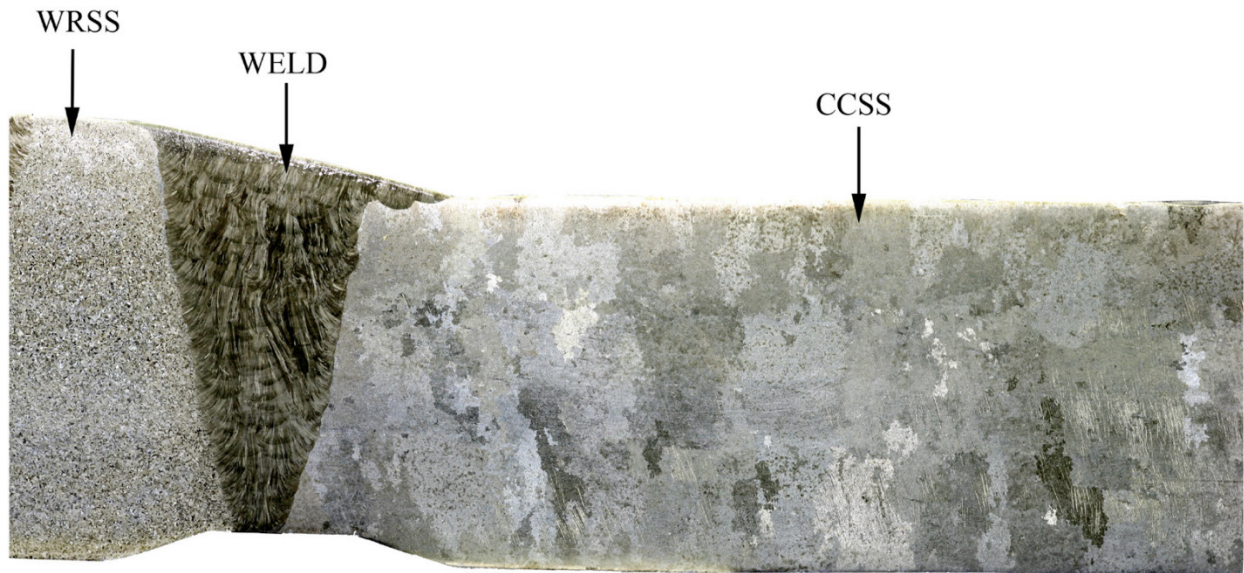


**Figure 8-4 Specimen ONP-D-5.** This specimen originated from the Westinghouse Owners Group and has a larger, coarse-grained equiaxed microstructure. Figure adapted from NUREG-CR/6933 (Anderson et al. 2007).



**Figure 8-5 Specimen B-519C.** This specimen from PNNL has a medium-grained, columnar microstructure with little or no banding. Figure adapted from PNNL-23393 (Crawford et al. 2014).

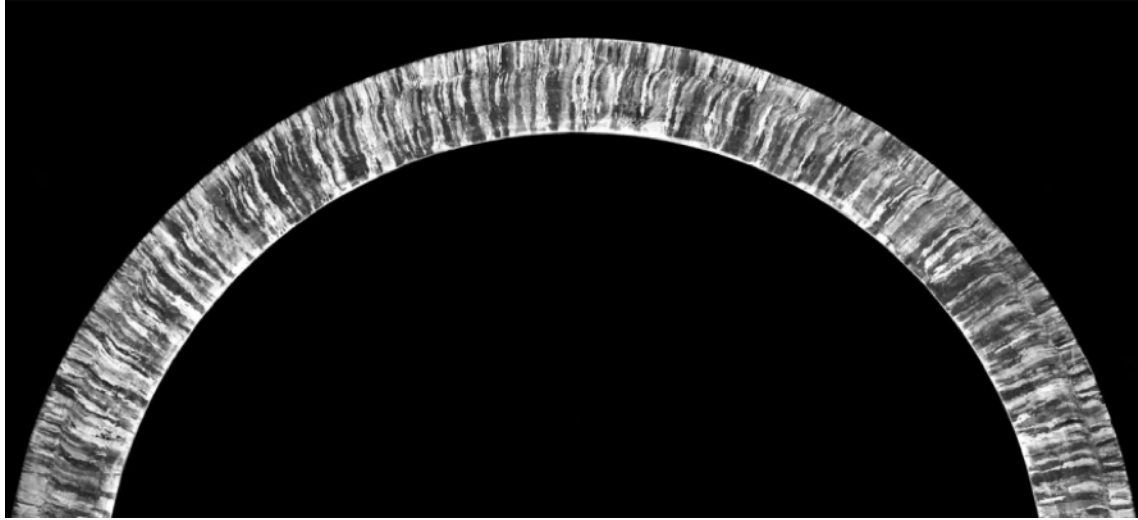


**Figure 8-6** Westinghouse Specimen. This specimen from Westinghouse, Inc. shows a columnar microstructure with large grains and some banding. Figure adapted from NUREG/CR-6933 (Anderson et al. 2007).

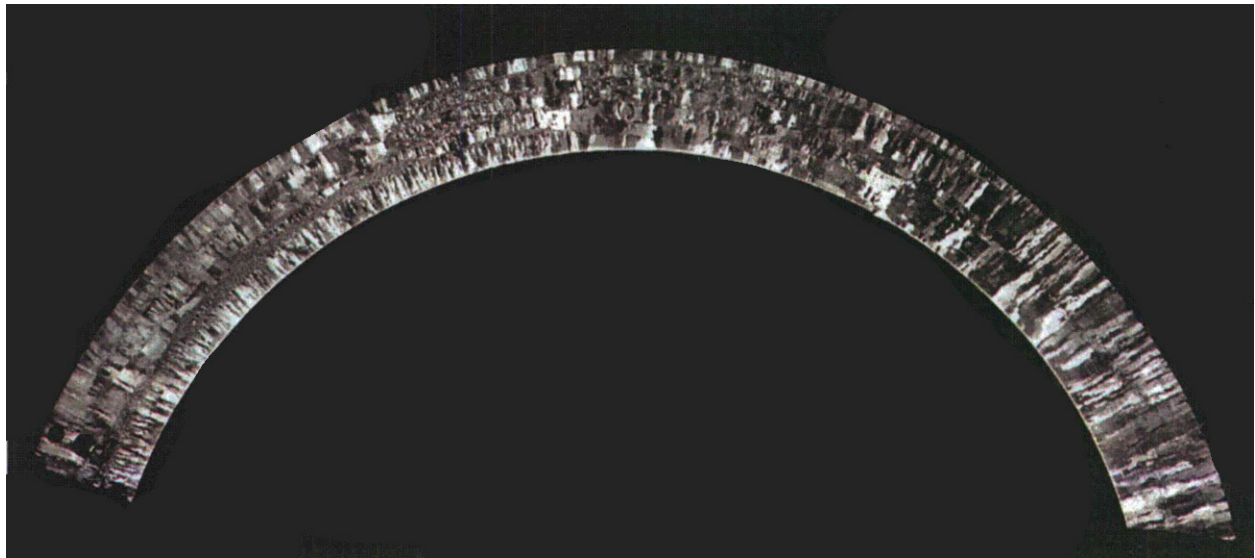


**Figure 8-7** IHI Southwest Specimen. Mixed/banded grain microstructure with considerable circumferential heterogeneity. Figure adapted from NUREG/CR-6933 (Anderson et al. 2007).



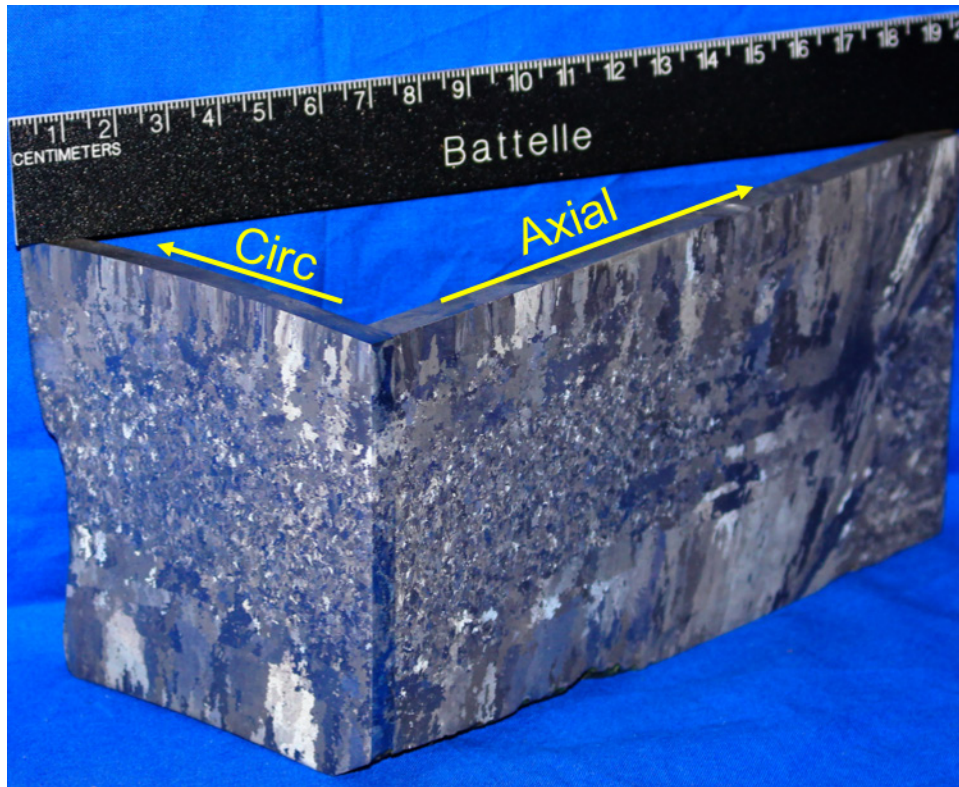


**Figure 8-8 Specimen 14C-146. Mixed/banded-grain microstructure, predominately equiaxed in the midwall regions and columnar near the OD and ID.**

Several specimens had both block ends accessible for scanning, but others had implanted or machined reflectors that inhibited scanning of one end; both ends were scanned when possible. Note that only one end of the WSS specimen was scanned, since the fine grain structure is homogeneous.

#### *8.1.2.2 Description of Ultrasonic Transducers*

Three PA-UT TRL transducers were used for data collection at frequencies of 500 kHz, 800 kHz, and 1.0 MHz [photographs and probe details are provided in Crawford et al. (2014)]. Contoured wedges were used with water coupling to maintain contact with the specimens' OD surfaces.

Based on a nominal speed of longitudinal sound waves in stainless steel of 5.64 mm/ $\mu$ s (0.222 in./ $\mu$ s), the wavelengths generated were approximately 11.2, 7.0, and 5.1 mm (0.44, 0.28, and 0.20 in.) for the 500 kHz, 800 kHz, and 1.0 MHz probes, respectively. Note that it is generally desirable for the grain size to wavelength ratio to be less than approximately 0.2 in order to be in the Rayleigh scattering regime and minimize grain interference (Wan et al. 2017). Overall, the mean grain sizes shown in Table 8-1 approximately meet this condition for the 500 kHz probe but not for the 800 kHz or 1.0 MHz probes. It is important to note, however, that individual large grains may have an effect on scattering that dominate the effect of many small grains (Anderson et al. 2007; Wan et al. 2017). Note that in columnar specimens such as B-519C, the maximum reported grain size may be along the length of a columnar grain.

Focal laws were developed and simulated in UltraVision using the full 10 $\times$ 5 element matrix in each probe for both transmitting and receiving. Due to the differences in specimen thicknesses,

focusing was recalculated for each specimen to maintain a constant-depth (also referred to as true-depth) focus, with the focal depth set to the specimen ID surface distance for each focal law, or metal path along the propagated angle. The focal laws ranged from 20°–70° in 5° increments—this same range of angles was used in data collection. A nominal longitudinal wave velocity of 5.64 mm/μs (0.222 in./μs) was used for the simulations. An example beam simulation for the 500 kHz transducer is shown in Figure 8-9. This simulation represents true-depth focusing on the ID surface for the thickest specimen: 14C-146, with a wall thickness of 86 mm (3.4 in). The dashed line indicates the highest angle where the sound field reaches the ID with at least –6 dB of the beam energy. Table 8-2 shows the highest incremental angle in the range for each focal depth that delivered at least –6 dB of the beam energy to the ID surface.

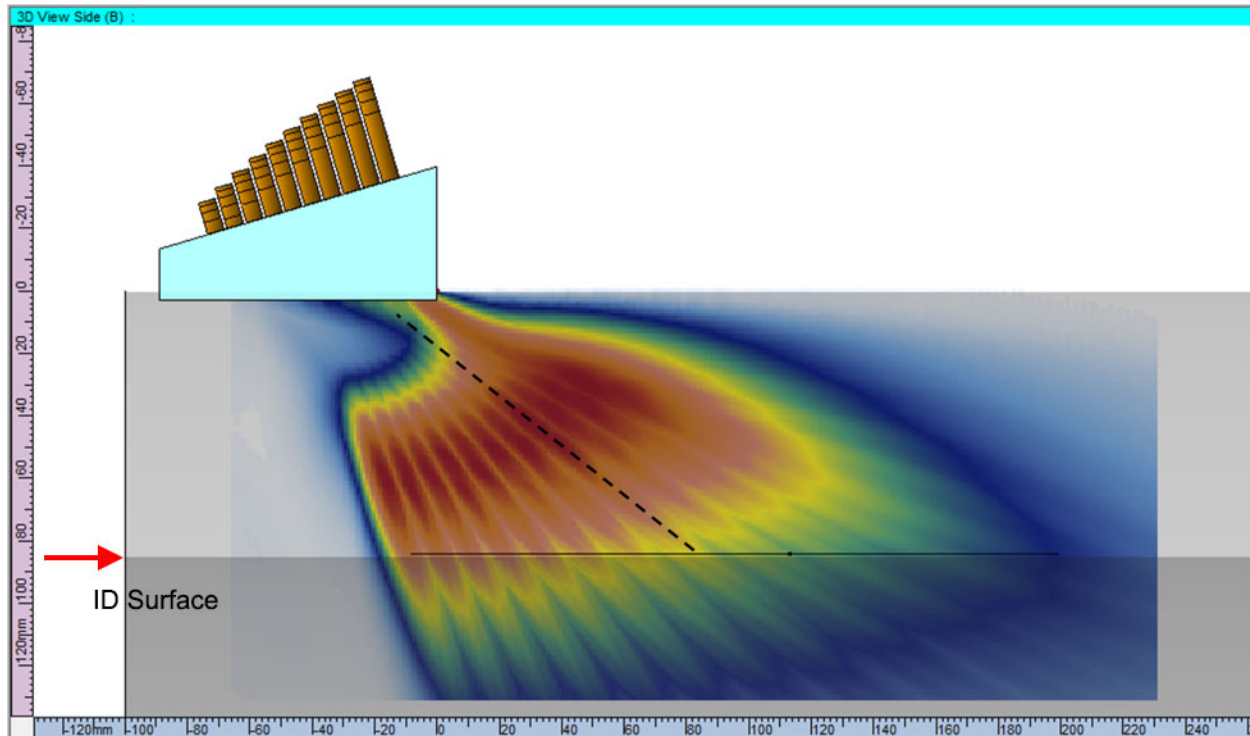


**Figure 8-9 Incremental Beam Simulations of 500 kHz TRL Transducer, 20°–70°**

**Table 8-2 Beam Models**

Focal Depth	Specimens	0.5 MHz	0.8 MHz	1.0 MHz
		–6 dB Angle	–6 dB Angle	–6 dB Angle
60–63 mm (2.4–2.5 in)	B-519E, B-519C, WSS, ONP-D-5, Westinghouse	70	60	55
83–84 mm (3.3 in)	Manoir, IHI SW, 14C-146	55	45	40

### 8.1.2.3 Description of Scans

Specimens were set up horizontally on a support structure. A ring track for an ATCO scanning unit was set up to be approximately concentric with each specimen's curvature. Raster scans were performed using a Zetec DYNARAY Lite and an MCDU-02 motor controller, both controlled

through UltraVision. The entire available specimen end was scanned, while avoiding regions with notches or other reflectors. Sections within about 50 mm (2 in.) from the edges of the blocks were not scanned due to the footprint of the probes. Table 8-3 shows the total length of the scans in the index (circumferential) direction. The index resolution was 2 mm (0.08 in.), and the scan (axial) resolution was 0.5 mm (0.02 in.). The end-of-block signal was peaked at about 80% full-screen-height at 20°. For scans, the full range of modeled refraction angles was used, 20°–70°, at 5° increments, except for the IHI specimen, which was only 155 mm (6.1 in.) wide. In that case, probes could only extend back far enough to allow a maximum angle of 45°.

**Table 8-3 Index Range**

Specimen	Index Range, mm (in.)
B-519E	74 (2.9)
Manoir skew 0	420 (16.5)
Manoir skew 180	450 (17.7)
ONP-D-5	200 (7.9)
B-519C	74 (2.9)
Westinghouse skew 0	500 (19.7)
Westinghouse skew 180	500 (19.7)
IHI skew 0	550 (21.7)
IHI skew 180	550 (21.7)
14C-146 section 1	300 (11.8)
14C-146 section 2	450 (17.7)
WSS	340 (13.4)

#### 8.1.2.4 Data Analysis

After data were collected on a specimen, the B-scan was used to select regions of the end-of-block response and material noise at the same depth for each refraction angle; Figure 8-10 shows an example of these regions. Only refraction angles with a discernable end-of-block response were used—for some specimens this was as high as 65°. Note that the 70° refraction angle never showed a definitive end-of-block response on any specimen (except for the WSS benchmark). Data in the selected regions were exported from UltraVision and imported into MATLAB for analysis.

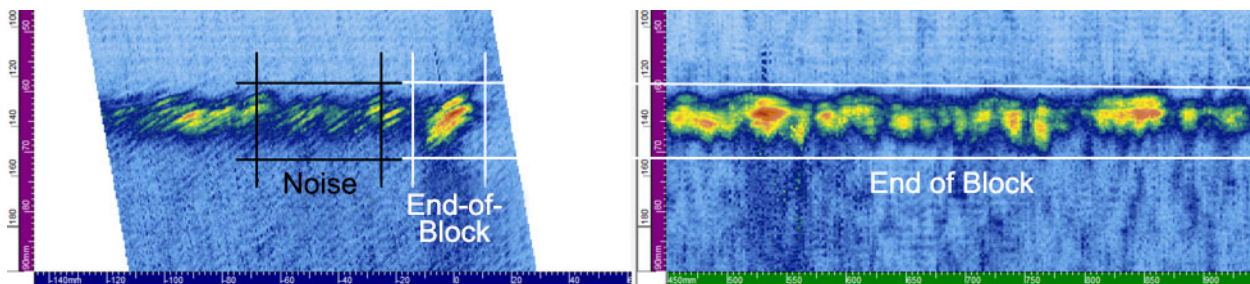


**Figure 8-10 Example of Acquired Data.** This figure shows an example of a B-scan (*left*) with end-of-block and noise regions enclosed, and the selected end-of-block D-scan (*right*).



An automated approach for data analysis was implemented in MATLAB to avoid subjectivity and to dramatically reduce the analysis time. Once imported into MATLAB, both the end-of-block and noise data regions were reformatted into maximum-amplitude end views, or D-scans. Figure 8-11 shows a comparison of the end-of-block D-scans from each scan at 30° refraction angle acquired at 500 kHz. Note that the extent of each scan depended on the specimen size (see Table 8-3), so the horizontal scale is not the same for all D-scans. However, the D-scans in Figure 8-11 are normalized to the same absolute signal intensity. The fine-grained WSS specimen is shown in the right, bottom-most panel. As expected, the end-of-block signal in the WSS specimen is strong and consistent along the entire length of the scan. This is in contrast to the IHI specimen (mixed/banded), where an end-of-block signal is barely identifiable, or to the ONP-D-5 specimen (equiaxed/coarse), where the end-of-block signal shows high spatial variability. With signal scattering and redirection varying from specimen to specimen and even within an individual specimen, it is not possible to predict the dropout, even with foreknowledge of the grain structure.

Next, echo-dynamic curves of the noise and end-of-block responses were calculated, representing the maximum signal (or noise) amplitude along the circumferential axis. The MATLAB program allowed some minor smoothing of the echo-dynamic curves by applying a filter to remove signal spikes caused by intermittent coupling issues or specimen surface roughness. The program then calculated the mean noise level and the 2:1 and 3:1 signal-to-noise threshold levels. Next, any regions where the corner signal fell below the 2:1 or 3:1 levels were flagged as “dropout” at that threshold level. Figure 8-12 shows an example of the echo-dynamic curves, the mean noise, and the 2:1 and 3:1 thresholds for the 500 kHz, 800 kHz, and 1.0 MHz probes (top to bottom in the figure). For each refraction angle, the program calculated the percentage of dropout at each threshold level, the length of each dropout region, the mean dropout length, and the maximum dropout length.

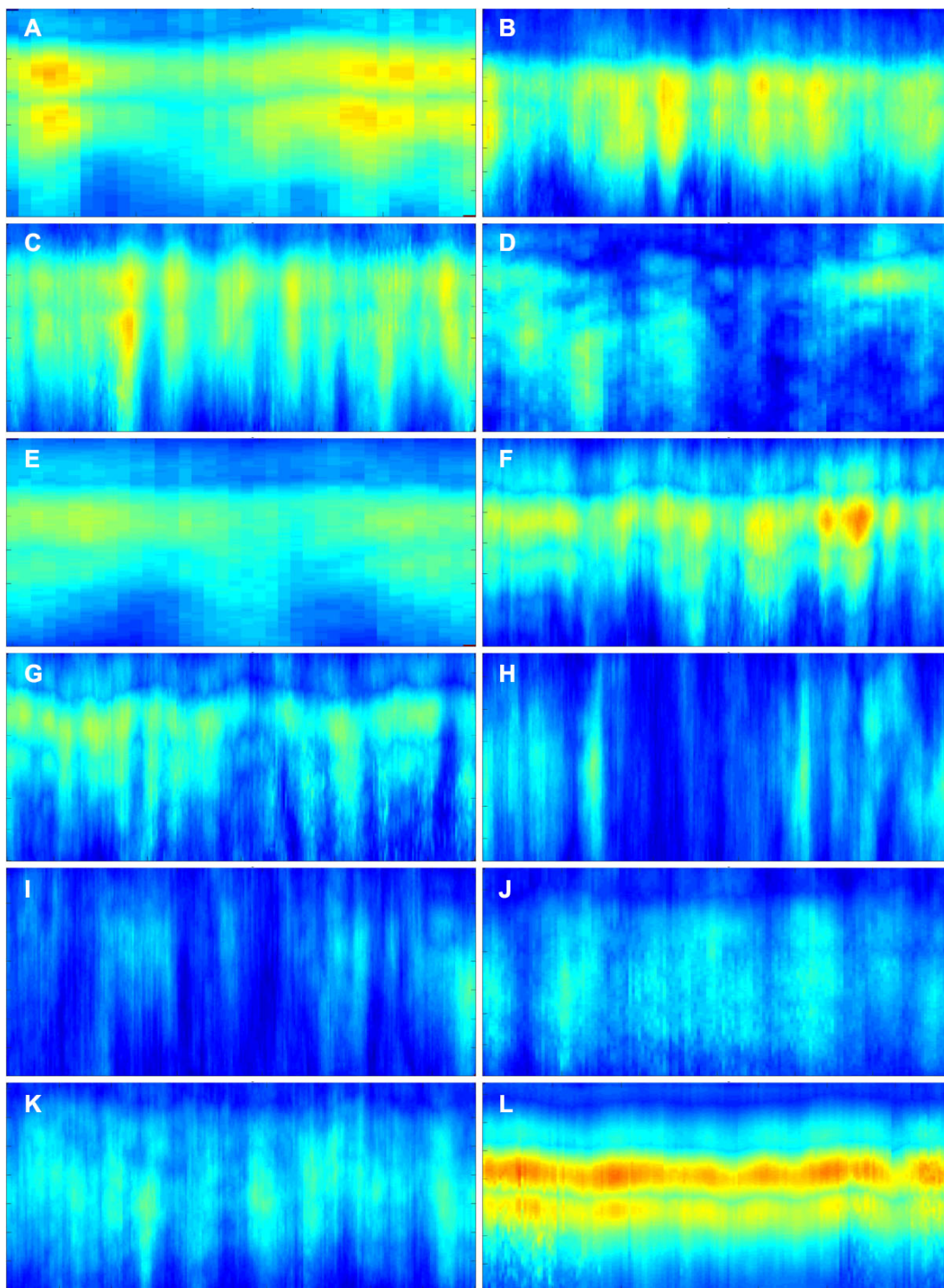


**Figure 8-11 End-of-Block Signal for All Specimens.** The end-of-block D-scan signal from each specimen at 500 kHz and 30° is shown. A) B-519E; B) Manoir (skew 0); C) Manoir (skew 180); D) ONP-D-5; E) B-519C; F) Westinghouse (skew 0); G) Westinghouse (skew 180); H) IHI (skew 0); I) IHI (skew 180); J) 14C-146 (section 1); K) 14C-146 (section 2); L) wrought stainless steel.

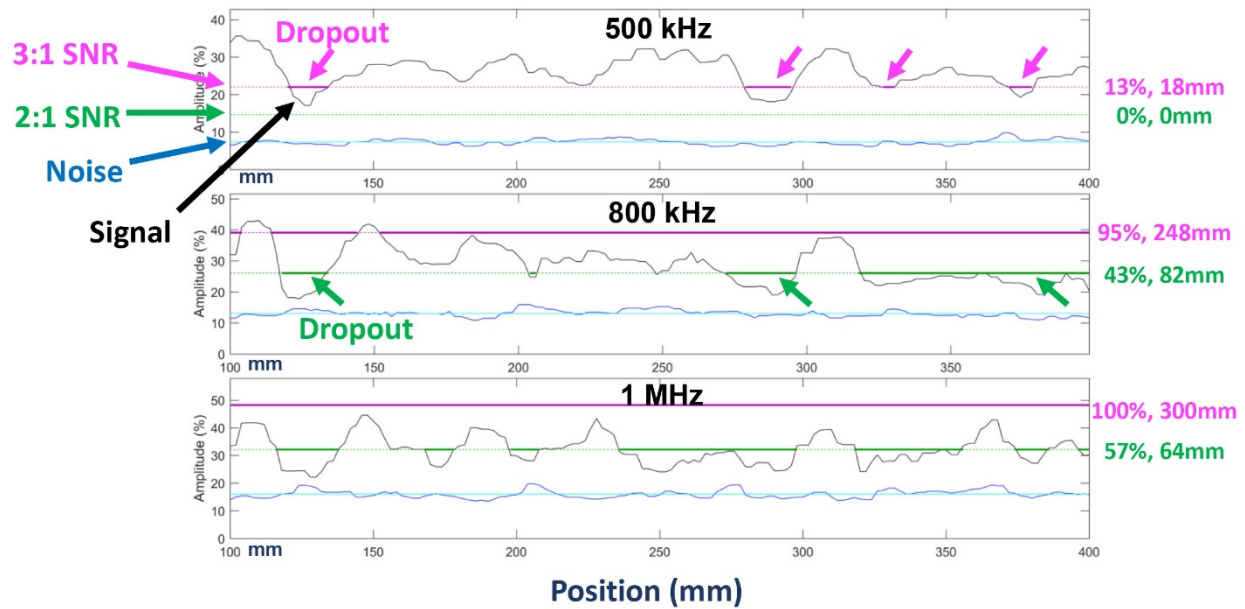


**Figure 8-12 Example of Data Analysis.** The end-of-block signal is shown as an echo-dynamic curve (black line). The mean noise (light blue line) was determined from the noise (dark blue line). Regions of dropout are identified as those with signal dropping below the 3:1 (pink) or 2:1 (green) SNR thresholds. Regions of dropout are shown with bold lines. Numbers on the right indicate the percentage dropout and maximum dropout length for each respective noise threshold. Data shown are from 14C-146 at 40°.

#### 8.1.2.5 Results

Figure 8-13 provides examples of the end-of-block signal responses and the associated signal dropout from the skew 180 scan of the Westinghouse specimen (columnar/banded microstructure) for a 25°–50° incremental range of focal laws at 500 kHz. This figure illustrates how the locations and severity of signal dropout can vary by focal law in a given specimen. For example, at 25° and 30°, dropout at the 3:1 SNR level occurred along most of the length of the block end, whereas at 40° and 45° there appears to be much less dropout, with the reduced signals isolated at only three or four locations.



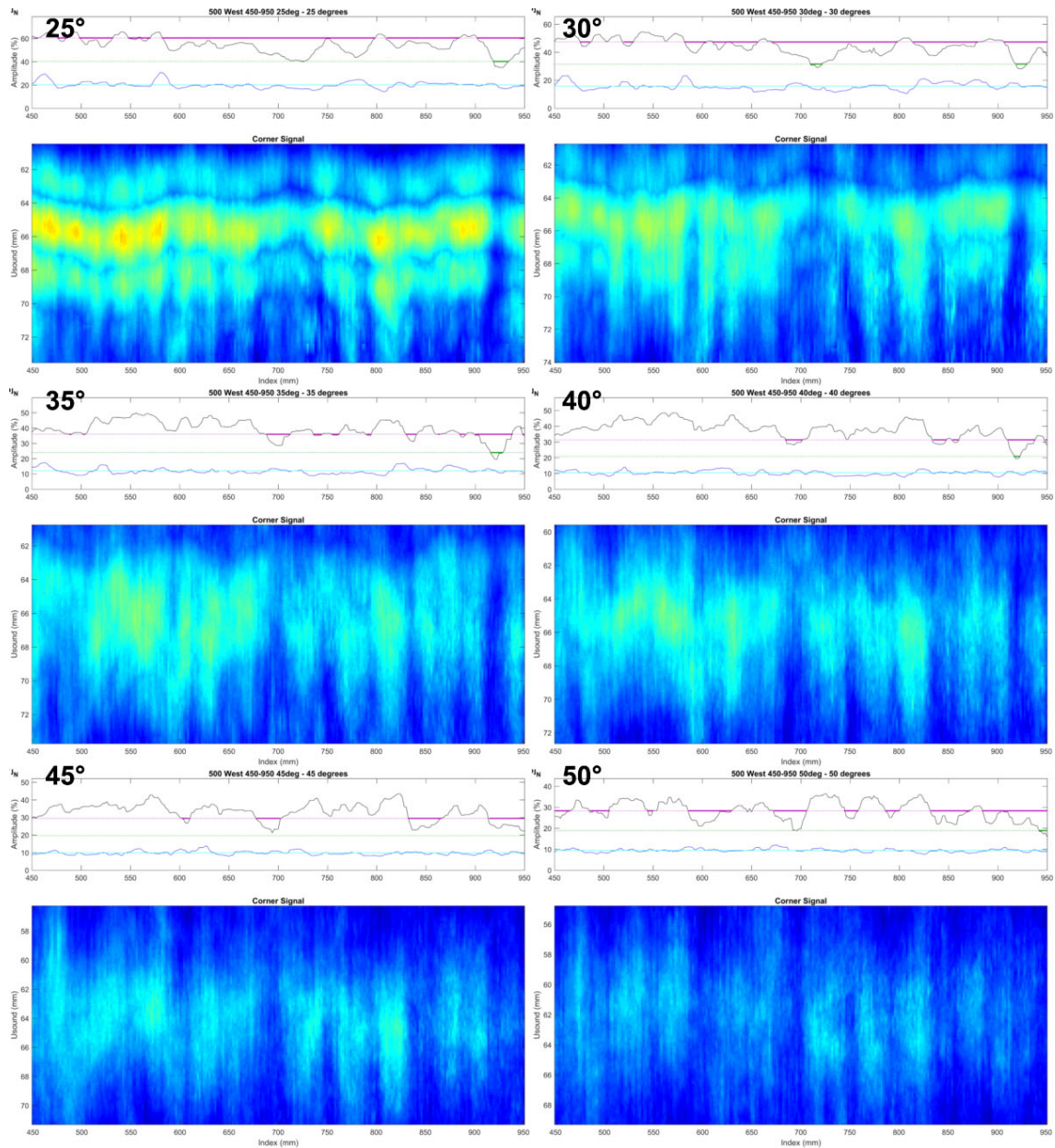


**Figure 8-13 Example Data from the Westinghouse Specimen. UT corner scan data and the associated 3:1 SNR dropout graphs are shown for 25°–50° refraction angles at 500 kHz.**

Figure 8-14 illustrates how the noise levels affected the end-of-block dropout at different refraction angles. This figure shows results from six of the 500 kHz scans as examples. The mean noise as a percentage of full-screen-height (FSH) and the percent dropout at 2:1 and 3:1 SNR (as a percentage of scan length) are plotted as a function of the refraction angle, with noise levels from the WSS scan included for comparison. For all cases, the noise was highest at the lowest refraction angle and decreased as the refraction angle was increased. The noise tended to level out at about 5%–10% FSH at the highest angles. The dropout was observed to be dependent on both the specimen and the noise level. In particular, specimens with the highest noise levels at low angles showed the most dropout at low angles. For example, ONP-D-5 (coarse-grain

equiaxed microstructure) and Westinghouse (columnar/banded microstructure) had noise levels near or above 30% FSH at the lowest refraction angle (above the nose level of the WSS specimen) and also displayed the highest dropout levels at that angle. By comparison, B-519C (all columnar microstructure) and 14C-146 (mixed/banded microstructure) had noise levels near 20% FSH at the lowest angle (at or below the noise level of the WSS specimen) and showed the least dropout. However, at the highest angles, where noise was lowest, all CASS specimens showed the most severe dropout. This is because, at these same high angles, the end-of-block signal intensity was weakest. At high angles, the combination of a longer metal path and probe focusing parameters when using TD (see Figure 8-9) resulted in more beam distortion and redirection through interaction with more grains. Note that the noise levels measured in the fine-grained WSS specimen were often comparable to those measured in the CASS specimens; however, there was zero dropout observed in the WSS specimen at any angle at both the 2:1 and 3:1 thresholds. This further indicates that, in addition to the noise level, the dropout is highly dependent on beam attenuation, distortion, scattering, and redirection due to CASS grain structures.

Table 8-4 shows the percentage of signal dropout at the 2:1 SNR level for each scan and each refraction angle. Data from all three transducers are included (top: 500 kHz, middle: 800 kHz, bottom: 1.0 MHz). The orange horizontal bars give an *at-a-glance* indication of the percentage of the scan that experienced dropout, with longer bars indicative of more dropout. The maximum dropout depicted by the orange bars is 100% of the scan length. Table 8-5 shows the maximum continuous dropout length at the 2:1 SNR level for each scan and each refraction angle, also including all three transducers. The red horizontal bars provide an indicator of the severity of the dropout and imply that any flaw with a length shorter than that depicted by the red bar would go undetected at the given refraction angle and probe frequency. The maximum tolerable dropout length depicted by the red bars was (arbitrarily) chosen to be 50 mm (2 in.).

Similar to Tables 8-4 and 8-5, Tables 8-6 and 8-7 show the percentage dropout and maximum continuous dropout length, respectively, for the 3:1 SNR threshold level. The tables show that the dropout is more severe (higher percentages and longer maximum lengths) at the 3:1 threshold level for most specimens. This is because it was common for the end-of-block signal to fall between the 2:1 and 3:1 SNR levels, resulting in comparatively less dropout at the 2:1 level than at the 3:1 level. This indicates that the signal levels were typically low enough that signals from approximately ideal, 100% through-wall reflectors do not consistently or reliably exceed 3:1 SNR levels in many CASS pipe specimens. The 3:1 SNR dropout threshold provided as little dropout as the 2:1 threshold for many refraction angles in the Manoir specimen (small-grain equiaxed), B-519C (columnar), and 14C-146 (mixed-grain banded).

The WSS specimen was also included in the tables to provide a direct comparison of CASS to a fine-grained material representing relatively insignificant effects on sound field propagation. Indeed, no dropout was observed in the WSS specimen at any refraction angle or probe frequency.

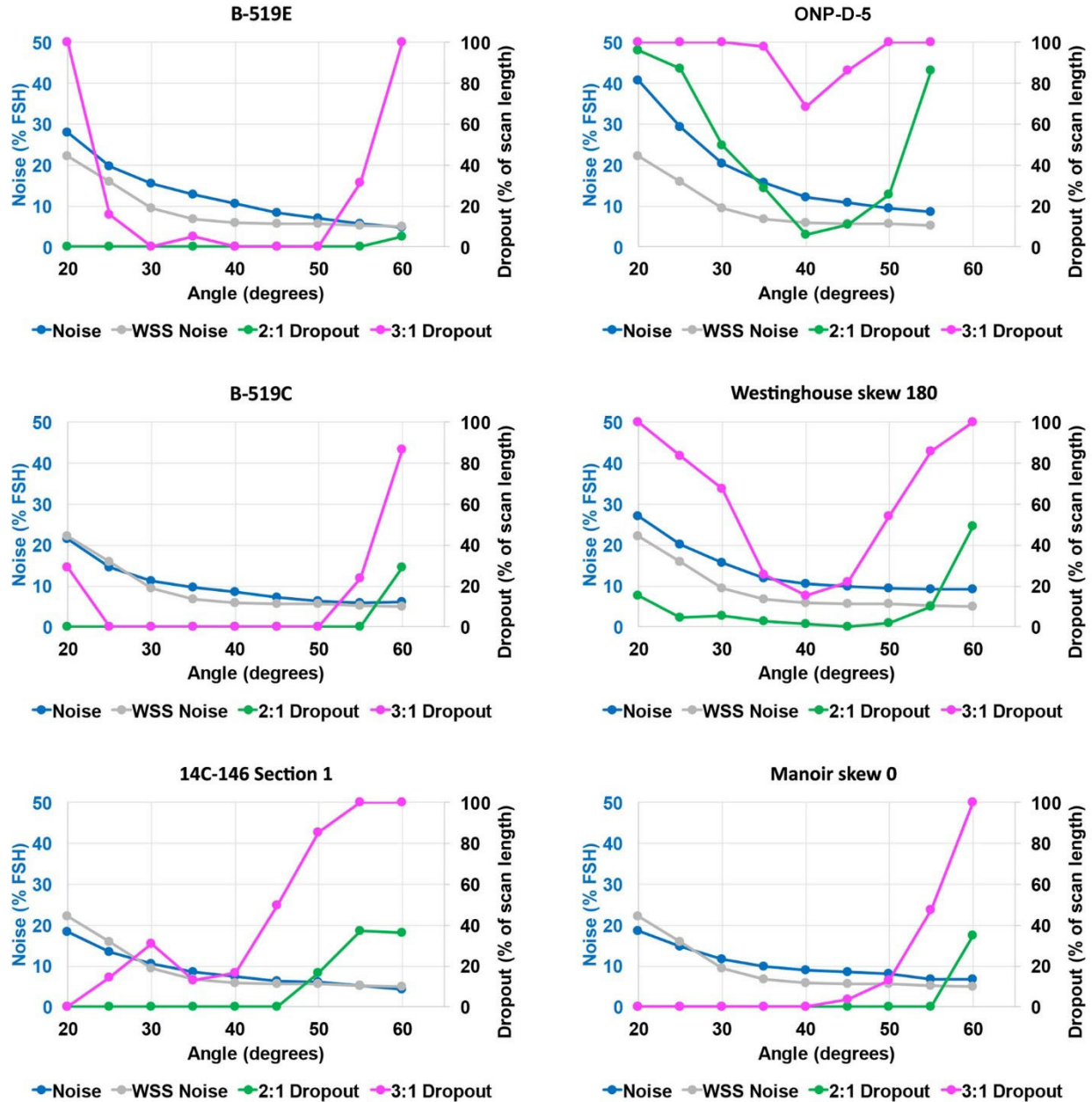


**Figure 8-14 Noise and Percent Dropout vs. Angle.** The noise (% of FSH, left axis) and dropout (% of scan length, right axis) at 500 kHz are plotted vs. refraction angle for several example scans. The noise levels from the WSS specimen are included for comparison.

Tables 8-4 through 8-7 also show that the dropout varied by transducer frequency as a function of grain structure, with both percent dropout and maximum dropout length increasing with increasing transducer frequency. As expected, the 500 kHz scans (top section of the tables) were the least affected by signal dropout, while the 1.0 MHz scans (bottom section) were most affected. However, even at 500 kHz, variable levels of signal dropout were observed for certain microstructures. Also, Tables 8-4 and 8-5 show that, at 2:1 SNR, the percent dropout and



maximum dropout length varied considerably from specimen to specimen. For example, at 500 kHz, specimens ONP-D-5 (equiaxed/coarse) and IHI (mixed/banded) showed the largest effects of signal dropout. The other specimens showed little to no dropout at lower angles, with dropout increasing at higher angles (typically 50° and higher). Interestingly, some specimens showed a “sweet spot,” or a mid-range refraction angle with the least dropout. For example, for ONP D-5, which had some dropout at every angle, there was a minimum of dropout that occurred at 40°. For the Westinghouse specimen (columnar/banded), a minimum occurred at 45°. These angles generally changed slightly with increasing probe frequency. Additionally, the two mixed/banded specimens (IHI and 14C-146) exhibited opposite dropout behaviors: signal dropout in the IHI specimen occurred primarily in the lower angles, whereas dropout in 14C-146 occurred primarily at higher angles. Similar patterns are shown in Tables 8-6 and 8-7, albeit with more overall dropout in most cases.

Table 8-4 Signal Dropout at the 2:1 SNR Level, by Percentage of Scanned Section

500 kHz													
Angle	B-519E	Manoir		ONP D-5	B-519C	Westinghouse		IHI		14C-146		Section 1	Section 2
		Skew 0	Skew 180			Skew 0	Skew 180	Skew 0	Skew 180				
20	0	0	0	96	0	0	15	43	77	0	0	0	0
25	0	0	0	87	0	0	4	33	33	0	0	0	0
30	0	0	0	50	0	0	6	21	23	0	0	0	0
35	0	0	0	29	0	0	3	11	12	0	0	0	0
40	0	0	0	6	0	0	2	1	11	0	0	0	0
45	0	0	0	11	0	0	0	0	0	0	0	0	0
50	0	0	0	26	0	0	2	0	0	0	0	0	0
55	0	0	0	86	0	4	10	0	0	17	9	0	0
60	5	35	25	0	29	34	49	0	0	37	19	0	0
65	0	0	0	0	0	66	49	0	0	36	14	0	0

800 kHz													
Angle	B-519E	Manoir		ONP D-5	B-519C	Westinghouse		IHI		14C-146		Section 1	Section 2
		Skew 0	Skew 180			Skew 0	Skew 180	Skew 0	Skew 180				
20	29	0	0	100	21	17	88	62	93	0	0	0	0
25	18	0	0	98	18	21	43	63	82	0	0	0	0
30	13	0	0	91	0	5	20	43	49	0	1	0	0
35	0	0	3	68	0	1	8	27	30	10	2	0	0
40	0	0	3	56	0	0	4	26	22	43	11	0	0
45	0	0	0	38	0	1	6	23	13	48	32	0	0
50	0	0	12	65	0	5	31	0	0	67	76	0	0
55	11	11	30	0	13	50	74	0	0	90	96	0	0
60	24	35	21	0	61	93	98	0	0	0	0	0	0
65	0	0	0	0	53	0	0	0	0	0	0	0	0

1 MHz													
Angle	B-519E	Manoir		ONP D-5	B-519C	Westinghouse		IHI		14C-146		Section 1	Section 2
		Skew 0	Skew 180			Skew 0	Skew 180	Skew 0	Skew 180				
20	11	0	0	98	0	39	89	73	91	6	0	0	0
25	0	0	0	100	0	22	55	72	64	25	9	0	0
30	11	0	1	85	0	4	21	51	41	46	10	0	0
35	8	0	3	68	0	0	8	43	21	47	32	0	0
40	0	0	6	59	0	0	13	29	16	57	63	0	0
45	8	2	7	71	16	2	21	34	9	83	89	0	0
50	18	19	21	83	21	29	55	0	0	95	99	0	0
55	53	49	56	0	87	88	95	0	0	99	0	0	0
60	76	73	82	0	0	0	0	0	0	0	0	0	0
65	0	0	0	0	0	0	0	0	0	0	0	0	0

– No corner signal detected.

Table 8-5 Signal Dropout at the 2:1 SNR Level, by Length of Maximum Dropout

500 kHz

Angle	B-519E	Manoir		ONP D-5	B-519C	Westinghouse		IHI		14C-146		Wrought
		Skew 0	Skew 180			Skew 0	Skew 180	Section1	Section 2			
20	0	0	0	170	0	0	46	190	264	0	0	0
25	0	0	0	160	0	0	18	94	84	0	0	0
30	0	0	0	64	0	0	14	68	52	0	0	0
35	0	0	0	50	0	0	14	52	56	0	0	0
40	0	0	0	12	0	0	8	4	30	0	0	0
45	0	0	0	16	0	0	0	0	0	0	0	0
50	0	0	0	32	0	0	10	-	-	14	20	0
55	0	0	0	82	0	12	16	-	-	22	24	0
60	4	88	34	-	18	74	36	-	-	24	16	0
65	-	-	-	-	-	160	44	-	-	-	-	0

800 kHz

Angle	B-519E	Manoir		ONP D-5	B-519C	Westinghouse		IHI		14C-146		Wrought
		Skew 0	Skew 180			Skew 0	Skew 180	Section1	Section 2			
20	22	0	0	200	16	24	200	98	300	0	0	0
25	14	0	0	166	14	26	52	102	186	0	0	0
30	10	0	0	128	0	10	38	82	66	0	4	0
35	0	0	12	90	0	6	16	80	72	10	6	0
40	0	0	14	48	0	0	12	94	28	82	14	0
45	0	0	0	32	0	6	12	42	20	84	46	0
50	0	0	24	30	0	12	36	-	-	84	66	0
55	8	26	86	-	10	36	74	-	-	98	342	0
60	12	46	60	-	46	174	264	-	-	-	-	0
65	-	-	-	-	28	-	-	-	-	-	-	0

1 MHz

Angle	B-519E	Manoir		ONP D-5	B-519C	Westinghouse		IHI		14C-146		Wrought
		Skew 0	Skew 180			Skew 0	Skew 180	Section1	Section 2			
20	8	0	0	162	0	38	92	106	134	8	0	0
25	0	0	0	200	0	22	44	114	72	20	14	0
30	8	0	4	122	0	12	38	88	62	42	16	0
35	6	0	14	58	0	0	16	152	30	46	24	0
40	0	0	24	52	0	0	16	78	22	64	48	0
45	4	8	18	48	12	8	28	112	18	68	122	0
50	6	26	32	84	16	26	42	-	-	156	212	0
55	14	60	80	-	52	146	148	-	-	250	-	0
60	52	76	96	-	-	-	-	-	-	-	-	0
65	-	-	-	-	-	-	-	-	-	-	-	0

- No corner signal detected.

Table 8-6 Signal Dropout at the 3:1 SNR Level, by Percentage of Scanned Section

500 kHz																
Angle	B-519E	Manoir		ONP D-5	B-519C	Westinghouse		IHI		14C-146		Wrought				
		Skew 0	Skew 180			Skew 0	Skew 180	Section1	Section 2							
20	100	0	0	100	29	45	100	89	100	0	0	0				
25	16	0	0	100	0	11	84	80	76	15	0	0				
30	0	0	0	100	0	0	68	54	77	31	4	0				
35	5	0	0	98	0	3	25	47	48	13	7	0				
40	0	0	0	68	0	0	16	33	45	17	6	0				
45	0	4	0	86	0	14	22	9	7	50	31	0				
50	0	13	2	100	0	23	54	-	-	85	73	0				
55	32	47	42	100	24	80	86	-	-	100	100	0				
60	100	100	99	-	87	99	100	-	-	100	100	0				
65	-	-	-	-	-	100	100	-	-	-	-	0				

800 kHz																
Angle	B-519E	Manoir		ONP D-5	B-519C	Westinghouse		IHI		14C-146		Wrought				
		Skew 0	Skew 180			Skew 0	Skew 180	Section1	Section 2							
20	100	2	14	100	87	80	100	91	99	39	0	0				
25	82	14	28	100	87	82	98	97	100	83	52	0				
30	74	17	35	100	26	43	83	95	89	78	48	0				
35	50	1	26	100	0	30	63	78	80	97	61	0				
40	37	0	27	98	0	28	66	71	61	95	90	0				
45	74	9	35	97	8	48	88	71	46	100	99	0				
50	66	55	53	100	24	84	98	-	-	100	100	0				
55	84	84	92	-	61	100	100	-	-	100	100	0				
60	100	100	96	-	84	100	100	-	-	-	-	0				
65	-	-	-	-	100	-	-	-	-	-	-	0				

1 MHz																
Angle	B-519E	Manoir		ONP D-5	B-519C	Westinghouse		IHI		14C-146		Wrought				
		Skew 0	Skew 180			Skew 0	Skew 180	Section1	Section 2							
20	74	8	48	100	100	91	100	97	100	99	48	0				
25	66	37	58	100	68	82	100	96	98	97	94	0				
30	87	34	44	100	53	50	94	89	90	100	100	0				
35	79	24	40	100	21	35	80	84	81	100	100	0				
40	82	20	43	98	21	36	86	76	69	100	100	0				
45	87	67	73	97	24	79	98	86	77	100	100	0				
50	100	94	100	100	34	98	100	-	-	100	100	0				
55	100	100	100	-	89	100	100	-	-	100	-	0				
60	100	100	100	-	100	-	-	-	-	-	-	0				
65	-	-	-	-	-	-	-	-	-	-	-	0				

- No corner signal detected.

Table 8-7 Signal Dropout at the 3:1 SNR Level, by Length of Maximum Dropout

500 kHz													
Angle	B-519E	Manoir		ONP D-5	B-519C	Westinghouse		IHI		14C-146		Wrought	
		Skew 0	Skew 180			Skew 0	Skew 180	Skew 0	Skew 180	Section1	Section 2		
20	74	0	0	200	22	36	550	220	550	0	0	0	
25	12	0	0	200	0	26	218	230	230	16	0	0	
30	0	0	0	200	0	0	130	218	192	24	20	0	
35	4	0	0	182	0	10	40	172	172	18	16	0	
40	0	0	0	78	0	0	30	68	100	18	10	0	
45	0	16	0	128	0	38	38	18	30	62	36	0	
50	0	28	8	200	0	42	68	-	-	132	48	0	
55	16	62	66	200	18	94	174	-	-	300	450	0	
60	74	420	426	-	48	352	500	-	-	300	450	0	
65	-	-	-	-	-	500	500	-	-	-	-	0	
800 kHz													
Angle	B-519E	Manoir		ONP D-5	B-519C	Westinghouse		IHI		14C-146		Wrought	
		Skew 0	Skew 180			Skew 0	Skew 180	Skew 0	Skew 180	Section1	Section 2		
20	74	10	38	200	66	130	500	122	522	48	0	0	
25	62	18	68	200	60	136	292	228	550	110	88	0	
30	44	24	78	200	20	82	110	224	254	70	44	0	
35	26	6	76	200	0	34	50	218	244	286	42	0	
40	24	0	44	164	0	34	68	220	214	248	192	0	
45	36	10	112	112	6	80	118	222	182	298	316	0	
50	26	90	168	200	18	102	186	-	-	298	452	0	
55	56	132	316	-	26	500	500	-	-	298	452	0	
60	74	420	412	-	52	500	500	-	-	-	-	0	
65	-	-	-	-	74	-	-	-	-	-	-	0	
1 MHz													
Angle	B-519E	Manoir		ONP D-5	B-519C	Westinghouse		IHI		14C-146		Wrought	
		Skew 0	Skew 180			Skew 0	Skew 180	Skew 0	Skew 180	Section1	Section 2		
20	52	18	46	200	74	298	500	230	550	200	58	0	
25	50	28	76	200	30	90	500	230	392	220	260	0	
30	36	38	108	200	22	46	292	226	194	300	400	0	
35	30	26	82	200	16	36	80	220	128	300	400	0	
40	52	24	80	112	16	36	124	220	92	300	400	0	
45	52	140	132	110	18	88	378	226	172	300	400	0	
50	74	132	450	200	20	358	500	-	-	300	400	0	
55	74	420	450	-	52	500	500	-	-	300	400	0	
60	74	420	450	-	74	-	-	-	-	-	-	0	
65	-	-	-	-	-	-	-	-	-	-	-	0	

- No corner signal detected.

#### 8.1.2.6 Discussion

This study of signal dropout was conducted on specimen block ends that represent 100% through-wall, machined reflectors with 2:1 and 3:1 SNR thresholds of detection. These represent minimum SNR levels necessary for detection on a best-case planar reflector. Detection of actual service-induced flaws is further complicated by size and morphology, both of which reduce or limit the amount of sound energy available to be returned to the transducer. Flaw detection will also be hindered by high noise levels in CASS, particularly at low refraction angles.

The range of least-affected refraction angles was shown to be unpredictable, as it varied with frequency as a function of specimen microstructure. The data show that there is an overall “window” of least-affected angles, or angles at which dropout is minimized within the full set of specimens, of approximately 20°–55°. That is, if this range of angles were used on all specimens, the least-affected angle of each specimen would fall within this range. During this initial research, focal laws were arbitrarily set at 5° increments. Depending on the application, angular increments smaller than 5° may be appropriate to maximize SNR for flaw detection; however, specific “best angles” for detection will be virtually impossible to know beforehand because the microstructures existing in field welds are unknown and vary as a function of spatial position.

The amount of dropout varied considerably from specimen to specimen and even within each individual specimen. As shown in Figure 8-11, the end-of-block signal within a given specimen may range from being relatively uniform, such as with B-519E (small-grained equiaxed microstructure), to being sporadic and spotty, such as with IHI (mixed/banded microstructure). This is further illustrated by Figure 8-13, where it is seen that within a single specimen the signal dropout can change in severity and location with different refraction angles. It is important to note that the amount and locations of signal dropout were unpredictable, even with foreknowledge of the grain structure from the cut and polished ends. Furthermore, grain structure may vary along the sound metal path throughout a given CASS material, so even if the structure is known at one cross-sectional plane (as in the case of the specimens used herein), the same structure may not be present throughout the scan or sound path. This is particularly evident in the Westinghouse specimen, where both ends of the specimen were scanned (i.e., probe skews 0 and 180). The dropout observed in the skew 180 scan was much worse than that in the skew 0 scan, especially for the 3:1 SNR threshold and the higher frequency probes. In addition, a review of the axial-plane microstructure of the Manoir specimen (14C-146) illustrated in Figure 8-8, shows the variability in grain size, type, orientation, and banding one may encounter when translating a probe along the pipe axis for examination of circumferentially oriented flaws.

The 500 kHz scans consistently showed the least overall amount of signal dropout, the shortest dropout lengths, the fewest affected angles, and the lowest mean noise levels. In conjunction with previous studies, such as shown in Chapter 7 of this report and (Crawford et al. 2014), these results provide further evidence that there is a clear advantage to using 500 kHz PA-UT with a range of applied angles for flaw detection in thick-walled CASS, as opposed to scanning with higher frequencies and/or limited angles. Low frequencies minimize the amount of signal redirection, attenuation, and scattering, which are the major causes of signal dropout, and chances of detecting actual flaws are enhanced.

No single angle, or set of only a few angles, could be shown to provide sufficient responses along the entire end-of block for detecting this ideal reflector through the varied microstructures. Thus, it would not be expected that applying only a limited set of angles (for instance, 2 or 3 angles) would provide adequate flaw responses in all cases. In light of the fact that the actual CASS microstructures in the field are unknown and considering that service-induced flaws would likely



not produce as relatively high responses as the ideal end-of-block reflectors used in this limited study, it would logically seem important to apply a wide range of propagation angles for reliable flaw detection to be enhanced.

### 8.1.3 Introducing Sufficient Sound Field Intensities

There is recognition in the research community, as well as with field ISI practitioners, that PA technologies offer significant advantages over conventional methods for generating coherent sound fields (Olympus 2014; Moran et al. 2017). The first obvious advancement is the ability to steer through many angles nearly simultaneously, thus allowing a greater amount of material volume to be examined with optimized propagation, i.e., a much better chance of striking potential reflectors at appropriate angles (nearly perpendicular to their reflecting surfaces) to produce the best signal responses for detection.

Yet, another advantage for PA over conventional UT lies with the ability to focus the sound fields into certain *areas of interest*; this capability may ultimately be more important for flaw detection in these coarse-grained CASS microstructures. The PA method utilizes many small individual emitters that are fired at specific, relative timings to produce multiple spherical beams in the component. These beam fronts interact through constructive and destructive interference, to form a new, integrated sound field (see previous Figure 6-4). This interaction can be made to occur such that an enhanced field intensity is produced at the proper metal sound path distance, or area of interest, i.e., to optimize sound field intensities for detection of ID surface-breaking planar flaws during ISI of piping weldments. Of course, the PA transducer must possess a sufficiently large enough active aperture to allow for appropriate beam formation to occur.

The capability to place sufficient UT energies into specific areas of interest within examined materials is the primary factor that enhances overall SNR. When applied to a dispersive and inherently noisy medium such as CASS, this capability becomes very important in order to provide minimum levels of returned energies for reliable flaw detection. A common way to assess sound field intensities that are present for flaw signals is by measuring relative SNRs of the reflected responses. Typically, SNRs less than two-to-one (2:1) have proven ineffective for reliable flaw detection with greater SNR values being highly recommended, especially in coarse-grained, inherently noisy materials (Anderson et al. 2014; Crawford et al. 2014). Evidence for the use of higher SNRs is also found in additional literature sources. For instance, the NDT Resource Center website (ISU 2012) states that a SNR of 3:1 (or 9.5 dB) is often required as a *minimum* value for reliable UT. Neumann (1989) requires a recording level for the signal to be at least 6 dB (2:1 SNR) above the peak noise level for the inspection of austenitic welds. Further, from Schuster et al. (1998), echoes with 6 dB or greater SNR correlated well with actual flaw positions and in Schuster et al. (2013) it was stated that round-robin testing results were unreliable when the SNR was less than 6 dB. PA technology, which allows for a focused, robust energy sound field to be formed in the examination area of interest, has proven to consistently provide SNRs above the minimum required for effective and reliable detection of flaws.

The PA technique described above is very different from a conventional method of developing ultrasonic sound fields. Typically, monolithic piezo-crystals are used for conventional UT techniques. At the frequencies necessary for adequate penetration in CASS (e.g., 500 kHz), these crystals are relatively large, on the order of inches in diameter. This size, while providing higher sound powers than smaller transducers, comes with accompanying near-field issues (already discussed earlier in this report). The near field is a volumetric area starting at the insonification point (face of the transducer) and extending through the wedge into the material along the propagation angle as a function of frequency and crystal diameter. It is a non-linear UT region that

is typically not reliable for flaw signal detection. Traditionally one tries to limit the length of the near field. At the end of the near field, the resultant sound beam (far field) begins to become linear and, more importantly, dispersive; i.e., beam spread occurs and sound field intensities diminish as a logarithmic function. Of course, the prediction of beam spread and overall sound field reduction is theoretical and traditionally based on nearly isotropic material behavior. This deleterious effect would be further pronounced in CASS materials.

Therefore, at the area of interest for ISI flaw detection (near the ID surface), the far field strength of conventional probes is reduced accordingly, and one typically tries to compensate for this by using dual TRL probe designs that (1) limit near field lengths due to the isolated (passive) receiver crystal, while (2) attempting to provide improved signal detection via the use of a probe roof angle to create a mechanical “cross-over” distance. This cross-over point is the distance along the metal path where the projection of transmit and receive far fields theoretically intersect. However, in coarse-grained CASS microstructures, the sound fields are distorted and re-directed along the metal path due to velocity variations by each grain of material being impinged; thus, the cross-over point is affected and flaw SNRs are significantly reduced. Both early research (Bates et al. 1987) and more recent studies provide evidence that conventional UT methods continue to be ineffective for the examination of coarse-grained CASS weldments (MacDonald et al. 2000; Dennis 2012; Sakamoto et al. 2012b). It is in recognition of this fact that in a recent rulemaking (82 FR 32934, July 18, 2017), the NRC imposed a condition on the use of ASME Code Case N-824 requiring that all examinations on CASS welds be performed using PA technology.

## **8.2 Use of Encoded Data with Volumetric Analytical Imaging Techniques**

Many national and international studies have been conducted to evaluate UT techniques for the examination of CASS weldments. The research has demonstrated that manual, fixed angle, non-encoded techniques using real-time transient signal analyses would not be expected to reliably detect service-induced flaws in CASS weldments. Studies as recent as 2017 using advanced probe technology reveal unsatisfactory results using conventionally-designed probes with conventional UT techniques.

CASS is an anisotropic and inhomogeneous material. The alloying elements and casting processes used in the fabrication of CASS can result in the formation of various grain structures – long columnar (dendritic) grain structures (approximately normal to the surface), equiaxed, or a mixed structure (banded) during the cooling and solidification process. As discussed in Jenson 2009, due to the anisotropic elastic properties of CASS, the beam transmitted through the macrograins undergoes amplitude distortions and phase aberration. The heterogeneous properties of CASS result in scattering of the incident energy in every direction. When measured by the receiver, the scattered field is the source of a strong background noise (i.e., structural noise). In addition, significant velocity differences as a function of spatial position on the component are possible in this material, leading to reflections at each grain boundary. Studies have shown that many acoustic beam propagation angles (i.e., PA probes) must be applied for the examination of CASS weldments to exploit any potential “windows” or paths for sound to optimally travel through the grain structure.

Another key to enabling the reliable detection of flaws in CASS weldments involves the acquisition of spatially encoded UT data. Spatially encoding the ultrasonic responses from the material and/or potential flaw reflectors allows off-line analytical methods via imaging techniques and manipulation of data to highlight suspect signals, or reduce the presence of collateral reflectors, to enable a qualified analyst to correctly interpret the multiple coherent responses that one encounters in CASS.

By spatially encoding the A-scans and presenting them in the form of a screen image, an examiner can visualize all the data simultaneously to see low-SNR anomalies that may otherwise be overlooked. This is possible because the human eye is acutely attuned to discriminate extremely subtle variations in color and texture. Analysts can also be trained to recognize a broad range of shapes, patterns, and signatures to readily recognize flaws and distinguish them from geometrical features, artifacts, and coherent material noise. Importantly, images also provide a permanent record that allow for documentation and comparisons over time. Thus, NDE imaging methods are key to being able to reliably detect, discern, classify, and document flaws.

Volumetric images are inherently three-dimensional, and with proper rendering software can be “sliced” in any orientation and viewed from all angles. In UT imaging, the primary visualization planes are the side view (B-scan), top view (C-scan), and end view (D-scan). These different views allow an analyst to inspect the data from multiple perspectives to gain a three-dimensional picture of the object being imaged. In addition, data can also be sliced along any plane to obtain cross-sectional views through the inside of the object. In PA-UT, specific inspection angles can also be isolated for analysis. This can be particularly helpful for characterizing the nature of a signal response that might vary with inspection angle. For example, a crack with a tilt will provide the strongest response when the incident sound is normal to the crack face.

Another advantage of encoded PA-UT is that there are multiple computational tools available to aid in visualization and analysis. For example, data merging can be used to display all of the acquired data simultaneously, including all A-scans, lines, and angles, to give overall compiled images; an example is shown in Figure 6-9. Merging is often implemented with interpolation, which can be used to fill in small gaps, such as missing pixels or inspection angles. Interpolation does not add information; rather, it gives the analyst a smooth rendition of the data to make visual interpretation more easily accomplished. Other tools include zooming, gating, and filtering. Zooming magnifies the image allowing for small features to be more easily seen; the impact of zooming will be limited by image resolution and possibly screen resolution. Gating isolates features of interest by limiting interference from background signals and noise. Filtering can be applied to reduce noise or to enhance image features and edges. Used separately or in combination, image analysis tools can greatly enhance an analyst’s ability to distinguish and isolate relevant features.

Another important advantage of encoded, volumetric UT images is the ability to make measurements directly from the images. Well-calibrated images present data with a quantitative measurement scale, usually in units of distance or time. Measurements are used to characterize a signal response by directly relating its physical size and location to the specimen being imaged. Measurements can be made in multiple spatial dimensions to characterize the length, width, and depth of an indication, all of which may be important parameters for determining the indication’s significance. Because the data are encoded, multiple analysts can examine the same data set to validate and confirm results, and measurements from current scans can be compared to those from previous, or future, scans to monitor an indication’s growth during service periods.

On the other hand, non-encoded UT provides an examiner with only an instantaneous, live view of information on a screen, and because the screen is constantly refreshing, the examiner is forced to assemble and form a mental “image” of the reflections during each scan. The transient signals may preclude the examiner from capturing all of the critical features, particularly those that are only slightly above the noise level. Furthermore, non-encoded data are visible for only the instant that they are acquired and can generally not be precisely reproduced. If an examiner’s attention is diverted from the screen for even a fraction of a second, important information may be overlooked.

Thus, non-encoded, or *real-time*, examinations, offer little help to the examiner for reliable signal interpretation. Typically, an examiner using a non-encoded technique must make a determination “on-the-fly” whether a particular transient signal on an instrument screen is a valid flaw response, a geometrical reflector, or simply spurious material noise, all of which are important issues in CASS due to the coarse-grained microstructures. In addition, non-encoded techniques are overwhelmingly *manual* methods, where the examiner manipulates a transducer by hand while attempting to assess these transient reflectors. In these applications, skilled hand-to-eye coordination is necessary to ensure that no flaw signals are missed, while ensuring that the volumes requiring examination are adequately insonified. In the presence of multiple coherent reflectors, as with CASS, this approach is not expected to be reliable. This is especially important when one considers the time constraints imposed on examiners due to outage schedules and occupational exposure limits.

Evidence for the inability of examiners to perform reliably using manual, non-encoded UT techniques can be found in a report assessing the failure of this application to detect five relatively deep through-wall flaws in a DMW at an operating plant (Anderson et al. 2014). It was found that, in the presence of a low SNR (2:1 or less) caused by the weldment and conventional probes being employed, the flaw persistence (time on the screen above the SNR threshold) was less than approximately 0.08 seconds, when scanned at or near the maximum scan speed (2 in./sec is the ASME Code-allowed value for manual examinations). This flaw persistence problem has been corroborated for CASS weldments by a new PNNL investigation.

In the new CASS study, the ultrasonic transducer applied was a dual-element 1.0 MHz conventional probe, operating in a TRL configuration. The integrated wedge was designed for a 45° longitudinal wave. The full specifications of the transducer, as provided by the manufacturer, are shown in Table 8-8. This is a typical configuration of probe design being used for conventional CASS examinations, and was loaned to PNNL by an ISI vendor for this study.

**Table 8-8 1.0 MHz Transducer Specifications**

Nominal Frequency, MHz	1.00
Center Frequency, MHz	0.98
Peak Frequency, MHz	0.98
–6 dB Bandwidth, %)	50
Wave Mode	Longitudinal
Refracted Angle, deg.	45
Element Size, mm (in.)	19.05 × 25.4 (0.75 × 1.0)
Cross-over depth, mm (in.)	2.0 (50.8)

PNNL elected to use a CCSS specimen (designated B-505) that contained a columnar microstructure piping segment joined to an equiaxed piping segment with a full penetration austenitic weld. The specimen thickness is 59.7 mm (2.35 in.), and both ends contain an ID machined notch that is 6.3 mm (0.25 in.) in depth, or approximately 10% through-wall, located parallel and adjacent to each machined end-of-block; see Figure 8-15. The notch length is approximately 57.2 mm (2.25 in.).

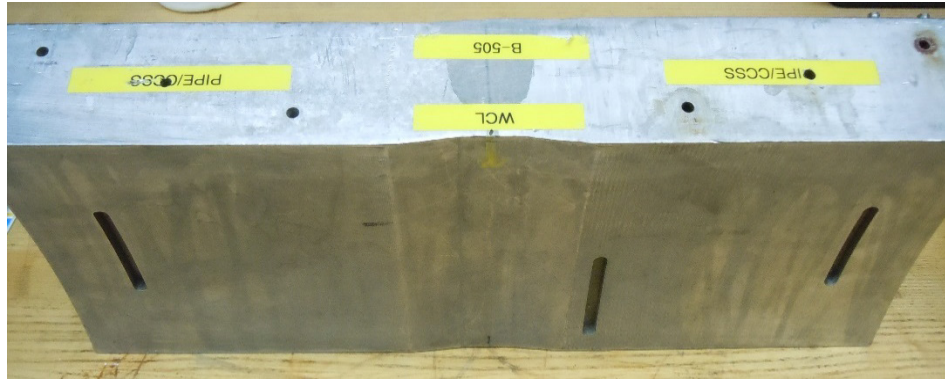


**Figure 8-15 Specimen B-505 Showing Machined ID Notches Used for Reflectors in This Flaw Persistence Study. Only the notches located parallel and adjacent to the end of block on each side were measured. Note the side-drilled holes and other notch near the weld counterbore were not measured and did not affect scans on the target notches.**

Data were acquired in an automated raster scan normal to the notches using a Zetec DYNARAY Lite instrument (via conventional single-channel operation) and the UltraVision software package in order to enable precise measurements of probe movement and speed (see Figure 7-6). Scans were collected using an XY ATCO scanner controlled by a MCDU-02 motor controller, which was also integrated into the software. The instrument, software, and scanning apparatus are all commercial off-the-shelf equipment. Data were encoded and collected using axial scanning with a resolution of  $0.5 \times 1.0$  mm ( $0.02 \times 0.04$  in.) over the entirety of the target notches and corner responses. Scans were performed at a speed of 15.2 mm/s (0.6 in./s) and collected using a unidirectional scanner pattern. This was completed for both the columnar and equiaxed material sides of the specimen, to potentially allow a comparison between the two CCSS materials.

It was noted that, after acquiring data on the notches, the 10% notch on the equiaxed microstructure end was not detectable with the 1.0 MHz conventional TRL probe. Therefore, analysis of flaw persistence focused solely on the columnar grain structure and the notch contained therein.

Due to the large, coarse grains of this particular CASS microstructure, noise caused by backscatter fluctuated on the order of 3%–25% of full screen height (FSH) based on position in the material at any given depth. The mean noise response is generally used to determine the noise level for calculation of SNR. However, for signal detection in a manual scan, the flaw signal must be visible above the noise peaks. Therefore, the mean of the noise peaks was used as the detection threshold. This is illustrated in Figure 8-16, where the mean noise for a single rectified A-scan, shown in blue, is around 7% FSH. Across an entire scan line, the peak noise values are recorded by the purple line, which has a mean of around 22% FSH, which is about 3× higher than the mean noise of the A-scan. If a 3:1 SNR threshold were to be used, then many of the noise spikes would exceed this if the mean A-scan noise were used as the noise threshold. Therefore, the conservative approach of using the mean value of the peak noise was taken as the noise level in SNR calculations.

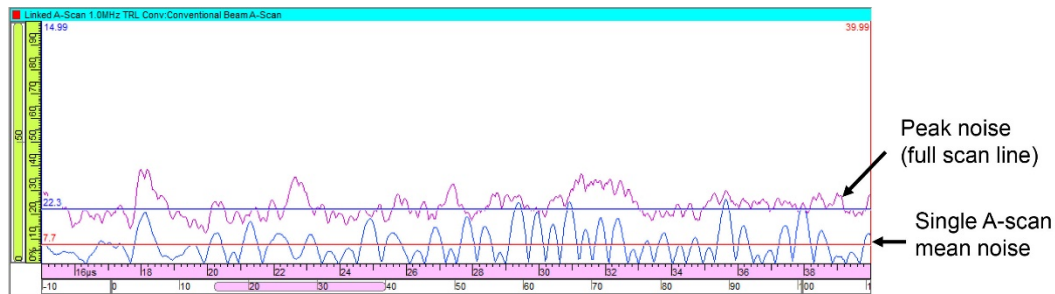


**Figure 8-16 Noise Level for a Single A-scan (blue) and Peak Noise of a Scan Area (purple)**

Following data acquisition, flaw persistence was measured using MATLAB. Two scan lines were chosen for analysis: the line with the highest amplitude response of the notch, and a line with a flaw response of just above 2:1 SNR. Figure 8-17 shows the C-scan image of the notch and corner response collected on the columnar side, highlighting the two scan lines that were selected for persistence analysis. For both of these scan lines, the probe positions were recorded where the SNR reached the 2:1 and (if applicable) the 3:1 thresholds.

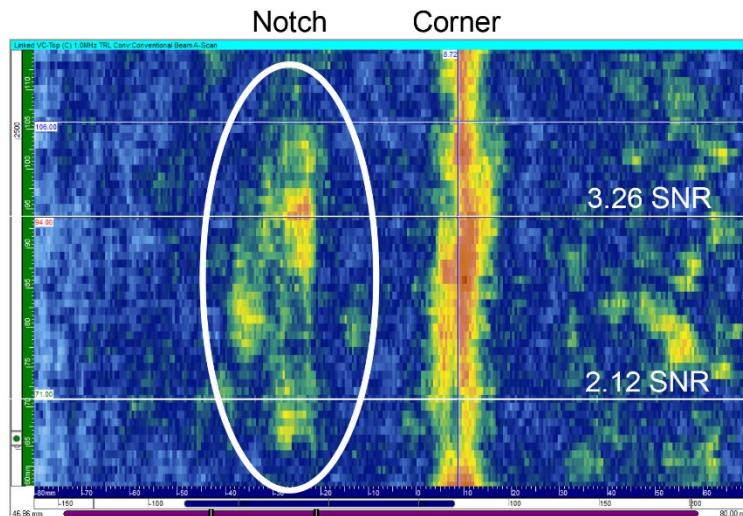


**Figure 8-17 C-scan of Notch and Corner Response Collected, Highlighting Analyzed Scan Lines. The two-line scans used for analysis are labeled with their maximum SNR levels: 3.26 and 2.12.**

Assuming constant inspection speeds of 25.4 and 51 mm/s (1.0 and 2.0 in./sec), the time the flaw was present at or above the 2:1 level was calculated. This duration was labeled as the flaw persistence. Table 8-9 shows the flaw persistence (in seconds) for the 10% notch at both scanning speeds. From the table, it can be seen that the notch signal of the scan line where the peak SNR (3.26) was recorded persists for less than 0.5 sec at a slow inspection speed. This persistence duration drops by half as the scan speed is doubled to 51 mm (2 in./sec). Note the actual maximum SNRs for the two scan lines are calculated in the first column of the table. For the scan line through the 2.12 SNR peak, the results are even less encouraging, with signals persisting for only 80 milliseconds at the 2 in./sec. scan speed.



**Table 8-9 Persistence Measurements along Scan Lines for Signals Above 2:1 SNR**

Maximum SNR along the Scan Line	Scan Length above 2:1 SNR, mm (in.)	Time above 2:1 SNR at 25.4 mm (1.0 in.)/ sec., sec.	Time above 2:1 SNR at 51 mm (2 in.)/sec., sec.
3.26	12.02 (0.47)	0.47	0.24
2.12	4.01 (0.16)	0.16	0.08

Similar to the previously cited work on a DMW (Anderson et al. 2014), as is shown from the very short flaw persistence times above a 2:1 SNR from which an examiner must visually detect a transient flaw response, it is highly unlikely that a non-encoded manual examination technique would be effective or reliable for consistent detection of flaws in CASS. It should be noted that the planar notch in specimen B-505 represents a liberal scenario for producing a flaw response; it is predicted that actual flaws, given the lower responses caused by their irregular shapes, would not result in signals from conventional UT that would stay above a 2:1 SNR for even the short length of times shown in this CASS material (Bates et al. 1987; Diaz et al. 1998). Finally, the microstructure within specimen B-505 is relatively finer than some other CASS specimens at PNNL. Some of the larger grained specimens were initially scanned and the conventional probe used for this study was unable to produce a response above ambient noise from the end-of-block (representing a 100% through-wall flaw) in those coarser microstructures.

Another consideration when attempting to examine CASS with non-encoded manual methods is the difficulty in manipulating the relatively large transducers. Low frequencies are needed for adequate sound penetration in CASS, and effective apertures of LF probes tend to be comparatively large. For example, a non-contoured probe with a 9 cm x 9 cm footprint, such as those in Figure 7-37, on the OD surface of a 91 cm (36 in.) diameter pipe would have about a 2 mm (0.08 in.) gap between the wedge and the specimen on each side of the probe. This results in search unit/wedge footprints that require wedge contouring for effective coupling to the component. These large footprint, surface-contoured probes eliminate an examiner's ability for manually skewing, or oscillating, the probe to enhance responses from flaws that are off-normal to the primary beam direction, effectively eliminating an examiner's capability to "peak out" transient reflectors through probe skewing in order to enhance signal response for discrimination, flaw detection, and characterization. Such off-normal, or tortuous, branched flaw morphologies are manifested in most service-induced degradation that has been experienced in operating NPPs, e.g., stress corrosion and thermal fatigue cracking.

As a final note, it is recognized that some in the U.S. commercial nuclear industry continue to assert that non-encoded, conventional UT techniques are satisfactory for examining CASS piping welds. However, PNNL is unaware of evidence of effective and reliable non-encoded CASS piping weld examinations using conventional UT.

### **8.2.1 The Use of Modeling to Facilitate Reliable Examinations**

Simple models have for decades been used to assess theoretical transducer performance, especially for the matrix designs typically applied in PA-UT. It is important to model, or simulate, the number of elements, their active and passive dimensions, and spatial separations in order to assess overall directivity and to eliminate unwanted sound field energies (grating lobes) that may occur in a non-optimized array. Many of the models used for this purpose were simple mathematical spreadsheets, or beam tracing approaches, and the simulations were limited to

assessing theoretical sound fields in isotropic media. Most often these models were applied by array manufacturers or NDE research organizations.

Thus, the widespread use of software that would allow simulated flaws to be represented in a component, allow theoretical reflections from these flaws, and enable analysis of factors such as sound field intensities and expected SNRs, is a relatively recent occurrence. Accordingly, there are no requirements in the U.S. nuclear industry addressing the use of these type of simulations. However, given that complex geometrical weld configurations with CASS materials present additional challenges to the performance of effective and reliable examinations, the application of modeling software to facilitate not only the design of probes but to optimize other examination parameters would be an important step, especially given the wide range of geometries that exist within operating NPPs.

Early software programs allowed the creation of 2D and 3D component configurations with simplified ray tracing to provide the user with insights on volumetric coverage and flaw detection potential, depending on reflecting surface orientations to relative beam profiles. Advancements in computer technology and software capabilities have allowed ever more sophisticated NDE modeling, with several of these simulation programs becoming commercially available. PNNL has been using a product named CIVA, developed by the Commissariat à l'énergie Atomique (CEA, or the French Atomic Energy Commission). The French CIVA project started in 1992, and benchmark study results have been presented by CEA at multiple conference venues since the early 2000s. CIVA is used in different industrial sectors and has been subjected to an extensive level of validation work. Validation efforts through simulations and empirical tests continue to be performed at PNNL, EPRI, and CEA, and regular participation in benchmark studies is expected to continue. Among the current benefits of modeling with CIVA are:

- Technique feasibility assessment without mockups or transducers
- Transducer design optimization with limited prototypical tests
- Visualization of sound fields to aid interpretation of observed signals
- Demonstration of critical flaw detection within inspection volumes on limited numbers of reference mockups
- NDE simulations for complex geometry technique qualification
- Potential to produce examination qualifications that can be more easily explained to regulators or defended during peer reviews.

It should be noted that the NRC and EPRI developed a cooperative statement of work for modeling and simulation in September 2016 (Weber and Wilmshurst 2016). While cooperation on this work will be mutually beneficial to both organizations, the planned end-use may be quite different. The EPRI NDE Center has been evaluating various ultrasonic modeling and simulation software packages to assist in enhancing inspection reliability, as a training tool, and assessing the potential to use software in lieu of manufacturing a significant number of mockups for UT performance demonstration. The NRC is sponsoring the cooperative work to provide an understanding of the capabilities and limitations of modeling and simulation when licensees employ simulations using these types of software as bases for limited examinations, or to justify the effectiveness of an examination, during the request for relief process.

Given that application of UT modeling is relatively recent in the U.S. nuclear industry, some skepticism exists with respect to the accuracy of the software. CEA staff discussed this issue in a September 27, 2011 interview (Extende S.A. 2011). The specific question was, "Is it a blocking

point to make a model based only on semi-analytical calculations?” CEA responded that semi-analytical models have two advantages: a reduction in calculation time and numerical cost, and a better understanding of the simulation results. In many configurations that require simulation, an NDT expert is often able to roughly define the parameters that would be applied to detect and/or characterize a given condition. CEA stated that CIVA is able to partially or completely simulate and optimize the method defined.

However, CEA also noted that for particularly complex configurations, semi-analytical methods have limitations, and it may be necessary to use numerical methods. This is an area that several research organizations are currently investigating. While 3D applications are very demanding in terms of calculation time and memory requirements, the numerical methods have been continuously improving. Overall, CIVA simulations are typically all semi-analytical; however, hybrid models that combine semi-analytical and numerical methods are also being pursued; e.g., EDF coupled CIVA with a finite-element code (ATHENA) (Chassignole et al. 2009) for certain 2D UT simulations, and continues to develop a 3D version of this approach.

Over the years, CIVA capabilities have been extended to take into account more complex probes, materials, flaws, and inspection procedures. For instance, NRC sponsored PNNL to develop formal mathematical theories for ultrasonic wave propagation in polycrystalline aggregates having both simple (composed of grains only) and complex microstructures (having macro-grains and sub-grains/colonies) that were incorporated into CIVA (Ahmed and Anderson 2009). Computations based on these theories were performed for ultrasonic backscatter power, attenuation due to scattering, and phase velocity dispersions. Furthermore, the expected propagation characteristics (attenuation coefficient and phase velocity) were computed for plane longitudinal waves propagating in (1) steels composed of randomly oriented grains, (2) [001] aligned grains encountered in austenitic stainless-steel welds and castings, and (3) duplex steels.

CEA also developed an analytical method of accounting for coarse-grained variability in CASS by using a Voronoi diagram approach (Jenson et al. 2009; Mahaut et al. 2009; EPRI 2018). Similar parametrical simulation studies have been performed to address optimization of probe design, extent of coverage, and detection and sizing capabilities (Le Ber et al. 2007) and to demonstrate the value of analytical design optimization in lieu of iterative prototype and test strategies (AREVA 2013).

Thus, the CIVA software package continues to be enhanced to provide more realism in simulations and usefulness to a variety of applications. Based on these improved capabilities, the NRC tasked PNNL to model and validate licensees’ requests for relief submittal information (see Appendix E for details) to provide insights into weldment coverage and expected flaw detectability. Listed below are the issues that were identified through the comparison of the licensee estimations of weldment coverage versus those depicted in the modeling results:

- The sound fields applied generally suffered from poor beam intensities in the appropriate component regions, indicating a potential for ID surface-breaking flaws to remain undetected. For the particular weld simulations, PA technology was modeled. However, PNNL’s sound beam assessments using CIVA generally revealed that active aperture dimensions and focal laws were less than adequate to fully interrogate the ID surface region with robust field intensities.
- Various licensees used multiple methods to calculate transducer fields and to estimate volumetric weld coverage. It was shown that there was generally good agreement between the estimated coverage and coverage as calculated by the CIVA software. The modeling

results reveal, however, that reliance on a percentage of volumetric weld coverage can be quite misleading with respect to the effectiveness of the examination.

- Modeling and sound field assessments generally revealed a lack of optimization of the active aperture and number of elements for the PA probes and focal laws applied. In addition, modeling revealed individual beam density profile issues such as improper focusing and inadequate beam intensities near the ID of the weld. These factors, as well as other issues such as poor or irregular coupling, would typically result in decreased flaw signal response, making flaw detection more challenging.
- Licensees did not use LF transducers optimized for CASS materials; thus, no attempt was made to examine the required portion of the CASS base metal and the weld material adjacent to the CASS.
- In some cases, attempts were made with the same probe used for the wrought side of the weld, and no coverage credit was taken, given the ineffectiveness of standard probes to examine CASS material.

The assessment discussed above highlights the type of basic insights one may gain from performing simulations. In the case of one of the licensees, it was noted that for an RCP discharge nozzle configuration having a CASS safe-end, the cross-sectional examination coverage in the circumferential scan direction (to detect axial flaws) was only 34% of the required volume. In another case, there was little coverage at the ID surface, and it was estimated that a flaw would need to grow to approximately 40% in through-wall depth before it could be reliably detected. While the OD examination surface contour/condition and branch connections often prevent complete coverage, the use of UT technology and procedures not optimized for these particular configurations was also a major contributor to the lack of coverage. Modeling may have been used to, for example, significantly improve probe design to enhance coverage and the effectiveness of the examinations in these cases. The results are discussed in greater detail in Appendix E of this report.

Given the complex microstructural variation and other contributing geometrical features for CASS weldments, it would seem prudent and is highly recommended that simulations be used to pre-validate the UT parameters for each application and to assess volumetric coverage using theoretically robust sound field intensities for the types and locations of flaws that could be manifested in CASS component welds. Recent modeling (Dib et al. 2017; Dib et al. 2018) has revealed that there exist a number of outstanding questions that still need to be assessed with regard to model accuracy, input sensitivities, and realistic and verifiable simulation output that should underpin one's confidence in using these types of tools. As discussed above, there are scenarios where simulations can identify significant deficiencies with respect to the actual quality of the sound fields generated. The addition of routine modeling to current practices has the potential to dramatically improve the quality of the examinations conducted; however, their value and effectiveness must be quantified and consistent protocols for use must be developed to provide modelers with a level playing field.

### **8.3 Training of Examiners for CASS Examinations**

As discussed previously in this chapter, generating adequate sound field intensities over an effective range of propagation angles using PA-UT is the best approach to compensate for much of the insonification issues encountered in CASS materials. In addition, examiners will need to learn to compensate for varied microstructures as they are discovered by using multiple imaging and data manipulation methods. This was recognized early in the CASS research as an important observation that came from the EPRI NDE Center CASS examination exercise in 1996 (Diaz et al.

2008b). It became evident during the data analysis phase of the exercise that CASS data interpreters should be trained using some set of consistent criteria (a well-defined set of rules for identification of flaw responses allowing for discriminating flaw indications from material structure or geometrical indications) (Diaz et al. 2008b). The notable variability between interpreters using the same data set was clearly evident. This variability remains a valid condition today, and potentially is even more important with the advent of advanced UT methods such as LF-PA.

In the ASME technical white paper supporting Code Case N-824 (ASME 2008), it is noted that:

*To be effective, training must be specific to the materials, examination methods and examination procedures to be applied. Awareness of the potential for beam splitting, beam distortion, and beam skewing will aid in selecting the appropriate test parameters for the examination of CASS components and in evaluating the test results. Hands-on laboratory examination of CASS welds containing known flaws in the base material and the weld, and geometrical conditions representing ID and OD features, component thickness, and surface conditions of the material to be examined is essential. Such examinations increase a test operator's proficiency and provide confidence in the soundness of the test procedure for flaw detection and sizing. Non-blind access to the training specimens is necessary to allow for appropriate feedback in development of procedures, equipment, and personnel.*

The use of modeling tools (simulations) may assist in providing this knowledge. However, the importance of experience on CASS specimens having a variety of realistic geometrical features and flaw placements cannot be overstated for imparting the requisite skills and knowledge needed to produce effective and reliable field examinations. This is recognized by industry and has been implemented by developing “hands-on” requirements contained in ASME XI, Appendix VII and CFR 50.55a. These personnel qualification requirements were developed over time as a result of findings made during the 1980s when IGSCC was being experienced in austenitic welds of BWR recirculation systems. These training methods have been validated many times during the course of performance demonstrations for austenitic piping welds.

There continues to be evidence that sufficient guided practice on flawed specimens is instrumental in elevating pass rates for candidates of the Performance Demonstrated Initiative (PDI), Supplement 2 (with IGSCC) performance demonstration certifications (EPRI 2007). This premise is analogous to CASS weldments, as inspections would be improved by specialized training in CASS microstructures that may be encountered, resultant sound field effects, and methods to discriminate between flaws, geometry, and other coherent noise in CASS configurations.

## **8.4 CASS “Best Effort” Examinations and the Need for Applicable Qualification Criteria**

### **8.4.1 Introduction**

A final item for consideration is an issue that may be hindering the development of performance demonstration rules. As required by ISI programs, examinations of CASS weldments are currently being conducted using the prescriptive requirements found in ASME Section XI, Appendix III. These conventional examinations have long been considered “best effort” due to the rudimentary UT parameters applied. As noted in the ASME white paper in support of Code Case N-824 (ASME 2008), however, the current examinations of CASS weldments are considered

inadequate. In recognition of this, many licensees may simply choose not to examine welds from the CASS side because a qualified CASS UT method has not as yet been developed. This results in the generation of many requests for relief due to examination coverage limitations, involving a commitment of significant resources at the NRC and within industry. Industry-funded efforts to date have primarily focused on the EPRI-administered PDI program that was originally established *to address Appendix VIII performance demonstration requirements in an efficient, cost-effective, technically sound, and unified manner* (EPRI 2010). Efforts to match this unified approach to a CASS UT qualification process have not been successful thus far. Research results suggest that it may be appropriate for other approaches to be considered.

#### **8.4.2 Discussion**

While the stated industry goal for PDI is to establish an efficient, cost-effective, and unified approach to meeting Section XI, Mandatory Appendix VIII, qualification issues, this approach may be stifling progress on the development of performance demonstration requirements for the examination of CASS weldments. Paragraph VIII-1100(e) of Appendix VIII states that “Any procedure qualified in accordance with this Appendix is acceptable.” Accordingly, both PA and conventional UT techniques have been qualified for examinations in wrought materials. Yet, with respect to UT applications, CASS materials are not comparable to other NPP component materials. The microstructure of CASS materials, coupled with the physics of mechanical wave propagation, drive the requirement for use of advanced UT methods for the examination of these variable, coarse-grained materials.

It is important to consider that performance demonstration requirements for CASS have not yet been established. Thus, any performance-based approach to CASS examinations should not necessarily be based on procedures that were developed for more isotropic materials, such as carbon steel or wrought stainless steel, that have much different sound propagation and attenuation properties than CASS. The approach ultimately adopted for CASS is therefore likely to differ significantly from those already established for other materials (Chockie and Griesbach 2013).

As an example, typical round robin detection performance success metrics are set at  $\geq 80\%$  for the detection rate and  $\leq 20\%$  for FCP. These values are generally based on historical performance demonstration requirements in fine-grained materials, such as carbon steel or wrought stainless steel. However, it is well known that the coarse grain structures in CASS pose unique challenges and make this material more difficult to examine. Research into CASS inspections have been ongoing for decades. Although PNNL’s research shows that the 80/20 POD/FCP performance demonstration threshold for CASS is attainable with current methods and technology, it is likely that these performance thresholds may not be appropriate for CASS (Anderson et al. 2007; Diaz et al. 2012; Crawford et al. 2015; Diaz et al. 2017). Therefore, PNNL proposes that the POD and FCP thresholds for flaws in CASS, as well as strategies for length and depth sizing, should be evidence-based and evaluated independently of the values (and their bases) that are currently used in Section XI, Appendix VIII Piping Supplements 2, 3, and 10.



## 9 CONCLUSIONS

This report has summarized historical and current information regarding the viability of applying advanced NDE, specifically UT, for examining CASS piping weldments to detect and characterize potential service-induced flaws in these components. The primary obstacles to effective examinations are the coarse-grained and wide-ranging spatial variability of the microstructures found between heats of castings and even within the same casting heat. This unpredictability of the microstructures in field use effectively eliminates nearly any approach to tailor certain UT parameters for application on specific CASS material grain structures.

Research by multiple national and international organizations demonstrate that low frequency PA-UT is be effective for detecting flaws in of CASS weldments. The use of LF UT enables adequate sound field penetration in these components, minimizing the effects of microstructural variability. PA-UT allows scans to be made with multiple angles nearly simultaneously. In addition, the inherent analytical capabilities of typical PA imaging software platforms are helpful for discriminating between flaws and geometrical responses. The application of PA-UT allows the optimization of sound field energies within the areas of interest, i.e., near the ID surface of the CASS weldment. PA-UT provides an effective approach for bringing adequate sound field intensities with sufficient SNR for reliable CASS examinations because of its ability to focus sound into the proper areas for flaw detection and its flexibility to be applied over multiple configurations. The ability to produce a robust SNR is an essential ultrasonic characteristic when an examiner is attempting to detect and distinguish flaw responses from other geometrical or metallurgical reflectors. Accordingly, it is important that associated PA focal laws be modeled effectively and applied to ensure robust sound field intensities in the proper areas of interest. Of course, it is necessary to have a sufficiently large active array aperture in order for robust sound fields to be produced in the targeted regions of material.

Based on years of domestic and international NDE research using LF-PA for CASS weldments in mockups, several technical conclusions with respect to the optimum frequencies to be applied have been reached. The foremost of these conclusions is that for CASS piping thicknesses greater than approximately 41 mm (1.6 in.), the use of 500 kHz PA-UT is necessary to provide adequate sound field penetration for flaw detection. Higher frequencies (up to 1.0 MHz) in this piping thickness should only be applied after a flaw is detected, to facilitate characterization, i.e., length-, and potentially, depth-sizing. However, the frequency for initial detection screening should not exceed 500 kHz.

In the case of CASS weldments with wall thicknesses equal to or less than 41 mm (1.6 in.), only a slightly higher (800 kHz) application has shown to be the most effective for overall detection, exhibiting better SNRs than higher frequencies in laboratory trials. Similar to the thick-walled recommendation, it may be appropriate to apply higher frequencies (1.5–2.0 MHz, depending on sound field coherency experienced) for flaw characterization, but it is not recommended to exceed 800 kHz for initial detection.

Research shows that the use of multiple angles over a specified range need to be applied in order to allow the best angles to penetrate the “windows” in varied CASS microstructures. Studies using PA-UT on flawed test specimens have concentrated on the use of refracted longitudinal beam angles between 35–53° for the detection and sizing of ID surface initiated flaws (Coaster 2005; Anderson et al. 2007; Crawford et al. 2011). Incident refracted longitudinal waves between 40–50° also result in the largest coefficient of reflection for ID surface initiated flaws (Krautkramer and

Krautkramer 1969). A condition in 10 CFR 50.55a allows the use of PA search units that produce angles including, but not limited to, 30°–55° with a maximum increment of 5° (82 FR 32934 2017).

Considering the conclusions above concerning a) the use of low frequencies for effective penetration, b) generating sufficient sound field intensities by applying PA technology, and c) performing scans over a wide range of angles with fine incremental steps to facilitate beam propagation in unknown microstructures, there remains one overarching issue that dominates these parameters for effective UT in CASS piping weldments. It has been shown that using non-encoded (real-time) scanning methods with transient signal analyses results in a poor likelihood that an examiner will be able to distinguish between coherent reflections caused by geometry or microstructural variations and responses caused by flaws in CASS weldments. Further, due to the potential for lower-than-normal SNRs in CASS, as opposed to those typically found in wrought materials, there is a real possibility that flaw signals may be overlooked due to their extremely short screen persistence times when scanning in a real-time mode. It is therefore concluded that real-time, non-encoded scans should not be employed for CASS components. Thus, in order to ensure that effective and reliable examinations are conducted, it is recommended that spatial encoding, coupled with off-line post-processing and imaging techniques, be used for CASS piping examinations, where possible.

The use of modeling to validate examination parameters was discussed in the previous chapter. It is concluded that even simple models, which only provide theoretical beam projections, are beneficial to examiners in facilitating choices for array probe design by defining active aperture sizes, to assist focal law development, to ensure appropriate beam intensities, and to optimize steering within the components being inspected. It is possible that more sophisticated simulations (including reflected signal response) could eventually be conducted reliably and effectively in the future, providing information on expected flaw detection capabilities and volumetric coverage.

Finally, as with any new approach or technology in NDE, the examination of CASS using LF-PA will require that fundamental knowledge and skills be developed for application by field examiners. Examples of information include casting processes that result in the unpredictable and highly variable microstructures, along with how these are expected to affect UT propagation in CASS. Best practices need to be developed to help examiners distinguish between coherent energies and varied modes returned from the coarse grains or geometrical features, and similar reflections from flaws, to enhance these examinations. In addition, it is recommended that examiners have access to suitable realistic CASS mockups with simulated service-induced flaws (cracks) for hands-on practice. It is concluded that formal classroom training and hands-on practice is paramount if effective and reliable examinations are to be performed on CASS. It is PNNL's position that training and qualification activities be developed as soon as possible to support performance demonstrations and field applications for CASS examinations.

The conclusions and recommendations provided here are generally consistent (although slightly more restrictive) with the requirements of ASME Code Case N-824, when implementing the NRC conditions imposed on the application of this Code Case. While the use of N-824 (with conditions) represents significant improvement over conventional UT for CASS examinations, there is an uncertain issue that remains with this approach. Code Case N-824, as an alternative to the existing, prescriptive UT requirements found in ASME Section XI, Appendix III, is only a *voluntary application* by users of the Code. Thus, while N-824 requirements, along with NRC conditions, represent enhancements to UT techniques for these coarse-grained weldments, the number of licensees that will choose to implement the Code Case for the examination of CASS weldments is uncertain.

As indicated by the NRC,<sup>6</sup> most of the plants currently operating have now been granted a 20-year extended license term. Since GALL aging management program commitments require the implementation of adequate inspection methods to ensure the detection of cracks for susceptible welds in CASS components, and because Section XI, Appendix VIII, Supplement 9, has yet to be developed, it would seem prudent for ASME Section XI to revise Code Case N-824 and Section XI, Appendix III Supplement 2 (which incorporated the Code Case into the Code in the 2015 Edition) to address NRC conditions. This would serve as a stop-gap measure to encourage the use of Code Case N-824 by industry while Supplement 9 is being developed.

With respect to development of ASME Appendix VIII, Supplement 9 performance demonstration requirements for CASS, the many years of domestic and international research cited in this report, currently pointing to the use of advanced LF-PA encoded UT methods, provides a fundamental and cohesive basis to support the feasibility of reliable CASS piping examinations. Thus, the ASME should continue moving forward with the development of Supplement 9 to provide a performance-demonstration approach for improving the effectiveness and reliability of UT examinations in CASS weldments. It is important to note that the current unified approach described by existing Appendix VIII requirements may not be entirely suitable for CASS materials due to their varied, extremely coarse-grained, and unique microstructures. Therefore, it is recommended that new methods to match the UT capabilities, limitations, and minimum detection requirements for CASS examinations be pursued.

---

<sup>6</sup> "Status of License Renewal Applications and Industry Activities" at [www.nrc.gov](http://www.nrc.gov).



## 10 REFERENCES

82 FR 32934. 2017. "Incorporation by Reference of American Society of Mechanical Engineers Codes and Code Cases." *Federal Register* 82(136):32934-32986. Nuclear Regulatory Commission, Washington, D.C. Available at <https://www.gpo.gov/fdsys/pkg/FR-2017-07-18/pdf/2017-14166.pdf>.

83 FR 40685. 2018. "Approval of American Society of Mechanical Engineers' Code Cases." *Federal Register* 83(159):40685-40703. Nuclear Regulatory Commission, Washington, D.C. Available at <https://www.govinfo.gov/content/pkg/FR-2018-08-16/pdf/2018-17650.pdf>.

Achenbach JD. 1992. "Mathematical Modeling for Quantitative Ultrasonics." *Nondestructive Testing and Evaluation* 8-9(1-6):363-377. DOI: 10.1080/10589759208952716.

Adler L and C Mattei. 2000. "Impacts of Nonlinear Acoustics on Nondestructive Evaluation and Acousto-Optics." In *Nonlinear Acoustics at the Turn of the Millennium: ISNA 15, 15th International Symposium*, pp. 317-320. September 1-4, 1999, Gottingen, Germany. DOI: 10.1063/1.1309231. AIP Conference Proceedings Vol. 524.

AEC. 1971a. "General Design Criterion (GDC) 14, Reactor Coolant Pressure Boundary." In *Appendix A to Part 50—General Design Criteria for Nuclear Power Plants*. Washington, D.C.: Atomic Energy Commission (AEC).

AEC. 1971b. "General Design Criterion (GDC) 30, Quality of Reactor Coolant Pressure Boundary." In *Appendix A to Part 50—General Design Criteria for Nuclear Power Plants*. Washington, D.C.: Atomic Energy Commission (AEC).

Ahmed S and MT Anderson. 2009. *Task 1 Final Report, Theoretical/Mathematical Modeling of Ultrasonic Wave Propagation in Anisotropic Polycrystalline Stainless Steels*. PNNL-18363. Richland, WA: Pacific Northwest National Laboratory.

Anderson MT, SL Crawford, SE Cumblidge, KM Denslow, AA Diaz and SR Doctor. 2007. *Assessment of Crack Detection in Heavy-Walled Cast Stainless Steel Piping Welds Using Advanced Low-Frequency Ultrasonic Methods*. NUREG/CR-6933, PNNL-16292. Washington, D.C.: U.S. Nuclear Regulatory Commission. ADAMS Accession No. ML071020410.

Anderson MT, AA Diaz, AD Cinson, SL Crawford, SE Cumblidge, SR Doctor, KM Denslow and S Ahmed. 2011. *An Assessment of Ultrasonic Techniques for Far-Side Examinations of Austenitic Stainless Steel Piping Welds*. NUREG/CR-7113, PNNL-19353. Washington, D.C.: U.S. Nuclear Regulatory Commission. ADAMS Accession No. ML12011A130.

Anderson MT, AA Diaz, AD Cinson, SL Crawford, MS Prowant and SR Doctor. 2014. *Final Assessment of Manual Ultrasonic Examinations Applied to Detect Flaws in Primary System Dissimilar Metal Welds at North Anna Power Station*. PNNL-22553. Richland, WA: Pacific Northwest National Laboratory. ADAMS Accession No. ML14080A002.

AREVA. 2013. *Modeling and Simulation -- Inspection Design & Qualification*. ANP:U-371-V2-13-ENG. Available at [http://us.areva.com/home/liblocal/docs/Catalog/PWR/ANP\\_U\\_371\\_V2\\_13\\_ENG\\_ModelingSimulation.pdf](http://us.areva.com/home/liblocal/docs/Catalog/PWR/ANP_U_371_V2_13_ENG_ModelingSimulation.pdf).

ASME. 2000. *Code Case N-504-2, Alternative Rules for Repair of Classes 1, 2, and 3 Austenitic Stainless Steel Piping, Section XI, Division 1*. NY: American Society of Mechanical Engineers.

ASME. 2008. *White Paper -- Technical Basis for Proposed Alternate Requirements for Ultrasonic Examination of Cast Austenitic Piping Welds from the Outer Diameter (OD) Surface; Case N-824: Alternate Requirements for Ultrasonic Examination of Cast Austenitic Piping Welds from the Outer Diameter (OD) Surface, Section XI, Division 1*. Washington, D.C.: U.S. Nuclear Regulatory Commission. Available at <https://adams.nrc.gov/wba/view>. ADAMS Accession No. ML17111A483.

ASME. 2012. *Code Case N-824, Ultrasonic Examination of Cast Austenitic Piping Welds from the Outside Surface, Section XI, Division 1*. NY: American Society of Mechanical Engineers. Approved October 16, 2012.

ASME. 2015. *Code Case N-838, Flaw Tolerance Evaluation of Cast Austenitic Stainless Steel Piping, Section XI, Division 1*. NY: American Society of Mechanical Engineers. Approved August 3, 2015.

ASNT. 2004. *Nondestructive Testing Handbook, Third Edition: Volume 5, Electromagnetic Testing*. eds: SS Udpa and PO Moore, Columbus, OH: American Society for Nondestructive Testing. ISBN 1-57117-046-4.

ASNT. 2012. *Nondestructive Testing Handbook, Third Edition: Volume 10, Nondestructive Testing Overview*. eds: GL Workman and PO Moore, Columbus, OH: American Society for Nondestructive Testing. ISBN 978-1-57117-187-0.

ASTM E2491-13. 2013. "Standard Guide for Evaluating Performance Characteristics of Phased-Array Ultrasonic Testing Instruments and Systems." ASTM International, West Conshohocken, WA.

Auld BA. 1973. *Acoustic Fields and Waves in Solids, Volume 1*, NY: John Wiley & Sons. ISBN 10-0471037001.

Bamford WH, El Landerman and E Diaz. 1985. "Thermal Aging of Cast Stainless Steel, and Its Impact on Piping Integrity." *Journal of Engineering Materials and Technology* 107(1):53-60. DOI: 10.1115/1.3225771.

Barat P, S De and SK Bandyopadhyay. 1998. "Fractal Property of Backscattered Acoustic Signals from Polycrystalline Aluminium." *Physics Letters A* 245(1):91-96. DOI: 10.1016/S0375-9601(98)00325-9.

Barkar T. 2018. *Modelling Phase Separation in Fe-Cr Alloys: A Continuum Approach*. Ph.D. Thesis, KTH Royal Institute of Technology, Stockholm, Sweden. Available at <http://www.diva-portal.org/smash/get/diva2:1250767/FULLTEXT01.pdf>.

Bates DJ, SR Doctor, PG Heasler and E Burck. 1987. *Stainless Steel Round Robin Test: Centrifugally Cast Stainless Steel Screening Phase*. NUREG/CR-4970, PNL-6266, PISC III Report No. 3. Washington, D.C.: U.S. Nuclear Regulatory Commission.

Becker FL, SR Doctor, PG Heasler, CJ Morris, SG Pitman, GP Selby and FA Simonen. 1981. *Integration of NDE Reliability and Fracture Mechanics, Phase 1 Report*. NUREG/CR-1696, PNL-3469 Vol. 1. Washington, D.C.: U.S. Nuclear Regulatory Commission.



Becker J, LJ Jacobs and J Qu. 2003. "Characterization of Cement-Based Materials Using Diffuse Ultrasound." *Journal of Engineering Mechanics* 129(12):1478-1484. DOI: 10.1061/(ASCE)0733-9399(2003)129:12(1478)).

Bedetti T, V Dorval, L Ducouso-Ganjehi, F Jenson, S Chatillon and A Derode. 2013. "Characterization and Modeling of Ultrasonic Structural Noise in Coarse-Grain Steel in the Diffusive Regime." In *Proceedings of the 2013 International Congress on Ultrasonics*, p. P0476. May 2-5, 2013, Singapore. DOI: 10.3850/978-981-07-5938-4\_P0476. Research Publishing, Singapore.

Bischof GT. 2008. Letter to NRC Document Control Desk. "Dominion Nuclear Connecticut, Inc., Millstone Power Station Unit 2, Summary of Reactor Coolant Pump Dissimilar Metal Weld Examinations." June 13, 2008, Glen Allen, VA: Dominion Nuclear Connecticut, Inc. ADAMS Accession No. ML081650454.

Bond LJ. 1990. "Numerical Techniques and Their Use to Study Wave Propagation and Scattering - A Review." In *Elastic Waves and Ultrasonic Nondestructive Evaluation: Proceedings of the IUTAM Symposium on Elastic Wave Propagation and Ultrasonic Evaluation*, pp. 17-28. July 30-August 3, 1989, Boulder, CO. Elsevier Science Publishers, North-Holland.

Buckin V, B O'Driscoll and C Smyth. 2003. "Ultrasonic Spectroscopy for Material Analysis. Recent Advances." *Spectroscopy Europe* 15(1):20-25.

Burckhardt CB, P-A Grandchamp and H Hoffmann. 1974. "Methods for Increasing the Lateral Resolution of B-Scan." In *Acoustical Holography: Volume 5*, pp. 391-413. ed: PS Green. Boston, MA: Springer US. DOI: 10.1007/978-1-4757-0827-1\_22.

Burridge R, P Chadwick and AN Norris. 1993. "Fundamental Elastodynamic Solutions for Anisotropic Media with Ellipsoidal Slowness Surfaces." *Proceedings of the Royal Society of London. Series A: Mathematical and Physical Sciences* 440(1910):655-681. DOI: 10.1098/rspa.1993.0039.

Busse LJ, HD Collins and SR Doctor. 1984. *Review and Discussion of the Development of Synthetic Aperture Focusing Technique for Ultrasonic Testing, SAFT UT*. NUREG/CR-3625, PNL-4957. Washington, D.C.: U.S. Nuclear Regulatory Commission.

Cantrell JH and WT Yost. 2001. "Nonlinear Ultrasonic Characterization of Fatigue Microstructures." *International Journal of Fatigue* 23:487-490. DOI: 10.1016/S0142-1123(01)00162-1.

Casto C. 2001. *V. C. Summer Hot Leg Nozzle-to-Pipe Weld Crack - Potential Generic Issues*. Memorandum to Jack R. Strosnider, April 2, 2001. Atlanta, GA: U.S. Nuclear Regulatory Commission, Region II. ADAMS Accession No. ML010930432.

Cereser Camara V, D Laux, G Despaux and D Baron. 2008. "Ultrasonic Critical Angle Reflectometry Applied to Porous Nuclear Fuel Mechanical Characterization." In *Acoustics '08*, pp. 2539-2543. June 29-July 4, 2008, Paris.

CGI. 2012. *Summary Report -- 4th International Workshop on the Future Directions for the Inspection of Cast Austenitic Stainless Steel Piping*. Seattle, WA: Chockie Group International, Inc. Available at <http://www.chockiegroup.com/pdf/Workshop4.pdf>.

Chassignole B, D Villard and M Dubuget. 2000. "Characterization of Austenitic Stainless Steel Welds for Ultrasonic NDT." In *Review of Progress in Quantitative Nondestructive Evaluation, Vol. 19*, pp. 1325-1332. July 25-30, 1999, Montreal, Canada. DOI: 10.1063/1.1307835. American Institute of Physics, Melville, NY.

Chassignole B, V Duwig, MA Ploix, P Guy and R El Guerjouma. 2009. "Modelling the Attenuation in the ATHENA Finite Elements Code for the Ultrasonic Testing of Austenitic Stainless Steel Welds." *Ultrasonics* 49(8):653-658. DOI: 10.1016/j.ultras.2009.04.001.

Chockie A and TJ Griesbach. 2013. "The Long Journey in the Development of ISI Rules for CASS Piping." In *ASME 2013 Pressure Vessels and Piping Conference*, p. V01AT01A058. July 14-18, 2013, Paris, France. DOI: 10.1115/PVP2013-98112. NY: American Society of Mechanical Engineers.

Chopra OK. 1991. *Estimation of Fracture Toughness of Cast Stainless Steel During Thermal Aging in LWR Systems*. NUREG/CR-4513, ANL-90/42. Washington, D.C.: U.S. Nuclear Regulatory Commission.

Chopra OK. 1994. *Estimation of Fracture Toughness of Cast Stainless Steel During Thermal Aging in LWR Systems*. NUREG/CR-4513, ANL-93/22, Revision 1. Washington, D.C.: U.S. Nuclear Regulatory Commission. ADAMS Accession No. ML052360554.

Chopra OK and AS Rao. 2016. *Estimation of Fracture Toughness of Cast Stainless Steel During Thermal Aging in LWR Systems*. NUREG/CR-4513, ANL-15/08, Revision 2. Washington, D.C.: U.S. Nuclear Regulatory Commission. ADAMS Accession No. ML16145A082.

Cinson AD and SL Crawford. 2010. "Looking Below the Surface with Ultrasonic Phased Array." *Quality Magazine*. Available at <http://www.qualitymag.com/articles/89769-looking-below-the-surface-with-ultrasonic-phased-array>.

Clayton TN, DS Kupperman and KJ Reimann. 1985. "Visualization of Ultrasonic Beam Distortion in Anisotropic Stainless Steel." *Journal de Physique Colloques* 46(C10):C10-795 to C10-799. DOI: 10.1051/jphyscol:198510174.

Clouet JF and JP Fouque. 1997. "A Time-Reversal Method for an Acoustical Pulse Propagating in Randomly Layered Media." *Wave Motion* 25(4):361-368. DOI: 10.1016/S0165-2125(97)00002-4.

Coaster DS. 2005. *Report from the Trial Phased Array Inspection of the Cast Stainless Steel Test Pieces*. R-T05-055 (Internal Report). WesDyne-TRC AB.

Crawford SL, AD Cinson, TL Moran, MT Anderson and AA Diaz. 2011. *Improvements in 500-kHz Ultrasonic Phased-Array Probe Designs for Evaluation of Thick Section Cast Austenitic Stainless Steel Piping Welds*. PNNL-20238. Richland, WA: Pacific Northwest National Laboratory.

Crawford SL, MS Prowant, AD Cinson, MR Larche, AA Diaz and MT Anderson. 2014. *Phased Array Ultrasonic Sound Field Mapping in Cast Austenitic Stainless Steel*. PNNL-23393. Richland, WA: Pacific Northwest National Laboratory. ADAMS Accession No. ML14155A165.

Crawford SL, AD Cinson, AA Diaz and MT Anderson. 2015. *Phased Array Ultrasonic Examination of Reactor Coolant System (Carbon Steel-to-CASS) Dissimilar Metal Weld Mockup Specimen*. PNNL-24920. Richland, WA: Pacific Northwest National Laboratory. ADAMS Accession No. ML16041A137.

Darbari GS, RP Singh and GS Verma. 1968. "Ultrasonic Attenuation in Carbon Steel and Stainless Steel at Elevated Temperatures." *Journal of Applied Physics* 39(5):2238-2245. DOI: 10.1063/1.1656537.

Dau G, MM Behraves, F Ammirato and B Stone. 1991. "Progress in EPRI Programs on Inspection of Cast Austenitic Stainless Steel." In *The Complementary roles of Fracture Mechanics and Non-destructive Examination in the Safety Assessment of Components: Proceedings of a Workshop*, pp. 337-360. October 3-5, 1988, Wuerenlingen, Switzerland. OECD Nuclear Energy Agency, Paris, France.

Davis JM and M Moles. 2007. "Phased Arrays vs. Phased Arrays – Beam Sweeping vs. Encoded Data Collection." *NDT.net*. Available at [www.ndt.net/search/docs.php?id=4807](http://www.ndt.net/search/docs.php?id=4807).

Declercq NF, R Briers and O Leroy. 2002. "The Use of Polarized Bounded Beams to Determine the Groove Direction of a Surface Corrugation at Normal Incidence, the Generation of Surface Waves and the Insonification at Bragg-Angles." *Ultrasonics* 40(1):345-348. DOI: 10.1016/S0041-624X(02)00119-1.

Dennis M. 2012. "Cast Stainless Steel Piping Update." In *4th International Workshop: Future Directions for the Inspection of Cast Austenitic Stainless Steel Piping*. May 24-25, 2012, Seattle, WA. Chockie Group International. PNNL-SA-77507. Available at <http://www.chockiegroup.com/pdf/Workshop4.pdf>.

Deutsch WAK and S Kierspel. 2012. "Manual Weld Inspection with Ultrasound - Conventionally or with Phased Arrays?" In *18th World Conference on Non-destructive Testing*. April 16-20, 2012, Durban, South Africa. British Institute of Non-Destructive Testing, Northampton, United Kingdom. Available at [http://www.ndt.net/article/wcndt2012/papers/560\\_wcndtfinal00560.pdf](http://www.ndt.net/article/wcndt2012/papers/560_wcndtfinal00560.pdf).

Diaz A, SL Crawford, RE Jacob, MR Larche, M Prowant, MT Anderson and C Nove. 2017. "Status Update of NDE Research at PNNL--CASS/DMW Examination Reliability." In *NRC-Industry Technical Exchange Meeting*. January 17-19, 2017, Rockville, MD. Pacific Northwest National Laboratory. PNNL-SA-123246. ADAMS Accession No. ML17013A628. Available at <https://www.nrc.gov/docs/ML1701/ML17013A628.pdf>.

Diaz AA, SR Doctor, BP Hildebrand, FA Simonen, GJ Schuster, ES Andersen, GP McDonald and RD Hasse. 1998. *Evaluation of Ultrasonic Inspection Techniques for Coarse Grained Materials*. NUREG/CR-6594, PNNL-11171. Washington, D.C.: U.S. Nuclear Regulatory Commission. ADAMS Accession No. ML14071A001.

Diaz AA, GJ Schuster, SL Crawford, KM Judd and SR Doctor. 2003. *Low-Frequency/SAFT-UT Data Fusion: Development and Evaluation of the Multi-Parameter Analysis Tool Set (MPATS)*. PNNL-26631. Richland, WA: Pacific Northwest National Laboratory. ADAMS Accession No. ML17213A607.

Diaz AA, RA Mathews, J Hixon and SR Doctor. 2007. *Assessment of Eddy Current Testing for the Detection of Cracks in Cast Stainless Steel Reactor Piping Components*. NUREG/CR-6929, PNNL-16253. Washington, D.C.: U.S. Nuclear Regulatory Commission.

Diaz AA, AD Cinson, SL Crawford, SE Cumblidge, KM Denslow, M Morra, MS Prowant and MT Anderson. 2008a. *Technical Letter Report: Assessment of Ultrasonic Phased Array Testing for Cast Austenitic Stainless Steel Pressurizer Surge Line Piping Welds and Thick Section Primary System Cast Piping Welds, JCN N6398, Task 2A*. PNNL-17698. Richland, WA: Pacific Northwest National Laboratory.

Diaz AA, RV Harris Jr. and SR Doctor. 2008b. *Field Evaluation of Low-Frequency SAFT-UT on Cast Stainless Steel and Dissimilar Metal Weld Components*. NUREG/CR-6984, PNNL-14374. Washington, D.C.: U.S. Nuclear Regulatory Commission.

Diaz AA, AD Cinson, SL Crawford, R Mathews, TL Moran and MT Anderson. 2009. *Technical Letter Report Assessment of Ultrasonic Phased Array Inspection Method for Welds in Cast Austenitic Stainless Steel Pressurizer Surge Line Piping JCN N6398, Task 1B*. PNNL-18596. Richland, WA: Pacific Northwest National Laboratory. ADAMS Accession No. ML092540501.

Diaz AA, AD Cinson, SL Crawford, R Mathews, TL Moran, MS Prowant and MT Anderson. 2012. *An Evaluation of Ultrasonic Phased Array Testing for Cast Austenitic Stainless Steel Pressurizer Surge Line Piping Welds*. NUREG/CR-7122, PNNL-19497. Richland, WA: Pacific Northwest National Laboratory. ADAMS Accession No. ML12087A061 and ML12087A063.

Dib G, SL Crawford, RE Jacob, MS Prowant and AA Diaz. 2017. *Validation of Ultrasonic Nondestructive Examination (NDE) Computational Models - Phase 1*. PNNL-26336. Richland, WA: Pacific Northwest National Laboratory. ADAMS Accession No. ML17082A190.

Dib G, MR Larche, MS Prowant, RE Jacob, P Ramuhalli and AA Diaz. 2018. *Ultrasound Modeling and Simulation: Status Update*. PNNL-28362. Richland, WA: Pacific Northwest National Laboratory. ADAMS Accession No. ML19010A072.

Doctor SR, TE Hall, LD Reid, SL Crawford, RJ Littlefield and RW Gilbert. 1987. *Development and Validation of a Real-Time SAFT-UT System for the Inspection of Light Water Reactor Components*. NUREG/CR-4583, PNL-5822, Vol. 2. Washington, D.C.: U.S. Nuclear Regulatory Commission.

Doctor SR, SM Bruemmer, MS Good, LA Charlot, TT Taylor, DM Boyd, JD Deffenbaugh and LD Reid. 1989. "Utilization of Ultrasonic Measurements to Quantify Aging-Induced Material Microstructure and Property Changes." In *Nondestructive Monitoring of Materials Properties Symposium*, pp. 143-149. November 28-30, 1988, Boston, MA. Materials Research Society, Pittsburgh, PA.

Doctor SR, GJ Schuster, LD Reid and TE Hall. 1996. *Real-Time 3-D SAFT-UT Evaluation and Validation*. NUREG/CR-6344, PNNL-10571. Washington, D.C.: U.S. Nuclear Regulatory Commission.

Dorval V, F Jenson, G Corneloup and J Moysan. 2009. "Simulation of Structural Noise and Attenuation Occurring in Ultrasonic NDT of Polycrystalline Materials." In *Ultrasonic Wave Propagation in Non Homogeneous Media*. eds: A Leger and M Deschamps. Berlin, Heidelberg: Springer. DOI: 10.1007/978-3-540-89105-5\_32.

Dorval V, F Jenson, G Corneloup and J Moysan. 2010. "Accounting for Structural Noise and Attenuation in the Modeling of the Ultrasonic Testing of Polycrystalline Materials." In *Review of Progress in Quantitative Nondestructive Evaluation*, Vol. 29, pp. 1309-1316. July 26-31, 2009, Kingston, RI. DOI: 10.1063/1.3362219. American Institute of Physics, Melville, NY.

Ensminger D. 1973. *Ultrasonics: The Low and High-Intensity Applications*, NY: M. Dekker, Inc. ISBN 0824711750, 9780824711757.

Ensminger D and LJ Bond. 2011. "Chapter 14: Medical Applications of Ultrasonic Energy." In *Ultrasonics: Fundamentals, Technology and Applications, Third Edition (Revised and Expanded)*, pp. 583-658. Boca Raton, FL: CRC Press. DOI: 10.1201/b11173-15.

EPRI. 2004. *Automated Phased Array UT for Dissimilar Metal Pipe Welds*. TR-1011054. Palo Alto, CA: Electric Power Research Institute (EPRI). Information provided from the abstract. The full report is not publically available.

EPRI. 2005a. *Assessment of Cast Stainless Steel Inspection*. Report 1011600. Palo Alto, CA: Electric Power Research Institute (EPRI).

EPRI. 2005b. *Assessment of Cast Stainless Steel Inspection*. Report 101160. Palo Alto, California: Electric Power Research Institute (EPRI).

EPRI. 2007. *Nondestructive Evaluation: Improving NDE Examiner Proficiency*. Product ID: 1015150. Palo Alto, CA: Electric Power Research Institute (EPRI).

EPRI. 2008. *Nondestructive Evaluation: Plant Aging/License Renewal Nondestructive Examination Gap Solutions and Strategies, Vol. 1*. EPRI Report 1016673, Technical Update. Palo Alto, CA: Electric Power Research Institute.

EPRI. 2010. *Performance Demonstration Initiative (PDI) - Program Description, Revision 4*. Technical Report 1020593. Palo Alto, CA: Electric Power Research Institute. Available at <https://www.epri.com/#/pages/product/1020593/>.

EPRI. 2017. *Nondestructive Evaluation: Cast Austenitic Stainless Steel Round-Robin Study Summary of Results*. 3002010314 Final Report. Palo Alto, CA: Electric Power Research Institute (EPRI).

EPRI. 2018. *Nondestructive Evaluation: Cast Austenitic Stainless Steel Round-Robin Study, Summary of Results, Revision 1*. 3002010314 Final Report. Palo Alto, CA: Electric Power Research Institute (EPRI). Available at <https://www.epri.com/#/pages/product/000000003002010314/>.

Ericsson L and MG Gustafsson. 1998. "Perception and Entropy Inspired Ultrasonic Grain Noise Suppression, Using Non Coherent Detector Statistics." In *7th European Conference on Non-destructive Testing*. May 26-29, 1998, Copenhagen, Denmark. Available at <http://www.ndt.net/article/ecndt98/simulat/360/360.htm>.

Extende S.A. 2011. "Interview - Steve Mahaut." Massy, France: Extende S.A. Accessed December 20, 2017. Available at <http://www.extende.com/steve-mahaut>.

Faidy C, G Martin, S Chapuliot, Y Kayser, N Safa, MF Cipierre, P Gilles, H Keinanen, A Laukkanen, A Sherry, D Lidbury, J Wintle, N Taylor, A Youtsos and G Lenkey. 2003. "Assessment of Aged Piping Dissimilar Metal Weld Integrity (ADIMEW)." In *Presented at FISA 2003, Proceedings of the EU Research in Reactor Safety, EC Luxembourg, EURATOM, Brussels (EUR 20281)*. November 10-13, 2003.

Faidy C. 2010. "Flaw Evaluation in Elbows Through French RSEM Code." In *ASME 2010 Pressure Vessels and Piping Conference: Volume 1*, pp. 771-778. July 18–22, 2010, Bellevue, Washington. DOI: 10.1115/PVP2010-25085. American Society of Mechanical Engineers, NY.

Feuilly N, O Dupond, B Chassignole, J Moysan and G Comeloup. 2009. "Relation Between Ultrasonic Backscattering and Microstructure for Polycrystalline Materials." In *Proceedings of the 35th Annual Review of Progress in Quantitative Nondestructive Evaluation, Vol. 28*, pp. 1216-1223. July 25-28, 2008, Chicago, IL. DOI: 10.1063/1.3114093. American Institute of Physics, Melville, NY.

Fink M, C Prada, F Wu and D Cassereau. 1989. "Self Focusing in Inhomogeneous Media with Time Reversal Acoustic Mirrors." In *1998 IEEE Ultrasonics Symposium Proceedings*, pp. 681-686. October 5-8, 1989, Sendai, Miyagi, Japan. DOI: 10.1109/ULTSYM.1989.67072. IEEE, Piscataway, NJ.

Frederick JR, JA Seydel and RC Fairchild. 1976. *Improved Ultrasonic Non-Destructive Testing of Pressure Vessels, Annual Progress Report, August 1, 1974-July 31, 1975*. NUREG-0007-1. Washington, D.C.: U.S. Nuclear Regulatory Commission.

Frederick JR, RC Fairchild and BH Anderson. 1977. *Improved Ultrasonic Nondestructive Testing of Pressure Vessels, Annual Progress Report, August 1, 1975-July 31, 1976*. NUREG-0007-2. Washington, D.C.: U.S. Nuclear Regulatory Commission.

Frederick JR, C Vanden Broek, S Ganapathy, M Elzinga, W De Vries, D Papworth and N Hamano. 1979. *Improved Ultrasonic Nondestructive Testing of Pressure Vessels*. NUREG/CR-0909. Washington, D.C.: U.S. Nuclear Regulatory Commission.

Frederick JR, et al. 1978. *Improved Ultrasonic Nondestructive Testing of Pressure Vessels, Annual Progress Report, October 1, 1976-September 30, 1977*. NUREG/CR-0135. Washington, D.C.: U.S. Nuclear Regulatory Commission.

Frederick JR, et al. 1979. *Improved Ultrasonic Nondestructive Testing of Pressure Vessels, Annual Progress Report, October 1, 1977-September 30, 1978*. NUREG/CR-0581. Washington, D.C.: U.S. Nuclear Regulatory Commission.

Frenet D, P Calmon, L Paradis, O Roy and M Ouafouh. 2000. "Modeling of Surface Acoustic Waves Reflected on Fluid-Loaded Solids. Application to Measurements on Anisotropic Materials with a Phased-Array Broadband Transducer." In *Review of Progress in Quantitative Nondestructive Evaluation*, pp. 1017-1024. July 25-30, 1999, Montreal, Quebec, Canada. DOI: 10.1063/1.1306155.

Ganapathy S, N Hamano, MR Bether, WS Wu, TG Dennehy, C Purnaveja, MM Murray, MB Etzinga and F Raam. 1981. *Ultrasonic Imaging Techniques for Real-time In-service Inspection of Nuclear Power Reactors*. NUREG/CR-2154. Washington, D.C.: U.S. Nuclear Regulatory Commission.



Ganapathy S, WS Wu and B Schmult. 1982. "Analysis and Design Considerations for a Real-Time System for Non-Destructive Evaluation in the Nuclear Industry." *Ultrasonics* 20(6):249-256. DOI: 10.1016/0041-624X(82)90045-2.

Ganapathy S and B Schmult. 1985. "Design of a Real-Time Inspection System for NDE of Reactor Vessels and Piping Components." *International Journal of Pressure Vessels and Piping* 20:17-41. DOI: 10.1016/0308-0161(85)90032-8.

Ganjeji L, C Poidevin, G Cattiaux and T Sollier. 2010. "Experimental and Numerical Study of Ultrasonic Propagation in Cast Stainless Steel Material." In *8th International Conference on NDE in Relation to Structural Integrity for Nuclear and Pressurised Components*, Berlin, Germany. Available at <http://www.ndt.net/article/jrc-nde2010/papers/108.pdf>.

Ganjeji L, F Jenson, G Cattiaux and T Sollier. 2013. "Inspection of CASS Components Using New Optimized Phased Array Probes." In *9th International Conference on NDE in Relation to Structural Integrity for Nuclear and Pressurized Components*, pp. 950-959. May 22-24, 2012, Seattle, WA. NDT.net. Available at <https://www.ndt.net/article/jrc-nde2012/papers/145.pdf>.

Ghoshal G and JA Turner. 2009. "Diffuse Ultrasonic Backscatter in a Two-Dimensional Domain." *Acta Mechanica* 205(1-4):35-49. DOI: 10.1007/s00707-009-0175-2.

Goebbels K. 1980. "Chapter 4, Structure Analysis by Scattered Ultrasonic Radiation." In *Research Techniques in Nondestructive Testing, Vol. IV*. ed: RS Sharpe. NY: Academic Press, Inc.

Goebbels K. 1994. *Materials Characterization for Process Control and Product Conformity*, Boca Raton, FL: CRC Press.

Good MS and LG Van Fleet. 1987. "Ultrasonic Beam Profiles in Coarse Grained Materials." In *8th International Conference on NDE in the Nuclear Industry*, pp. 657-666. November 17-20, 1986, Kissimmee, FL. American Society for Metals, Metals Park, OH.

Good MS and LG Van Fleet. 1988. "Mapping of Ultrasonic Fields in Solids." In *Review of Progress in Quantitative Nondestructive Evaluation, Vol. 7*, pp. 637-646. June 22-26, 1987, Williamsburg, VA. Plenum Publishing Corp., NY.

Good MS and ER Green. 1989. "Mapping of 1-MHz, 45° Longitudinal Fields in Centrifugally Cast Stainless Steel." In *Review of Progress in Quantitative Nondestructive Evaluation, Vol. 8*, pp. 889-896. Plenum Publishing Corp., NY.

Good MS, BP Hildebrand and CM Batson. 1991. "Phase Mapping of Ultrasonic Fields Passed Through Centrifugally Cast Stainless Steel." In *Review of Progress in Quantitative Nondestructive Evaluation*, pp. 1975-1982. July 15-20, 1990, La Jolla, CA. DOI: 10.1007/978-1-4615-3742-7\_109. Plenum Press, NY.

Griesbach TJ, G Cofie and RO McGill. 2007. "An Update on Flaw Tolerance Evaluation Studies on Thermally Aged Cast Austenitic Stainless Steel Piping." In *6th International Conference on NDE in Structural Integrity for Nuclear and Pressurized Components*. October 8-10, 2007, Budapest, Hungary.

Griesbach TJ, D Dedhia, DO Harris, NG Cofie, K Amberge and A Alleshwaram. 2014. "The Influence of Flow Strength and Fracture Toughness on the Computed Reliability of Thermally Aged Grade CF8M Cast Austenitic Stainless Steel Piping." In *Proceedings of the ASME Pressure Vessels and Piping Conference (PVP-2014)*. July 20-24, 2014, Anaheim, CA. DOI: 10.1115/PVP2014-28089. American Society of Mechanical Engineers, NY.

Griesbach TJ, D Dedhia, DO Harris, NG Cofie, A Alleshwaram and K Amberge. 2015. "Further Validation of the Technical Basis of Code Case N-838 for Flaw Tolerance Evaluation of CASS Piping." In *Proceedings of the ASME Pressure Vessels and Piping Conference (PVP-2015)*. July 19-23, 2015, Boston, Massachusetts. DOI: 10.1115/PVP2015-45191. American Society of Mechanical Engineers, New York.

Grimes CI. 2000. Letter to Mr. Douglas J. Walters (Nuclear Energy Institute). "License Renewal Issue No. 98-0030, Thermal Aging Embrittlement of Cast Austenitic Stainless Steel Components." May 19, 2000, Washington, D.C.: Nuclear Regulatory Commission. ADAMS Accession No. ML003717179.

Gunaratne GPP and K Christidis. 2002. "Material Characterization in Situ Using Ultrasound Measurements." *IEEE Transactions on Instrumentation and Measurement* 51(2):368-373. DOI: 10.1109/19.997839.

Hall TE, LD Reid and SR Doctor. 1988. *The SAFT-UT Real-Time Inspection System - Operational Principles and Implementation*. NUREG/CR-5075, PNNL-6413. Washington, D.C.: U.S. Nuclear Regulatory Commission.

Hamano N. 1980. *Deconvolution of Ultrasonic Nondestructive Testing Data*. Ph.D. Thesis, University of Missouri, Columbia, MO.

Hamlin DR and JL Jackson. 1981a. *Program for Field Validation of the Synthetic Aperture Focusing Technique for Ultrasonic Testing (SAFT-UT), Quarterly Progress Report, November 1980-January 1981*. NUREG/CR-1885, Vol. 2. Washington, D.C.: Nuclear Regulatory Commission.

Hamlin DR and JL Jackson. 1981b. *Program for Field Validation of the Synthetic Aperture Focusing Technique for Ultrasonic Testing (SAFT-UT), Quarterly Progress Report, February-April 1981*. NUREG/CR-1885, Vol. 3. Washington, D.C.: Nuclear Regulatory Commission.

Hannemann R, R Marklein, KJ Langenberg, C Schurig, B Köhler and F Walte. 2000. "Ultrasonic Wave Propagation in Real-Life Austenitic V-butt Welds: Numerical Modeling and Validation." In *Review of Progress in Quantitative Nondestructive Evaluation, Vol. 19*, pp. 145-152. July 25-30, 1999, Montreal, Canada. DOI: 10.1063/1.1306045. American Institute of Physics, Melville, NY.

Heasler PG and SR Doctor. 1996. *Piping Inspection Round Robin*. NUREG/CR-5068, PNL-10475. Washington, DC: U.S. Nuclear Regulatory Commission.

Heasler PG and SR Doctor. 2003. *A Comparison of Three Round Robin Studies on ISI Reliability of Wrought Stainless Steel Piping*. NUREG/CR-6795, PNNL-13873. Washington, D.C.: U.S. Nuclear Regulatory Commission.

Hildebrand BP, MS Good and AA Diaz. 1991. *Ultrasonic Classification of Centrifugally Cast Stainless Steel Utilizing the Rayleigh Critical Angle Technique*. Richland, Washington: Pacific Northwest National Laboratory.

ISU. 2012. "Signal-to-Noise Ratio." Ames, IA: NDT Resource Center, Center for NDE, Iowa State University (ISU). Accessed December 21, 2017. Available at <http://www.ndt-ed.org/EducationResources/CommunityCollege/Ultrasonics/Physics/signaltonoise.htm>.

Jackson JL. 1978a. *Program for Field Validation of the Synthetic Aperture Focusing Technique for Ultrasonic Testing (SAFT-UT)--Analysis Before Test*. NUREG/CR-0288. Washington, D.C.: Nuclear Regulatory Commission.

Jackson JL. 1978b. *Program for Field Validation of the Synthetic Aperture Focusing Technique for Ultrasonic Testing (SAFT-UT) Midyear Progress Report*. NUREG/CR-0290. Washington, D.C.: Nuclear Regulatory Commission.

Jackson JL. 1981. *Program for Field Validation of the Synthetic Aperture Focusing Technique for Ultrasonic Testing (SAFT-UT), Quarterly Progress Report, August-October 1980*. NUREG/CR-1885, Vol. 1. Washington, D.C.: Nuclear Regulatory Commission.

Jacob RE, AE Holmes, MS Prowant, TL Moran and AA Diaz. 2018. *Interim Analysis of the EPRI Cass Round Robin Study*. PNNL-27712. Richland, WA: Pacific Northwest National Laboratory. ADAMS Accession No. ML18219B319.

Jansson C. 1990. "Degradation of Cast Stainless Steel Elbows After 15 Years in Service." Presented at *Fontevraud II International Symposium*, September 10-14, 1990, Vattenfall Energisystem.

Jayakumar T, A Kumar and B Raj. 2008. "Ultrasonic Characterization of Austenitic Stainless Steels." In *Proceedings of the 34th Annual Review of Progress in Quantitative Nondestructive Evaluation, Volume 27*, pp. 1162-1169. July 22-27, 2007, Golden, CO. American Institute of Physics, Melville, NY.

Jenson F, L Ganjeji, C Poidevin, G Cattiaux and T Sollier. 2009. "Modelling of Ultrasonic Propagation in Cast Stainless Steels with Coarse Grained Structures." In *Proceedings of the 7th International Conference on NDE in Relation to Structural Integrity for Nuclear and Pressurised Components*. May 12-14, 2009, Yokohama, Japan. European Commission Joint Research Centre, Luxembourg. Available at <http://www.ndt.net/article/jrc-nde2009/papers/42.pdf>.

Jeong H, J-S Lee, Y-H Jeong, S-M Bae and CH Lee. 2009. "Investigation of Ultrasonic Beam Focusing Effects for Inhomogeneous Media Using the Time Reversal Method." In *Proceedings of the 35th Annual Review of Progress in Quantitative Nondestructive Evaluation, Vol. 28*, pp. 113-120. July 25-28, 2008, Chicago, IL. DOI: 10.1063/1.3114083. American Institute of Physics, Melville, NY.

Jerebtsov SN, AA Kolomenskii and HA Schuessler. 2004. "Characterization of a Polycrystalline Material with Laser-Excited Nonlinear Surface Acoustic Wave Pulses." *International Journal of Thermophysics* 25(2):485-490. DOI: 10.1023/B:IJOT.0000028483.75351.e7.

Johnson SA, JF Greenleaf, FA Duck, A Chu, WR Samayoa and BK Gilbert. 1975. "Digital Computer Simulation Study of a Real-Time Collection, Post-Processing Synthetic Focusing Ultrasound Cardiac Camera." In *Acoustical Holography: Volume 6*, pp. 193-211. ed: N Booth. Boston, MA: Springer US. DOI: 10.1007/978-1-4615-8216-8\_10.

Katzman ES. 2013a. Letter to NRC Document Control Desk. "St. Lucie Unit 1, Docket No. 50-335, Inservice Inspection Plan, RAI Reply to Fourth Ten-Year Interval Unit 1 Relief Request No. 5, Revision 0." July 30, 2013, Jensen Beach, FL: Florida Power & Light Company. ADAMS Accession No. ML13219A254.

Katzman ES. 2013b. Letter to NRC Document Control Desk. "St. Lucie Unit 1, Docket No. 50-335, Inservice Inspection Plan, Fourth Ten-Year Interval Unit 1 Relief Request No. 5, Revision 0." February 4, 2013, Jensen Beach, FL: Florida Power & Light Company. ADAMS Accession No. ML13046A101.

Kerbrat E, C Prada, D Cassereau and M Fink. 2003. "Imaging in the Presence of Grain Noise Using the Decomposition of the Time Reversal Operator." *The Journal of the Acoustical Society of America* 113(3):1230-1240. DOI: 10.1121/1.1548156.

Krautkramer J and H Krautkramer. 1969. *Ultrasonic Testing of Materials*, Berlin: Springer-Verlag.

Kretschmann H-J and W Weinrich. 2004. "Ultrasound Techniques." In *Cranial Neuroimaging and Clinical Neuroanatomy: Atlas of MR Imaging and Computed Tomography, 3rd Ed.*, pp. 17-18. NY: Thieme.

Kröening M, A Bulavinov, KM Reddy, F Walte and M Dalichow. 2008. "Improving the Inspectability of Stainless Steel and Dissimilar Metal Welded Joints Using Inverse Phase-Matching of Phased Array Time-Domain Signals." In *17th World Conference on Nondestructive Testing*. October 25-28, 2008, Shanghai, China. Available at <https://www.researchgate.net/publication/26920046>.

Kulkarni SS and JD Achenbach. 2008. "Structural Health Monitoring and Damage Prognosis in Fatigue." *Structural Health Monitoring* 7(1):37-49. DOI: 10.1177/1475921707081973.

Kumar A, T Jayakumar, P Palanichamy and B Raj. 1999. "Influence of Grain Size on Ultrasonic Spectral Parameters in AISI Type 316 Stainless Steel." *Scripta Materialia* 40(3):333-340. DOI: 10.1016/S1359-6462(98)00435-7.

Kupperman DS, KJ Reimann and DI Kim. 1981. "Ultrasonic Characterization and Microstructure of Stainless Steel Weld Metal." In *Proceedings of Nondestructive Evaluation: Microstructural Characterization and Reliability Strategies*, pp. 199-216. October 5-9, 1980, Pittsburg, PA. The Metallurgical Society of AIME, Warrendale, PA.

Kupperman DS, KJ Reimann and J Abrego-Lopez. 1987. "Ultrasonic NDE of Cast Stainless Steel." *NDT International* 20(3):145-152. DOI: 10.1016/0308-9126(87)90401-9.

Kurozumi Y. 2004. "Influence of Ultrasonic Incident Angle and Defect Detection Sensitivity by Cast Stainless Steel Structure." In *ASME/JSME 2004 Pressure Vessels and Piping Conference, Recent Advances in Nondestructive Evaluation Techniques for Material Science and Industries*, pp. 207-214. July 25-29, 2004, San Diego, CA. DOI: 10.1115/PVP2004-2838. ASME, NY.

Lapides ME. 1991. *Cast Austenitic Stainless Steel Sourcebook*. TR-100034. Palo Alto, CA: Electric Power Research Institute.

Le Ber L, O Roy and P Benoist. 2007. "Ultrasonic Phased Array Inspection Modeling with CIVA: Reconstruction and Simulation of Data." In *Conference on Modelling in Non-Destructive Testing*, Pretoria, South Africa. ndt.net. Available at <http://www.ndt.net/article/modellingNDT2007/10.pdf>.

Libby HL. 1971. *Introduction to Electromagnetic Nondestructive Test Methods*, NY: Wiley-Interscience.

Liess O. 2008. "Curvature Properties of the Slowness Surface of the System of Crystal Acoustics for Cubic Crystals." *Osaka Journal of Mathematics* 45(1):173-210.

Lindgren M and T Lepistö. 2004. "On the Stress vs. Barkhausen Noise Relation in a Duplex Stainless Steel." *NDT & E International* 37(5):403-410. DOI: 10.1016/j.ndteint.2003.11.005.

Liu X, S Takamori, Y Osawa and F Yin. 2006. "Diffraction Correction in the Measurement of Ultrasonic Attenuation." *Materials Science and Engineering: A* 442(1):527-531. DOI: 10.1016/j.msea.2006.02.229.

Lobkis OI and RL Weaver. 2001. "On the Emergence of the Green's Function in the Correlations of a Diffuse Field." *The Journal of the Acoustical Society of America* 110(6):3011-3017. DOI: 10.1121/1.1417528.

MacDonald D, M Dennis, J Landrum and GP Selby. 2000. *Phased Array UT Performance on Dissimilar Metal Welds: Interim Report*. TE-1000116. Charlotte, NC: EPRI Nondestructive Evaluation Center, Electric Power Research Institute.

Mahaut S, M Darmon, S Chatillon, F Jenson and P Calmon. 2009. "Recent Advances and Current Trends of Ultrasonic Modelling in CIVA." *Insight - Non-Destructive Testing and Condition Monitoring* 51(2):78-81. DOI: 10.1784/insi.2009.51.2.78.

Malcolm AE, JA Scales and BA van Tiggelen. 2004. "Extracting the Green Function from Diffuse, Equipartitioned Waves." *Physical Review E* 70:4. DOI: 10.1103/PhysRevE.70.015601.

Mandal S, SK Mishra, A Kumar, I Samajdar, PV Sivaprasad, T Jayakumar and B Raj. 2008. "Evolution and Characterization of Dynamically Recrystallized Microstructure in a Titanium-Modified Austenitic Stainless Steel Using Ultrasonic and EBSD Techniques." *Philosophical Magazine* 88(6):883-897. DOI: 10.1080/14786430801989799.

Miralles R and L Vergara. 1999. "Ultrasonic Characterization of Scattering Media by Higher Order Spectra: A Cumulant Derivation." In *Proceedings of the IEEE Signal Processing Workshop on Higher-Order Statistics*, pp. 367-370. June 14-16, 1999, Caesarea, Israel. DOI: 10.1109/HOST.1999.778760. IEEE, NY.

Miralles R, L Vergara and J Gosalbez. 2004. "Material Grain Noise Analysis by Using Higher Order Statistics." *Signal Processing* 84(1):197-205. DOI: 10.1016/j.sigpro.2003.10.007.

Moran TL, SL Crawford, MS Prowant, MR Larche, TS Hartman and MT Anderson. 2017. *Comparing Conventional and Phased Array Ultrasonic Techniques for Assessing Welding Fabrication Flaws in Carbon Steel Piping*. PNNL-26467. Richland, WA: Pacific Northwest National Laboratory. ADAMS Accession No. ML17055A585.

Morris CJ and FL Becker. 1982. *State-of-Practice Review of Ultrasonic In-service Inspection of Class I System Piping in Commercial Nuclear Power Plants*. NUREG/CR-2468, PNL-4026. Washington, D.C.: U.S. Nuclear Regulatory Commission.

Moysan J and G Corneloup. 2000. "Ultrasonics Back-Scattering Measurements for New Anisotropy Indicator Construction." In *15th World Conference on Non-Destructive Testing*. October 15-21, 2000, Rome. Available at <http://www.ndt.net/article/wcndt00/papers/idn308/idn308.htm>.

Neumann AWE. 1989. "On the State of the Art of the Inspection of Austenitic Welds with Ultrasound." *International Journal of Pressure Vessels and Piping* 39(4):227-246. DOI: 10.1016/0308-0161(89)90087-2.

NRC. 2001. *Generic Aging Lessons Learned (GALL) Report*. NUREG-1801. Washington, D.C.: U.S. Nuclear Regulatory Commission.

NRC. 2004. *Cracking in Pressurizer Safety and Relief Nozzles and in Surge Line Nozzle*. Information Notice 2004-11. Washington, D.C.: U.S. Nuclear Regulatory Commission (NRC). May 6, 2004. ADAMS Accession No. ML041260136.

NRC. 2010. *Generic Aging Lessons Learned (GALL) Report - Final Report*. NUREG-1801, Rev. 2. Washington, D.C.: U.S. Nuclear Regulatory Commission. ADAMS Accession No. ML103490041.

NRC. 2011. *Addendum of Memorandum of Understanding between U.S. Nuclear Regulatory Commission and Electric Power Research Institute on Cooperative Nuclear Safety Research -- Memorandum of Understanding for Nondestructive Examination*. Washington, D.C.: U.S. Nuclear Regulatory Commission. ADAMS Accession No. ML103080165.

O'Neill B and RG Maev. 2002. "Integral Approximation Method for Calculating Ultrasonic Beam Propagation in Anisotropic Materials." In *Acoustical Imaging*, pp. 237-244. ed: H Lee. Boston, MA: Springer US. DOI: 10.1007/0-306-47108-6\_34.

Olympus. 2014. *Phased Array Testing -- Basic Theory for Industrial Applications -- NDT Field Guides*. Waltham, MA: Olympus Scientific Solutions Americas.

Ostrovsky LA, PA Johnson and TJ Shankland. 2000. "The Mechanism of Strong Nonlinear Elasticity in Earth Solids." In *Nonlinear Acoustics at the Turn of the Millennium: ISNA 15, 15th International Symposium*, pp. 75-84. September 1-4, 1999, Gottingen, Germany. DOI: 10.1063/1.1309181. AIP Conference Proceedings Vol. 524.

Pade ER and JF Enrietta. 1981. *Reliability of Ultrasonic Test Method for Detecting Natural Fatigue Cracks in Centrifugally Cast Stainless Steel Pipe*. WCAP-9894. Pittsburgh, PA: Westinghouse Electric Corp.

Pao Y-H. 1983. "Elastic Waves in Solids." *Journal of Applied Mechanics* 50(4b):1152-1164. DOI: 10.1115/1.3167197.



Papadakis EP. 1959. "Correction for Diffraction Losses in the Ultrasonic Field of a Piston Source." *The Journal of the Acoustical Society of America* 31(2):150-152. DOI: 10.1121/1.1907684.

Papadakis EP. 1966. "Ultrasonic Diffraction Loss and Phase Change in Anisotropic Materials." *The Journal of the Acoustical Society of America* 40(4):863-876. DOI: 10.1121/1.1910159.

Papadakis EP. 1968. "Buffer-Rod System for Ultrasonic Attenuation Measurements." *Journal of the Acoustical Society of America* 44(5):1437-1441.

Papadakis EP. 1984. "Absolute Measurements of Ultrasonic Attenuation Using Damped Nondestructive Testing Transducers." *Journal of Testing and Evaluation* 12(5):273-279. DOI: 10.1520/JTE10727J.

PISC. 1993. *Evaluation of the Inspection Results of the PISC III Safe-end Assembly No. 25*. PISC III Report No. 25, EUR 15370 EN. Ispra Site: Commission of the European Communities, Joint Research Centre.

PNNL. 2013a. *Technical Letter Report, Evaluation of Licensee's Alternative to 10 CFR 50.55a(g)(6)(ii)(F) for Limitations to Volumetric Examinations of Dissimilar Metal Welds, Entergy Operations, Inc., Arkansas Nuclear One, Unit 2 – Docket Number 50-368*. Richland, WA: Pacific Northwest National Laboratory. ADAMS Accession No. ML13113A218.

PNNL. 2013b. *Technical Letter Report, Evaluation of Licensee's Alternative to 10 CFR 50.55A(G)(6)(II)(F) for Limitations to Volumetric Examinations of Dissimilar Metal Welds, Constellation Energy, Calvert Cliffs Nuclear Power Plant – Docket Number 50-318*. Richland, WA: Pacific Northwest National Laboratory. ADAMS Accession No. ML13113A233.

PNNL. 2013c. *Technical Letter Report, Evaluation of Alternative to 10 CFR 50.55a(g)(6)(ii)(F)(4) for Limitations to Volumetric Examinations of Dissimilar Metal Welds, Florida Power & Light, St. Lucie Power Plant Unit 1 – Docket Number 50-335*. Richland, WA: Pacific Northwest National Laboratory. ADAMS Accession No. ML14149A195.

Prada C, E Kerbrat, D Cassereau and M Fink. 2002. "Time Reversal Techniques in Ultrasonic Nondestructive Testing of Scattering Media." *Inverse Problems* 18(6):1761. DOI: 10.1088/0266-5611/18/6/320.

Prine DW. 1972. "Synthetic Aperture Ultrasonic Testing." In *Proceedings of the Engineering Applications of Holography Symposium*, pp. 287-294. February 16-17, 1972, Los Angeles, CA. Society of Photo-optical Instrumentation Engineers (SPIE), Bellingham, WA.

Pudovikov S, A Bulavinov and R Pinchuk. 2012. "Innovative Ultrasonic Testing (UT) of Nuclear Components by Sampling Phased Array with 3D Visualization of Inspection Results." In *8th International Conference on NDE in Relation to Structural Integrity for Nuclear and Pressurised Components (JRC-NDE 2010)*. October 29-November 1, 2010, Berlin, Germany. NDT.net. Available at <https://www.ndt.net/article/jrc-nde2010/papers/113.pdf>.

Pyle SL. 2011. Letter to NRC Document Control Desk. "Use of Alternate ASME Code Case N 770-1 Baseline Examination Request for Alternative ANO2-ISI-007, Arkansas Nuclear One, Unit 2, Docket No. 50-368, License No. NPF-6." November 30, 2011, Russellville, AR: Entergy Operations, Inc. ADAMS Accession No. ML113340158.

Pyle SL. 2012a. Letter to NRC Document Control Desk. "Arkansas Nuclear One, Unit 2 - Response to the Request for Additional Information " April 13, 2012, Russellville, AR: Entergy Operations, Inc. ADAMS Accession No. ML12104A066.

Pyle SL. 2012b. Letter to NRC Document Control Desk. "Response to Second Request for Additional Information Request for Alternative ANO2-ISI-007 Code Case N-770-1 Baseline Examination, Arkansas Nuclear One, Unit 2." September 10, 2012, Russellville, AR: Entergy Operations, Inc. ADAMS Accession No. ML12255A388.

Pyle SL. 2012c. Letter to NRC Document Control Desk. "Additional Information Related to Request for Alternative ANO2-ISI-007 Code Case N-770-1 Baseline Examination, Arkansas Nuclear One, Unit 2." May 21, 2012, Russellville, AR: Entergy Operations, Inc. ADAMS Accession No. ML12142A319.

Ramamoorthy SK, Y Kane and JA Turner. 2004. "Ultrasound Diffusion for Crack Depth Determination in Concrete." *Journal of Acoustical Society of America* 115(2). DOI: 10.1121/1.1642625.

Ramuhalli P, MS Good, AA Diaz, MT Anderson, BE Watson, TJ Peters, M Dixit and LJ Bond. 2009. *Ultrasonic Characterization of Cast Austenitic Stainless Steel Microstructure: Discrimination between Equiaxed- and Columnar-Grain Material – An Interim Study*. PNNL-18912. Richland, WA: Pacific Northwest National Laboratory.

Ramuhalli P, LJ Bond, R Mathews, KC Roberts, RV Harris Jr., AA Diaz, MT Anderson and CO Ruud. 2010. *In-situ Characterization of Cast Austenitic Stainless Steel Microstructure: An Interim Study*. PNNL-19325. Richland, WA: Pacific Northwest National Laboratory. ADAMS Accession No. ML103370373.

Ramuhalli P, RM Meyer, AD Cinson, TL Moran, MS Prowant, BE Watson, R Mathews, RV Harris, AA Diaz and MT Anderson. 2013. "In-situ Characterization of Cast Stainless Steel Microstructures." In *9th International Conference on NDE in Relation to Structural Integrity for Nuclear and Pressurised Components*, pp. 920-928. May 22-24, 2012, Seattle, WA. PNNL-SA-87840. Available at <http://www.ndt.net/article/jrc-nde2012/papers/142.pdf>.

Rishel RD. 1988. *Demonstration of Flaw Detection and Characterization Capabilities for Ultrasonic Examination of Main Coolant Loop Welds*. WCAP-11778. Pittsburgh, PA: Westinghouse Electric Corporation.

Ruiz A, N Ortiz, H Carreón and C Rubio. 2009. "Utilization of Ultrasonic Measurements for Determining the Variations in Microstructure of Thermally Degraded 2205 Duplex Stainless Steel." *Journal of Nondestructive Evaluation* 28(3):131. DOI: 10.1007/s10921-009-0055-7.

Ruud CO, AA Diaz and MT Anderson. 2009. *Grain Structure Identification and Casting Parameters of Austenitic Stainless Steel (CASS) Piping*. PNNL-19002. Richland, WA: Pacific Northwest National Laboratory. ADAMS Accession No. ML100252084.

Ruud CO, P Ramuhalli, RM Meyer, AA Diaz and MT Anderson. 2016. *CASS Ferrite and Grain Structure Relationship*. PNNL-25537. Richland, WA: Pacific Northwest National Laboratory. ADAMS Accession No. ML16203A140.

Sagar SP, N Parida, S Das and RN Ghosh. 2007. "Precipitation Hardening Study of Ageing of Maraging Steel Using Ultrasonic Technique." In *Proceedings of the National Seminar on Non-Destructive Evaluation*. December 7-9, 2006, Hyderabad. Indian Society for Non-Destructive Testing. Paper TP-99.

Sakamoto K, T Furukawa, I Komura, Y Kamiyama and T Mihara. 2012a. "Study on the Ultrasound Propagation in Cast Austenitic Stainless Steel." *E-Journal of Advanced Maintenance* 4(1). Available at [http://www.jsm.or.jp/ejam/Vol.4No.1/AA/AA37/EJAM\\_CASS\\_Paper\\_sakamoto\\_Final\\_0419\\_.pdf](http://www.jsm.or.jp/ejam/Vol.4No.1/AA/AA37/EJAM_CASS_Paper_sakamoto_Final_0419_.pdf).

Sakamoto K, T Furukawa, I Komura, Y Yagihashi and T Mihara. 2012b. "Capability of Ultrasonic Testing for Cast Austenitic Stainless Steel in Japanese Pressurized Water Reactors." *E-Journal of Advanced Maintenance* 4(1). Available at [https://www.technologydesign.com/files/technical\\_knowledge/Application\\_Notes\\_and\\_FAQs/Application\\_Notes/STAINLESS\\_STEEL\\_-\\_Heavy\\_Walled\\_Pressurised\\_Reactors.pdf/](https://www.technologydesign.com/files/technical_knowledge/Application_Notes_and_FAQs/Application_Notes/STAINLESS_STEEL_-_Heavy_Walled_Pressurised_Reactors.pdf/).

Sarpün İH and MS Kılıçkaya. 2006. "Mean Grain Size Determination in Marbles by Ultrasonic First Backwall Echo Height Measurements." *NDT & E International* 39(1):82-86. DOI: 10.1016/j.ndteint.2005.06.010.

Sayers CM. 1984. "Texture Independent Determination of Residual Stress in Polycrystalline Aggregates using Rayleigh Waves." *Journal of Physics D: Applied Physics* 17(12):L179-L184.

Scales JA and AE Malcolm. 2003. "Laser Characterization of Ultrasonic Wave Propagation in Random Media." *Physical Review E* 67:7. DOI: 10.1103/PhysRevE.67.046618.

Scherer AE. 2006a. Letter to NRC Document Control Desk. "Docket Nos. 50-361 and 50-362, Additional Information Supporting the Third Ten-Year Inservice Inspection (ISI) Interval Relief Request ISI-3-24 and ISI-3-25 for the Use of Structural Weld Overlay and Associated Alternative Repair Techniques. San Onofre Nuclear Generating Station, Units 2 and 3." September 29, 2006, San Clemente, CA: Southern California Edison. ADAMS Accession No. ML062760233.

Scherer AE. 2006b. Letter to NRC Document Control Desk. "Docket Nos. 50-361, Third Ten-Year Inservice Inspection (ISI) Interval Relief Request ISI-3-18 Use of Structural Weld Overlay and Associated Alternative Repair Techniques. San Onofre Nuclear Generating Station, Unit 2." February 22, 2006, San Clemente, CA: Southern California Edison. ADAMS Accession No. ML060550423.

Scherer AE. 2009. Letter to NRC Document Control Desk. "Docket Nos. 50-361 and 50-362, Inservice Inspection of Structural Weld Overlay. San Onofre Nuclear Generating Station, Units 2 and 3." August 10, 2009, San Clemente, CA: Southern California Edison. ADAMS Accession No. ML092230577.

Schuster GJ, SR Doctor and PG Heasler. 1998. *Characterization of Flaws in U.S. Reactor Pressure Vessels: Density and Distribution of Flaw Indications in PVRUF*. NUREG/CR-6471, PNNL-11143, Vol. 1. Washington, D.C.: U.S. Nuclear Regulation Commission.

Schuster GJ, SL Crawford, AA Diaz, PG Heasler and SR Doctor. 2013. *Reliability of Ultrasonic In-Service Inspection of Welds in Reactor Internals of Boiling Water Reactors*. NUREG/CR-7159; PNNL-14561. Washington, D.C.: U.S. Nuclear Regulatory Commission. ADAMS Accession No. ML13115A688.

Segura A, P Lanceleur, J-F De Belleval, J-M Gherbezza and F Lesage. 2009. "Influence of Anisotropy for the Characterization of Internal Imperfections in Pipes by Ultrasonic Non-Destructive Testing." *NDT.net* 2009-05. Available at <http://www.ndt.net/article/ndtnet/2009/segura.pdf>.

Seydel JA. 1978. "(Signal Processing) Methods Development." In *Improved Ultrasonic Nondestructive Testing of Pressure Vessels, Annual Progress Report, October 1, 1976-September 30, 1977*. ed: JR Frederick. Washington, D.C.: U.S. Nuclear Regulatory Commission. NUREG/CR-0135.

Sgard FC, N Atalla and J Nicolas. 2000. "A Numerical Model for the Low Frequency Diffuse Field Sound Transmission Loss of Double-Wall Sound Barriers with Elastic Porous Linings." *The Journal of the Acoustical Society of America* 108(6):2865-2872. DOI: 10.1121/1.1322022.

Sheppard CJR, W Gong, K Si, CH Wong and NG Chen. 2009. "Imaging Through Scattering Media Using D-shaped Apertures." In *Focus on Microscopy 2009*. April 5-8, 2009, Krakow, Poland.

Sofka CM, D Lin and RS Adler. 2005. "Advantages of Color B-mode Imaging With Contrast Optimization in Sonography of Low-Contrast Musculoskeletal Lesions and Structures in the Foot and Ankle." *Journal of Ultrasound in Medicine* 24(2):215-218. DOI: 10.7863/jum.2005.24.2.215.

Stanley JJ. 2012. Letter to NRC Document Control Desk. "Calvert Cliffs Nuclear Power Plant Unit No. 2; Docket No. 50-318, Relief Request for Unit 2 Dissimilar Metal Butt Welds Baseline Examinations (RR-ISI-04-07A)." June 7, 2012, Lusby, MD: Constellation Energy Generation Group, Calvert Cliffs Nuclear Power Plant, LLC. ADAMS Accession No. ML12164A372.

Stanley JJ. 2013. Letter to NRC Document Control Desk. "Calvert Cliffs Nuclear Power Plant Unit No. 2; Docket No. 50-318, Response to Request for Additional Information - Relief Request RR-ISI-04-07A, Dissimilar Metal Butt Welds Baseline Examinations." January 10, 2013, Lusby, MD: Constellation Energy Generation Group, Calvert Cliffs Nuclear Power Plant, LLC. ADAMS Accession No. ML13015A007.

Stella J, J Cerezo and E Rodríguez. 2009. "Characterization of the Sensitization Degree in the AISI 304 Stainless Steel Using Spectral Analysis and Conventional Ultrasonic Techniques." *NDT & E International* 42(4):267-274. DOI: 10.1016/j.ndteint.2008.11.005.

Sullivan EJ and MT Anderson. 2012. *Technical Letter Report Assessment of the Weld Overlays for Mitigating Primary Water Stress Corrosion Cracking at Nickel Alloy Butt Welds in Piping Systems Approved for Leak-Before-Break*. PNNL-21660. Richland, WA: Pacific Northwest National Laboratory. ADAMS Accession No. ML13330A803.

Taylor TT. 1984. *An Evaluation of Manual Ultrasonic Inspection of Cast Stainless Steel Piping*. NUREG/CR-3753, PNL-5070. Washington, D.C.: U.S. Nuclear Regulatory Commission.

Te-Ming T, C Chin-Hsing and IC Chein. 1998. "A Noise Subspace Projection Approach to Target Signature Detection and Extraction in an Unknown Background for Hyperspectral Images." *IEEE Transactions on Geoscience and Remote Sensing* 36(1):171-181. DOI: 10.1109/36.655327.

Terao D. 2006. Letter to Mr. Richard M. Rosenblum (Southern California Edison Company). "San Onofre Nuclear Generating Station, Unit 2 - Re: Request for Relief from the Requirements of the American Society of Mechanical Engineers Boiler and Pressure Vessel Code (TAC No. MD0191)." December 14, 2006, Washington, D.C.: Nuclear Regulatory Commission. ADAMS Accession No. ML063110322.

Thompson RB, FJ Margetan, P Haldipur, L Yu, A Li, P Panetta and H Wasan. 2008. "Scattering of Elastic Waves in Simple and Complex Polycrystals." *Wave Motion* 45:655-674. DOI: 10.1016/j.wavemoti.2007.09.008.

Trautwein A and W Gysel. 1982. "Influence of Long-Time Aging of CF8 and CF8M Cast Steel at Temperatures Between 300 and 500°C on Impact Toughness and Structural Properties." In *STP 756, Stainless Steel Castings*, pp. 165-189. eds: VG Behal and AS Melilli. Philadelphia, PA: ASMT International.

Tsao JC. 2006. Letter to Jack Rainsberry. "Request for Additional Information, Third Ten Year Inservice Inspection Interval Relief Request ISI-3-18 Use of Structural Weld Overlay. San Onofre Nuclear Generating Station, Unit 2." March 7, 2006, Washington, D.C.: U.S. Nuclear Regulatory Commission. ADAMS Accession No. ML061100366.

Turner JA and RL Weaver. 1995. "Time Dependence of Multiply Scattered Diffuse Ultrasound in Polycrystalline Media." *The Journal of the Acoustical Society of America* 97(5):2639-2644. DOI: 10.1121/1.411895.

Turner JA. 1999. "Elastic Wave Propagation and Scattering in Heterogeneous, Anisotropic Media: Textured Polycrystalline Materials." *The Journal of the Acoustical Society of America* 106(2):541-552. DOI: 10.1121/1.427024.

Uddin MF, GM Wilkowski, S Pothana and FW Brust. 2017. "Flaw Evaluation Procedure for Cast Austenitic Stainless Steel Materials Using Thermal Aging Models." In *Proceedings of the ASME 2017 Pressure Vessels & Piping Conference*. July 16-20, 2017, Waikoloa, HI. American Society of Mechanical Engineers, NY.

Vasudevan M and P Palanichamy. 2002. "Characterization of Microstructural Changes During Annealing of Cold Worked Austenitic Stainless Steel Using Ultrasonic Velocity Measurements and Correlation with Mechanical Properties." *Journal of Materials Engineering and Performance* 11(2):169-179. DOI: 10.1361/105994902770344231.

Vengrinovich V, V Tsukerman, Y Denkevich and D Bryantsev. 2006. "New Parameters to Characterize Internal Stresses via Barkhausen Noise." In *9th European Conference on Non Destructive Testing (ECNDT 2006)*. September 25-29, 2006, Berlin. NDT.net. Paper Th.4.2.4.

Vignon F, JF Aubry, M Tanter and M Fink. 2005. "High Resolution Ultrasonic Brain Imaging: Adaptive Focusing Based on Twin-Arrays." In *Proceedings of the IEEE International Conference on Acoustics, Speech, and Signal Processing (ICASSP '05)*, pp. v/973-v/976. March 18-23, 2005, Philadelphia, PA. DOI: 10.1109/ICASSP.2005.1416468. IEEE, Piscataway, NJ.

Wan T, T Naoe, T Wakui, M Futakawa, H Obayashi and T Sasa. 2017. "Effects of Grain Size on Ultrasonic Attenuation in Type 316L Stainless Steel." *Materials* 10(7):753. DOI: 10.3390/ma10070753.

Weaver RL. 1982. "On Diffuse Fields in Solid Media." *Journal of Acoustical Society of America* 71(6):1608-1609. DOI: 10.1121/1.387816.

Weaver RL and W Sachse. 1994. "Diffusion of Ultrasound in a Glass Bead Slurry." *Journal of Acoustical Society of America* 97(4):2094-2102. DOI: 10.1121/1.412002.

Weaver RL and OI Lobkis. 2000. "Temperature Dependence of Diffuse Field Phase." *Ultrasonics* 38:491-494. DOI: 10.1016/S0041-624X(99)00047-5.

Weaver RL and OI Lobkis. 2005a. "The Mean and Variance of Diffuse Field Correlations in Finite Bodies." *The Journal of the Acoustical Society of America* 118(6):3447-3456. DOI: 10.1121/1.2109307.

Weaver RL and OI Lobkis. 2005b. "Fluctuations in Diffuse Field-Field Correlations and the Emergence of the Green's Function in Open Systems." *The Journal of the Acoustical Society of America* 117(6):3432-3439. DOI: 10.1121/1.1898683.

Weber MF and N Wilmshurst. 2016. *Memorandum of Understanding between U.S. Nuclear Regulatory Commission and Electric Power Research Institute, Inc. on Cooperative Nuclear Safety Research*. Washington, D.C.: U.S. Nuclear Regulatory Commission. ADAMS Accession No. ML16223A497.

Weber MF and N Wilmshurst. 2017. *Addendum to Memorandum of Understanding between U.S. Nuclear Regulatory Commission and Electric Power Research Institute, Inc. on Cooperative Nuclear Safety Research -- Nondestructive Examination (NDE)*. Washington, D.C.: U.S. Nuclear Regulatory Commission. ADAMS Accession No. ML16138A556.

White PJ, S Whalen, SC Tang, GT Clement, F Jolesz and AJ Golby. 2009. "An Intraoperative Brain Shift Monitor Using Shear Mode Transcranial Ultrasound." *Journal of Ultrasound in Medicine* 28(2):191-203. DOI: 10.7863/jum.2009.28.2.191.

Wilcox PD, C Holmes and BW Drinkwater. 2007. "Advanced Reflector Characterization with Ultrasonic Phased Arrays in NDE Applications." *IEEE Transactions on Ultrasonics, Ferroelectrics and Frequency Control* 54(8):1541-1550. DOI: 10.1109/TUFFC.2007.424.

Willems H and K Goebbels. 1982. "Characterization of Microstructure by Scattered Ultrasonic Waves." In *Proceedings of the 10th World Conference on Non-Destructive Testing*, pp. 39-45. August 24-26, 1982, Moscow, Russia.

Yu CJ, JC Conway, CO Ruud and KJ Kozaczek. 1992. "Ultrasonic Characterization of the Effect of Cold Work and Grain Size in Copper and 68:32 Brass Sheets." *Journal of Materials Science* 27(19):5174-5180. DOI: 10.1007/BF00553388.

Zhang J, B Drinkwater and P Wilcox. 2008. "Defect Characterization Using an Ultrasonic Array to Measure the Scattering Coefficient Matrix." *IEEE Transactions on Ultrasonics, Ferroelectrics and Frequency Control* 55(10):2254-2265. DOI: 10.1109/TUFFC.924.



## **APPENDIX A     HISTORICAL CASS RESEARCH**

This appendix addresses over 40 years of CASS-related activity beginning in 1976 with the WEC study. The appendix provides a “timeline” of industry research efforts in this regard. The numerous presentations and papers summarized here reveal what did, or did not work, and the evolution of the state-of-the-art. The summaries of the topics addressed herein contain sufficient detail to provide the reader with the proper context for each topic. The most significant research findings and events were treated more thoroughly in the body of this report. The summarizations in this appendix are intended to provide an understanding of the inter-relationship of certain research and events. References are provided for those wishing to obtain greater detail and insights.

### **A.1 Why Has CASS Research Persisted Over 40 Years?**

Any discussion of the history of CASS research inevitably leads to the question of why the research has lasted for over 40 years. Given the length of time over which the research has been conducted, it is sometimes assumed that UT is not an effective CASS inspection tool or that CASS components are not inspectable. However, from a review of the main text of the report, the reader will understand that recent research results have shown that CASS components may be effectively and reliably inspected by using the proper UT techniques. This is further substantiated by the industry’s development of Code Case N-824. Thus, a response to why the research has persisted for 40 years is multifaceted and somewhat complex.

It was understood from the beginning that the large-grained and anisotropic microstructure of CASS materials would present unique inspection challenges. NRC regulations require the periodic inspection of piping weldments in primary coolant piping systems using qualified inspection techniques and personnel. To satisfy regulatory requirements and begin to address the CASS inspection challenge, WEC performed the first study in 1976 to determine the inspectability of CF8M CASS materials (Pade and Enrietta 1981). In the 1980s, PNNL performed an industry survey and conducted several round-robin studies, and EPRI sponsored a number of CASS trials to evaluate the state-of-the-art in UT. Altogether, these studies and trials showed that conventional UT techniques produced poor results with respect to the reliable inspection of CASS weldments (Taylor 1984; Heasler and Doctor 1996).

With no incidents of service degradation having been reported and the continuing poor results from industry CASS trials (even with the state-of-the-art conventional techniques at that time), some in the industry began to question the resources being focused on the inspection of CASS weldments. After all, CASS had been chosen as a piping material in certain applications because of its fracture toughness and corrosion resistance. Another factor that influenced funding priorities was the emergence of SCC in PWR SG tubes and IGSCC in BWR primary coolant piping. Reallocation of funding meant that, for many years, the industry did not support CASS-related research.

In order to move the development of CASS inspection provisions forward, ASME formed the Task Group on CASS Inspection in 1997. The charter of the task group was to resolve the issues concerning CASS inspection and propose ASME Code actions to complete Section XI, Appendix VIII, Supplement 9. One of the issues for the task group was that certain Appendix VIII criteria could not reliably be met for CASS material, i.e., at least 80% POD, and at most, a 10% false call rate.

Based on their review of CASS inspection tests over the next few years, the task group members concluded that UT examinations conducted from the outside surface of CASS piping weldments continued to have a lower POD and a higher false call rate than other components addressed by Section XI, Appendix VIII. The task group proposed to the ASME Section XI committee to which it reported (i.e., Subcommittee on Nuclear Inservice Inspection) that the effort to develop Appendix VIII, Supplement 9, be abandoned until improved inspection systems were developed. The subcommittee rejected the request and directed the task group to carry on their efforts to develop CASS inspection qualification requirements. One of the reasons for the rejection of the request was the negative feedback from the Section XI NRC representatives. As discussed in NRC presentations at the second CGI CASS workshop (see Appendix B), there were thermal aging embrittlement concerns with respect to CASS piping, and license renewal inspection requirements had been developed. The NRC needed to ensure the structural integrity of the plant systems and components.

An equal motivation for the task group proposal to abandon the effort was the lack of industry support for this effort. As stated in Chockie and Griesbach (2013),

*For many years some believed that the inspection of CASS as specified in the ASME Code may not be warranted. This was based on the fact that even severely aged CASS is considered capable of tolerating major flaws.*

As also stated in the summary of the group discussions from the workshop, [Discussions with respect to the development of CASS examination requirements] "... brought up the concern that the industry would not want to fund any work for a subject that is not yet a problem."

ANL published reports discussing thermal aging embrittlement as a potential CASS degradation mechanism in 1991 (Chopra 1991, 1994). Nonetheless, in the late 1990s, an ASME Code Section XI proposed action was drafted to delete the requirements for the inspection of CASS weldments. The NRC did not support the proposed action, which ultimately was not approved by ASME. The industry position to support the deletion of CASS inspection requirements focused on three items: degradation had not been reported, an effective UT technique did not exist, and requiring the inspection of CASS weldments resulted in unnecessary occupational exposure.

In response to the lack of industry UT research and the proposed Section XI action, the NRC directed PNNL in 2001 to conduct a literature search to discover if there were recent reports from any organizations conducting active investigations with respect to the inspection of CASS materials (see Foreword, page v of Diaz et al. 2012). Inquiries were made by NRC and PNNL representatives to national and international research organizations. No active CASS inspection research programs were found. The NRC directed PNNL to evaluate state-of-the-art technical approaches that might be applied to CASS components, their associated DMWs, and other coarse-grained components that are similarly difficult to inspect.

The investigation into the inspection of CASS components was one of many NRC-funded PNNL projects. Fluctuations in congressionally authorized NRC budgets sometimes resulted in CASS funding being diverted to other projects. This caused delays, for example, in designing and purchasing LF transducers and equipment. As a consequence, little progress was made in some years. In other years, certain objectives were realized, but delays in other objectives extended the overall research timeline by several years.

In 2000, the NRC published a letter (Grimes 2000) containing criteria to determine the susceptibility of CASS components to thermal aging embrittlement. Aging management requirements specific to CASS would appear for the first time with the publication of NUREG-1801, Rev. 0, in July 2001 (NRC 2001). The industry decision to more seriously investigate CASS inspection techniques was based primarily on the need to comply with license renewal term commitments.

In addition to the need to comply with license renewal commitments, another factor in the industry decision to restart CASS research was the publication of NUREG/CR-6933 (Anderson et al. 2007) and PNNL-18596 (Diaz et al. 2009) showing that the application of LF-PA-UT techniques to thick- and thin-walled CASS piping could produce effective and reliable inspections. NRC staff began to make presentations at conferences, workshops, and ASME Code meetings reminding industry participants that CASS components were in safety-significant locations in the reactor pressure boundary. The presentations reinforced the following: (1) NDE is part of the NRC's defense-in-depth approach to regulating; (2) there are currently no qualified NDE techniques for CASS; (3) there are thermal aging embrittlement concerns with CASS materials; (4) one of the purposes of performing effective and reliable inspections is to discover if degradation mechanisms are occurring that were not considered in the design, and (5) the NRC must ensure the structural integrity of safety-related plant systems and components.

In 2012, ASME published Code Case N-824, which was developed specifically to provide ASME-approved requirements for the inspection of CASS weldments. The provisions of the Code Case were based on previous work and, most recently, the PNNL thick- and thin-walled inspection research results. On July 18, 2017, a final rule was published in the *Federal Register* (82 FR 32934) approving the use of Code Case N-824 with conditions.

As previously discussed, casting processes resulted in significant CASS microstructural variability. It has been postulated that knowledge of the microstructure may allow optimization of the UT method to overcome the deleterious effects of these coarse-grained materials. One of the objectives under the NRC sponsored research program was the development of an ultrasonic method to classify and size the grain structure in situ. PNNL investigated the potential to use ultrasonic and electromagnetic methods for classification and/or characterization of material microstructures in CASS components from the OD (Ramuhalli et al. 2010).

CEA and IRSN have conducted a number of investigations to improve transducers and signal processing for the inspection of CASS components. A paper at the 9<sup>th</sup> International Conference on NDE in Relation to Structural Integrity for Nuclear and Pressurized Components in 2012 describes acceptable results obtained using a 500 kHz dual element PA probe (Ganjehi et al. 2013). It should be noted that the results obtained by CEA confirm the results obtained by PNNL report (Crawford et al. 2011). The PNNL report discussed the evolution of 500 kHz PA probes (third generation) and the associated electronics and scanning protocol.

Domestic and international CASS-related research efforts continue. As discussed in detail in this report, casting processes resulted in significant CASS microstructure variability requiring optimization of inspection variables. There are research efforts underway to improve the in-situ characterization of CASS components so that inspection parameters can be optimized. Equipment manufacturers have been improving their LF multichannel instruments. CASS aging results in decreases in ductility, fracture toughness, and impact resistance, and many organizations continue to investigate CASS component tolerance to flaws. New research results may impact the manner in which licensees manage the effects of aging in the license renewal term.

While ASME has approved Code Case N-824 for use, the NRC only approved it for implementation starting in July 2017, with conditions. Thus, it is unlikely that its provisions have been implemented because the industry will have to develop CASS inspection procedures and train personnel. It is further anticipated that implementation of the Code Case will reveal areas requiring enhancement. In addition, the EPRI NDE Center only recently evaluated the results of a CASS round-robin study (EPRI 2017). A portion of PNNL's assessment of the round-robin has also been published (Jacob et al. 2018). The round-robin results (both EPRI's and PNNL's) will likely be influential with respect to the development of Section XI CASS examination provisions and industry inspection procedures.

## **A.2 Significant Research Findings or Events That Influenced CASS Research**

### **A.2.1 Westinghouse Electric Corporation Study**

In 1976, WEC initiated a program to determine the inspectability of CF8A, Type 304 CASS. PNNL assessed this program and summarized the results (Taylor 1984). One objective of the program was to determine the size of the minimum through-wall mechanical fatigue crack that could reliably be detected. Other variables such as crack location (inside or outside surface), the effects of welding position (vertical, overhead, and downhand [flat position]) on the metallurgical structure of the weld, and inspector experience were also evaluated. The test specimens contained no geometrical reflectors (e.g., surface features or transitions) to hinder ultrasonic inspection. WEC reported that 80% detection had been achieved without false calls for mechanical fatigue cracks that were 20% through-wall (Pade and Enrietta 1981). The study also showed that inspector experience had little effect on performance. However, the PNNL assessment revealed a key issue that raised concerns about the WEC study: the samples used in the study were machined into rectangular cross sections and the mechanical fatigue cracks were grown across the entire sample at a uniform depth. These parameters were considered questionable because they did not represent actual piping geometries or more realistic elliptical crack shapes or profiles.

### **A.2.2 State-of-Practice Review**

PNNL conducted a survey sponsored by the NRC to determine the state of practice of ultrasonic ISI of primary system piping in LWRs. Personnel at four utilities, five inspection organizations, and three domestic reactor manufacturers were interviewed. The intent of the study was to provide a better understanding of the actual practices employed for ISI and the difficulties encountered. Among the principal findings were that the selection of ultrasonic search units (and their operating parameters) was highly variable, confidence in the ability to detect defects was highest for ferritic piping and lowest for CASS piping, and recording of geometrical indications during baseline preservice inspection or ISI was not consistent (Morris and Becker 1982). The finding with respect to the lack of confidence in the inspection of CASS piping was in opposition to the published results of the WEC study cited above.

### **A.2.3 PIRR Round Robin Study**

As a result of the conflicting information, the NRC sponsored PNNL to conduct a round-robin study beginning in 1981–1982. The PIRR study was the earliest CASS round robin and assessed the capability of the U.S. nuclear industry to detect and size cracks in CASS weldments similar in configuration to those in the primary coolant system piping installed in NPPs. One objective of the study was to assess the reliability of ISI by evaluating the POD and false call rate of conventional UT methods applied to CASS (Heasler and Doctor 1996).

For use in the study, CASS pipe rings were welded together. The pipe samples contained blended weld crowns and counterbores. TFCs ranging in depth from 5–50% through-wall were grown in the pipe samples. The shape, tightness, and roughness of TFCs generally make them more difficult to detect in comparison to mechanical fatigue cracks, which were used in the 1976 WEC study. Inspection teams first used their own field procedures and then used a procedure written by PNNL. A time limit of 30 minutes for data acquisition was imposed to be consistent with respect to the time limitations imposed by occupational exposure procedures during field inspections. In addition, inspectors had to be certified as at least UT Level II to discover, or detect, the ultrasonic indications, which is the standard protocol for field examination personnel.

Six teams participated in the round robin; one of teams was considered to have achieved reliable detection. Three teams detected less than 30% of the defects, the fourth achieved a higher score through gross overcall, and two declared a “no test,” stating they had no confidence in their ability to inspect CASS pipe. The second part of the round-robin test required each team to use a preselected instrument and search unit, and a UT procedure developed by PNNL for optimized inspection of CASS. The ISI teams were allowed to practice with this equipment and procedure on cracked and uncracked CASS specimens. The appearance and response behavior of the crack signals were demonstrated to the teams, then the teams completed another test matrix to measure their detection reliability with the “improved procedure.” These results showed little or no improvement in detection reliability (Taylor 1984).

#### **A.2.4 PNNL/Westinghouse Collaboration**

PNNL and WEC collaborated on a program to resolve the apparent differences between the two studies. The results of this collaboration were also published in NUREG/CR-3753 (Taylor 1984). The cooperative program was designed as a limited round robin. Only cast austenitic pipe specimens were examined. A field inspection team from WEC examined two sets of test specimens: CASS specimens fabricated by WEC containing mechanical fatigue cracks and specimens fabricated by PNNL containing TFCs. To allow a meaningful analysis, the same test protocol as that used during the PIRR was used. During the PIRR study, all teams used dual-element longitudinal wave search units. Some of the search units used a zone isolation, or zone focus, principle; some did not. A zone focus approach, as related to TRL probes, is the application of a complementary roof angle for both the transmitting and receiving sides of the probe to enable a theoretical “cross-over” point along a prescribed metal path distance. The WEC team used a search unit designed with a water column with a finger-controlled bladder to allow inspection angle tweaking and skewing during scanning to search for “windows” through the coarse grains to enhance crack detection.

Following are the results of inspecting the CASS specimens fabricated by WEC (mechanical fatigue cracks):

- When considering both cracked and uncracked specimens, the team properly characterized 17 of 22 samples.
- When considering cracked and uncracked specimens separately, the team properly characterized 9 of 14 cracked samples; all uncracked samples were characterized properly.
- None of the samples produced recordable indications along the entire crack length.

These results are in agreement with the WEC study (Pade and Enrietta 1981). Detection probability was very good for cracks with depth greater than 15% through-wall.

For the inspections of CASS specimens fabricated by PNNL (TFCs), the results followed the trend of the four teams that inspected these specimens during the PIRR.

- Out of 29 inspections of cracked specimens, only two cracks were detected.
- None of the crack samples produced a recordable signal along its entire length.
- The only unusual feature of the WEC team's performance was the absence of false calls.

Based on NDE measurements, it was estimated that the depth range of both the Westinghouse and PNNL cracks were about the same, between 0% and 30% through-wall.

The data analysis indicated that the most significant factor for crack detection was flaw type. Mechanical fatigue cracks (open and planar) had a reasonably high POD; tight, rough TFCs were essentially undetectable with the then-current field ultrasonic inspection techniques. The only signals interfering with crack detection were metallurgical reflectors. Neither set of test samples contained geometric reflectors at the weld root or crown. Ultrasonic signals from cracks in the PNNL samples were generally of very low amplitude, often no greater than signals reflected coherently from grain boundaries. By contrast, signals from the WEC fatigue cracks were higher in amplitude; in fact, the response from all cracks was greater than or equal to the 4.76 mm (3/16 in.) side-drilled hole calibration reflector.

The original WEC study (WCAP-9894, Pade and Enrietta 1981) did not address the subject of sizing. The PNNL PIRR depth sizing data was too sparse for statistical analysis; however, the teams that did attempt to size did not do well. The experimental data from all three studies (WEC, PIRR, and collaborative study) showed that no crack in either set of test samples produced detectable signals along its entire length. Therefore, it was concluded that current techniques applied in the field would not accurately characterize either the length or depth of cracks in CASS components.

#### **A.2.5 PISC Centrifugally Cast Stainless Steel Round Robin Test**

In 1984, an international round robin sponsored by the NRC, the Organization for Economic Cooperation, and the Commission of the European Communities was initiated. The results were reported in NUREG/CR-4970, PNL-6266, PISC III Report No. 3, entitled, *Stainless Steel Round Robin Test: Centrifugally Cast Stainless Steel Screening Phase*, published in October 1987 (Bates et al. 1987). One particular test was performed by PNNL for the NRC and PISC, denoted as the Centrifugally Cast Stainless Steel Round Robin Test (CCSSRRT), was a blind test that contained both uncracked and cracked samples. The intent of the test was to identify the most promising ISI procedures and provide input to a more in-depth future study. The CCSSRRT was patterned after the PIRR. Fifteen CCSS pipe sections containing welds and laboratory-grown TFCs in both columnar and equiaxed base materials were used.

The CCSS pipe material was from two different heats of ASTM A-351 Grade CF8A (which is a cast 304 material). Many of these samples contain welds located approximately in the middle of each section and were made by welders qualified to meet Section III requirements of the ASME Code. The welds in these samples were made under shop conditions but were typical of field practice. The weld crowns were ground relatively smooth and blended with the parent pipe, although troughs between weld paths were still present. The cracks in the CCSSRRT pipe sections were created using laboratory methods developed at PNNL that have proven useful in producing realistic surface-connected TFCs. The flaws in the CCSSRRT specimens were basically considered to be planar cracks, parallel to the weld centerline and perpendicular to and



connected to the ID. As previously indicated, the tightness and roughness of the TFCs generally make them more difficult to detect in comparison to mechanical fatigue cracks.

The pipe specimens were inspected by a total of 18 teams from Europe and the United States using a variety of NDE techniques. Several of the procedures demonstrated a potential for discriminating between cracked and uncracked material. LF-SAFT yielded positive results with respect to performance (70% POD with a 30% FCP). The high number of false calls reported by many of the inspection teams made it difficult to demonstrate that some of the procedures were effective with respect to discrimination of signals from cracks versus those signals from the coarse-grained microstructure.

### **A.2.6 Wolf Creek Workshop**

The EPRI NDE Center sponsored the Wolf Creek CASS workshop (on behalf of the Wolf Creek Nuclear Operating Company) in 1988 as mentioned in NUREG/CR-6594, PNNL-11171, entitled, *Evaluation of Ultrasonic Inspection Techniques for Coarse-Grained Materials* (Diaz et al. 1998). Regarding the purpose of this workshop, the NRC staff had questions with respect to the effectiveness of the planned WEC inspections to be performed at Wolf Creek to satisfy the requirements of Section XI. The NRC staff requested that WEC provide a demonstration of the planned inspections.

WEC responded to the NRC request by sending personnel to Wolf Creek with some CCSS specimens with mechanical fatigue cracks. The NRC staff requested support from PNNL in assessing the effectiveness of the WEC inspection method. PNNL personnel traveled to Wolf Creek with specimens from the PIRR study containing TFCs.

The WEC team used a LF search unit with fixed inspection angles. The results mirrored those from the PNNL/WEC collaboration in that the technique used could detect mechanical fatigue cracks but had limited success in detecting TFCs. WEC used the technique to perform the Section XI examinations as the NRC staff determined that the technique was the “best at that time.”

A report entitled, “Progress in EPRI Programs on Inspection of Cast Austenitic Stainless Steel,” contains data on the ISI vendor capability assessment and crack detectability from the Wolf Creek workshop (Dau et al. 1991). Results from the workshop were also provided in EPRI Report TR-1011600 (EPRI 2005b), as well as results from a workshop sponsored by EPRI and hosted by the Yankee Atomic Electric Company/Northeast Utilities. A combined summary is provided in Chapter A.2.10 below.

### **A.2.7 Initial Efforts to Develop SAFT**

Studies and field experience had exposed the limitations of conventional inspection methods. The NRC sponsored a review and evaluation of the considerable amount of SAFT-UT research that had been conducted in the late 1970s and early 1980s to determine the state of the art and the possible application to coarse-grained materials such as CASS and DMWs (Busse et al. 1984). PNNL performed a significant level of work investigating SAFT-UT. The last report discussing the application of a LF-SAFT technique was published in 2008 (Diaz et al. 2008b). For convenience, all SAFT research will be summarized in this section before returning to the historical timeline.

Efforts to assess lower frequencies and longer wavelengths was encouraged by work at ANL that used a laser interferometric technique to map the ultrasonic displacement profile from a

transducer beam that had propagated through CCSS pipe material. The research measured distortions of pulsed ultrasonic beams produced by 2.25 MHz conventional piezoelectric transducers by scanning the back surface of the samples with a laser interferometer (Claytor et al. 1985). The measurements showed how the beams from the transducers could be skewed, focused, or defocused after passing through the CCSS samples.

PNNL also conducted beam profiling activities with conventional single-element probes and showed the distortion that occurred with a vertically polarized shear wave probe as compared to a longitudinal wave probe (Good and Van Fleet 1987, 1988; Good et al. 1991). PNNL began to explore the effects of probe frequency in greater depth in the mid-1980s, including the use of probes in the 250–450 MHz range (Diaz et al. 1998 [NUREG/CR-6594]; Diaz et al. 2008 [NUREG/CR-6984]). Much of this work provided a foundation for the eventual application of LP-PA technology for the examination of coarse-grained materials and components (Diaz et al. 1998; Diaz et al. 2009).

The first application of SAFT was to improve the lateral resolution of airborne radar mapping systems (Prine 1972; Burckhardt et al. 1974). The original ultrasonic applications of SAFT were based on this radar experience. Digital SAFT processing was demonstrated in the area of NDT by the University of Michigan (Frederick et al. 1976) and in medical imaging at the Mayo Clinic (Johnson et al. 1975). NUREG/CR-3625 (Busse et al. 1984) described the early SAFT developmental efforts in greater detail.

Initial research sponsored by the NRC focused on the potential use of SAFT for the UT of NPP components and was performed at the University of Michigan (Frederick et al. 1976; Frederick et al. 1977; Frederick 1978, 1979; Frederick et al. 1979; Ganapathy et al. 1981; Ganapathy et al. 1982; Ganapathy and Schmolt 1985), at the University of Missouri at Columbia (Seydel 1978; Hamano 1980), and at Southwest Research Institute (Jackson 1978a, b; Hamlin and Jackson 1981a, b; Jackson 1981). The second year's work at the University of Michigan concentrated primarily on extending the SAFT-UT processing algorithm to three-dimensional data sets (Frederick et al. 1977). This extension involved significant changes in data collection, processing, and display techniques. The focus of the program at Southwest Research Institute beginning in 1977 was to build upon the techniques developed by the University of Michigan group by improving the ultrasonics and electronics “front-end” of the SAFT-UT system.

As stated in NUREG/CR-3625 (Busse et al. 1984), “Broad industry acceptance of SAFT-UT as a practical NDT inspection technique can only be gained, however, when a field-worthy SAFT-UT inspection system is produced.” The report noted that such a system must be capable of both shear wave and longitudinal wave SAFT, convenient to use, and produce images that are complete and easily interpreted. In addition, the report noted that two aspects of SAFT-UT performance must be demonstrated before field-worthy, real-time SAFT-UT can become a reality. First, it had to be demonstrated that SAFT-UT was reliable for detecting and imaging vertical or near-vertical defects in reactor components. Second, it had to be demonstrated that it was possible to very quickly perform a large number of mathematical operations so that SAFT-UT could be conducted in real time.

During the 1980s, NRC tasked PNNL with developing procedures for system calibration and field operation to validate the system through laboratory and field inspections and generate an engineering database to support ASME Code acceptance of the technology. Pursuant to the NRC request, efforts to design, fabricate, and evaluate a real-time flaw detection and characterization system based on SAFT-UT was performed (Doctor et al. 1987).

The purpose of SAFT-UT was to produce high-resolution images of the interior of opaque objects. The goal of the work presented in the 1987 Doctor report was to develop and implement methods that could be used to detect and quantify the extent of defects and cracks in critical components of nuclear reactors (pressure vessels, primary piping systems, and nozzles). Experimental results as well as theoretical background that underlie synthetic aperture focusing were provided.

The laboratory environment results indicated the feasibility of applying a high-resolution imaging system for the inspection of critical NPP components. With the development of a special-purpose, real-time SAFT processor, the transfer of this defect detection and imaging technology from the laboratory to the field appeared to be both practical and feasible.

By September 1985, a SAFT-UT system had been developed and was operational (Doctor et al. 1987). The system was taken to Commonwealth Edison for the purpose of demonstrating in-field processing for the first time. A narrow-gap pipe weldment containing fabrication flaws was examined. In addition, data were collected on a PISC II plate and compared to other PISC II team performances. The SAFT-UT results were better than the overall average and also better than the average of the teams using advanced UT methods.

NUREG/CR-5075, PNL-6413, *The SAFT-UT Real-Time Inspection System – Operational Principles and Implementation* (Hall et al. 1988) documented the design of a complete field system, with a detailed description of the operation of the software and hardware.

SAFT-UT technology had been shown to provide significant enhancements to the inspection of materials used in U.S. NPPs. NUREG/CR-6344, PNNL-10571, *Real-Time 3-D SAFT-UT System Evaluation and Validation* (Doctor et al. 1996) provided guidelines for the implementation of SAFT-UT technology and showed results from its application. Development of a SAFT real-time processor was also discussed and other improvements were described, including a robotic scanner.

It should be noted that while no reports specifically addressing SAFT were developed from 1997–2007, the NRC continued to sponsor SAFT enhancement, and the technique continued to be applied in the laboratory. However, in the mid-2000s, research efforts began to transition toward the use of LF-PAs.

## **A.2.8 LF-SAFT Performance Evaluation**

The primary focus of the work described in NUREG/CR-6984, PNNL-14374, *Field Evaluation of Low-Frequency SAFT-UT on Cast Stainless Steel and Dissimilar Metal Weld Components* (Diaz et al. 2008b) was to provide information to the NRC on the utility, effectiveness, and reliability of UT inspection techniques as related to the ISI of coarse-grained primary piping components in PWRs.

The research results detailed in NUREG/CR-6984 include a performance evaluation conducted by PNNL. In 1997, PNNL staff traveled to the EPRI NDE Center in Charlotte, North Carolina, to conduct a performance evaluation of the LF-SAFT inspection technique on samples from the inventory of WOG CASS and DMW sections. The access to representative materials and configurations was significant with respect to the PNNL investigation of this challenging problem. Prior to the start of the evaluation, staff from EPRI, PNNL, and the NRC agreed to mutually interact throughout the exercise, sharing ultrasonic data and pertinent information associated with the inspection problem to more effectively conduct a thorough evaluation of the LF inspection technique coupled with SAFT.

A zone-focused, multi-incident angle, LF (250–450 kHz) inspection protocol coupled with SAFT was used in the performance demonstration. The primary focus of the trials was to assess enhancements made to the software (especially a noise-reduction algorithm for application to the pre- and post-SAFT processed data sets).

Approximately 20 CASS specimens (PNNL and EPRI) were examined using the LF-SAFT examination protocol. Four examination angles were used (0°, 30°, 45°, and 60° from both sides of the weld) in the longitudinal wave mode, in a pitch-catch configuration.

Results clearly showed that the LF-SAFT inspection technique was capable of providing quality detection, localization data, and accurate length sizing information. Where the outside surface was sufficient for adequate transducer placement and coupling, the inspection protocol had the capability to consistently detect inside surface-breaking thermal and mechanical fatigue cracks greater than approximately 35% through-wall depth, and 3.81 cm (1.5 in.) in extent and longer, in typical CASS and DMW piping components. Fabricated 10% deep circumferential notches, 25% deep circumferential sawcuts, end-of-block corner traps, and 1.59 mm (1/16 in.) diameter circumferential side-drilled holes were detected as well.

### **A.2.9 PISC Round Robin Study**

PNNL participated in PISC, a 15-year international effort coordinated by the Commission of the European Communities Joint Research Center to evaluate the capabilities of ISI procedures. The program was divided into three phases (PISC I from 1975–1980, PISC II from 1981–1985, and PISC III from 1986–1995). Round-robin exercises were a central feature of each phase.

An investigation of three safe-end assemblies was conducted under PISC III and the results published in 1993 (PISC 1993). The objective was to identify effective inspection techniques and procedures, with emphasis on actual field ISI procedures. The PISC III specimen Assembly No. 25 was intended to simulate a PWR safe-end; that is, ferritic steel nozzle, stainless steel safe-end, and CASS primary piping. The ferritic nozzle was stainless steel clad and Inconel buttered, and the safe-end was forged and Inconel welded to the nozzle end. During manufacturing of the assembly, flaws were intentionally introduced by different implanting techniques. It was inspected with typical ultrasonic techniques from the outside (contact probes) and from the inside (focusing probes) and with radiographic techniques.

Assembly No. 25 was circulated in 10 countries and inspected by 15 teams between March 1988 and December 1990. Few teams provided detailed results for each technique considered in their procedure, which made it difficult to identify effective techniques for a given procedure. While detection performance was relatively high, the correct rejection frequency was noticeably lower (beneath 70%). As a general rule, high detection rates were obtained at the cost of oversizing, rejection of acceptable flaws, or high false call rates. There was a large spread in flaw sizing.

At the end of the testing, a group of experts conducted a supplementary inspection in October 1991. Five small flaws were introduced in the DMW area. For the OD inspection, the best inspection results were obtained from automatic scanning while recording at low level (10–25% distance amplitude correction, or at system noise level). The best inspection results for application from the inside diameter were obtained from automatic scanning using focusing probes.

As discussed in EPRI Report TR-1011600 (EPRI 2005b), one of the lessons learned from the PISC III activities was the superiority of automated scanning systems over manual scanning for UT inspection of coarse-grain material such as CASS. With the automated system, the A-scan RF

or rectified data is captured and digitally stored in a computer. Once in the computer, these data can be processed to display B-scans or C-scans. The inspectors can then make their analyses by viewing the information provided in these A-, B-, and C-scan images.

A disadvantage of manual UT inspection systems is that there is no permanent electronic or photographic record of the inspection. A defect must be identified by the intensity and continuity of a signal in the A-scan. However, with poor SNR, as is often the case in CASS material, the identification of a defect signal is quite difficult using a manual system.

PISC testing focused on several materials. In 1989–1990, an austenitic steel testing study was also conducted under PISC III. Results from this round robin were reported in NUREG/CR-6795, PNNL-13873, *A Comparison of Three Round Robin Studies on ISI Reliability of Wrought Stainless Steel Piping* (Heasler and Doctor 2003). While testing did not include CASS materials, some of the results are relevant to the CASS inspection challenges and are briefly discussed here.

In the austenitic steel testing study, few inspectors demonstrated acceptable skills with respect to flaw sizing and correct rejection frequency. Given that CASS microstructures presented a greater inspection challenge, it would have been expected that even fewer inspectors would be able to demonstrate acceptable skills on CASS materials. The study reinforced results from other studies that significant improvements in inspector skill levels were needed.

The study also revealed that there would be a shortage of qualified inspectors unless improvements were implemented. While the POD from this study would be considered acceptable from a defense-in-depth perspective, the ASME Code, Appendix VIII, Supplement 2, demonstration requirements for crack depth sizing demanded better performance than the average skills that were measured in the study. The study showed that only the best performers would become qualified to inspect nuclear components, and, in order to increase the number of qualified depth sizing inspectors, significant improvements in inspector skill levels, inspection equipment, and/or the procedures would be needed.

#### **A.2.10 Yankee Atomic Electric Company/Northeast Utilities Workshop**

In the early 1990s, the industry held a number of exercises to determine the reliability of the data obtained from ultrasonic examinations of CASS components. In 1992, Yankee Atomic Electric Company and Northeast Utilities, with the assistance of the EPRI NDE Center, sponsored a workshop to determine realistic expectations for flaw detection by experienced vendors and researchers using their most current technology. Interested and qualified vendors were invited to demonstrate their equipment and capabilities.

EPRI Report TR-1011600 (EPRI 2005b) summarizes the CASS workshops at Wolf Creek in 1988 and at Yankee Atomic/Northeast in 1993. The report indicates that seven assemblies were examined from the OD at the 1988 Wolf Creek workshop. The report does not indicate the number of specimens examined at the Yankee Atomic/Northeast workshop. A summary of the results from five assemblies were provided in the report:

1. Statically Cast Stainless Steel Elbow to Wrought Stainless Steel Pipe
  - a. This configuration exists in six welds in each loop of the primary coolant system
  - b. Second highest detection rate for both manual and automated inspection, and lowest false call rate (6–7%)

2. Statically Cast Stainless Steel Elbow to Wrought Carbon Steel Nozzle/Safe End
  - a. This configuration exists in three welds in each loop of the primary coolant system
  - b. One of the lowest detection rates
  - c. False call rate varied from 5–26%
3. Centrifugally Cast Stainless Steel Pipe to Statically Cast Stainless Steel Elbow
  - a. This configuration exists in six welds in each loop of the primary coolant system
  - b. One sample had the highest detection rate of the samples tested
  - c. High false call rate – from 13–34%
4. Centrifugally Cast Stainless Steel Pipe to Wrought Carbon Steel Nozzle/Safe End
  - a. This configuration exists in one weld in each loop of the primary coolant system
  - b. One of the lowest detection rates
  - c. High false call rate – from 26–36%
5. Centrifugally Cast Stainless Steel Pipe to Statically Cast Stainless Steel Pump
  - a. This configuration exists in one weld in each loop of the primary coolant system
  - b. The lowest detection rate of the samples tested
  - c. False call rate varied from 7–26%

It was noted that access for inspection may often be limited, such as for elbow-to-pipe configurations (either wrought or CCSS pipe) where the access to the pipe side of the weld is often restricted by branch connections or reactor building structure. Also, in the case of the nozzle/safe-end-to-pipe or to-elbow configuration, access to nozzle side of the weld is limited by the nozzle geometry on the outer surface.

#### **A.2.11 EPRI Flaw Detection Round Robin**

In March 1993, PNNL participated in an EPRI round robin to determine the reliability of the data obtained from ultrasonic examinations of CASS components (see NUREG/CR-6984, Diaz et al. 2008b). It was a blind test to evaluate SAFT in a field situation. The intent was to determine realistic expectations for flaw detection by experienced vendors and researchers using their most current technology. At the time of scheduling PNNL's participation, the SAFT system had been relocated to the Pressure Vessel Research User Facility at Oak Ridge National Laboratory for ongoing work on other NRC projects. To meet the deadline, a team from PNNL traveled to Oak Ridge in late April 1993 with all of the necessary scanning electronics to participate in the exercise. EPRI agreed to ship a set of practice CASS specimens and the complete set of round-robin test specimens to the user facility and allotted the PNNL team one full week to complete calibration, setup, data acquisition, data analysis, and final reporting. During the exercise, EPRI and Northeast Utilities personnel supervised PNNL's efforts.

The PNNL team was provided with two sets of CASS specimens; a practice (training) set consisting of one CASS calibration block and three fitting-to-pipe sections, and a test set consisting of eight CASS fitting-to-pipe and pipe-to-pipe sections. All but three specimens originated from WOG, with the remaining three specimens provided by PNNL. The PNNL inspection team used its prototype LF transducer (350 kHz) coupled with the post-processing SAFT algorithm that had



been developed for use on CASS specimens. EPRI did not provide formal documentation to workshop participants. However, the POD versus FCP was plotted for the benefit of the workshop participants. The results were encouraging as the PNNL team scored higher than all other automated inspection teams, with a FCP of 30% and a POD and correct interpretation of 70%.

#### **A.2.12 INSS CASS Round Robin**

EPRI Report TR-1011600 (EPRI 2005b) discusses the results of an Institute for Nuclear Safety Systems, Inc., (Japan), round-robin piping study conducted in the mid-1990s to assess the effectiveness of advanced inspection techniques. The program, supported by Battelle Memorial Institute and the Joint Research Centre (JRC) of the European Commission, involved four international inspection teams (four different organizations) and two full-scale pipe mockups—a cast pipe-to-cast elbow and a wrought pipe-to-cast elbow. The program involved blind tests from the OD of the samples. The data were analyzed by the JRC following the PISC guidelines to determine the effectiveness and capabilities (detection, rejection, acceptance, false calls, and sizing) of the four inspection teams. For example, ASME Table IWB-3514-2 was used as the rejection and acceptance criteria.

The coarse-grained structure of the materials and physical limitations of the geometry seriously challenged the ability of the teams to detect, locate, and size the flaws. The main conclusion of the EPRI report was that the capability exists to inspect the CASS assemblies, and the primary factors that influence the inspection capability are the:

- Use of state-of-the-art UT equipment and scanners
- Selection of appropriate transducers
- Experience and expertise of the inspectors.

The round robin demonstrated that the perfect inspection system does not exist and that inspection qualification is needed to ensure that the inspection system (the equipment, procedures, and personnel) is appropriate and meets the established requirements.

#### **A.2.13 Ringhals CASS Inspections**

EPRI Report TR-1011600 (EPRI 2005b) discusses a pilot project initiated in 1997 to qualify ISI on a statically cast RCP at the Ringhals site in Sweden (there are three Westinghouse-designed PWR plants at the site). In 1995, the Swedish Nuclear Power Inspectorate (SKI) developed more stringent requirements for volumetric inspections. The new rules required performance demonstration for all NDE ISI activities.

Subsequent to the establishment of the new requirements, Westinghouse and AIB-Vinçotte International were chosen to develop a combined UT and ET procedure for the examination from the ID of the RCP casing welds and the pump-to-inlet elbow weld. The inspection volume was the inner one-third of the wall thickness. The project used a dedicated automated robot system with twin-crystal (TRL) search units to avoid the field implementation difficulties associated with the size of standard focusing transducers. The TRL units were developed based on the experience gained in the PISC III program. In that program, it was observed that the beam focusing technique yielded good results on heavy section components made from cast or wrought austenitic structures. Curved piezoelectric elements were used to provide an acoustic focusing effect to the pseudo-focusing resulting from the convolution of the transmitter and receiver beams. The procedure also used the time-of-flight diffraction method with single crystal compression wave probes. ET was used to confirm the presence of surface-breaking flaws and to accurately measure their length.

As listed in EPRI TR-1011600, the results from the qualification of the examination procedure and equipment using a full-size pump mockup were:

- Near-surface flaws were reliably detected
- Through-wall sizing was performed with errors less than 4 mm (0.16 in.)
- The pulse-echo examination revealed all embedded flaws within the volume to be examined, without reporting any false calls.

For both data acquisition and data interpretation (flaw detection and flaw sizing), the inspectors met the qualification criteria during blind tests on real defects. Subsequent to the completion of the program, the following CASS material inspections for the Swedish utilities were qualified:

- Pump body (Ringhals Units 2–4) – the inspection performed from inside covers the inner third (i.e., about 70 mm [2.8 in.]
- Nozzle-to-pipe welds, inlet and outlet nozzles (Ringhals Units 2–4) – the inspection performed from inside covers the inner third of wall thickness (i.e., 28 mm [1.1 in.] and 25 mm [1.0 in.] of base material of each side of weld)
- Ringhals Unit 2, nozzle-to-pipe weld
  - CASS elbow (SA351 CF8M material) connected to the inlet nozzle (A376 304N forged stainless steel pipe for the outlet nozzle)
- The nozzle material is carbon steel, clad with 308L stainless steel
- The weld volume contains of 308 stainless steel and 309 stainless steel buttering
- Ringhals units 3 and 4, safe-end to pipe weld
  - CASS elbow (SA351 CF8A material) connected to the inlet nozzle
  - CASS pipe (SA351 CF8M material) connected to the outlet nozzle
- Safe-end material is A182 316 wrought stainless steel
- The weld volume contains 308L stainless steel.

The pump casings for all three Ringhals PWRs have subsequently been successfully inspected using the automated scanning system.

#### **A.2.14 Seabrook Station Field Exercise**

During mid-January 1996, PNNL staff participated in a field exercise to examine thick section, CASS components (see NUREG/CR-6594, Diaz et al. 1998). The exercise was conducted in coordination with NRC Region I inspectors and Seabrook Station engineers. The inspectors were conducting an independent assessment of current industry inspections of CASS components. The opportunity to perform data acquisition using laboratory equipment in a field environment with NRC inspection personnel and utility personnel proved to be very informative.

A side-by-side comparison was conducted of transducers ranging from 350 kHz to 1.0 MHz as a function of material structure, flaw size and geometrical reflectors, frequency, beam processing angle, etc. Statically cast elbows (most oriented vertically with 40° bends) within the Unit 2 reactor were the only NPP components available for inspection. The degree of material variability was quite high from component to component as indicated by velocity data acquired as a function of position and incident angle in these materials.

A calibration block supplied by the utility was inspected, as were a number of WOG CASS specimens. The LF-SAFT technique was the only method that provided good detection, localization, and sizing data for a 10% deep, 0.32 cm (0.13 in.) thick, 2.54 cm. (1.0 in.) long circumferential notch in the calibration block. This technique also identified the axial notch and proved useful for detecting 1/2-T and 3/4-T side-drilled holes (0.32 cm. diameter) in both orientations, as well as a continuous corner trap response over the entire width of the calibration block at 45°, and semi-continuous responses at 30° and 60°. The surface geometries on the OD surface of the WOG specimens often precluded PNNL staff from examining the welds with the full contingent of incident angles due to the large probe size employed, and on two occasions only a far-side inspection using a single angle of incidence could be performed. Some data was acquired on the WOG specimens and existing cracks were detected in most cases; however, depth information was poor in comparison to actual depths.

Analysis of the Seabrook Station data indicated that the LF-SAFT technique was more promising for detecting indications than the standard conventional probe inspection protocol then currently used by industry. The field test was invaluable as it provided PNNL staff with a more realistic view of the many differences between laboratory experiments and actual field data acquisition issues. The information obtained from this exercise allowed PNNL to assess the LF-SAFT technique from the standpoint of effectiveness, potential utility of the technique in the field, access and coupling limitations, environmental constraints, and a variety of other parameters arising under field conditions that do not typically exist in the laboratory.

This exercise yielded an important observation. It became evident during data analysis that there was considerable variability between interpreters using the same data set. Therefore, *CASS data interpreters should be trained using some set of consistent criteria for discriminating flaw indications from material structure or geometrical indications.*

#### **A.2.15 Eddy Current Testing as a Complementary Technique**

On October 12, 2000, workers at the Virgil C. Summer Nuclear Station discovered signs of primary system piping leakage inside the reactor containment building (Casto 2001). The Summer Nuclear Station is a WEC-designed PWR. The plant was shut down at the time for a scheduled refueling outage. Workers removed insulation covering the piping from the reactor vessel and the SGs. They discovered an essentially through-wall 2 in. long axial crack with a 3/16 in. exit point “weep hole” at the outside surface in a nozzle-to-pipe DMW. The crack had allowed water to leak out while the plant was operating. The cracking was later determined to be caused by PWSCC, primarily attributed to high residual stresses on the inside surface of the DMW. At the Summer Nuclear Station, the nozzle-to-pipe welds were field welded during construction. The area where the leak occurred had significant repairs and surface grinding from the inside that resulted in higher tensile stresses on the inside surface. The ASME Code does not limit or provide guidance on the extent of repairs for these DMWs.

A considerable amount of boric acid deposits was found in containment as a result of the leak (estimated to be in excess of 100 lb. (45 kg) [Casto 2001]). A review of the 1993 ultrasonic data shows that transducer decoupling occurred at the location of the large axial crack and resulted in that area not being fully inspected. Although decoupling occurred in this area, the total volume inspected met Code requirements. The lack of NDE detection was partially attributed to the contribution of surface contour, surface roughness, and probe physical parameters inhibiting a successful inspection.

UT inspections performed after the discovery of the leakage identified the large crack that had leaked. ET was performed as a complementary method to the UT, and ET detected a number of smaller cracks that had not been identified by UT; however, at this time, ET was not an approved Section XI inspection method for this purpose. The UT had been subjected to the performance demonstration process specified in Appendix VIII, but there were no similar requirements for demonstrating ET inspection practices. As there were no Section XI requirements addressing the use of ET in this manner, this made the NRC's acceptance of the ET results problematic. A number of issues were identified in the licensee's root cause analysis as contributing to the large crack not being detected; for example, surface contour, surface roughness, and detector physical parameters.

To assess the effectiveness and reliability of ET as a complementary ISI technique, and to determine if ET was a feasible method for crack detection in CASS, PNNL investigated a range of specimens from four different sources: WOG CASS pipe specimens with thermal and mechanical fatigue cracks and a WEC vintage CASS blank spool piece, PNNL specimens containing TFCs, Southwest Research Institute specimens of highly coarse-grained blank spool pieces, and an IHI Southwest Technologies, Inc., vintage CASS blank spool piece. The PNNL study showed that if the inner surface was accessible, the ET method as applied in the study was very effective for the detection of these types of surface-breaking cracks (Diaz et al. 2007). Further, the results showed that all ID surface-breaking cracks in every test sample were detected with very good SNRs.

The results from the PNNL research were used to develop Section XI Code Case N-773, *Alternatives Qualification Criteria for Eddy Current Examinations of Piping Inside Surfaces*. The provisions of this Code Case allow the use of ET to complement UT on the inside surfaces of austenitic, dissimilar metal and clad piping welds to assist in the interpretation of flaws as being surface-connected and to provide surface flaw detection in specific areas of insufficient UT probe contact.

#### **A.2.16 Heavy-Wall CASS Piping Study**

Based on the notable results from the LF-SAFT performance demonstration at EPRI as well as increasing laboratory capabilities using LF-PAs, PNNL assessed the capability of LF-PAs to penetrate vintage thick-walled (65–80 mm or 2.6–3.2 in.) CASS weldments and piping segments. Tests were performed to assess the capability of LF UT to detect inside surface-breaking cracks in CASS reactor piping weldments as applied from the outside surface of the components (Anderson et al. 2007).

For this study, vintage piping segments were made available for testing by EPRI, IHI Southwest Technologies, Inc., and the WOG. Because these are vintage materials and there were a limited number of material suppliers during the time that these plants were constructed, it is believed that the specimens represent CASS materials that were used for fabricating primary loop piping in all WEC-designed PWRs.

Longitudinal waves produced by dual PAs operating at 500 kHz, 750 kHz, and 1.0 MHz, and a conventionally-designed, dual-element UT transducer operating at 400 kHz (using LF-SAFT methods), were applied to thick-walled, unflawed CASS piping segments to determine whether ultrasound at these frequencies could adequately penetrate the varied microstructures and to assess inherent background noise that may interfere with detection and characterization of flaws. Line scans adjacent to the welds were performed using inspection angles from 30–60°.

The examination of the unflawed EPRI, WEC, and IHI Southwest piping segments indicated that a LF-PA-UT technique was capable of penetrating relatively thick-walled sections of piping. With the examination capabilities demonstrated, PNNL initiated the next phase of the study, which was examining cracked specimens. Fifteen welded piping segments on loan to PNNL by EPRI (WOG specimens) that were fabricated to be typical of primary coolant loop components in WEC-designed plants were examined. The WOG specimens contained ID, surface-breaking, thermal, or mechanical fatigue cracks on either side of the weld. Similar specimens originally fabricated for PISC in the early to mid-1980s were also examined. The PISC configurations were typical of those installed in PWR primary coolant circuits, and the weldments contained mechanical and TFCs, also on either side of the weld.

The same transducers and frequencies were applied to the cracked specimens. Crack detection was made by careful analyses of composite data images acquired from both the CCSS and SCSS sides of the weld. The work indicated that the lower two frequencies (400 and 500 kHz) produced the best results. Signal loss and associated high background noise were observed in certain vintage CASS microstructures. The initial base material analyses indicated that CASS microstructures could produce regions of diminished UT response for a segment corner reflector (i.e., essentially, a 100% through-wall flaw). The 500 kHz PA data show that background UT noise due to scattering from the CASS grains did not appear to cause detected responses that could be misinterpreted as a crack.

Overall, the 500 kHz PA proved to be the best performer, with a combined detection rate of approximately 77% (91% from the SCSS and 63% from the CCSS). The performances of the 750 kHz and 1.0 MHz arrays were significantly affected by the microstructure of the CASS materials, with combined detection rates of around only 50% for these frequencies. With respect to the conventionally designed dual transducer operating at 400 kHz, certain vintage CCSS microstructures, especially those with multiple layers and grain sizes on the order of 20–25 mm (0.8–1.0 in.), produced signal loss and high background noise in certain areas of the tested segments. The areas of diminished UT response caused the SNR to fall below 2:1. The advantage of PA was that multiple-angle beams were electronically transmitted nearly simultaneously, enabling better penetration when a wide range of grain sizes and shapes was confronted.

Length sizing was attempted for all detected cracks. Measurements were made by using standard 6 dB drop and loss-of-signal techniques to ascertain the overall flaw lengths. The results were poorer than expected. Because of beam redirection and partitioning, the length-sizing RMSE was approximately 24 mm (0.95 in.) for the 500 kHz PA. The 1.0 MHz array performed better, with an RMSE of approximately 20 mm (0.79 in.); however, as stated above, the detection capability at 1.0 MHz was poor. As evidenced by the RMSE values obtained in this study, the coarse microstructure results in degradation of length-sizing capability for thick-walled CASS components. The general trend for these LF-PAs is to undersize the length of the cracks. This is consistent with results of the ID corner reflector responses on the base CCSS segments in that portions of the crack response may be significantly diminished over the crack length so that images of the flaws can appear shorter than their actual length. Also, if shallow flaws cannot be reliably detected, and the crack shape tends to be semi-elliptical so that the ends have only limited areas for reflection, the length of the crack will be undersized.

The PNNL report (Anderson et al. 2007) detailed the investigation of effective and reliable methods for the examination of thick-walled CASS components. The results of this study contributed significantly to the technical bases supporting ASME Code Case N-824, which was approved by the ASME over 5 years later (October 2012).

Returning to the research discussed in NUREG/CR-6933 (Anderson et al. 2007), in addition to the demonstrated superiority of PA-UT over conventional UT methods, this research demonstrated the need for post-acquisition analysis. As discussed in the report, post-acquisition data analysis allows an investigator to view the different response images in a given scan and discriminate between the various features in a specimen. Images were provided displaying the results for an inspection angle of 35°, which showed reflections from the counterbore of a pipe. When the 53° angle was displayed, other features such as weld root become visible. Finally, when 65° data was displayed, the targeted flaws become visible. Post-acquisition images afforded by PA analysis software provide fundamentally important capabilities for discrimination of responses in coarse-grained materials.

#### **A.2.17 Proposed Demonstration of CASS UT Technique for Weld Overlays on Pressurizer DMWs**

On February 22, 2006, a licensee requested approval from the NRC for an alternative to Section XI repair/replacement requirements (Scherer 2006b); specifically, to perform structural weld overlay repairs on three pressurizer safety relief valve line nozzle-to-safe end DMWs and one pressurizer spray line nozzle-to-safe end weld. The safe-ends of the three-pressurizer safety relief valve lines are CASS.

Prior to this request, ISI examinations detected axial indications in two of the pressurizer safety relief valve line welds. Through supplemental examinations, the utility concluded that the axial indications were fabrication flaws. However, in order to mitigate any future PWSCC and eliminate dependence on the Alloy 82/182 weld as the pressure boundary, the licensee decided to perform full structural weld overlays on all four welds.

As discussed in the December 14, 2006, NRC Safety Evaluation of the relief request (Terao 2006), Code Case N-504-2 (ASME 2000) contains provisions for the design of weld overlays and requires UT examination of the weld overlay and the upper 25% of the base metal beneath the overlay. Examinations from the Alloy 82/182 ferritic steel side of the nozzles were performed using Section XI, Appendix VIII, Supplement 11. UT examination from the CASS side of the weld is required to be performed using Section XI, Appendix VIII, Supplement 11, personnel and procedures. Supplement 11 qualification requires blind performance demonstrations on representative mockups containing representative construction flaws. At the time of the repair, the utility did not have access to such mockups and could not qualify personnel and procedures. In lieu of the required examination of the CASS base material, a best-effort UT examination was performed.

One of the issues discussed in the NRC staff request for additional information (Tsao 2006) was the concern that the indications could grow through-wall creating a leakage path into the overlay. There was also a concern that the inspection methods proposed might not detect potential cracking in the safe-end. In their response to the Staff's RAI dated March 17, 2006 (ADAMS ML 060800401, non-publicly available),<sup>7</sup> the utility indicated that it would coordinate with the EPRI NDE Center in developing techniques and a qualification process to demonstrate that the best-effort UT technique had the ability to detect flaws in CASS material.

The utility indicated that it believed this after-the-fact demonstration was appropriate because: (1) the full structural weld overlay does not take any credit for the original weld, (2) the material

---

<sup>7</sup> ADAMS ML 060800401, non-publicly available. This same information is contained in a publicly available document from the licensee (Scherer 2006a).



used in the weld overlay is PWSCC resistant Alloy 52M, and (3) the detected flaws were near the ID which would be well within the favorable compressive stress field induced by the weld overlay, and thus limit growth of the flaws. The NRC approved the alternative examination technique and after-the-fact demonstration process.

However, in a letter dated August 10, 2009 (Scherer 2009), the utility informed the NRC that it would be unable to meet the commitment to demonstrate a UT technique that had the ability to detect flaws in CASS material. The EPRI NDE Center had fabricated several samples to match the configurations at the plant and examined the samples with various techniques. An evaluation of the applied UT inspection techniques showed that none were successful. The utility noted that the required ISI of weld overlays would continue to be performed using the best-available technique.

#### **A.2.18 Far-Side Weld Examination Investigation**

The results of this study were discussed in NUREG/CR-7113 (Anderson et al. 2011). The purpose of the study was to assess the capabilities of UT for the examination of austenitic stainless-steel piping welds from the far side. It should be noted that the specimens examined in the far-side study did not contain CASS materials. However, insights from the far-side study are directly applicable to the examination of CASS weldments conducted from the far-side.

For example, as described in a letter from the Millstone Power Station, Unit 2, dated June 13, 2008 (Bischof 2008), a manual far-side ultrasonic examination technique was applied to eight high safety significant reactor coolant pump inlet and outlet DMWs from the ferritic-side. With respect to the CASS safe-end, it was examined to the extent possible on a "best effort" basis from the far side of the weld using an Appendix VIII, Supplement 10, procedure. Coverage of the CASS volume was claimed if it could be interrogated by at least one beam angle, either 45° or 60°, in the axial scan direction. Further, the percentage of coverage of the entire examination volume was determined by combining the Appendix VIII and "best effort" percentages. The coverage claimed will be discussed later in this section after the insights from the far-side study are discussed.

In another example, the licensee for St. Lucie, Unit 1, requested relief from an NRC requirement related to ASME Code Case N-770-1 that essentially 100% coverage be achieved (Katzman 2013b). No interrogation of the DMWs were performed from the CASS-side. As stated in the licensee's letter, "However, as shown in the figures, the theoretical beam path extends into the cast material for the examinations performed from the carbon steel side of the weld. While the coverage is not included in the Table, UT examinations conducted using Appendix VIII qualified procedures also provide reasonable assurance for the detection of flaws on the cast side of dissimilar metal welds, even though there is presently no standardized process to qualify them." Reasonable assurance will also be discussed later in this section after the insights from the far-side study are discussed.

##### *Far-side study scope*

The far-side study was conducted in several phases. Vintage wrought stainless steel piping was examined at PNNL. Field-removed piping segments from several BWR primary recirculation systems containing service-induced IGSCC were examined at the EPRI Nondestructive Evaluation Center, in Charlotte, North Carolina, to compare results. It should be noted that some of the EPRI specimens were part of a practice set and some were part of a secure set used for blind performance demonstration tests. The secure and practice data results were combined in the analysis to give a larger sample population and to protect the integrity of the secure set.

The welds assessed at PNNL were examined with PA technology operating at 1.5 MHz, a low frequency SAFT method operating in the 250–400 kHz regime, and an encoded conventional (monolithic transducer element) ultrasonic technique operating at 2.0 MHz (a frequency typical for examinations of piping welds in the field). While the conventional transducers represent those typically used during manual performance demonstrations, all data were acquired with automated scanners, and digitally stored for off-line image analyses. The EPRI specimens were examined only with PA-UT.

### *Insights*

What are the insights from the far-side study that can be used to conduct more effective and reliable examinations of CASS weldments? The first insight is that state-of-the-art UT needs to be applied to compensate for the acoustic deterioration caused by the materials to be examined. Far-side austenitic weld inspection procedures continue to perform unsatisfactorily due, in part, to the coarse microstructure that characterizes these weld materials (MacDonald et al. 2000). Further, the extremely anisotropic nature of CASS base materials makes them even more difficult to examine as the reflection of an ultrasound wave is highly spatially dependent at any given point in the material. The far-side and CASS studies have shown that ultrasonic flaw responses are often obscured by noise and scattered energy from the material structure. Material conditions in both cases lead to severe attenuation (primarily scattering), sound beam re-direction and/or partitioning, changes in acoustic velocity as a function of spatial position on the component, and refraction/reflection of sound energy at grain boundaries, root conditions, counterbore, and weld fusion lines. The complexity inherent in these challenging inspection scenarios translates into a lower SNR, difficulties in signal (echo) discrimination, and the potential for incomplete insonification of the component. In the far-side data, the weld response was lower by 2–3 dB than the base material. Studies have shown that the responses of sound waves propagated through CASS materials are decreased by as much as 5 dB. As a reminder, every 6-dB drop represents a point where field intensity is diminished by 50% of the initial maximum.

The second insight is that the far-side study reinforces the results observed in CASS studies, i.e., PA-UT methods have to be applied to CASS weldments to ensure the performance of effective and reliable examinations. The PA ultrasonic inspection provided the best results in the far-side study, detecting nearly all of the flaws from the far side. Very small flaws (<10% through-wall) were only consistently detected by PA. Accordingly, given that the conventional UT results were inferior to PA when examining austenitic materials, it cannot be expected that conventional UT would be effective on CASS materials which are much more difficult to examine. As indicated previously, the secure and practice data results were combined in the analysis to give a larger sample population and to protect the integrity of the secure set. Given that PA-UT detected nearly all of the flaws, the decreased performance of the other methods can be seen in the combined far-side detection rate of approximately 69%.

A third insight from the far-side study is the connection between detection rate and specular reflection. For the laboratory specimens, FlawTech TFCs were implanted in the heat-affected zones of the specimens. While these flaws are similar in nature to service-induced flaws, it should be noted that service-induced flaws such as IGSCC or PWSCC tend to exhibit more branching and faceting than the planar flaws used in this study. In general, planar flaws produce specular reflections that can be more readily detected, whereas branched and faceted flaws can return noncontiguous (or partitioned) sound fields, which can be redirected at multiple angles. This makes the branched and faceted flaws more difficult to discriminate from other acoustic noise sources. Redirection of the sound field is even greater in CASS weldments making it more difficult to detect flaws when complete weld examination cannot be achieved.

The fourth insight is the potential to miss flaws due to variation in amplitude response. The far-side study showed that the ultrasonic response from a continuous feature on the far side of a weld could have variable amplitude along the feature's length. In some cases, the feature appeared as a series of shorter responses. This could translate into an inability to detect tip signals when conducting far-side examinations or failing to recognize a flaw. Variations in amplitude response along the length are even more frequent in CASS weldments (see discussion section of this report).

The above discussions lead to a common, primary issue for far-side and CASS examinations – signal discrimination; is the ultrasonic response being generated from a geometrical condition, material noise, or a flaw? The data, whether from the near side or the far side, were generally cluttered with many signals to consider. In addition, the austenitic and CASS studies show material effects causing lower responses (2–5 dB). Welds/base regions are different materials thus creating boundary conditions that can attenuate or redirect sound from the desired target area. Signal discrimination is generally the most challenging aspect of flaw detection. The far-side results showed that, in general, cracks on the small end of the observed length range could be confused with material noise, and cracks on the long end of the range could be confused with part geometrical reflectors such as counterbore or weld root. Medium to long indications whether from a flaw or geometry could also exhibit signal drop out due to sound-field redirection, scattering, or attenuation. Signal discrimination in CASS materials would be considerably more difficult than for IGSCC in austenitic materials.

#### *Application of insights of far-side study to CASS far-side examinations*

At Millstone 2, coverage of the CASS volume was claimed when interrogated by at least one beam angle, either 45° or 60°, in the axial scan direction. Neither the various CASS-related national and international research studies that have been conducted nor the far-side study support this claim. The issues with respect to the application of manual, conventional UT techniques interpreted in real-time for the examination of CASS components have been thoroughly discussed in this report. In addition, the far-side examination that was conducted was best effort (i.e., not qualified). Further, the far-study showed the significant decline in detection rate that occurs from conventional examinations through the weld as a result of the material considerations discussed above. As stated in the far-side report, in the case of wrought stainless steel piping components, it is the austenitic weldment and as-built conditions that adversely impact the inspection effectiveness. Manual ultrasonic inspection techniques used in industry do not reliably and consistently achieve the desired detection reliability from the far side of the weld.

With respect to the St. Lucie 1 examinations, it was stated that using Appendix VIII qualified procedures provide reasonable assurance for the detection of flaws on the cast side of DMWs. The examinations were conducted using a PA UT Appendix VIII, Supplement 10, procedure in conjunction with mandatory elements of MRP-139 per the implementation protocol of NEI 03-08. In the far-side study, very small flaws (<10% through-wall) were consistently detected by PA-UT. However, with respect to far-side examinations, as with any UT technique applied, acoustic physics must be optimized to produce quality inspection. The UT procedure applied by the licensee has not been qualified for the examination of CASS components.

### A.2.19 Pressurizer Surge Line Investigation

In March 2012, the NRC published NUREG/CR-7122, PNNL-19497, entitled, *An Evaluation of Ultrasonic Phased Array Testing of Cast Austenitic Stainless Steel Pressurizer Surge Line Piping Welds* (Diaz et al. 2012). Interim results had been provided in two PNNL TLRs: PNNL-17698, *Assessment of Ultrasonic Phased Array Testing for Cast Austenitic Stainless Steel Pressurizer Surge Line Piping Welds and Thick Section Primary System Cast Piping Welds* (Diaz et al. 2008a), and PNNL-18596, *Assessment of Ultrasonic Phased Array Inspection Method for Welds in Cast Austenitic Stainless Steel Pressurizer Surge Line Piping* (Diaz et al. 2009).

The PNNL study was performed at the request of the NRC to investigate the potential for the effective and reliable inspection of pressurizer surge-line piping in response to cracking discovered in pressurizer safety and relief nozzles and surge-line DMWs, where the safe ends may be fabricated from CASS. The occurrences were summarized in NRC Information Notice 2004-11, "Cracking in Pressurizer Safety and Relief Nozzles and in Surge Line Nozzle," published on May 6, 2004 (NRC 2004).

The PNNL investigation to evaluate the capabilities of PA-UT methods as applied to thinner CASS pressurizer surge-line piping and associated welds began in 2006. For this investigation, PNNL was able to obtain some vintage pressurizer surge-line piping formed in the 1970s that was representative of typical pressurizer surge lines and various safe-ends in Combustion Engineering-designed plants. Since the pressurizer material was vintage, the sample specimens provided a range of grain structure conditions found in plants. The material comprising these components included CCSS pipe segments and SCSS elbows, with dimensions of approximately 31–36 cm (12–14 in.) OD and approximately 33 mm (1.3 in.) wall thickness.

The interim TLRs discussed the capabilities of various NDE techniques to detect, localize, and size cracks in the pressurizer surge lines. Accordingly, the summary below focuses on the final report that provided the results of the most effective and reliable inspection techniques.

A set of ten TFCs were implanted into three original CASS pressurizer surge-line welds (salvaged from cancelled plants). The cracks were implanted using a cyclic induction heating process that grows TFCs directly in the specimen material. The resultant crack morphology is a product of the specimen composition and microstructure. Additionally, three in situ grown cracks were placed near the weld heat-affected zone of the base material of one pipe specimen, and two in situ grown validation flaws were developed in a representative test pipe specimen. The flaw depths of the implanted cracks ranged from approximately 10–50% through-wall, but the majority of the cracks were 20–30% through-wall, or approximately 6–10 mm (0.25–0.4 in.) deep. Flaw lengths ranged from approximately 50–150 mm (2.0–6.0 in.), with the majority of flaws in the 50–75 mm (2.0–3.0 in.) range. All but one flaw was positioned in the weld. The in situ grown cracks were generally smaller in overall dimensions than the TFCs. It is believed that certain characteristics of in situ grown cracks, such as branching, surface facets, and local discontinuities, are more representative of service-induced cracks.

Custom arrays, operating nominally at 800 kHz, 1.0 MHz, 1.5 MHz, and 2.0 MHz were employed to examine the piping. Responses from these cracks were used to evaluate detection and sizing performance of the longitudinal mode, transmit-receive matrix PA probes applied. In addition, to provide an external confirmatory data set (discussed in NUREG/CR-7122), an ISI supplier was contracted to examine two of the CASS pressurizer specimens using PDI-qualified procedures and equipment. Personnel from LMT, Inc. visited PNNL in July 2010 to conduct an examination of

the implanted flaws in the pressurizer surge-line specimens using an ASME Section XI, Appendix VIII qualified procedure. LMT used their equipment to perform a blind examination (encoded PA).

All of the cracks in the specimens, implanted and in situ grown, were detected from both the CCSS (pipe) and the SCSS (elbow) sides of the weld using all four frequencies, except for one crack from the SCSS elbow side at 800 kHz because geometrical constraints precluded effective coupling of the PA probe. The flaws were detected and sized with good signal-to-noise values; PNNL reported SNR values in the 13.7–21.2 dB range and LMT reported a 10.2–13.2 dB range. The length sizing of these implanted flaws at 1.5 MHz by LMT had a 5.7 mm (0.22 in.) RMSE and the PNNL data had RMSE values of 5.9, 7.4, 9.0, and 9.7 mm (0.23, 0.29, 0.35, and 0.38 in.) for probe frequencies of 0.8, 1.0, 1.5, and 2.0 MHz, respectively. Thus, all error values are within the 19.05 mm (0.75 in.) ASME Code allowable limit for length. The depth sizing of these flaws by LMT had a 1.5 mm (0.06 in.) RMSE and the PNNL data had a 1.5, 1.2, 0.7, and 1.3 mm (0.06, 0.05, 0.03, and 0.05 in.) RMSE values for the same four probe frequencies above. These error values all fall within the ASME Code allowable limit of 3.18 mm (0.125 in.) for depth.

This research demonstrated that state-of-the-art PA inspection approaches are capable of detecting cracks in CASS components and associated weldments where the wall thickness is generally less than 50 mm (2 in.). The results provided the basis for the provisions in Code Case N-824 for the examination of thin-walled CASS piping.

#### **A.2.20 Examination of Florida Power & Light Carbon Steel to CASS DMW Mockup**

Technical Letter Report PNNL-24920, entitled, *Phased Array Ultrasonic Examination of Reactor Coolant System (Carbon Steel-to-CASS) Dissimilar Metal Weld Mockup Specimen*, was published in November 2015 (Crawford et al. 2015). PNNL staff had the opportunity to travel to the EPRI NDE Center in the summer of 2009 to conduct LF-PA-UT on a large-bore, reactor coolant system pipe/elbow-to-safe-end mockup. There are very few vintage materials or specimens available for investigations, which is an issue that has existed since CASS studies were first initiated. Thus, NRC and PNNL recognized this as a great opportunity to acquire data on a rare CASS specimen.

This mockup was fabricated by FlawTech, Inc., and the configuration originated from the St. Lucie nuclear power station. These plants are Combustion Engineering-designed reactors. The mockup consisted of a carbon steel elbow with stainless steel cladding joined to a CASS safe-end with a DMW and is owned by Florida Power & Light. The St. Lucie mockup is a 360° full-round specimen made from SA 516 Gr70 carbon steel (elbow) with 308/309 stainless steel cladding and Inconel 82/182 butter and is welded to an A351 CF8M CASS safe-end. The carbon steel nozzle has a nominal OD of 95.2 cm (37.5 in.) and a 9.7 cm (3.8 in.) wall thickness. The CASS safe-end has a nominal OD of 91.9 cm (36.3 in.) and a 7.9 cm (3.1 in.) wall thickness.

While the mockup contained both axially and circumferentially oriented flaws, only the nine circumferentially oriented flaws were examined in the PNNL study. In addition, PA-UT data were acquired only from the CASS safe-end side of the weld, which is considered to be the material most challenging to UT examination. This subset of nine implanted flaws included six TFCs and three electro-discharge machine (EDM) notches. All of the TFCs were implanted in the weld and butter regions. The circumferential EDMs were solely contained in the CASS safe-end. The TFCs were approximately 20–80% through-wall.

Two PNNL-designed, PA probes (500 and 800 kHz) were evaluated in this detection and characterization study. The probes are representative of those that could be employed during an ISI on coarse-grained components, depending on specimen configuration and in-field access constraints. All data were obtained using spatially encoded, manual scanning techniques. The effects of such factors as line-scan versus raster-scan examination approaches were evaluated, and PA-UT detection and characterization performance were assessed as a function of inspection frequency and wavelength.

All six TFCs were detected by line and raster scans using the 500 and 800 kHz PA probes. Both probes detected the largest EDM notch. Two of the EDM notches were not detected by the 500 kHz probe. All of the EDM notches were detected by the 800 kHz probes; however, one was only detected through a raster scan and one was only detected through the line-scan. The three EDM notches were placed in the CASS pipe material away from the weld/butter region in close proximity to an ID counterbore. A strong response from the counterbore at times masked the notch response. If viewed from the carbon steel nozzle side of the weld, the angle of the machined counterbore would be more parallel to the ultrasonic beam than perpendicular to it as on the CASS safe-end side. With the sound field nominally parallel to the counterbore, there would be little or no returned counterbore signal, possibly allowing better flaw detection of the shallower EDM notches.

All of the circumferentially oriented TFCs were detected and length sized within the ASME criterion. Length-sizing accuracy was assessed with RMSE calculations for all nine reflectors for each frequency and scanning method. Depending on probe frequency and scanning method, the RMSE values were between 9.5 and 12.7 mm (0.37 and 0.50 in.) and within the Section XI length-sizing acceptance criterion of RMSE value less than 19.05 mm (0.75 in.). Flaw tip signals were generally not observed for the shallow flaws (< 15 mm or 0.59 in.) as they were masked by the ID corner signal. One tip signal was not above the background noise level in the line-scan data.

Depth sizing was performed only when flaw tip diffracted signals were observed. Depth-sizing error values as measured by RMSE were 5.4 mm (0.21 in.) for 500 kHz data and 7.9 mm (0.31 in.) for the 800 kHz data, above the ASME Code criterion of less than 3.81 mm (0.125 in.). Flaw depth is determined from the difference between the ID flaw corner response and the flaw tip response. Typically, the ID corner response from a flaw was maximized at a refracted angle of 40°–45°. In contrast, optimized refracted angles for tip signal responses varied with flaw depth. These refracted angles ranged from 45°–70° with shallower flaw tips detected at the lower angles and deeper flaw tip signals detected at the higher angles. This broad range of angles is easily captured in PA data whereas multiple probes would be needed with a conventional single-angle probe approach.

Average SNR values for the 500 kHz data were nominally 16 dB ( $\approx 6:1$ ) for line scan data and 14 dB ( $\approx 5:1$ ) for raster data. The SNR values in the 800 kHz data were approximately 12.7 dB ( $\approx 4:1$ ) for both line and raster data.

A general conclusion resulting from this study is that acquisition of spatially encoded data is important to providing an effective and more reliable means for both detection and characterization of flaws. With regard to flaw placement relative to detection impact, it was observed that the axial position of a circumferentially-oriented flaw, with respect to weld and counterbore geometry, affected detection and depth sizing. Encoded data is invaluable for discriminating between geometrical and flaw indications in coarse-grained materials such as CASS where there is a lot of background noise. Typical short flaw responses (persistence) during a manual scanning operation makes discriminating very challenging.



While the 800 kHz data provided better flaw resolution, there was typically an increase in grain noise leading to lower SNR values as compared to the 500 kHz data. This was anticipated and is predominantly due to the fact that the wavelength using the 800 kHz probe is beginning to approach the average size of the CASS grain diameters, increasing the effects of attenuation (i.e., scatter) with increasing frequency.

#### **A.2.21 CASS Ferrite and Grain Structure Relationship**

In July 2016, PNNL published Technical Letter Report PNNL-25537, entitled, *CASS Ferrite and Grain Structure Relationship* (Ruud et al. 2016). The report documented research to determine whether, based on experimental measurements, a correlation existed between grain structure in CASS piping and the ferrite content of the casting alloy. The motivation for this research was the fact that UT is strongly influenced by size and type of CASS grain structures. Knowledge of this grain structure could help improve the ability to interpret UT responses, thereby improving the overall reliability of UT inspections of CASS components. The investigation was performed as a potential first step to determining the grain structure for use as a tool in improving the reliability of inspection methods.

Literature reviews indicated there may be a correlation between CASS microstructures and ferrite concentrations (delta ferrite content of the casting alloy). Ferrite can be measured in situ and nondestructively using electromagnetic induction technology. XRF may also be used to nondestructively measure the elemental content of the pipe in situ; the measured elemental content may be applied to a mathematical model to calculate the ferrite content of the alloy. XRF spectroscopy makes use of the characteristic radiation fluoresced from each element to determine elemental composition of materials.

An electromagnetic induction-based instrument called a Feritscope and an XRF analyzer were used to conduct these tests at PNNL on a number of CASS specimens readily available from previous studies where grain structure had been characterized. Ferrite and elemental analysis were conducted on the outside surface, inside surface, and accessible through-wall sections of these specimens. The resulting data sets were analyzed to determine the correlation between ferrite content (measured and calculated) and CASS grain structure. The grain structure was quantified in terms of the percentage of columnar grains and the sensitivity of any perceived correlation to a number of variables examined (such as changes in ferrite over the outside surface, inside surface, or through-thickness).

The data showed an apparent correlation between the percent columnar grains and the calculated percent ferrite in that the higher the percent ferrite the more columnar grains will be present. A key result of this study showed no apparent correlation between XRF-calculated and Feritscope-measured ferrite. This result supported the viewpoint that the calculated ferrite is based on chemistry from XRF measurements and affected only by the casting conditions; whereas, the factors affecting the measured Feritscope ferrite may include variations in the casting process from foundry to foundry, heat of welding, thermal stress relief, and machining. Further, the data supported the conclusion that Feritscope-measured ferrite content was probably too sensitive to post-casting processes to be a reliable indicator of casting conditions. The correlations in this report were based on a small statistical sampling of CCSS heats and only four of the seven pertinent elements.

While it was determined there were correlations between grain structure as defined by percent columnar grains and ferrite content as calculated from XRF measurements of elemental content, it was also determined that the correlation did not adequately capture the volumetric variation of grain structure. CEA has continued to assess potential methods to evaluate the microstructure of CASS materials as part of the NRC/IRSN cooperative research project. The overall objective of the development of a classification method for CASS components would be to apply the most effective UT techniques to reduce the impact of the microstructure on inspection performance.

### **A.3 Conclusion**

This appendix addressed significant PNNL CASS-related research findings and events that have occurred over the last 40 years. It should be noted that certain PNNL reports, such as those addressing casting process parameters and their resultant impact on grain structures in LWR CASS piping, were not discussed in the appendix as they were discussed in the body of this report.

## **APPENDIX B      WORKSHOPS - INSPECTION OF CASS PIPING**

In 2005, Chockie Group International (CGI) undertook the initiative to bring together interested parties to begin to work in an integrated manner to improve the inspection of CASS NPP components. CGI is a consulting engineering company located in Seattle, Washington. A series of four workshops were held between May 2006 and May 2012 with a select group of experienced participants to review the current state-of-the-art for the NDE of CASS piping; determine what type, if any, research was underway; identify and discuss the gaps (e.g., equipment, procedures, training, flaws); and consider the possibility of how to address these gaps.

Each of the workshops was well attended. The following list of organizations actively participated in at least one of the four workshops described here:

- AREVA NP, Inc.
- AREVA NP Uddcomb AB
- CEA (Commissariat à l'énergie atomique)
- De-Tect Non-Destructive Services
- Dominion Generation
- Duke Energy
- IHI Southwest Technologies, Inc.
- EPRI
- EDF R&D
- FlawTech, Inc.
- Georges Bezdikian Consulting Co.
- IHI Corporation
- IMASONIC S.A.
- Japan Nuclear Energy Safety Organization
- Korea Institute of Nuclear Safety
- LABORELEC
- LMT, Inc.
- Mitsubishi Heavy Industries, LTD. (MHI)
- Pacific Northwest National Laboratory
- QPro Technical Services
- Ringhals NPP
- RTQP Ringhals AB
- Southern Nuclear Company
- Structural Integrity Associates
- Swedish NDT Qualifications Centre
- Trueflaw Ltd
- U.S. Nuclear Regulatory Commission
- Vattenfall Ringhals AB
- Vinçotte
- WesDyne International

## **B.1 First Workshop**

The first workshop was held in San Diego, California, on May 13, 2006. The summary report from the first workshop, including presentations, is available at <http://www.chockiegroup.com/pdf/Workshop1.pdf>.

The first workshop provided an opportunity for attendees to: meet experts from other organizations conducting research associated with the inspection of CASS components; and discuss the status of CASS inspection capabilities, experiences, and general issues. Break-out sessions were held in the afternoon with attendees being divided into two groups to identify issues and potential steps to address them. One group examined inspection technologies, and gaps, with respect to improving effectiveness and reliability. The second group reviewed the issue of CASS flaw tolerance and the determination of critical flaw sizes in CASS components. The two groups then reconvened to prepare a list of recommended next steps.

Using the input from the two groups, the participants collectively established six areas for further investigation:

1. Define the allowable flaws
2. Characterize the plant components
3. Apply advanced (newer) inspection techniques
4. Develop open, non-blind procedure qualifications
5. Evaluate probes and equipment for optimum performance
6. Develop smaller and more flexible probes.

## **B.2 Second Workshop**

The second workshop was held in June 15-16, 2009 in Seattle, Washington. The CGI summary report from the second workshop, including presentations, is available at <http://www.chockiegroup.com/pdf/Workshop2.pdf>. It should be noted that the summaries below refer to workshop presentations and not to papers or reports from those organizations, unless stated otherwise.

The primary objective of the second workshop was to build upon the results of the first workshop and to establish the foundations for cooperative initiatives. NDE is part of the NRC's defense-in-depth approach to regulating, and a qualified NDE technique for the inspection of CASS components does not exist. As stated in the NRC presentation:

*"Though operational experience has not identified failures, longer-term operation may present issues with embrittlement mechanisms or potentially with SCC. Potential for new degradation mechanisms in CASS components could challenge structural integrity and functionality of the reactor coolant system. The inability to inspect CASS components challenges our ability to demonstrate the structural integrity of plants."*

There were several notable presentations. PNNL summarized the results of their latest research using lower-frequency PAs to inspect CASS pressurizer surge lines. The research showed that it was relatively easy to detect, length size, and depth size circumferentially oriented TFCs in this smaller-bore CASS in a certain range of frequencies. PNNL had published an interim TLR on the initial work in 2008 (Diaz et al. 2008a). Following a discussion among the participants, EPRI agreed to conduct confirmatory research and pending the findings, develop an ASME code case

addressing the examination of thin-walled CASS components. EPRI discussed their confirmatory research efforts at workshops three and four (see below).

An EPRI Senior Project Engineer discussed an on-going project to address PWSCC in Alloy 82/182 butt welds. The significance of the project to the examination of CASS components is that a large number of these butt welds contain CASS safe-ends. Because there is no qualified CASS examination method, as much as 50% of the required Section XI examination volume of these weldments cannot be effectively examined in many cases. EPRI indicated that mockups of reactor cooling (carbon elbow to CCSS pipe), shutdown cooling (nozzle to CCSS safe-end), and surge line (nozzle to CCSS safe-end) piping had been fabricated for current and future research activities.

Senior engineers from the Ringhals 2 NPP in Sweden summarized a round robin to assess the aging of CASS components. Ringhals 2 was commissioned in May 1975. Testing revealed significant degradation in hot leg properties (operating temperature approximately 325°C [617°F]). There was less degradation in the crossover leg (operating temperature 291°C [556°F]). Impact testing revealed there was conservatism in fracture toughness values. These results are consistent with the investigations conducted by organizations such as ANL that have shown that thermal aging embrittlement of CASS components can occur during an initial reactor design lifetime of 40 years. Thermal aging embrittlement is discussed in section 4 of this report.

Moving forward, the workshop participants recommended that:

1. The CASS workshops be held yearly to facilitate improved international cooperation,
2. EPRI and NRC expand cooperation.

### **B.3 Third and Fourth Workshops**

The last two workshops that were held are discussed collectively because the activities summarized below were incomplete at the time of the third workshop, and the fourth workshop presentations built upon the third workshop information.

The third workshop was held on January 28–29, 2011, in Seattle, Washington. There were 32 participants from eight countries—Finland, Sweden, Belgium, France, Canada, Japan, South Korea, and the United States. They represented utilities, vendors, regulators, inspection companies, and research organizations. The CGI summary report from the third workshop, including presentations, is available at <http://www.chockiegroup.com/pdf/Workshop3.pdf>.

The fourth and final workshop on the inspection of CASS piping was held in May 22–25, 2012, in Seattle, Washington. Twenty-three participants from six countries were in attendance (Finland, Sweden, France, Canada, Japan, and the United States). See CGI (2012) for the CGI summary report from the fourth workshop, including presentations. It should be noted that the summaries below refer to workshop presentations and not to papers or reports from those organizations, unless stated otherwise.

An EPRI program manager summarized research efforts at the EPRI NDE Center with respect to thin-walled CASS piping. EPRI had examined three SCSS elbows as well as a section of 40.6 mm (1.6 in.) thick CASS pressurizer surge line piping from a cancelled nuclear plant that contained TrueFlaw implanted thermal fatigue flaws. Data were obtained using three instruments and four transducers. Two of the transducers were PAs and two were conventional but all were at the frequency of 1.5 MHz. As would be expected, lower SNRs were obtained for the induced thermal

fatigue flaws (from TrueFlaw) as compared to weld-implanted thermal fatigue flaws (from FlawTech). In addition, the flaws from TrueFlaw were typically smaller than the FlawTech flaws. With respect to the induced flaws, the PA data were generally of a higher SNR than the conventional data (by as much as 5 dB). The EPRI results were consistent with those observed by PNNL in its research.

Initial results from the EPRI laboratory examination of CCSS piping greater than 51 mm (2 in.) in thickness were also described. The study utilized conventional and PA-UT techniques with frequencies from 500 kHz to 1.5 MHz. EPRI determined that inspection angles greater than 40° were not effective for flaw detection. In addition, UT frequencies greater than 500 kHz were reported as not useful. These results were also consistent with those observed by PNNL in its research. The significance of these results is discussed in detail in Section 6 of this report in the discussion of the effectiveness and reliability of conventional and PA probes and corresponding best frequencies.

SIA representatives provided an update on their efforts to develop a PFM model for estimating the reliability of CASS and acceptable flaw sizes. A PFM Code had been developed to perform probability of failure calculations and sensitivity studies for fully aged CF8M CASS piping, and SIA found the initial results to be encouraging. The SIA representatives stated, however, that a number of issues with the model remained to be addressed and additional data and information was needed. While it was indicated that funding issues had limited progress, it should be noted that SIA subsequently completed this work and presented its results in conference papers (Griesbach et al. 2014; Griesbach et al. 2015). It should also be noted that while there is general agreement in the industry with respect to the maximum UT flaw sizing sensitivities derived from the model (i.e., the smallest flaw that UT must be capable of detecting), discussions are ongoing regarding several flaw evaluation flaws that have been proposed.

A consultant<sup>8</sup> from France gave a presentation that provided the workshop participants with a detailed understanding of the rationale, activities, and results of the CASS aging management program at Électricité de France (EDF) during the period that he was manager at EDF.

EDF identified thermal aging of CASS and the decrease in material toughness as a potential safety issue in the 1980s. The margins with respect to rupture decrease with time in operation, thus requiring an integrity assessment and toughness evaluation. The EDF program initiated to assess thermal aging focused on metallurgical aspects. While outward signs of CASS weldment degradation had not been observed at any NPPs, poor examination results were being reported from the various CASS research projects and round robins being conducted at that time (as discussed in the historical overview of CASS-related research in Appendix A to this report). Accordingly, a determination of material properties and mechanical analyses were used in the fitness for service assessment. Goals of the program were to: assess the integrity of CASS elbows during all loading conditions over the initial 40 years of operation; develop criteria for assessing the probability of rupture over the lifetime of the components; and plan for potential component replacement.

Under this program, material properties (toughness evaluations) of CASS components were evaluated by taking boat samples from in-plant components (valves and elbows), ingots obtained from manufacturers, and elbows replaced during SG replacements. EDF inspected CASS elbows

---

<sup>8</sup> Georges Bezdikian was the project manager at Électricité de France for CASS life management from 1993 to 2007. He is now retired from EDF with his own consulting company.



using gamma radiography and penetrant testing to characterize fabrication flaws. Metallurgical analyses were then used to define flaw acceptance criteria.

A methodology was developed to assess crack resistance. The crack growth evaluations considered surface cracks (shrinkage cavities) identified and repaired during component fabrication, a reference defect assumed as a surface crack (conservative approach), and defects postulated in all zones of the elbows. Postulated transients were applied for 40–60 years.

Using the data gathered, prediction formulas for mechanical characteristics of aged materials were developed (the mechanical analyses included assessment of margins), predictions of the fatigue and tearing behavior of the casting defects were enhanced, and improvements in ISI were implemented. Analyses showed very good correlation between toughness measurements on samples removed from elbows and the prediction criteria developed by EDF.

Based on the data and analyses, EDF determined that the elbows were acceptable for 40 years of operation, but additional monitoring and evaluation would be employed during the period of extended operation (i.e., the next 20 years). However, given the predicted degradation and the cost of the enhanced ISI requirements over time, EDF concluded that the CASS elbows should be replaced whenever the SGs were replaced. Mr. Bezdikian noted in his presentation that 23 CASS elbows had been replaced (i.e., by 2012). An additional three elbows were to be replaced in the near-term.

#### **B.4 Impact of Workshops**

CGI is to be commended for its part in advancing the state-of-the-art in CASS research and inspection. Many international organizations participated in the workshops, and substantial progress was made on a number of key issues as a result of the collective research generated from participation in these events. A recommendation from the second workshop, for example, for the NRC and EPRI to expand cooperation on CASS research efforts led to an NRC/EPRI cooperative agreement that was signed in March 2011. The research conducted by PNNL and the confirmatory EPRI testing helped spearhead the development of Code Case N-824 for the examination of CASS weldments. The information with respect to thermal aging provided by organizations participating in the workshop reinforced the regulatory need to address thermal aging of CASS components in the license renewal term. As a consequence, a new EPRI/SIA effort was initiated to explore the use of PFM to determine allowable flaw sizes in CASS components and for identifying target flaw sizes for NDE that will ensure safe operation considering possible flaw growth. The result was the development of Code Case N-838.

The influence of the workshops has been far reaching. The NRC/EPRI March 2011 agreement has been updated, and CASS related activities continue. Periodic discussions between the key research organizations with respect to the latest developments also continue.



## **APPENDIX C      COOPERATIVE AND INTERNATIONAL CASS RESEARCH**

### **C.1 Background**

One outcome of the CGI workshops (Appendix B) was the NRC staff action to increase its outreach to domestic and international organizations to assess the state-of-the-art with respect to the inspection of CASS components.

### **C.2 NRC/EPRI NDE Agreement**

In 2007, the NRC and EPRI signed a MOU to allow and encourage cooperation in nuclear safety research. The MOU on cooperative nuclear safety research was updated on September 30, 2016, (Weber and Wilmshurst 2016). Since the signing of the initial MOU in 2007, a number of addenda to the MOU have been developed to cooperatively conduct research into various technical areas. However, none of the initial addenda addressed the NDE of vessels and piping systems.

An NDE-related addendum was signed for the first time on March 22, 2011 (NRC 2011). The period of performance has been extended several times and currently runs through September 30, 2021 (Weber and Wilmshurst 2017). The tasks addressed in the addendum cover a wide range of subjects and components, but the following discussion will only cover the CASS-related tasks.

The intent of the cooperation addressing CASS was to deal with all aspects of NDE including methods, procedures, equipment, and personnel. The overall objectives were to identify and evaluate the effectiveness of NDE methods in detecting and characterizing flaws, to evaluate the reliability of NDE methods for selected examinations, and to evaluate aspects of inspector qualifications.

Attachment 2 of the March 2011 cooperative agreement addressed the research activities specific to CASS. The NRC was responsible for conducting laboratory examinations of large-bore and small-bore CASS piping specimens using LF-PA probes. The results of the PNNL large- and small-bore CASS piping laboratory investigations have been discussed in detail elsewhere in this report (Anderson et al. 2007; Diaz et al. 2012). The NRC was also responsible for investigating in situ microstructural characterization. PNNL conducted literature searches to locate the theoretical work on ultrasonic field behavior in CASS-like materials to better understand how the microstructure impacts the different measurement types (e.g., backscatter, attenuation, diffuse field, birefringence, etc.). Evaluations of these techniques to determine the potential for in situ characterization of CASS grain structures were documented in several PNNL TLRs (Ramuhalli et al. 2009; Ramuhalli et al. 2010; Ramuhalli et al. 2013).

With respect to EPRI's role and responsibilities under the CASS scope of work, EPRI was responsible for collecting data regarding the locations of CASS piping in operating plants (to the extent possible for the material specification records that are available). EPRI was also tasked with evaluating existing field conditions that may impact CASS examinations performed from either the OD or ID of pipe welds. Finally, weld-specific analyses were to be conducted to determine the susceptibility of CASS piping weld locations to thermal fatigue. This work culminated with the EPRI sponsored development of the PFM model for flaw tolerance evaluations of aged CASS piping (Griesbach et al. 2014). The PFM model is discussed in this report under the section addressing Code Case N-838. A new task was added in a revised NDE

addendum signed on February 14, 2017 (Weber and Wilmshurst 2017). This task was focused on development and implementation of a CASS round-robin study (RRS) to assess the capabilities of currently available NDE techniques and to identify areas in need of improvement. As stated by EPRI in their final report on the RRS (EPRI 2017), the objectives of the CASS-RRS were to: (1) quantitatively assess volumetric examination techniques for the detection, sizing, and characterization of flaws in CASS test specimens; (2) evaluate the NDE techniques applied by experienced ISI practitioners for capability and effectiveness; (3) quantify the performance of the current NDE technology and personnel in terms of POD and FCP; and (4) identify any shortcomings in the current CASS mockup manufacturing techniques. The NRC sponsored PNNL's participation in the RRS. It should be noted that PNNL applied a LF-PA technique described in NUREG/CR-6933 in this RRS. Several industry NDE vendors also participated. PNNL was tasked with conducting independent analyses of data collected by all participants. NRC and EPRI were each responsible for developing final reports evaluating the results. PNNL's initial evaluation of the RRS has been published and is available to the public (Jacob et al. 2018). A more detailed report will be published once EPRI releases mockup information.

### **C.3 International CASS Research**

#### **C.3.1 CASS-Related Research at CEA**

Structural noise and attenuation can cause significant losses in detection performances in the ultrasonic NDE of coarse-grained metals, such as CASS. The transmitted field is strongly affected by the anisotropic behavior of the macrograins as it propagates through the CASS metallurgical structure. The Commissariat à l'énergie Atomique (CEA, or the French Atomic Energy Commission) developed a software product named CIVA for ultrasonic simulation. Research at CEA has led to the addition of subroutines to address heterogeneous materials such as CASS.

A number of important advances in CASS modeling are summarized in this section. The information is relevant to the discussion of CASS as in separate studies the NRC requested that PNNL evaluate the capabilities and limitations of CIVA. In addition, at the request of the NRC, PNNL used CIVA to assist in assessing three separate requests from licensees to perform alternative examinations of RCP-to-primary coolant piping DMWS that included CASS safe-ends.

PNNL developed formal mathematical theories for ultrasonic wave propagation in polycrystalline aggregates having both simple (composed of grains only) and complex microstructures (having macrograins and sub-grains/colonies) (Ahmed and Anderson 2009). Computations based on these theories were performed for ultrasonic backscatter power, attenuation due to scattering, and phase velocity dispersions. These theories have been incorporated into CIVA.

At the 7<sup>th</sup> International Conference on NDE in Relation to Structural Integrity for Nuclear and Pressurized Components in 2009 (Jenson et al. 2009), CEA presented an approach to compute wave propagation in heterogeneous materials such as CASS. The geometrical properties of the component structure were mimicked using Voronoi diagrams and the elastic properties of the macrograins (or cells) were approximated by a distribution of wave velocities. Ultrasonic waves were then propagated through the structure by a software algorithm. The presentation cautioned that while the algorithm reproduced the fluctuations in amplitude and time of flight of the back wall and end-of-block corner-trap responses, other sources of attenuation would have to be addressed to more accurately predict the losses in a propagating field.

Dorval et al. 2009 describes the noise and attenuation models that have been developed and incorporated into the CIVA 9 software package. Computations were run with the models, and the

results were compared to a set of measurements. Attenuation was correctly predicted by the algorithm. The results of the structural noise algorithm were encouraging. When noise was plotted as a function of time, some differences between predicted and measured values were observed; however, both the peak noise and noise amplitude were underestimated. This paper also describes the theory behind a model that can compute both noise and attenuation. A method to generate noise based on this model with a limited number of calculations was developed. While the results of the new algorithm were encouraging, discrepancies were observed between the simulated and measured noise amplitude.

CEA published the results of a subsequent study (Dorval et al. 2010). A method had been developed to model noise and attenuation based on a scattering model. Comparison of the predicted results to the validation measurements showed excellent agreement with respect to the variations of noise as a function of time. The approach is limited to single scattering. The modeling of multiple scattering to mimic the noise occurring in coarse grain blocks was the focus of ongoing research.

CEA has continued to improve the noise and attenuation models. For example, a presentation at the 2013 International Congress on Ultrasonics entitled, "Characterization and Modeling of Ultrasonic Structural Noise in Coarse-Grain Steel in the Diffusive Regime" (Bedetti et al.), described efforts to model scattering by the microstructure and simulation of noise based on experiments using CASS. It was determined that the simulation method used was able to correctly predict the evolution of noise in a case where multiple scattering is dominant. The results were incorporated into CIVA.

CEA has performed a number of experimental examinations on CCSS pipe representative of material used in the French PWR primary loop piping to evaluate LF-PAs for the inspection of CASS piping. As reported at the 8<sup>th</sup> International Conference on NDE in Relation to Structural Integrity for Nuclear and Pressurized Components (Ganjehi et al. 2010), two PA probes (500 kHz and 800 kHz) were applied to a CCSS specimen with an OD of 937 mm (36.9 in.) and an ID of 787 mm (31.0 in) to assess detection capability using the end-of-block corner echo. It was reported that the 500 kHz PA provided a much better ability to detect the corner echo than the 800 kHz PA.

In a subsequent research study building on the results of the above study [as reported at the 9<sup>th</sup> International Conference on NDE in Relation to Structural Integrity for Nuclear and Pressurized Components (Ganjehi et al. 2013)], CEA performed experimental examinations on a Manior CCSS specimen (OD of 937 mm (36.9 in.) and an ID of 787 mm (31.0 in); the manufacturer of the primary loop pipes currently used in French nuclear power plants) using a new 500 kHz dual element phased array probe specifically designed for the inspection of thick-walled CCSS. The 500 kHz PA probe was able to detect all of the defects in the specimen with a mean SNR higher than 12 dB. An application of signal processing methods to multi-angle inspection results showed an improvement in detection performances.

### **C.3.2 CASS Investigations by JNES et al. – Ultrasound Propagation in CASS**

JNES, the Japan Power Engineering and Inspection Corporation (JPEIC), and the University of Toyama conducted a study to investigate properties such as beam skewing, sound dispersion, and attenuation in CASS specimens (Sakamoto et al. 2012a). This section discusses the results of this study, and the relationship of the study to CASS research and PWR primary coolant piping in the U.S.

The authors state in the JNES paper that one of the objectives of the study was to provide information to Japanese inspection personnel regarding the propagation of ultrasound in CASS materials. A second objective was to use the knowledge obtained in the investigation to develop a CASS piping simulation model.

A CASS welded joint specimen identical to the most recent primary coolant piping system configuration in Japanese PWRs was used in the investigation as well as three CF8M calibration blocks. The configuration and microstructures of the test pieces were as follows: a pipe-to-pipe mockup (columnar-to-columnar microstructures), two calibration blocks with equiaxed microstructures, and one calibration block with a columnar microstructure. The IDs of the test pieces were either 736 mm (29 in.) or 787.4 mm (31 in.) with wall thicknesses being approximately 75 mm (3 in.).

As discussed in the Sakamoto paper, CASS primary coolant piping in Japanese PWR plants consists mostly of coarse columnar grain structures, and many of the columnar grains in the specimens used for the study extend nearly the entire thickness of the specimens. It should be noted that the microstructure of typical Westinghouse PWR CASS primary coolant piping in the U.S. also exhibits very long grains similar to those observed in the Japanese study, i.e., columnar dendritic (Anderson et al. 2007). Thus, the results of the study with respect to ultrasonic propagation are relevant.

The surfaces of the Japanese test specimens were highly polished in order to conduct metallographic analyses. In order to fully understand the structure, grain orientation, and phase, a scanning electron microscope (SEM) using an electron backscatter diffraction technique was applied. The accelerated electrons in the primary beam of a SEM are diffracted by the atomic layers in crystalline materials. These diffracted electrons are detected when they impinge on a phosphor screen and generate visible lines, called “Kikuchi bands,” or electron backscatter patterns (EBSPs). These patterns provide projections of the geometry of the lattice planes in the crystal; thus, they give direct information about the crystalline structure and crystallographic orientation of each grain.

Using the EBSP technique, the crystal orientation maps of the CASS were acquired. The maps show the orientation of each region as observed from the radial direction (normal to the page). Snapshots of the wave propagation in CASS were obtained by high-resolution visualization techniques. The technique allowed ultrasound beam propagation such as skew due to the coarse-grained and acoustically anisotropic crystal structures to be observed.

It is well known that high attenuation and noise are key adverse factors with respect to conducting effective UT of CASS piping. Although a variety of research efforts have previously been conducted, this study evaluated sound velocity, attenuation, and noise measurements to fully understand the various attributes associated with ultrasonic propagation in the CASS specimens applied in this study. The evaluations revealed that attenuation and noise levels were greater in the columnar-grained than in the equiaxed specimens.<sup>9</sup>

---

<sup>9</sup> It should be noted that PNNL conducted a similar type of study (Crawford et al. 2014) to assess attenuation from scattering. The purpose of the PNNL study was to better understand the impacts of CASS microstructures on sound field coherence and propagation. PA ultrasonic beam formation was characterized in terms of beam scatter, partitioning, and redirection using some of the same CASS specimens from the earlier PNNL thick-walled piping studies (Diaz et al. 1998; Anderson et al. 2007). The equiaxed microstructure produced the greatest scatter while the columnar microstructure produced the least. As

### C.3.3 UT CASS Piping Inspection Capabilities

JNES, JPEIC, and the University of Toyama teamed to conduct another study to assess the accuracy of detection and sizing of ID-initiated flaws using UT from the OD surface of CASS piping. As stated in the Sakamoto et al. (2012b) paper, primary coolant piping systems are safety-related, and missed flaws, false calls, and the potential for poor sizing performance are of great concern in Japan and other countries.

Twelve large-bore thick-walled test specimens were used in this study: four specimens containing a CCSS CF8M piping segment butt welded to a SCSS piping segment; four CCSS piping segments; one safe-end forging butt welded to a CCSS CF8A piping segment; one CCSS CF8A piping segment butt welded to a CCSS CF8A piping segment; one CCSS CF8M piping segment butt welded to a SCSS elbow; and one CCSS CF8M segment butt welded to a SCSS elbow. All of the test specimens simulated primary coolant piping in Japanese PWRs except for the forged safe-end to CCSS specimen that represented the Westinghouse PWRs in Korea. Each specimen had at least one circumferential fatigue crack, and one specimen also contained an axial crack. The cracks were induced by various means (three-point bend cyclic loading, cyclic loading, and TFCs).

Flaw detection and sizing were performed using three conventional UT techniques that are currently applied during ISI in Japan and two PA-UT techniques. The conventional probes operated at a frequency of 1.0 MHz. The PA-UT probes operated at frequencies of 500 kHz and 1.0 MHz, respectively.

Flaws ranged from 3.8 mm (0.16 in.) to 56.2 mm (2.2 in.) in through-wall depth. The PA-UT techniques detected all of the flaws. In addition, the matrix PA-UT techniques were able to depth size all flaws approximately that were at least 30 mm (1.2 in.) through-wall or greater in depth. Conventional, encoded UT techniques detected most of the flaws. However, non-detection using the conventional UT was observed for flaws of approximately 20 mm (0.8 in.) through-wall and smaller. As stated in Sakamoto et al. (2012b), the conventional UT techniques were considered inadequate for depth sizing, and difficulties were also encountered in length sizing flaws.

One of the reasons for conducting the study was to assess the conservatism of the structural integrity evaluations for CASS piping systems postulating 60 years of thermal aging. It was concluded from the evaluations that structural integrity in Japanese PWRs can be assumed for thermally aged CASS piping at 60 years with a flaw 20% through-wall and 100% around the circumference. Accordingly, for a pipe of 77.8 mm (3 in.) in wall thickness, a UT technique would have to be able to reliably detect a 15.6 mm (0.6 in.) through-wall flaw to meet the 20% criterion. The conventional UT techniques used in the study began to miss flaws of approximately 20 mm (0.8 in.) through-wall and smaller. Thus, it was determined that the structural integrity of CASS piping could not be ensured through the use of these conventional UT examination techniques.

---

expected, columnar microstructures produce the greatest partitioning and equiaxed the least. The mixed and banded microstructures showed various combinations. Scattering increased with increasing frequency in the equiaxed and columnar specimens but partitioning was similar across all of the probe frequencies applied. With respect to assessing whether the beam effectively insonified the intended target, the results of the study showed that the mixed banded microstructure (as compared to equiaxed and columnar microstructures) appeared to cause the largest beam shifts (in both the circumferential and through-wall extent).



### **C.3.4 Swedish Radiation Safety Authority (Strålsäkerhetsmyndigheten)**

#### *C.3.4.1 Thermal Aging Embrittlement in Hot Leg PWR CASS Elbows*

The first CASS elbow in each PWR hot leg and crossover leg connected to the steam generator (SG) head were replaced in conjunction with the SG replacements at Ringhals Unit 2 in 1989. The unit had been operating for 15 years. The removed hot leg and crossover leg elbows were investigated for mechanical degradation. Significant degradation in the tensile and fracture toughness of the CASS elbows in the hot legs was discovered. The crossover leg elbows showed minor degradation. The material test results were discussed in a presentation at the Fontevraud II International Symposium (Jansson 1990).

The hot leg operating temperature at Ringhals 2 was originally 325°C (617°F). To extend the life of the old SGs, the reactor power was lowered to 80% in 1986 decreasing the hot leg temperature to 303°C (577°F). The elbows were fabricated from CF8M CASS. Test rings were examined with a ferrite meter to measure the ferrite content at the ID at three different heights as well as through the wall thickness from the end surface. Test coupons were removed from the locations of highest ferrite content. Around 700 measuring points were recorded with a Förster instrument. The ferrite content varied from 1.5–22.5%. The hot leg elbows had a ferrite content a few percent higher than the crossover leg, but the variations within each ring were much higher. The investigation revealed that the measured ferrite content was closer to micrograph results than the calculated values from the chemical analysis.

Tensile, impact (KCU [Charpy U] and KCV [Charpy V]), and  $J_{IC}$  fracture mechanics testing were conducted. Charpy U notch testing revealed that time at temperature had caused a significant decrease in toughness of the elbows (more pronounced for the hot leg than the crossover leg). Impact testing for Charpy V notch specimens was performed from –196°C (–321°F) to +225°C (437°F). The Upper Shelf Energy level was significantly lowered from time at temperature in the hot leg (the crossover leg showed a very minor decrease). While the  $J_{IC}$  values at 320°C (608°F) were well above the established lower bound used in fracture mechanics calculations, it should be noted that the testing was conducted after only 15 years with respect to time at operating temperature.

### **C.3.5 Initial Efforts to Use Modeling to Predict Embrittlement**

The following work by a group of researchers at the KTH Royal Institute of Technology, AB Sandvik Materials Technology, and Chalmers University of Technology (these three organizations are in Sweden) is summarized here due to the various efforts to develop an ultrasonic method to classify and size CASS grain structure in situ (Barkar 2018). The paper discussed efforts to make microstructural predictions from simulations. Embrittlement in ferrite and duplex stainless steels can develop after several years or decades. The large time span in which embrittlement may occur is one of the reasons for developing models using software platforms to predict the timescale and morphology of the spinodal decomposition. The Thermo-Calc and DICTRA software packages were used to simulate spinodal decomposition in the Fe-Cr system. In making microstructural predictions from simulations, these tools ensured a consistent approach for evaluating inter-diffusion mobility and gradient energy. A consistent treatment is important to being able to accurately predict microstructures and mechanical properties. A preliminary simulation study showed that the addition of 0.11 mass% Mn, for example, had a large effect on the decomposition kinetics.

## APPENDIX D MPATS DETECTION AND CHARACTERIZATION CRITERIA

The Multi-Parameter Analysis Tool Set (MPATS) analysis is focused on detailed criteria for identifying or rejecting regions as cracked in the material, where ultrasonic signal amplitude anomalies (SAAs) occur. These criteria are based on acquiring some combination of redundancy in the ultrasonic data as a function of the various inspection parameters which include examination incident angle, driving frequency of the transducer, and scan direction. Based on the PNNL research to date, there are nine specific criteria that the data analyst or automated software platform must consider during the evaluation process, and these are described below. The diagram in Figure D-1 illustrates the examination volume of interest for crack identification as it relates to component geometry.

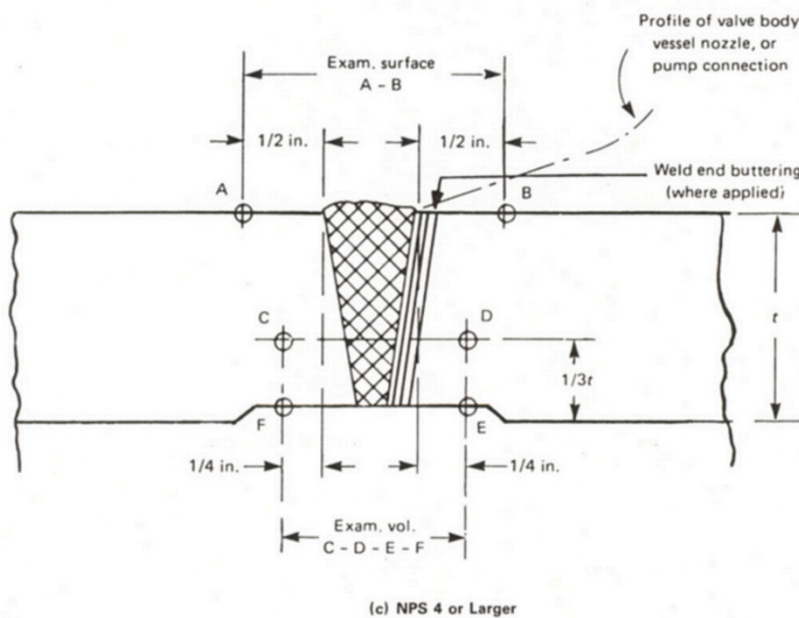


**Figure D-1 Illustration Defining the Examination Volume. Reprinted from ASME 2001 Edition, Section XI, by permission of The American Society of Mechanical Engineers. All rights reserved.**

1. SAAs occurring in the volumetric space between the top edges of the two counterbore slopes will be fully examined. SAAs occurring outside of this region will not be examined. This is due primarily to the high amplitude signal returns scattered from counterbore geometry effectively masking any cracking that may exist in this area.
2. If the full complement of inspection angles was used in the examination ( $0^\circ$ ,  $30^\circ$ ,  $45^\circ$ , and  $60^\circ$ ), coinciding SAAs *should* occur from at least one inspection angle from both sides of the weld, in order for the indication to be further considered as evidence of cracking. Exceptions may be made to this if, for instance, strong SAAs are evident from only one side due to unusual material or surface conditions on the adjacent side precluding the acquisition of useable data.

3. If the full complement of inspection angles were used in the examination, coinciding SAAs must occur at more than one examination frequency, or more than one examination incident angle, or more than one scan direction (from data acquired from the other side of the weld), or some combination thereof, in order to establish a degree of redundancy that allows the inspection analyst to determine whether or not the SAA is evidence of cracking.
4. SAAs may occur above, on, or below the back-surface line appearing on the SAFT images. Differences in position of  $\pm 1.27$  cm ( $\pm 0.5$  in.) above or below this line are not significant, and SAA position will be measured from the peak amplitude point. When an SAA occurs in this region, its tail will be included in the boxed examination region of the image. When the back-surface line is positioned accurately, corner trap signal returns from cracking in the material will result in SAAs that lie just on the back-surface line, with the majority of the SAA below the line. The accuracy of the back-surface line is a function of the material velocity and transducer delay, and the actual position of an SAA relative to this line is a function of incident angle, acoustic velocity, frequency, wavelength, and zone focal dimensions of the transducer. Because material velocity varies with spatial position and incident angle in the material, inaccuracies must be allowed for. The  $0^\circ$  data acquired from both sides of the weld is used to determine ID surface contouring, and nominal wall thickness data are used to substantiate the ultrasonic data on the SAFT images. Depending on the differences between the nominal wall thickness data and the  $0^\circ$  ultrasonic profiling data, the actual z-axis dimension of the volume boxed for examination can range up to 3.81 cm (1.5 in.) in total length.
5. SAAs should have some degree of characteristic shape (either circular or elliptical) to them, with somewhat smooth contours on their edges, as opposed to random, blotchy, scattered amplitude blips that appear with little symmetry and rough contours. Also, SAAs should have reasonable and proper orientation with respect to the examination incident angle of the insonifying beam. A perpendicular orientation is normal.
6. SAAs occurring very near the edge of the material under test (especially in the case of curved pipe sections) will be discounted due to edge scattering effects. The side wall of the pipe section acts as a mirror to reflect more energy back to the receive element than would normally occur if no edge existed. This can be minimized by starting the transducer at a point on the pipe OD surface where no overlap exists between the transducer face and the edge of the pipe, but this effectively decreases the width of the scan on the ID surface.
7. Differences in lateral position of  $\pm 1.27$  cm ( $\pm 0.5$  in.) or less are not significant, except at a single examination incident angle with multiple frequencies.
8. Length and depth sizing will be performed from the most continuous SAFT-processed image where the SNR is high, if a data file of this nature exists; however, in most cases, the composite data will be plotted using spreadsheet analysis and data resolution of 2.54 mm (0.1 in.) in the x- and y-axes. If tip signal returns exist, depth measurements will be made using the most continuous SAFT-processed image. In the case of length sizing and localization (positioning), the  $-3$  dB points will be used to “clip” the data from the background noise, and the data points will be extracted from the SAFT images and plotted on a spreadsheet. Generally, the accuracy of length sizing and crack positioning will be  $\pm 1.27$  cm ( $\pm 0.5$  in.) in both circumferential and axial directions. If one data file exhibits a strong SNR, and the SAA of interest is coincident in other scans, this data file may be used for location and sizing; however, in general when no single data file can be judged to exhibit these characteristics, the composite data will be plotted, and the data will be averaged graphically in order to determine location and size.

9. The analysis protocol will provide sizing and location data that is referenced to the OD surface dimensions and will compensate for transducer overlap and nominal beam position in the material.

These criteria were used in manual analysis procedures during the field trials of the LF-SAFT during early November 1997, at the EPRI NDE Center. A select number of the most impactful criteria were used in development of the MPATS software for this effort (Diaz et al. 2003).



## **APPENDIX E      CASS WELDMENT EXAMINATION COVERAGE ISSUES**

### **E.1 Background**

PNNL performed an assessment for the NRC of the use of weld overlays (WOL) as a mitigation strategy. The assessment was discussed in a PNNL TLR (PNNL-21660, Sullivan and Anderson 2012). The effectiveness of WOLs as related to the inspection requirements of Code Case N-770-1, as conditioned in §50.55a, were also evaluated. The evaluation of the inspection requirements included detailed discussions of the inspection challenges associated with certain CASS weldments in Westinghouse and Combustion Engineering (CE) designed plants. The information in PNNL-21660 regarding the limitations to obtaining complete coverage of CASS butt welds in these plant types was obtained from discussions with industry inspection experts.

Unrelated to PNNL-21660, the NRC requested that PNNL evaluate three requests from licensees to conduct alternative examinations. The draft of PNNL-21660 was completed in early 2012. The evaluations of the three licensee alternatives were conducted by PNNL in late 2012 and early 2013. Thus, the results of the PNNL evaluations were not considered in PNNL-21660. This section discusses the PNNL evaluations of the licensee alternatives with respect to items such as calculated by algorithm versus modeled weld coverage, sound field intensities, and flaw detection.

Examination weld coverage was addressed in several appendices to PNNL-21660. Appendix C, "Dissimilar Metal Weld Inspection Limitations of a Typical Westinghouse Plant," describes the Alloy 82/182 butt welds that are typically found in a Westinghouse-designed plant. Appendix D, "Dissimilar Metal Weld Inspection Limitations of a Typical Combustion Engineering (CE) Plant," addresses piping welds in a typical CE-designed plant.

The three licensee submittals to the NRC requesting approval of alternatives addressed DMWs associated with RCP-to-primary coolant piping (that included CASS materials). The licensees requested approval for alternative examination requirements because full coverage on either the axial scans for the subject DMWs (for detection of circumferentially oriented cracking) could not be obtained, limited coverage was obtained on the circumferential scans (for detection of axially oriented cracking), or both. As illustrated in the appendices of PNNL-21660, licensees are unable to meet the Section XI requirement to examine essentially 100% of the designated weld volume for many CASS weldments because there is currently no qualified examination method for CASS materials; of the OD surface contour/condition; and there are obstructions such as instrumentation, safety injection, charging, and spray nozzle connections.

For the analyses, PNNL used the CEA-developed CIVA software package to assess the UT performed. CEA (Commissariat à l'énergie atomique et aux énergies alternatives) is the French Atomic Energy Commission. The CIVA project started in 1992, the software platform is a semi-analytical modeling tool dedicated to NDE modeling and simulation. CIVA is widely used in different industrial sectors and has been subjected to an extensive amount of validation work. Validation efforts continue through experimental tests at CEA and regular participation in benchmark studies. Benchmark study results have been presented by CEA at the Review of Progress in Quantitative Nondestructive Evaluation conference every year since 2004. The CIVA software package allows defects to be represented in a component with theoretical modeling of sound beams. Factors such as sound field intensity and SNR can then be analyzed. Ongoing confirmatory research associated with CIVA NDE modeling and simulation applicability is currently being sponsored at PNNL by the NRC's Office of Research.

Previous PNNL CIVA evaluations of the licensee alternatives were based on actual transducer design parameters and component geometry information provided by the licensees. Three general points should be noted with respect to the modeling performed. First, the sound fields are modeled using a lossless isotropic material; that is, specific parameters such as actual grain sizes and structures, velocity ranges, and other material variables that will result in sound beam attenuation, sound beam re-direction, and decreased SNR are unknown and therefore not considered. The second general point is that the available modeling software packages assume perfect contact between the probe and component, and thus transducer coupling issues were not considered. Surface irregularities can cause intermittent and unpredictable losses of ultrasonic transducer coupling that may affect signal response amplitudes and transmitted sound beam coherence. This can be more pronounced with PA probes that are used in all Code Case N-770-1 examinations. In addition, probe wedges with flat contact surfaces are frequently used which would contribute to coupling inconsistencies in regions where the component surface is irregular or non-uniform, or if the probe were to rock during circumferential scans on the component. No information was provided by the licensees with respect to the actual weld profiles, so idealized surfaces were modeled under perfectly flat conditions. Third, the factors discussed above typically decrease the amplitudes of signal responses from the actual flaws, resulting in lower SNRs, making flaw detection significantly more challenging.

## **E.2 Three Licensee Alternatives**

### **E.2.1 Arkansas Nuclear One, Unit 2**

By letter dated November 11, 2011 (Pyle 2011), and with subsequent information in letters dated April 13 (Pyle 2012a), May 21 (Pyle 2012c), and September 10, 2012 (Pyle 2012b), the licensee, Entergy Operations, Inc., submitted to the NRC an alternative to the requirements of Code Case N-770-1. The licensee submitted the alternative because of limited volumetric examination coverage achieved for two DMWs at Arkansas Nuclear One, Unit 2 (ANO-2). The NRC TLR evaluating the ANO-2 request is available at ADAMS Accession No. ML13113A218 (PNNL 2013a).

The first weld addressed in the submittal was a full penetration DMW on the RCP discharge nozzle joining the carbon steel, ID clad primary piping to a CASS safe-end. The safe-end is welded directly to the RCP pump housing. The licensee calculated the total volumetric coverage as 73.8%. Coverage for the inner one-third of the weld could only be obtained in the buttering and portions of the weld nearest the weld fusion zones. No coverage was obtained in the center of the weld for the inner one-third, due primarily to weld OD surface features. No coverage was obtained on the CASS safe-end.

PNNL modeled the ultrasonic beam applied to this weld, and the modeling revealed individual beam density profile issues. The licensee's PA was operated with focal laws defined to produce (active axis) steered beams from 0°–80°, at 1° increments, each focused at approximately 122 mm (4.8 in.) of metal path after exiting the probe. This focal length is beyond the ID surface for steered beams less than around 20°, and only produces –6 dB field densities at the ID for beams at approximately 20°–25°. In a similar manner, it was observed that steered beams above approximately 65°–70° would not produce useful beam profiles for detecting flaws near the ID because they are focused at too short a metal path length. The model also predicted that all sound beams above approximately 30° would have less than –6 dB beam intensities near the ID of the weld. The –6 dB value represents a point where field intensity is diminished by 50% of the initial maximum value. The above factors, as well as other potential coupling issues described in



Chapter E.1 of this appendix, would typically lower the amplitudes of reflected energies from flaws, resulting in decreased SNR, which would make flaw detection significantly more challenging.

The second weld in the ANO-2 request was a full penetration DMW on the RCP suction nozzle joining the carbon steel, ID clad primary piping to a CASS safe-end. The safe-end is welded directly to the RCP pump. The weld has an OD taper. No coverage was obtained on the ID-to-OD region of the weld nearest the CASS fusion zone. No coverage was obtained on the CASS safe-end.

PNNL evaluated theoretical detection of the licensee-postulated ID-connected circumferential flaw originating in the susceptible material region using modeled defect responses. The semi-elliptical planar defect was defined to have an arc length of 254 mm (10 in.) and a maximum through-wall extent of 30.5 mm (1.2 in.) at the crown of the flaw. The flaw was placed in the butter/weld region of the component and was connected to the ID surface. The A-scan image showed that a 30° angle does not result in a strong ID corner-trap response from the flaw, as angles of 30° and above are projected to be higher than the ID-connected region (a lower angle is required from this scan position to insonify the ID-connection region). While a low amplitude “top-of-flaw” response was observed indicating that a postulated flaw of 30.5 mm (1.2 in.) through-wall extent could possibly be detected at 30°, that angle beam would be unable to assess whether the flaw could be considered as ID-connected because this angle does not adequately insonify the ID flaw corner-trap region. It was postulated that a lower inspection angle, such as approximately 20°, could potentially result in a modest amplitude response from the ID corner trap of this flaw. As the scan progressed from the start position toward the weld region, the postulated flaw disappeared from view in the simulation.

At the request of the NRC, a second evaluation was conducted using the previously defined semi-elliptical planar flaw to determine the effect of through-wall depth on the top-of-flaw response at a 30° inspection angle. It was observed from the modeling results that a flaw with a maximum through-wall extent of 35.6 mm (1.4 in., or over 40% through-wall) yields the highest theoretical top-of-flaw response (lowest delta amplitude) when using a 30° beam.

The second weld evaluated was a full penetration DMW on the RCP suction nozzle joining carbon steel, ID clad, primary piping to a CASS safe-end. The safe-end is welded directly to the RCP housing. This weld also has an OD taper between the ferritic elbow and the CASS safe-end.

PNNL’s model did not agree with the licensee’s stated coverage. There was an area less than -6 dB on the ID of the weld. In order for the lower angles (20°–25°) to extend to their maximum -6 dB length, electronic lateral skewing was required. While focal laws were produced to laterally skew the beam by 10° down into the weld ID, the actual array matrix would only produce an approximate 4° skew. This is because only two elements in the probe used for the examination exist in the passive axis of the array. The overall sound field suffered from poor field densities of the steered beams above about 30°. The sound field intensity profiles for 20°–80° showed that only projected angles below 30° produced focused energies, at or above -6 dB, at the ID surface of these welds.

There are several key observations from the theoretical model that raised questions regarding the overall effectiveness of the examinations. When one considers the optimum range of impingement angles for flaw detection in the subject welds, and the best theoretical sound field intensities that could be expected, insufficient acoustic energy at the PDI-UT-10 angles (42°–45°) was generated by the PA probe and focal laws used for detecting axially oriented PWSCC. This

would be especially true for shallow cracks, on the order of 20%–30% through-wall and smaller. Further, the model predicted that only angles below about 25° appear to provide adequate ( $\geq -6$  dB) sound fields to facilitate detection.

## **E.2.2 Calvert Cliffs Nuclear Power Plant**

By letter dated June 7, 2012 (Stanley 2012), and with subsequent information in a letter dated January 10, 2013 (Stanley 2013), the licensee, Constellation Energy, submitted an alternative to the examination requirements of Code Case N-770-1 for two welds. PNNL's TLR on the evaluation of the alternative examination is available under ADAMS Accession No. ML13113A233 (PNNL 2013b).

The examination of a full penetration DMW on the RCP suction nozzle joining carbon steel, ID clad primary piping to a CASS safe-end will be considered here. The CASS safe-end is welded directly to the RCP housing. The cross section of the weld varies. A region of the weld at the ID nearest the carbon steel in the susceptible Alloy 82/182 weld/buttering has the potential to contain an undetected PWSCC flaw that is 5.1 mm (0.2 in.) through-wall and 10.2 mm (0.4 in.) long. According to the industry's Performance Demonstration Initiative (PDI) generic DMW ultrasonic procedure, the optimum ID impingement angle for detecting PWSCC for this weld is in the range of 55°–60°, vis-à-vis, the transmitted refracted angle should be in the range of 42°–45°.

Given the PA parameters employed by the licensee, the models showed partial agreement with coverage maps provided the licensee. The potential flaws of the size postulated could go undetected during an inspection due to lack of sufficient beam intensity at the ID surface region; that is, full coverage (using  $-6$  dB field intensities) is not obtained with beam steered angle ranges of between 42°–46° (optimized for ID impingement) even with electronic lateral skewing of  $\pm 10^\circ$ . The beam computation models show that a flaw height of approximately 12.7 mm (0.5 in) could exist before the  $-6$  dB sound field at 42° would be able to detect the tip of the flaw.

## **E.2.3 St. Lucie Nuclear Power Plant**

By letter dated, February 4, 2013 (Katzman 2013b), Florida Power and Light, Inc. (the licensee), submitted an alternative to the NRC regulations to implement Code Case N-770. Additional information was provided by the licensee in a letter dated July 30, 2013 (Katzman 2013a). PNNL's evaluation is available at ADAMS Accession No. ML14149A195 (PNNL 2013c).

The axial examination for detecting circumferentially oriented flaws is physically limited by two nozzles (resistance temperature detector and spray) that extend along a circumferential arc. These obstructions result in varying limitations along the scan path on the OD surface. As a result of these limitations, the licensee postulated ray trace coverage and the maximum circumferential PWSCC flaw that could be detected. It should be noted that in accordance with MRP-139, "Inspection Examination Volume Coverage," per EPRI-DMW-PA-1, Rev. 1, only examination volume coverage for beam angles between 40°–50° can be credited. It was calculated that a flaw 195 mm (7.7 in.) in length and 32.5 mm (1.3 in.) in through-wall extent would be detected in the region of examination restricted by the nozzles.

The licensee's PA probe was operating with focal laws defined to produce steered active axis beams from 25°–70°, focused at approximately 76 mm (3.0 in.) of metal path after exiting the probe. This focal length is short of the ID surface for the range of steered beams; especially for the beam angles between 40° and 50°. The theoretical metal path as calculated along a 40° refracted angle originating from the exit point of the wedge (component OD surface) and traveling

to the ID of the component is nominally 96.2 mm (3.79 in.). Therefore, the model predicted that all sound beams in the accredited angle range (40°–50°) to have less than –6 dB beam intensities near the ID of the weld. The model predicted –1 dB ID coverage of the weld for the 40° inspection angle (4 times lower initial sound energy).

The second weld addressed in this licensee request was a full penetration on an RCP outlet nozzle joining the carbon steel primary piping to a CASS safe-end. The carbon steel piping was clad on the ID, and the CASS safe-end was welded directly to the RCP housing. The axial examination for detecting circumferentially oriented flaws was physically limited by a spray nozzle. The nozzle limited scanning access over an OD circumferential length of 197.6 mm (7.78 in.). MRP-139 was also used to calculate ray trace coverage for this weld.

A postulated ID-connected circumferential flaw originating in the susceptible material region 40% through-wall flaw (32.5 mm [1.2 in.]) was evaluated. The modeling showed that due to the limited access caused by the spray nozzle, a 40% through-wall flaw (33 mm [1.3 in.]) would not be detected in the location suggested by the licensee. The model predicted that the flaw would have to grow to a minimum of 40.6 mm (1.6 in., approximately 50% through-wall) before it would be reasonable to expect detection of a top-of-flaw (tip signal) response to be reliably detected given the PA examination technique parameters used.

### **E.3 Insights**

As previously indicated, although the modeling evaluations were based on actual transducer design parameters and component geometry information provided by the licensees, factors such as the effects of material microstructures, surface conditions, weld profiles, and transducer coupling could not be considered. All of these factors result in sound beam attenuation, sound beam re-direction, and decreased SNR. These factors can only decrease the amplitudes of signal responses from actual flaws, resulting in lower SNR, and further degrade sound field coherence, making flaw detection significantly more challenging.

Overall, the modeling revealed that the sound fields applied generally suffered from poor field densities, especially at the ID surface region. Sound field assessments generally revealed a lack of optimization of the number of elements of the PA probes and the focal laws employed. The modeling revealed that the examination of these welds would be dramatically improved if adequate insonification of the ID of CASS materials associated with DMWs could be achieved.



## **APPENDIX F      LITERATURE REVIEW FOR CASS RESEARCH**

### **F.1 Introduction**

It has been theorized that in situ characterization of the microstructure of CASS components has the potential to improve inspections by providing opportunities to optimize the UT system for specific grain structures and provide targeted examiner training. As discussed elsewhere in this report, CASS components can have equiaxed, columnar, or mixed grain structures resulting in a range of acoustic attenuation, scattering, and beam distortion. The difficulty in reliable ultrasonic NDE of CASS components is largely due to detrimental effects of wave interactions with the coarse-grain microstructures.

In March 2010, PNNL conducted a review of 50 years of literature relevant to acoustic-wave interactions with coarse-grained materials. This review was never published and is presented here in this Appendix. The review was conducted to assess the current state of knowledge on wave-microstructure interactions and to assess the state of the art in nondestructive microstructure characterization techniques using acoustic or electromagnetic methods. Given that there had been numerous studies conducted over many years, it was hoped that the literature search would reveal some promising techniques to facilitate the development of novel ultrasonic microstructure characterization tools for CASS components.

The PNNL literature search revealed, however, that in situ characterization of CASS microstructures for the optimization of inspection capabilities for specific grain structures is in its early stages. Should in situ characterization be pursued in the future, the literature search also revealed certain gaps. At this time, it appears unlikely that a single measurement type (such as attenuation or time-of-flight alone) will provide sufficient information to correctly identify the diverse microstructural categories in CASS materials. In that case, a range of measurements will be necessary for accurate microstructure characterization in CASS. It may be possible to use signal processing tools to enhance the SNR and compute key attributes from the measurements and use model-based iterative algorithms to solve the inverse problem of microstructural characterization and categorization given the enhanced measurements.

### **F.2 Literature Search Summary**

The literature search revealed that a number of national and international organizations have conducted theoretical work on ultrasonic field behavior in CASS-like materials to better understand how the microstructure impacts the different measurement types (e.g., backscatter, attenuation, diffuse field, birefringence, etc.). Papers were found by several French organizations for example (Moysan and Corneloup 2000; Feuilly et al. 2009). Because CASS-like materials do not appear to be amenable to analytical solutions at the present time, the focus has shifted to modeling and simulation.

While the focus has currently shifted away from in situ characterization of the microstructure of CASS components, one of the objectives in developing this report was to summarize the current state-of-the-art sufficiently for researchers and NDE practitioners that might be conducting future investigations. The information in this section provides considerable background on past efforts should additional research efforts be planned.

### **F.3 Casting Processes and Microstructure**

Technical Letter Report PNNL-19002 (Ruud et al. 2009) described PNNL efforts to investigate the various piping casting processes used for NPPs during construction from the 1960s through 1980s and the resultant impact on grain structures. Information was obtained from manufacturers on casting process parameters and what might be expected in terms of their effects on microstructure. PNNL obtained vintage CCSS and SCSS specimens from various sources and has conducted a number of investigations with respect to characterization of microstructures. The following characteristics were found in the specimens, dependent on the casting process:

- Variable grain sizes and shapes, depending on casting methods and parameters
- Uniform radially oriented columnar grains (basaltic, or columns that form during cooling)
- Large, uniform equiaxed grains with no directional preference
- Eclectic mixture of columnar and equiaxed grains
- Variation radially by layer (banding)
- Variation by axial and circumferential position within a given component
- Unpredictability of exact microstructure, even when knowing the casting methods used
- Significant delta ferrite content.

### **F.4 Acoustic Wave Behavior**

As acoustic waves interact with materials, scattering of energy occurs at interfaces such as grain boundaries. In general, the scattering behavior of ultrasonic waves from single scatterers may be broadly classed into three regimes: Rayleigh, geometric, and stochastic (Ensminger and Bond 2011). In the Rayleigh regime, the scatterer or grain size ( $d$ ) is small relative to the wavelength  $\lambda$  of the acoustic wave used, typically,  $d/\lambda \gg 1$  (Goebbels 1994). The scattering behavior may be described using geometric principles. As the ratio of the grain size to wavelength increases, the interactions between the wave and the grains increase, resulting in higher levels of scattering. For intermediate wavelengths, however, the observed acoustic behavior depends on unknown and effectively random grain orientations and properties and is best described using stochastic methods.

In CASS materials, the grain sizes can vary over a large range and, therefore, the scattering behavior can range from Rayleigh to geometric regimes in a single material volume. Thus, the mean grain size is often used instead of  $d$  to describe the scatterer size and the dominant scattering regime. For coarse-grained CASS specimens,  $\lambda$  must typically be very large (very LF) to ensure scattering in the Rayleigh regime. In addition to decreasing the ratio of mean grain size to wavelength moving material-ultrasonic interactions toward a regime of quasi-isotropic behavior, the use of LF decreases interference from ultrasonic backscatter and increases penetration because the scattering portion of attenuation is reduced.

Studies have shown that there is little beam distortion for a 500 kHz shear wave in either equiaxed-grain CCSS or columnar-grain CCSS; however, high beam distortion is apparent for 1.0 MHz waves. Similarly, there is little beam distortion for a 500 kHz longitudinal wave in equiaxed-grain CCSS, while a lens effect appears for columnar-grain CCSS due to the ray deviation or skewing effect. Distortions are seen at higher frequencies (Good et al. 1991; Thompson et al. 2008).

An alternative classification of wave-scattering behavior may be made based on the acoustic properties of the scatterer. When the acoustic impedance contrast between the scatterer and the host material is small, the scattering phenomenon is characterized as “weak,” while “strong” scattering refers to the case when the acoustic impedance contrast is high. Elastic wave scattering in coarse-grained materials (such as CASS) is generally due to strong multiple scattering, i.e., the scattering behavior may range from Rayleigh to geometric regimes in a single material volume (Thompson et al. 2008).

The behavior of acoustic waves in solids is also a function of the wave mode. The three bulk wave modes usually considered are longitudinal (called L or P), horizontally polarized shear (SH), and vertically polarized shear (SV). In addition to these modes, surface and plate wave modes (and others) can also be generated, depending on the particular inspection parameters and component geometry. In general, for coarse-grained materials, acoustic wave propagation is a function of the microstructure, frequency, and wave mode. Coarse-grained materials can have random equiaxed, columnar, or mixed grain structures. Depending on the frequency (or equivalently, the wavelength) and mode of the acoustic wave, a range of behaviors may be observed in all of these grain structures. For instance, large equiaxed-grain structures will typically result in elevated attenuation, scattering, and beam distortion. In an equiaxed material, this behavior will be independent of the angle of incidence (Turner 1999). Lower frequencies (larger wavelengths) tend to have the lowest attenuation because the behavior is in the quasi-isotropic or quasi-Rayleigh regime. On the other hand, in columnar grains, the result is largely dependent on the incidence angle relative to the grain orientation. Waves propagating along the columns will be minimally attenuated. Beam bending and splitting may take place depending on the mode used. Transverse to the columns, the material behaves as an equiaxed material. Again, LF implies quasi-isotropic behavior.

Anisotropy in materials such as CASS can arise from texture/structure (grain size and orientation), composition variations and contamination, stress, or deformation. Texture anisotropy appears to have the highest impact on ultrasonic wave propagation, followed by stress (Segura et al. 2009). The choice of the wave mode significantly impacts ultrasonic characterization of CASS. L-wave probes are commonly used due to issues of ray skew, backscatter, and attenuation inherent to SV waves in coarse-grain material or strongly textured material. However, the use of shear waves, while relatively uncommon in these materials, may provide additional information for microstructural characterization. Auld (1973) gives a general discussion of acoustic propagation within anisotropic material and derives slowness (inverse velocity) relationships for L waves, SV waves, and SH waves. Liess (2008) and Burridge et al. (1993) discuss the properties of slowness surfaces, with specific reference to orthorhombic, transversely isotropic, and cubic structures. Acoustic attenuation is a signal loss mechanism that consists of components due to both scattering and absorption. For large grains, which are common to CASS material, scattering may extend beyond the Rayleigh regime and enter the stochastic and geometric regimes, depending on the wave frequency and wave mode. The use of low frequencies decreases the ratio of mean grain size to wavelength and moves material-ultrasonic interactions toward a regime of quasi-isotropic behavior, decreases interference from ultrasonic backscatter, and increases penetration because the scattering portion of attenuation is reduced. However, the use of lower frequencies for inspection decreases the achievable spatial resolution for flaw localization.

Another phenomenon common to CASS is ultrasonic beam distortion or phase distortion of a wave front. Beam distortion is evident when sound speed variations from grain-to-grain is on the order of  $\pm 3\%$ , or greater (Thompson et al. 2008). Similar studies showed that there is little beam distortion for a 500 kHz longitudinal wave in equiaxed grain CCSS, while a lens effect appears for columnar-grain CCSS due to the ray deviation or skewing effect. High beam distortion was



apparent for 1.0 MHz waves. Comparisons of shear waves to longitudinal waves have been made. The frequency for shear waves is doubled (versus longitudinal wave measurements) to keep the wavelength-to-grain size constant for comparing wave data. The comparisons show that a longitudinal wave is less distorted than the shear wave in CCSS for roughly the same wavelength-to-grain size ratio.

## **F.5 Potential Approaches for In Situ Microstructure Characterization**

Ultrasonic inspection of CASS materials can be challenging due to phenomena such as sound speed variation, ultrasonic beam deviation, attenuation, background acoustic noise caused by scattering, and phase variations across a wave front. Knowledge of the microstructure could improve the inspectability of a given component, by knowing whether a method exists for the given microstructure, and then matching the inspection method to the characterized microstructure. Further, ultrasonic inspection parameters could potentially be optimized for given CASS microstructures. Finally, the use of signal processing tools to improve parameters such as SNR could improve interpretation of the measured data if the microstructure were known.

Key to in situ microstructure characterization using acoustic methods is improved understanding of the different phenomena that arise from the interactions between acoustic waves and coarse-grained microstructure. Phenomena such as sound speed variation, beam deviation, attenuation, noise, and phase variations could potentially form the basis for ultrasonic methods of classifying and characterizing CASS microstructures. Two key interrelated issues must be addressed to achieve the characterization of microstructure. The first of these is determining which measurements should result from a given combination of microstructure and the interaction of acoustic energy with the microstructure. The second is data interpretation or characterizing and categorizing the microstructure from the measured data.

## **F.6 Methods for Characterizing CASS Microstructures**

For homogeneous materials, metallography is an ideal approach to microstructure characterization. As previously discussed, CASS microstructure can be highly variable within a component making metallography unsuitable. In addition, less invasive approaches to microstructure characterization are generally preferred in an NPP environment.

The methods revealed by the literature search for microstructure characterization of materials can be divided into two categories: acoustic and non-acoustic. The acoustic techniques have greater potential and are discussed in depth below. With respect to the non-acoustic methods (electromagnetic and optical) that have been applied in other fields, they are limited in their in-situ capabilities and, thus, are only briefly mentioned here.

Electromagnetic methods encompass a large range of techniques, from eddy currents to magnetic Barkhausen emission (Lindgren and Lepistö 2004; Vengrinovich et al. 2006). These approaches rely on local changes in electrical conductivity and magnetic permeability. While effective, such methods are largely surface (or near-surface) characterization techniques and have been primarily used to characterize microstructural changes due to stresses, fatigue, or other types of degradation. The use of electromagnetic methods for microstructure characterization at significant depths in specimens requires the use of very low frequencies that would result in a loss in spatial resolution. Optical characterization is applicable only to the surface and normally requires damaging the part to be characterized.

However, several acoustic techniques were identified with potential for microstructural characterization of a coarse-grained material such as CASS:

- Ultrasonic velocity (sound speed/time of flight)
- Ultrasonic attenuation
- Beam mapping
- Diffuse fields.

These ultrasonic measurement methods are discussed below.

### **F.6.1 Ultrasonic Velocity (Sound Speed/Time of Flight)**

Ultrasonic wave speed is a fundamental acoustic property that is dependent on material density and microstructural variations. Wave propagation speed in isotropic homogeneous materials is a constant that is a function of the wave mode. In anisotropic and heterogeneous materials, the wave speed depends on the wave mode, propagation angle (anisotropy), and spatial location (heterogeneity). L-wave and SH-wave sound speeds vary a relatively small percentage as a function of orientation with respect to the crystal axes. The SV-wave sound speed, however, varies by a large percentage as a function of orientation with respect to the crystal axes. The use of velocity variation to characterize microstructure has been investigated by several researchers. Ramuhalli et al. (2009) presented preliminary experimental verification that the time of flight (which is related to the speed through the ultrasonic path length) of longitudinal and shear waves may be used to sort between pure columnar grain and pure equiaxed microstructures in CASS. The data presented validated prior experiments by Kupperman et al. (1981; 1987).

Wave speed has also been correlated to other microstructural parameters such as grain size in polycrystalline materials (Yu et al. 1992), annealing and degree of recrystallization (Vasudevan and Palanichamy 2002; Jayakumar et al. 2008), precipitation and precipitation hardening (Sagar et al. 2007; Jayakumar et al. 2008), degree of cold work (Yu et al. 1992), residual stress and texture (Jayakumar et al. 2008), and sensitization (Stella et al. 2009). The measurement of wave speed can potentially be used to quantify anisotropy by revealing variations in speed. Vasudevan and Palanichamy (2002), on the other hand, use L-wave speeds for their work on austenitic stainless steel. Often, the measurement of wave speed (particularly for small specimens) can be difficult, and methods for reliable measurements are needed. Frenet et al. (2000), for instance, presents a leaky Rayleigh wave velocity measurement technique that does not require moving the (focused) transducer. Note that wave speed measurements for multiple wave modes (longitudinal and shear) are often used to determine time-of-flight ratios, which are then correlated to the microstructural damage or evolution (Jayakumar et al. 2008; Ramuhalli et al. 2009). The use of ratios removes dependency on specimen thickness or variations in path length. Further, wave speed measurements at several frequencies (so-called ultrasonic spectroscopy) have been proposed for material characterization (Buckin et al. 2003).

### **F.6.2 Ultrasonic Attenuation**

Attenuation of acoustic waves in polycrystalline materials results from a number of factors, including absorption, scattering, beam divergence, and magnetoelastic hysteresis. Attenuation due to scattering in metals varies generally as the fourth power of frequency (for both longitudinal and shear waves) (Ensminger and Bond 2011) and is a function of the scattering cross section, orientation of the grains/grain boundaries, and the anisotropic nature of the material. Attenuation can be determined by measuring the decay of the back-surface reflection in a normal incidence

ultrasonic measurement though such measurements typically require correction for beam spreading (Papadakis 1959, 1966; Darbari et al. 1968; Papadakis 1968, 1984; Liu et al. 2006) and component/reflector curvature (Gunarathne and Christidis 2002). Typically, attenuation measurements using back-wall reflections use a buffer rod to help distinguish the front- and back-surface reflections and to provide a reference amplitude (Papadakis 1968). Often, attenuation is measured as a function of frequency; this is also sometimes referred to as ultrasonic spectroscopy (Buckin et al. 2003).

Attenuation measurements, through the use of decay coefficients, have been used to characterize materials in situ (Gunarathne and Christidis 2002). Other studies have related attenuation to grain-size variations in metals (Jayakumar et al. 2008) and marbles (Sarpün and Kılıçkaya 2006), damage detection at high temperatures (Jayakumar et al. 2008), and degree of sensitization (Stella et al. 2009). Measurements of attenuation may be made at one or more frequencies using either contact (Stella et al. 2009) or immersion transducers. Note that both simulation (Chassignole et al. 2009) and experimental studies (Kupperman et al. 1981; Ramuhalli et al. 2009) of attenuation variation have been correlated to microstructure characteristics in CASS specimens, though all of these studies were preliminary. Data on a large number of specimens, with mixed microstructures, would be necessary before attenuation may be used as a standalone microstructure characterization technique. Additionally, attenuation based on back-wall reflection measurements is a bulk characterization technique. Attenuation computed from backscatter measurements (see below) may have the potential for microstructure characterization as a function of depth in the material.

### **F.6.3 Beam Mapping**

Different microstructures give rise to various anomalies in the direction of sound propagation. This can plausibly be used to an advantage through mapping the beam in order to deduce the spatial distribution of the microstructure. Beam mapping, while theoretically applicable to microstructure characterization, is difficult to use in practice because the interior of the material is not available. Instead, the field measurements at the surface must be used to deduce the microstructure. This suggests that methods from stereology may be applicable. Claytor et al. (1985) used a laser interferometer to measure the longitudinal displacement at ultrasonic frequencies on the surface of CASS specimens when the incident beam was on the opposite surface. Distortion in the form of beam skewing, focusing, or defocusing were clearly apparent, though no attempt was made to characterize the microstructure, on the basis of these measurements. Surface beam mapping (or phase field mapping) in CASS specimens using critical angle measurements was shown to correlate with microstructure although the studies were conducted with a limited number of specimens. Critical angle reflectometry measurements for reflection coefficient determination have also been used for characterizing porosity in nuclear fuel (Cereser Camara et al. 2008).

### **F.6.4 Diffuse Field**

Diffuse field measurements have been proposed for a range of characterization applications, from rocks (Scales and Malcolm 2003; Malcolm et al. 2004) to polycrystalline metals (Weaver 1982; Turner 1999; Ghoshal and Turner 2009). When a material is insonified with ultrasonic energy, grain scattering results in a portion of the energy being multiply-scattered before returning to the receive transducer; i.e., multiply-scattered wave transport is when a wave propagates through a sufficiently disordered medium, it will undergo many scattering events. This can lead to diffusive transport, or in the worst case, localized behavior in which transport comes to a halt. For times that are large when compared to the first direct reflection (Lobkis and Weaver 2001), the propagation behavior of the scattered energy satisfies a diffusion equation and the resulting field

measurement is referred to as the diffuse field measurement. However, the diffuse field measurement is a stochastic quantity due to the random nature of the multiple scattering. Theoretical analysis and modeling of diffuse field phenomena has been done by several researchers (Weaver 1982; Turner and Weaver 1995; Turner 1999; Sgard et al. 2000; Lobkis and Weaver 2001; Weaver and Lobkis 2005b, a; Ghoshal and Turner 2009). The diffuse field depends on a range of factors including temperature (Weaver and Lobkis 2000). Diffuse field measurements have been applied in the experimental characterization of high scattering materials with random structure such as cement-based materials (Becker et al. 2003) and have been shown to correlate with crack length in concrete (Ramamoorthy et al. 2004).

Diffuse fields have also been studied in polycrystalline media (Turner and Weaver 1995). These studies presented both theoretical development and some experimental verification of the diffuse field phenomenon. Multiple scattering is typically considered in any diffuse field theoretical development. Ghoshal and Turner (2009) discussed the theoretical investigation of backscatter in polycrystalline materials. Similar measurements for semi-solid materials (such as slurries) have also been conducted, with diffusion parameters recovered from the data (Weaver and Sachse 1994). Ghoshal and Turner (2009) investigated theoretically (and confirmed experimentally) diffuse field backscatter in polycrystalline materials. This may be a useful tool to characterize microstructures in CASS. While these (and other similar) studies have shown the diffuse field phenomena in highly scattering anisotropic materials, there appears to be little effort in the characterization of material microstructure from diffuse field data. For CASS microstructure characterization using backscattered measurements, the key issue will be frequency selection. A monochromatic ultrasonic signal may be necessary for this application. In addition, a large aperture may be needed to get sufficient penetration in CASS materials.

Diffuse field measurements present intriguing possibilities for CASS microstructure characterization. To date, however, diffuse fields have been used to characterize heterogeneous and anisotropic media such as cement paste and concrete. No published literature on diffuse fields for coarse-grained microstructure characterization was found. Key features from the diffuse field measurements include the time-of-arrival of the energy peak, peak value of the energy, diffusivity, and dissipation. The variation of these parameters as a function of frequency can potentially be used for CASS microstructure characterization.

## **F.7 Other Approaches**

The measurement methods below are discussed in a separate section because either little research was found with respect to application to coarse-grained materials or the method is largely theoretical. Those methods include:

- Scattering, with full-matrix capture
- Acoustic backscatter
- Spectral processing
- Shear wave birefringence
- Time reversal
- Medical imaging
- Shear wave modulence
- Nonlinear acoustics.

### **F.7.1 Scattering, with Full-Matrix Capture**

In full-matrix capture, an array of transducers is used. Each element of the array is pulsed in sequence to insonify the component (each element is used as the transmitter in turn), and all elements are used to receive the scattered/reflected signal (resulting in a measurement matrix where all potential transmit-receive pairs are used). Alternatively, the elements of the PA are pulsed with specified phase delays. The resulting ultrasonic signal is focused at a specific location due to constructive and destructive interference of the individual wave fronts. Such full-matrix measurements may be post-processed to synthetically focus the ultrasonic beam at all points in the specimen (Wilcox et al. 2007) to give the amplitude, orientation, and specularity of any reflectors.

A variation on this approach uses the scattering matrix, where a transmit-receive array covers all incidence angles (Zhang et al. 2008). In either case, the predominant application of this technique has been to characterize flaws in the specimen. Other variations on this approach are to use multiple arrays (Kröening et al. 2008), with one transducer transmitting and all listening. This “sampling phased array” system with “inverse phase matching” results in measurements that are processed using SAFT-like algorithms to improve resolution. This approach may be good for inspecting thick specimens, and some figures were provided in the literature on beam profiles in composites (heterogeneous anisotropic materials). This could have possibilities for CASS characterization.

### **F.7.2 Acoustic Backscatter**

Scattering in the direction of the transmitting transducer is often referred to as backscatter. However, the scattered energy at any angle (relative to the transmit direction) can be measured if a receiver can be placed appropriately. Backscatter measurements have been used for a range of material characterization applications. The backscattered signal has been correlated with grain size (Willems and Goebbels 1982; Feuilly et al. 2009). Multiple scattering will become significant the larger the grain size, however, and the technique will have limitations. Moysan and Corneloup (2000) discussed the use of backscatter attenuation to characterize texture and orientation in transversely isotropic welds. Backscattered acoustic signals from annealed polycrystalline aluminum possess fractal characteristics (Barat et al. 1998), and a grain size distribution can be deduced to match the distribution obtained experimentally in polycrystalline materials. Miralles et al. (2004) and Miralles and Vergara (1999) presented a different approach to grain structure/size determination using backscatter. They used high-order statistics and derived relations between the material and transducer parameters and the first, second, and third order cumulants of the backscattered signal.

The ability to time-gate a signal and select backscatter from a specific region in the material may make backscattering (and high-order statistics) attractive for CASS microstructure characterization. However, it is not clear if such an approach will work for materials with strong multiple scattering, and in such cases, the backscattered measurement may only be indicative of bulk properties. Note that, with multiple scattering, the backscatter measurement shows a peak that is delayed relative to the single scattering case (Turner and Weaver 1995), and the delay is a function of the grain size, angle of incidence and measurement, and the frequency. It is, however, not clear how scattering measurements may apply to coarse-grained materials, where there may be only a few grains that the ultrasonic beam interacts with prior to reflection from the back surface (Goebbels 1980). In such a case, it is likely that the scattered field will resemble the single-scattering scenario more than the strong multiple-scattering scenario. Note that in CASS materials (or in anisotropic inhomogeneous materials in general), the beam-bending and splitting

that is likely to occur, particularly with angle-beam incidence, makes microstructure characterization using angle-beam incidence a difficult proposition if the goal is to classify microstructure as a function of depth/location. On the other hand, angle-beam incidence backscatter can potentially be used to do bulk microstructure classification.

### **F.7.3 Spectral Processing**

Full-matrix measurements have the potential for characterization of reflectors; however, a processing technique that works with single pulse-echo measurements may be just as effective. Jayakumar and colleagues (Kumar et al. 1999; Jayakumar et al. 2008) discussed the use of spectral processing (strictly speaking, spectral features) to determine grain size. Back-surface reflections were Fourier transformed, and the full width at half maximum of the spectrum was shown to correlate well with grain size. This feature was also shown to be robust to inadequate coupling. Alternative features include the critically reflected longitudinal-wave transit time, which correlates with residual stress. Other potential features include the power spectrum from contact pulse-echo measurements (Stella et al. 2009), which is a potentially useful feature that correlates with degree of sensitization (local chromium carbide precipitation and chromium depletion leading to increased susceptibility to IGSCC) in stainless steels.

### **F.7.4 Shear Wave Birefringence**

Birefringence is a phenomenon in which two waves of the same mode and frequency, but different polarizations can propagate with different velocities. Shear waves traveling through an oriented anisotropic medium, with polarization at an angle to the orientation, undergo changes in polarization due to birefringence (Ensminger 1973). This phenomenon has been used to measure residual stresses in materials (Sayers 1984), as well as microstructure variations due to aging in stainless steel (Doctor et al. 1989; Ruiz et al. 2009). However, there appears to be little literature on the use of this phenomenon for coarse-grained microstructure characterization.

### **F.7.5 Time Reversal**

Time-reversal acoustics has been proposed as a viable technique for imaging of flaws in nonhomogeneous media. The basic idea behind time-reversal is the invariance of the time-reversal operator (Fink et al. 1989; Clouet and Fouque 1997) in lossless (characterized by or causing no dissipation of energy) media (Prada et al. 2002; Kerbrat et al. 2003). Under these circumstances, it has been shown that by emitting the time-reversed measurement due to a source, at a set of transducers, the acoustic field formed a focus at the acoustic source. The time-reversal measurements may be made either using an iterative approach, or using the decomposition of the time-reversal operator (Kerbrat et al. 2003). In either case, the technique was seen to suppress noise from a highly scattering medium while improving the imaging and localization capabilities of flaws in heterogeneous media. However, it is not clear how anisotropic media affect the time-reversal focusing effect. Jeong et al. (2009) discussed time-reversal simulation in anisotropic media, and showed that, as long as the ultrasonic beam was along the axis of symmetry of anisotropic media (such as, for instance, in transversely isotropic media), the focusing effect was still valid. Whether this effect is present for off-axis incidence is still to be determined. Time-reversal ultrasonics fundamentally act to mitigate the effect of scattering noise; it is not clear whether this technique can be used to isolate the scattering noise and characterize microstructure.

The decomposition of the time-reversal operator adaptation of the time-reversal approach uses the singular value decomposition of the array impulse response (obtained by using full-matrix capture methods). The number of significant singular values of the response matrix is equal to the number of flaw-like scatterers in the material. In general, the remaining singular values are typically related to the measurement noise, including noise from scattering in the material. It is likely that by examining the “noise” subspace of the response matrix (i.e., the smallest singular values), we may be able to obtain microstructure information. Again, this approach does not appear to have been investigated in the published time-reversal literature, although there are noise-subspace-based analysis techniques in other applications such as hyperspectral image analysis (Te-Ming et al. 1998).

### **F.7.6 Medical Imaging**

One point to be taken from the medical literature is the importance of presentation methods. For example, Sofka et al. (2005) reported that color presentation with enhanced contrast enabled better diagnoses than the conventional gray-scale imaging, and that presentation of multiple planes was better for some purposes than full three-dimensional visualization. Imaging with D-shaped apertures is an optical microscopy technique for imaging through scattering media. Sheppard et al. (2009) described a renewed interest in this old technique, with some new methods. The aperture shape reduced scattering by separating illumination and reception paths. A two-frequency approach provided further improvement in depth of penetration, using a fluorescence response. While fluorescence is not an ultrasonic phenomenon, it may have an analogue in ultrasonic resonance response or nonlinear acoustics.

Ultrasonic imaging through the skull presents some similarities to CASS inspection. Vignon et al. (2005) described the use of twin linear arrays in pitch-catch mode to reduce the aberrations caused by the irregularity of the skull. White et al. (2009) found that using shear rather than longitudinal mode improved the ability to image through the skull. Kretschmann and Weinrich (2004) discussed a number of methods used in cranial ultrasonic imaging, some of which may have applicability to CASS characterization.

### **F.7.7 Shear Wave Modulus**

Shear wave modulus (Sagar et al. 2007) has been used to study precipitation hardening in maraging steels, ultrasonic C-scan imaging of microstructure and grain size during dynamic recrystallization in stainless steel alloys (Mandal et al. 2008), and a non-coherent detector (Ericsson and Gustafsson 1998) with entropy-based performance metric to reduce backscatter noise in CASS inspection. While this approach is used to remove noise, it could perhaps also be used to characterize grain noise and, consequently, the grain structure. Circularly polarized waves have been reported for determining surface corrugation direction (Declercq et al. 2002), which suggests that the same technique could be used to determine internal crystal orientation. Further, two U.S. patents refer to generating and using elliptically or circularly polarized acoustical waves for seismic characterization.

### **F.7.8 Nonlinear Acoustics**

Nonlinear acoustics has been used in recent years as an important NDE tool for fatigue crack detection in polycrystalline materials (Cantrell and Yost 2001) as well as material degradation detection (Adler and Mattei 2000; Kulkarni and Achenbach 2008). In nonlinear acoustics, an incident single-tone ultrasonic beam is applied to the material under test. A nonlinear response results in the presence of higher harmonics, from which a nonlinearity parameter can be



computed (Cantrell and Yost 2001). The nonlinear elastic response is postulated to be due to structural inhomogeneity and defects as well as adsorbed and free fluids contained in the soft inclusions (Ostrovsky et al. 2000). Nonlinear acoustics measurements appear to have seen relatively little application to microstructure characterization, though Jerebtsov et al. (2004) discussed nonlinear surface acoustic wave generation and acoustic/elastic constant determination in coarse-grained steel.

## **F.8 Simulation and Analytical Models**

The most common approaches used to gain insights into acoustic responses are simulation models and analytical models. Advances in mathematical modeling to improve the understanding of ultrasonic wave behavior in solids have been studied for years (e.g., Pao 1983). Analytically calculated solutions are available for simple scattering geometries, but the study of ultrasonic waves in inhomogeneous, anisotropic materials requires the use of numerical techniques. Most numerical techniques solve the partial differential equations that govern the behavior of elastic waves in solids. Among these, the more commonly used techniques include the finite element method, finite difference method, and hybrid finite element/finite difference methods (Bond 1990), although developments in this area include the boundary-element method (Bond 1990; Achenbach 1992) and the elasto-dynamic finite integration technique (Hannemann et al. 2000).

Pure analytical approaches to describing acoustic behavior are somewhat limited; for instance, O'Neill and Maev (2002) derive an analytical approximation to convergent ultrasonic beam behavior in anisotropic materials. Modeling approaches that solve the governing equations for wave propagation typically provide the best descriptions (Chassignole et al. 2000), though they can be computationally intensive. Modeling methods based on a combination of analysis and approximation enable a full study of the complex behavior of acoustic waves in coarse-grained materials. Three generic classes of models have been used in the simulation modeling of acoustic wave propagation behavior in coarse-grained materials. Each of these classes of models has specific advantages (Bond 1990). Finite element methods numerically solve the governing differential equations for acoustic wave propagation. The solution is typically computed by dividing the problem domain into small regions called elements and minimizing a functional in each of these elements. The finite difference method of simulation computes the wave field on a predefined set of grid points. The spatial and temporal evolution of the unknown quantity (such as pressure) is given by a set of (typically coupled) partial differential equations. The finite difference method replaces spatial derivatives with finite difference operators that are defined using neighboring points on the grid. Ray tracing provides an approximate solution to the wave propagation behavior when the wavelengths are much smaller (or larger) than the grain sizes. The resulting model is typically applied only to single scatterers embedded in an isotropic medium, with the modeling of multiple scattering being difficult in this framework. Many of the studies cited above use commercially available tools for the forward modeling. Ray trace and semi-analytical tools include CIVA,<sup>10</sup> UTSim,<sup>11</sup> and Imagine3D.<sup>12</sup> Finite element-based packages include ATHENA, PZFlex,<sup>13</sup> COMSOL Multiphysics,<sup>14</sup> and Ansys<sup>15</sup> although commercial finite element

---

<sup>10</sup> <http://www.civa.cea.fr/scripts/home/publigen/content/templates/show.asp?P=55&L=EN>

<sup>11</sup> <http://www.cnde.iastate.edu>

<sup>12</sup> <http://www.utex.com/Products/Simulation/I3d/Imagine3D.htm>

<sup>13</sup> <http://www.pzflex.com/about.aspx>

<sup>14</sup> <http://www.comsol.com/products/>

<sup>15</sup> <http://www.ansys.com/products/default.asp>

tools are somewhat limited in their ability to model elastic waves in solids. Recent developments include the hybridization of CIVA with ATHENA.

Modeling is a useful tool in understanding the behavior of ultrasonic beams in specific microstructure distributions. The key issues in this context are:

- Obtaining information on elastic constants and anisotropy as well as grain shapes and sizes to ensure that the model is actually representing the physical microstructure.
- Validating the model; validation efforts may need some fundamental studies on beam mapping inside the material. Such a study can be undertaken, for instance, by repeatedly machining the specimen to remove a thin section and measuring the ultrasonic field distribution and material parameters (as described in Crawford et al. 2014).
- Determination of the best modeling tool (finite element, finite difference, elasto-dynamic finite integration, boundary element, etc.) for these studies in terms of accuracy and computation time. From the literature analysis, it appears that ray-trace techniques may be the fastest solution for modeling, although finite-element-based models may have better accuracy.

## **F.9 Conclusions**

The literature search revealed that most of the investigations determining wave behavior (ultrasonic beam propagation) in coarse-grained structures address materials that have a single microstructural form (either equiaxed or columnar). The exception seems to be beam propagation from base materials (typically assumed to be homogeneous isotropic) into welds (columnar grains). These studies provide insight into ultrasonic beam propagation in coarse-grained materials.

Further, the literature search has revealed that in situ characterization of CASS microstructures for the optimization of inspection capabilities for specific grain structures is in its early stages. Low frequency PA-UT techniques will continue to advance potentially to a level where in situ characterization would provide little added benefit. Should in situ characterization be pursued in the future, however, the literature search has revealed certain gaps. Little information exists on beam propagation in layered or banded coarse-grained materials, or techniques for the interpretation of measurements for characterizing and categorizing microstructure. At this time, it appears unlikely that a single measurement type (such as attenuation or time-of-flight alone) will provide sufficient information to correctly identify the diverse microstructural categories in CASS materials. In that case, a range of measurements will be necessary for accurate microstructure characterization in CASS. It may be possible to use signal processing tools to enhance the SNR and compute key attributes from the measurements and use model-based iterative algorithms to solve the inverse problem of microstructural characterization and categorization given the enhanced measurements.

**BIBLIOGRAPHIC DATA SHEET**

(See instructions on the reverse)

1. REPORT NUMBER  
(Assigned by NRC, Add Vol., Supp., Rev.,  
and Addendum Numbers, if any.)

**NURE/CR-7263  
PNNL-28840**

2. TITLE AND SUBTITLE

**NDE Reliability Issues for the Examination of CASS Components**

3. DATE REPORT PUBLISHED

MONTH	YEAR
<b>September</b>	<b>2019</b>

4. FIN OR GRANT NUMBER

5. AUTHOR(S)

R.E. Jacob, S.L. Crawford, T.L. Moran, M.R. Larche, M.S. Prowant,  
A.A. Diaz, C.A. Nove

6. TYPE OF REPORT

Technical

7. PERIOD COVERED (Inclusive Dates)

8. PERFORMING ORGANIZATION - NAME AND ADDRESS (If NRC, provide Division, Office or Region, U. S. Nuclear Regulatory Commission, and mailing address; if contractor, provide name and mailing address.)

Pacific Northwest National Laboratory  
P.O. Box 999  
Richland, WA 99352

9. SPONSORING ORGANIZATION - NAME AND ADDRESS (If NRC, type "Same as above", if contractor, provide NRC Division, Office or Region, U. S. Nuclear Regulatory Commission, and mailing address.)

Division of Engineering  
Office of Nuclear Regulatory Research  
U.S. Nuclear Regulatory Commission  
Washington, DC 20555-0001

10. SUPPLEMENTARY NOTES

11. ABSTRACT (200 words or less)

Pacific Northwest National Laboratory has performed nondestructive examination (NDE) research under the sponsorship of the U.S. Nuclear Regulatory Commission (NRC) to evaluate state-of-the-art technical approaches for examining safety-related nuclear reactor components that pose significant challenges to traditional NDE methods. A specific area of research in this regard is the volumetric examination of coarse-grained, Cast Austenitic Stainless Steel (CASS) weldments and base materials. The primary objectives of the report are to assess the overall feasibility for advanced NDE methods to reliably and effectively examine field CASS piping components, and to determine if techniques similar to those described in existing standards could be applied to develop performance demonstration requirements for CASS piping components. This report discusses improving the reliability of CASS examinations through the use of advanced low-frequency phased array techniques, coupled with other "best practice" examination parameters, and makes recommendations regarding the development of effective performance-based qualifications for CASS weldments. In addition to the PNNL research documented here, over 230 publications have been reviewed in the development of this document, making this report a useful resource for engineers and scientists involved in NDE of CASS for purposes of inservice inspection on existing plants during current and extended periods of operation.

12. KEY WORDS/DESCRIPTORS (List words or phrases that will assist researchers in locating the report.)

Nondestructive Examination, Phased-Array Ultrasonic Testing, Inservice Inspection,  
Cast Austenitic Stainless Steel, Performance Demonstration, Modeling and  
Simulation

13. AVAILABILITY STATEMENT

unlimited

14. SECURITY CLASSIFICATION

(This Page)

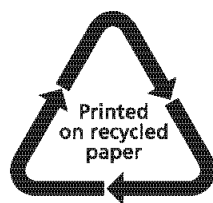
unclassified

(This Report)

unclassified

15. NUMBER OF PAGES

16. PRICE



Federal Recycling Program





UNITED STATES  
NUCLEAR REGULATORY COMMISSION  
WASHINGTON, DC 20555-0001

OFFICIAL BUSINESS



**NURE/CR-7263**

**NDE Reliability Issues for the Examination of CASS Components**

**September 2019**